POLITECNICO DI MILANO
DIPARTIMENTO DI MATEMATICA

PH. D. COURSE IN MATHEMATICAL ENGINEERING -
XVIII CICLE

NUMERICAL MODELING OF DEFECTIVE BOUNDARY PROBLEMS IN INCOMPRESSIBLE FLUID-DYNAMICS

Applications to Computational Haemodynamics

Advisor: Prof. Alessandro Veneziani
Ph.D. school coordinator: Prof. Filippo Gazzola
Candidate: Christian Vergara

ACCADEMIC YEAR 2005–2006

Contents

Chapter 1

Motivations and State of the Art

1.1 Introduction

The mathematical modelization of many fluid-dynamics phenomena leads to Partial Differential Problems, like the *Navier-Stokes* or the *Euler* equations. In view of a numerical resolution of these problems, it is very important to specify a suitable domain in which the equations are solved. In many engineering fluid dynamics problems, this computational domain is part of a system or a network. In this case, a part of the boundary does not correspond to a physical wall, and it is just introduced to limit the domain of interest. The prescription of boundary conditions on such *artificial* boundaries can be source of numerical inaccuracies. In particular, in different contexts of internal fluid dynamics there is sometimes the problem of managing numerically *defective boundary data sets*, namely data that are not enough to have a mathematically well posed problem.

One of the fluid-dynamics field in which there is often the problem of managing defective boundary problems is *haemodynamics* (see [14, 15, 56, 70]). In fact, it is quite typical in this case to have only average data from the clinical measurements. Another example concernes fluid jets. In particular, it is often the case that in the simulation of a fluid through a hole in a plane, only the flux through the aperture is available as boundary information (see [28]). The same situation occurs also in the internal combustion problems. However, in other engineering field there could be the problem of managing this kind of data. For example, in the mass-transport problem, modeled with a diffusion-convective-reaction equation, it is often difficult to obtain pointwise informations concerning the concentration on a surface. Nevertheless, since the field that mainly inspired and justified the present work is haemodynamics, we focus on the Navier-Stokes equations, that are suitable for a mathematical description of blood in specific physiological conditions (see [54, 17] and Section 3.1.2).

In this context, the problem of the defective boundary data has been analyzed at the mathematical and numerical levels since about ten years (see [28, 68]). For instance, it can be happen in solving fluid problems in a network of pipes to have at the inlet only the flow rate (*flow rate problem*). At the practical level, in the engineering literature this problem has been solved by choosing a velocity profile fitting the given flow rate. Since the numerical solution obtained in this way is strongly affected by the selected profile, a common approach is to enlarge the computational domain, in order to reduce the effect of the "arbitrary" profile prescription in the zone of interest. In [28] a different, mathematically more sound, approach is proposed. This is based on finding a suitable variational formulation of the flow rate problem able to include the given data. The defective data set is completed by homogeneous natural boundary condition for the selected variational formulation. However, this approach is somehow problematic at the numerical level, since it requires the definition of non-standard finite dimensional subspaces. A different strategy, based on a Lagrange multiplier approach, has been therefore proposed in [14] for the steady Stokes problem. With this approach, the finite dimensional environment for the numerical solution refers to standard functional spaces and therefore a particular attention was given to this strategy.

Another defective boundary problem arises when only an average pressure is available (*mean pressure problem*). In this case, the approach relying on finding a suitable variational formulation able to include the given data leads to reliable results only with particular computational domains.

Defective boundary problems are therefore far to be analysed and treated in a satisfactory and exhaustive way. For this reason, the present work has addressed in finding new formulations and numerical strategies for the prescription of defective data sets. We can essentially split this work into three subparts. In the first one (Chapter 2), we consider only the flow rate problem and we extend to a general case the strategy proposed in [14]. In the second part (Chapter 3), we aim at applicating this strategy in *computational haemodynamics*. In particular, thanks to the right prescription of a flow rate boundary condition, it was possible to introduce in current clinical practice an improvement in estimate the flow rate measure with a *Doppler* velocimetry technique. Finally, in the third part (Chapter 4), we introduce and test a completely new approach for the prescription of defective boundary conditions, based on the control theory. This strategy has the advantage that can be applied both to the flow rate and to the mean pressure problem as well.

In the sequel of this Chapter, we introduce the Navier-Stokes equations (Section 1.2.1) and we present the defective boundary problems (Section 1.2.2). We address with more details the haemodynamics problem in Section 1.2.3. Then, we

review the strategies introduced in literature for these kind of problems (Section 1.3).

1.2 Navier-Stokes equations and defective boundary conditions

1.2.1 General settings

In this section, we introduce the Navier-Stokes equations for the description of an incompressible fluid. Referring to the computational domain $\Omega \subset \mathbb{R}^d$, $d = 2, 3$, in Figure 1.1, let us consider the momentum and the mass conservation laws for an incompressible fluid (see [55, 32]):

$$\begin{cases} \rho \dfrac{D\boldsymbol{u}}{Dt} - \nabla \cdot \sigma = \rho \boldsymbol{f}, \quad (t, \boldsymbol{x}) \in Y_T := (0, T] \times \Omega \\ \dfrac{\partial \rho}{\partial t} + \nabla \cdot (\rho \boldsymbol{u}) = 0, \quad (t, \boldsymbol{x}) \in Y_T \\ \boldsymbol{u}|_{t=0} = \boldsymbol{u}_0, \quad \boldsymbol{x} \in \Omega \end{cases} \tag{1.1}$$

where $\boldsymbol{u}(t, \boldsymbol{x})$ is the velocity field (indicated as all the vectors in bold), σ the

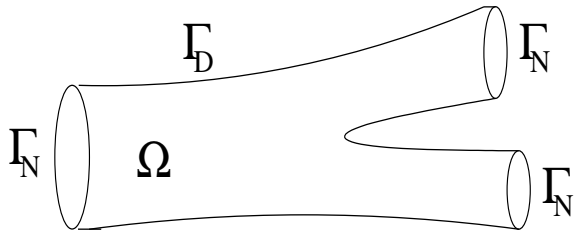

Figure 1.1: Reference computational domain Ω.

Cauchy stress tensor, $\rho(t, \boldsymbol{x})$ the density, T the final time, $\boldsymbol{u}_0(\boldsymbol{x})$ the *initial condition* and $\boldsymbol{f}(t, \boldsymbol{x})$ a forcing term. Moreover,

$$\frac{D\boldsymbol{u}}{Dt} = \frac{\partial \boldsymbol{u}}{\partial t} + (\boldsymbol{u} \cdot \nabla)\boldsymbol{u}$$

is the *material time derivative* of the velocity field in an *Eulerian* framework. We refer to the second of (1.1) as the *incompressible constraint*.

In the present work, we consider a particular class of fluid. In particular, we assume the density ρ constant in space (*homogeneous* fluid) and in time. Moreover, we consider a linear relation between σ and the *rate of deformation tensor*

$$s = \frac{1}{2}(\nabla \boldsymbol{u} + (\nabla \boldsymbol{u})^t).$$

In particular, we consider a *Newtonian* fluid, featuring

$$\sigma = -pI + 2\mu s,$$

where μ is the kinematics viscosity (assumed to be constant), $p(t, \boldsymbol{x})$ the pressure and I the $d \times d$ identity tensor. Therefore, let us consider the *Navier-Stokes equations* for a homogeneous incompressible Newtonian fluid:

$$\begin{cases} \rho \dfrac{\partial \boldsymbol{u}}{\partial t} - \nabla \cdot \mu(\nabla \boldsymbol{u} + (\nabla \boldsymbol{u})^t) + \rho(\boldsymbol{u} \cdot \nabla)\boldsymbol{u} + \nabla p = \rho \boldsymbol{f}, \quad (t, \boldsymbol{x}) \in Y_T \\ \nabla \cdot \boldsymbol{u} = 0, \quad (t, \boldsymbol{x}) \in Y_T \\ \boldsymbol{u}|_{t=0} = \boldsymbol{u}_0, \quad \boldsymbol{x} \in \Omega \end{cases} \tag{1.2}$$

When we can neglect the convective term $\rho(\boldsymbol{u} \cdot \nabla)\boldsymbol{u}$, we recover the so called *Stokes equations*. Otherwise, when the convective term is replaced by $\rho(\boldsymbol{\beta} \cdot \nabla)\boldsymbol{u}$, with $\boldsymbol{\beta}$ a given velocity field, we have the *Oseen equations*. In particular, a part from Section 3.4, we consider equations (1.2) in rigid domains, so that Ω is constant in time.

From the mathematical viewpoint, the 3D (2D) fluid-dynamics problem, described by the incompressible Navier-Stokes equations, requires the assignment of three (two) scalar conditions on each boundary point. Namely, referring to Figure 1.1, we can prescribe the velocity field (*Dirichlet* boundary condition):

$$\boldsymbol{u}|_{\Gamma_D} = \boldsymbol{g}, \quad t \in (0, T] \tag{1.3}$$

or the *stress tensor* (*Neumann*/natural boundary condition):

$$(\sigma \boldsymbol{n})|_{\Gamma_N} = \boldsymbol{h}, \quad t \in (0, T] \tag{1.4}$$

where $\boldsymbol{g}(t, \boldsymbol{x})$ and $\boldsymbol{h}(t, \boldsymbol{x})$ are given functions definied on the boundary, $\Gamma_D \cup \Gamma_N = \partial\Omega$ and $\Gamma_D \cap \Gamma_N = \varnothing$ and $\boldsymbol{n}(\boldsymbol{x})$ is the unit normal vector to $\partial\Omega$.

In view of a numerical discretization of equations (1.2), (1.3) and (1.4), we introduce a suitable *variational formulation* (see [55]). Let us set:

$$\begin{cases} (\boldsymbol{v}, \boldsymbol{w}) = \displaystyle\int_\Omega \boldsymbol{v} \cdot \boldsymbol{w} \, d\omega \\ b(q, \boldsymbol{v}) - \displaystyle\int_\Omega q \, \nabla \cdot \boldsymbol{v} \, d\omega \end{cases}$$

and the following space

$$\boldsymbol{V}_D = \boldsymbol{H}^1_{\Gamma_D}(\Omega) = \{\boldsymbol{v} \in \boldsymbol{H}^1(\Omega) : \boldsymbol{v}|_{\Gamma_D} = \boldsymbol{0}\},$$

with $\boldsymbol{H}^1(\Omega)$ the usual Sobolev space. Moreover, given a generic Hilbert space $\boldsymbol{W}$, let us denote

$$\boldsymbol{W}^* = \{\boldsymbol{v} \in \boldsymbol{W} : \nabla \cdot \boldsymbol{v} = 0\}.$$

Let us notice that applying the divergence of σ in $(1.2)_1$, we could take into account the incompressibility constraint $(1.2)_2$. In this case, we would obtain:

$$\nabla \cdot \mu(\nabla \boldsymbol{u} + (\nabla \boldsymbol{u})^t) = \mu \triangle \boldsymbol{u} + \mu \nabla(\nabla \cdot \boldsymbol{u}) = \mu \triangle \boldsymbol{u}. \tag{1.5}$$

Different variational formulations are obtained by taking into account (1.5). In particular, we obtain the following (see [55]):

Problem 1 *Given $\boldsymbol{u}_0 \in \boldsymbol{L}^2(\Omega)^*$, $\boldsymbol{f} \in L^2(0,T;\boldsymbol{L}^2(\Omega))$, find $\boldsymbol{u} \in L^2(0,T;\boldsymbol{V}_D) \cap L^\infty(0,T;\boldsymbol{L}^2(\Omega))$ and $p \in L^2(0,T;L^2(\Omega))$, such that, for each $t \in (0,T]$:*

$$\begin{cases} \rho\Big(\dfrac{\partial \boldsymbol{u}}{\partial t}, \boldsymbol{v}\Big) + a(\boldsymbol{u},\boldsymbol{v}) + \rho((\boldsymbol{u}\cdot\nabla)\boldsymbol{u},\boldsymbol{v}) + b(p,\boldsymbol{v}) = \rho(\widetilde{\boldsymbol{f}},\boldsymbol{v}) + (\boldsymbol{h},\boldsymbol{v})_{L^2(\Gamma_N)} \\ b(q,\boldsymbol{u}) = 0 \end{cases}$$

for all $\boldsymbol{v} \in \boldsymbol{V}_D$ and $q \in L^2(\Omega)$ and with the initial condition $\boldsymbol{u}|_{t=0} = \boldsymbol{u}_0$.

In Problem 1, we set

$$a(\boldsymbol{v},\boldsymbol{w}) = a_L(\boldsymbol{v},\boldsymbol{w}) = \mu \int_\Omega \nabla \boldsymbol{v} : \nabla \boldsymbol{w}\, d\omega \tag{1.6}$$

if (1.5) is considered, while

$$a(\boldsymbol{v},\boldsymbol{w}) = a_C(\boldsymbol{v},\boldsymbol{w}) = \mu \int_\Omega (\nabla \boldsymbol{v} + (\nabla \boldsymbol{v})^t) : \nabla \boldsymbol{w}\, d\omega \tag{1.7}$$

otherwise. These two treatments of the viscous term lead to different natural boundary conditions as well. In particular, if (1.6) holds, condition (1.4) becomes

$$(-p\boldsymbol{n} + \mu \nabla \boldsymbol{u}\ \boldsymbol{n})|_{\Gamma_N} = \boldsymbol{h}, \quad t \in (0,T].$$

On the contrary, if (1.7) holds, condition (1.4) becomes

$$(-p\boldsymbol{n} + \mu(\nabla \boldsymbol{u} + (\nabla \boldsymbol{u})^t)\boldsymbol{n})|_{\Gamma_N} = \boldsymbol{h}, \quad t \in (0,T]. \tag{1.8}$$

From the physical point of view, the latter choice is more correct, since it contains the exact form of the rate of deformation tensor. In fact, it is commonly used when the Navier-Stokes equations are considered in moving domains, where it is necessary that the stress given by the fluid to the structure is of the type (1.8) (see [25]). Nevertheless, in rigid domains formulations based on (1.5) are often used. In the sequel, we refer to (1.5) and (1.6) as "laplacian", while to the one given by (1.7) as "complete". Other variational formulations leading to different natural boundary conditions can be considered as well (see [3, 28, 68] and Section 1.3). We point out that if $\boldsymbol{g} \neq \boldsymbol{0}$ in (1.3), in Problem 1 $\widetilde{\boldsymbol{f}}$ includes also the terms arising from a lifting procedure and $\boldsymbol{u}$ has to be intended belonging to $\boldsymbol{V}_D$.

1.2.2 Defective boundary conditions

In many fluid-dynamics problems the numerical simulations aim at obtaining some quantitative informations on a local phenomenon, confined in a domain that is part of a complex system or a network. Therefore, in order to obtain numerical results with a reasonable computational cost, it is necessary to consider a bounded domain including the zone of interest. In this computational domain a subset of the boundary corresponds to a real/physical wall. For example, in the domain in Figure 1.2 (right), Γ_w is a physical boundary. For what concernes this portion of boundary, we assume the hypothesis of *no-slip* condition, i.e. the complete adherence of the fluid on the wall. This hypothesis, if the motion occurs in rigid domains, leads to the homogeneous Dirichlet boundary condition:

$$\boldsymbol{u}|_{\Gamma_w} = \mathbf{0}, \quad t \in (0, T] \tag{1.9}$$

On the other hand, another part of the boundary ($\Gamma_0 \cup \Gamma_1 \cup \Gamma_2$ in Figure 1.2, right)

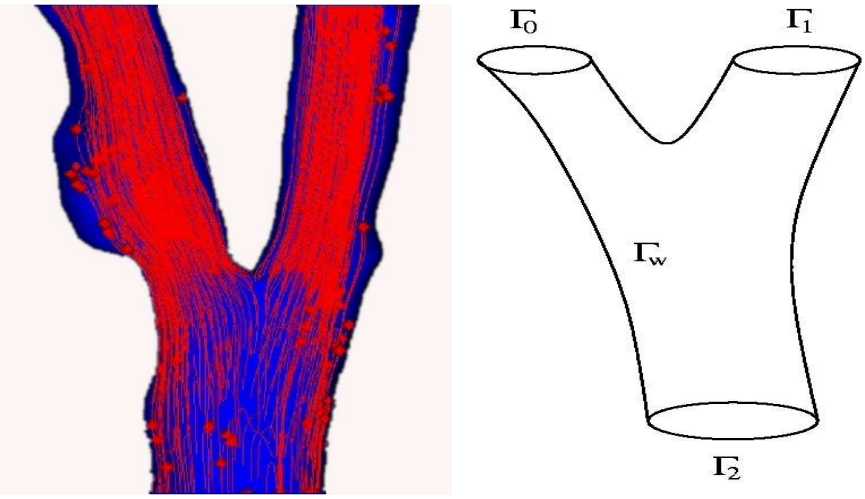

Figure 1.2: An example of a truncated domain Ω: a tipical vascular district. We detect the "physical" boundary (the vascular wall Γ_w) and the "artificial" boundaries Γ_0, Γ_1 and Γ_2.

does not correspond to a physical wall and it is just introduced to limit the domain of interest. The surfaces belonging to this part of the boundary are called *artificial* sections, since they are the interface of the district with the other parts of the circulatory system. For example, this situation occurs often in haemodynamics, where the computational domain is a truncated part of the complex vascular tree. In Figure 1.3 an example of such domain in haemodynamics is shown.

As already pointed out in the Introduction, the prescription of suitable boundary conditions on the artificial sections is a major issue in many fluid-dynamics

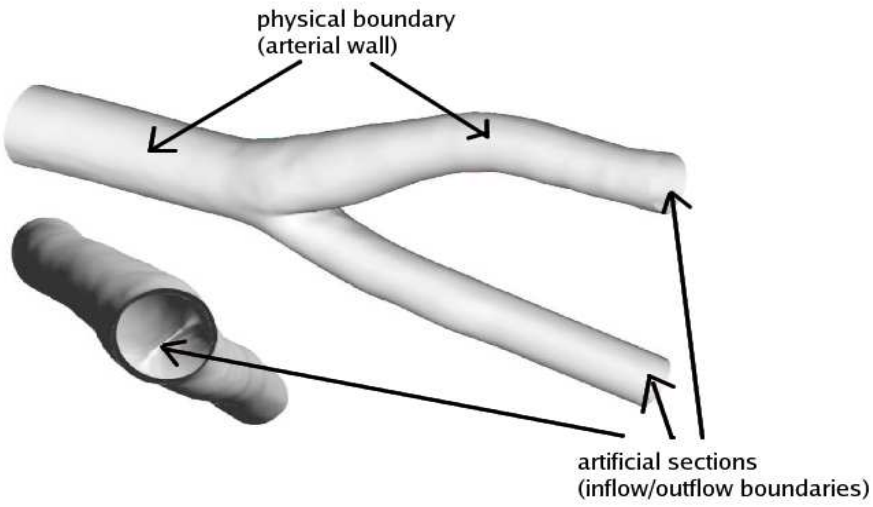

Figure 1.3: Carotid bifurcation geometry: it is possible to detect the "physical" and the "artificial" boundaries (cast by D. Liepsch - FH Munich)

problems. On one hand, it is sometimes difficult to obtain realistic informations on such boundaries. On the other, in many applications these informations (when available) refer often to an average datum. Namely, let us suppose to have $m+1$ artificial section Γ_i, $i = 0, \ldots, m$. For example, if we refer to the computational domain Ω in Figure 1.2, right, we have $m = 2$. It is worth considering *flow rate* conditions on such surfaces

$$\rho \int_{\Gamma_i} \boldsymbol{u} \cdot \boldsymbol{n} \, d\gamma = Q_i, \quad \forall i = 0, \ldots, m, \quad t \in (0, T] \tag{1.10}$$

where $Q_i = Q_i(t)$ are given. Similarly, we can deal with *mean pressure* conditions:

$$\frac{1}{|\Gamma_i|} \int_{\Gamma_i} p \, d\gamma = P_i, \quad \forall i = 0, \ldots, m, \quad t \in (0, T] \tag{1.11}$$

where $|\Gamma_i|$ is the measure of Γ_i and $P_i = P_i(t)$ are given data. In the sequel we refer to *flow rate problem* when we prescribe conditions like (1.10) and to *mean pressure problem* if we prescribe conditions like (1.11). Other conditions can be considered as well. However, here we mainly focus our attention on these ones. Conditions (1.10) and (1.11) are clearly not sufficient to achieve a well-posed mathematical problem (*defective boundary condition*) that needs pointwise conditions like (1.3) or (1.4). Specific strategies in order to fill this gap are therefore mandatory.

1.2.3 The haemodynamics case

We present now, by way of example, the haemodynamics case, that inspired and motivated the present work. The behaviour of the blood in a vascular district in non-pathological situations and in vessel sufficiently large (with radius $\geq$ 0.1, *cm*) can be described as a homogeneous incompressible Newtonian fluid (see [17, 18, 54] and Chapter 3 for a more detailed description). In haemodynamics the prescription of boundary data on the artificial sections can be based on clinical measurements. Nevertheless, pointwise data are often not available. In fact, the most commom measurement techniques used in the clinical practice, as the velocimetry Doppler technique (see [74]), give only *average* data like the flow rate and the mean pressure, over small volumes of blood or area of the lumen. Figures 1.4 shows two examples of measured physiological flow rate and mean pressure, respectively. In the last years, more sophisticated techniques, as the nuclear magnetic resonance, allow to obtain data concerning pointwise informations on an artificial section. However, these techniques are still expensive and not always available. Alternatively, when no clinical data are available, it

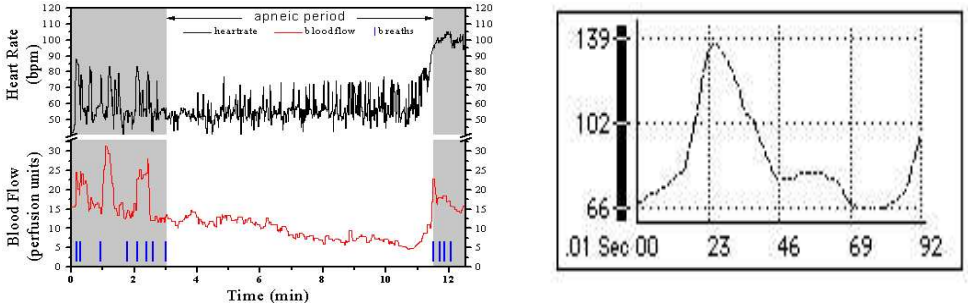

Figure 1.4: Examples of clinical measure: aortic flow rate during an apnoea test (left) and aortic mean pressure (right).

is possible to resort to the so-called *geometrical multiscale approach*, where different mathematical models for the circulation, with a different level of detail, are matched for the simulation of the whole vascular network. In particular the computational domain is coupled with a *reduced model*, taking into account the remainder of the cardiovascular system (see [51, 56] and Section 3.3). In this case, the different models need to be suitably matched at the interfaces (given by artificial sections). A common approach for the numerical treatment of this problem is to resort to iterative techniques inspired by *domain decomposition* methods, in which the 3d and the reduced models are solved alternatively and the matching conditions become boundary conditions for the two models. Nevertheless, from the mathematical view point, the reduced models deal with average

data. Therefore, in this case, the solution of the 3d problem still requires to solve a defective boundary problem (see Figure 1.5).

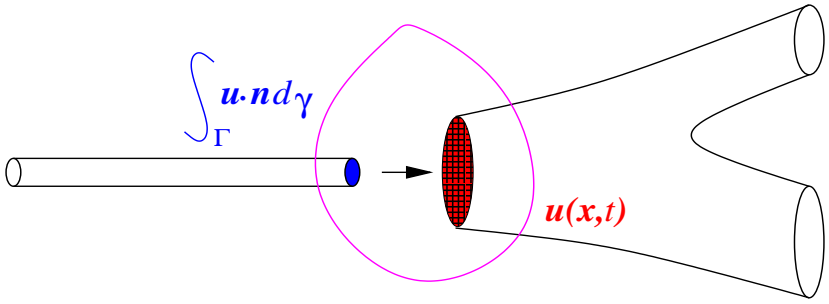

Figure 1.5: Coupling between a reduced and a three-dimensional model: the latter (on the right) receives an average datum from the first one.

We conclude that haemodynamics numerical simulations, concerning realistic geometries and physiological data, involve quite often *only average boundary conditions* on the artificial sections.

1.3 State of the art

In this section we summarize the strategies introduced in order to complete the defective boundary conditions. In particular in Section 1.3.1 we present three strategies for the flow rate problem. Section 1.3.2 is devoted to the mean pressure problem.

1.3.1 Flow rate problem

Let us consider the flow rate problem given by (1.2), (1.9) and (1.10). Since we refer to a rigid domain Ω (see Figure 1.2, right), let us notice that we can prescribe arbitrarily the flow rates (1.10) on all but one the artificial sections, for example on $\Gamma_1, \Gamma_2, \ldots, \Gamma_m$. Indeed, due to the mass conservation and the rigidity of the walls, on Γ_0 we have:

$$Q_0 = \rho \int_{\Gamma_0} \boldsymbol{u} \cdot \boldsymbol{n}\, d\gamma = -\sum_{i=1}^{m} \rho \int_{\Gamma_i} \boldsymbol{u} \cdot \boldsymbol{n}\, d\gamma = -\sum_{i=1}^{m} Q_i. \tag{1.12}$$

Moreover, for the sake of simplicity, let us suppose here and in the sequel of this work that $\rho = 1$.

A practical approach

The most common strategy used in the engineering literature in order to complete these defective boundary data consists in choosing *a priori* a velocity profile $\boldsymbol{g}_i$ on each section Γ_i where the flux is prescribed, fitting the given flow rate Q_i. Therefore, we resort to a Dirichlet boundary conditions like (1.3), such that (see Figure 1.6):

$$\int_{\Gamma_i} \boldsymbol{g}_i \cdot \boldsymbol{n}\, d\gamma = Q_i, \quad \forall i = 0, \ldots, m, \quad t \in (0, T],$$

with the values Q_i satisfying the constraint (1.12). This approach is not al-

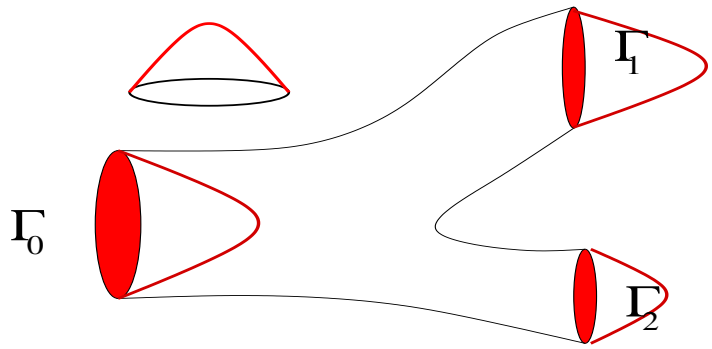

Figure 1.6: Example of a selected velocity profile prescribed at the artificial sections.

ways feasible, for istance for real geometries when an analytical expression for the profile is not available. In particular let us notice that an analytical solution is available only for a cylindrical domain perfused by a steady or a sinusoidal flow rate. In these cases we refer to the *Poiseuille* and the *Womersley* solution, respectively (see [68, 78, 29]). For a different flow rate perfusing a cylinder, a feasible approach is to decompose the wave form of the flow rate into its Fourier components and to combine basic Womersley solutions correspondly to each frequency component. Strictly speaking, this approach is exact only if the problem at hand is linear. Therefore, when the Navier-Stokes equations are considered and, in particular, for increasing values of the *Reynolds number* $Re = VL/\mu$, with V and L a characteristic velocity and a characteristic length respectively, this approach gives an approximate "feasible" solution. In general, for a realistic computational domain it is not possible to know *a priori* the exact velocity profile to be prescribed on the boundaries neither in the steady nor in the periodic case. Nevertheless, in these cases, if the artificial sections are circular, it is a common

practice to impose anyway a parabolic, a Womersley or a flat velocity profile. Since the numerical solution is strongly affected by the arbitrary selected profile, the computational domain is quite often enlarged letting the profile to develop, in order to reduce the effect of the profile prescription in the zone of interest. Obviously, this approach presents the drawback of increasing the computational costs. In particular, the higher the Reynolds number the larger has to be the enlarged zone, since the fluid needs more space to develop fully. In particular, for steady flows in a cylindrical domain, it is possible to define a characteristic length equal approximately to $0.058 \cdot D \cdot Re$ (where D is the diameter of the inlet section) at which a centreline velocity is within 1% of its final value (see [76]). A similar dependence on Re is recognized also for a non cylindrical domain and for an unsteady flow. However, in the unsteady case the development of the profile can be problematic. For example, it has been proven in [59] that for high Reynolds numbers, in a cylindric domain perfused by a periodic flux, the enlargement of 40 diameters may not be sufficient to recover the analytical (Womersley) solution if a parabolic profile is prescribed as boundary condition at the inlet. If the section where the flow rate is prescribed is not circular, some authors proposed to use anyway the Womersley solution as boundary condition, extending the computational domain by some arterial diameters, such that the cross-section transition leads to a perfectly circular artificial section in the actual geometry. Alternatively, in [79] it has been proposed to write the Womerley solution on a circle using the equivalent radius, i.e. the radius of a circle with the same area of the artificial section, and then to linearly map this profile on the original section. Nevertheless, also in this case it is necessary to extend the computational domain. Finally, we highlight that in some realistic cases, a wrong choice of the prescribed velocity profile, could lead to an error also in the computation of global quantities, such as the flow division (see e.g. [40]). Although quite simple and popular, this approach can be therefore source of serious inaccuracies and computational costs increase.

In Section 2.4 we present an error analysis of this approach.

Variational formulation-based approach

A different approach has been proposed in [28] with the aim of fulfilling flux conditions in a less perturbative way. In particular, we do not prescribe explicitely further conditions, but we try to find a variational formulation for the flow rate problem able to incorporate the (defective) boundary conditions. In such a way, the natural boundary conditions associated to the selected variational formulation are implicitely prescribed, making it well-posed the mathematical problem.

Referring to Figure 1.2, let us introduce the following spaces:

$$\begin{cases} \boldsymbol{V} = \boldsymbol{H}^1_{\Gamma_w}(\Omega) = \{\boldsymbol{v} \in \boldsymbol{H}^1(\Omega) : \boldsymbol{v}|_{\Gamma_w} = \boldsymbol{0}\} \\ \boldsymbol{V}_0 = \{\boldsymbol{v} \in \boldsymbol{V} : \displaystyle\int_{\Gamma_i} \boldsymbol{v} \cdot \boldsymbol{n}\, d\gamma = 0,\ \forall i = 0, \ldots, m\} \\ W' = \{\phi : \boldsymbol{W} \to \mathbb{R} \quad \text{linear and continuous}\} \end{cases} \tag{1.13}$$

where $\boldsymbol{W}$ is a generic functional space. It can be proven (see [3]) that there exists a set of functions $\{\boldsymbol{b}_1, \ldots, \boldsymbol{b}_m\}$, such that:

$$\begin{cases} \displaystyle\int_{\Gamma_j} \boldsymbol{b}_i \cdot \boldsymbol{n}\, d\gamma = \delta_{ij}, \quad \forall i, j = 1, \ldots, m, \\ \displaystyle\int_{\Gamma_0} \boldsymbol{b}_i \cdot \boldsymbol{n}\, d\gamma = -1, \quad \forall i = 1, \ldots, m. \end{cases} \tag{1.14}$$

Let us consider the Navier-Stokes equations with the "laplacian" treatment of the viscous term and in free divergence subspaces. Therefore, let us introduce the following variational formulation for the flow rate problem (1.2), (1.9), (1.10) and (1.12) (see [28, 68]):

Problem 2 *Given $\boldsymbol{u}_0 \in \boldsymbol{V}^*$, $\boldsymbol{f} \in L^2(0,T;\boldsymbol{L}^2(\Omega))$ and $m+1$ functions $Q_i \in C^0([0,T])$ satisfying the constraint (1.12) and setting*

$$\boldsymbol{\phi}(t, \boldsymbol{x}) = \sum_{i=1}^{m} Q_i(t) \boldsymbol{b}_i(\boldsymbol{x}),$$

find $\boldsymbol{u} \in L^2(0,T;\boldsymbol{V}^*) \cap L^\infty(0,T;\boldsymbol{L}^2(\Omega)^*)$ such that:

$$\begin{cases} \boldsymbol{u} - \boldsymbol{\phi} \in L^2(0,T;\boldsymbol{V}_0^*) \\ \left(\dfrac{\partial \boldsymbol{u}}{\partial t}, \boldsymbol{v}\right) + a_L(\boldsymbol{u}, \boldsymbol{v}) + ((\boldsymbol{u} \cdot \nabla)\boldsymbol{u}, \boldsymbol{v}) = (\boldsymbol{f}, \boldsymbol{v}) \end{cases}$$

for all $\boldsymbol{v} \in \boldsymbol{V}_0^*$ and with the initial condition $\boldsymbol{u}|_{t=0} = \boldsymbol{u}_0$.

Given $\boldsymbol{w} \in \boldsymbol{L}^2(\Omega)$ and $\boldsymbol{v} \in \boldsymbol{V}$, let us set

$$\begin{cases} \|\boldsymbol{w}\| = \|\boldsymbol{w}\|_{\boldsymbol{L}^2(\Omega)} = \displaystyle\int_\Omega |\boldsymbol{w}|^2\, d\omega \\ \|\boldsymbol{v}\|_{\boldsymbol{V}} = \|\nabla \boldsymbol{v}\| \end{cases}$$

In [28] it is proven the well-posedness of Problem 2:

Theorem 1 *For sufficiently smooth data Q_i with $\sum_i |Q_i|$ and $\|\boldsymbol{u}_0\|_{\boldsymbol{V}}$ small enough, Problem 2 is locally well-posed, i.e. there exists a time T^* such that a solution $\boldsymbol{u}$ exists for any $t \in (0, T^*)$.*

Let us investigate which boundary conditions are implicitely associated to the formulation of Problem 2. To this aim, let us introduce the set of m functions:

$$\begin{cases} C_i(t) = & C_0(t) + \displaystyle\int_\Omega \boldsymbol{f} \cdot \boldsymbol{b}_i d\omega - ((\boldsymbol{u} \cdot \nabla)\boldsymbol{u}, \boldsymbol{b}_i) + \\ & \displaystyle - \sum_{j=1}^{m} Q_j(t) a_L(\boldsymbol{b}_j, \boldsymbol{b}_i) - \Big(\frac{\partial \boldsymbol{u}}{\partial t}, \boldsymbol{b}_i\Big), \qquad i = 1, \ldots, m, \end{cases} \tag{1.15}$$

where C_0 is an arbitrary function of t. Observe that C_i, for $i = 1, \ldots, m$, depends on t and $\boldsymbol{u}$, but is indipendent of $\boldsymbol{x}$. We have the following result (see [68]):

Theorem 2 *Problem 2 is equivalent to the problem given by (1.2), (1.9), (1.10), (1.12) and the following conditions:*

$$(-p\boldsymbol{n} + \mu \nabla \boldsymbol{u}\ \boldsymbol{n})|_{\Gamma_i} = -C_i \boldsymbol{n} \quad i = 0, \ldots, m, \tag{1.16}$$

where the C_i are specified by (1.15).

Let us notice that the equivalence of the two problems has to be intended in the following sense: the smooth solutions of the problem given by (1.2), (1.9), (1.10), (1.12), (1.16) and (1.15) solve Problem 2. Conversely, if $\boldsymbol{u}$ is a solution of Problem 2, then there exists a function $p \in L^2(0, T; L^2(\Omega))$ such that $(\boldsymbol{u}, p)$ satisfies problem given by (1.2), (1.9), (1.10), (1.12), (1.16) and (1.15). Since C_0 is an arbitrary function of time, without loss of generality, in the sequel we consider the following Neumann condition on Γ_0:

$$(-p\boldsymbol{n} + \mu \nabla \boldsymbol{u}\ \boldsymbol{n})|_{\Gamma_0} = \boldsymbol{0}. \tag{1.17}$$

It is clear that the additional boundary condition implicitely hidden in Problem 2 are normal Neumann conditions costant in space and *zero tangential stress* (see conditions (1.16)). We point out that the conditions implicitely prescribed by Problem 2 would be different using the "complete" treatment of the viscous term. In particular, in this case (1.17) and (1.16) would be replaced by

$$\begin{cases} (-p\boldsymbol{n} + \mu(\nabla \boldsymbol{u} + (\nabla \boldsymbol{u})^t)\boldsymbol{n})|_{\Gamma_0} = \boldsymbol{0} \\ (-p\boldsymbol{n} + \mu(\nabla \boldsymbol{u} + (\nabla \boldsymbol{u})^t)\boldsymbol{n})|_{\Gamma_i} = -C_i \boldsymbol{n} \quad i = 1, \ldots, m. \end{cases} \tag{1.18}$$

Nevertheless, this choice it is not suitable for the computation of Poiseuille flow in a straight rigid cylindrical pipe when a flow rate (or a mean pressure) is imposed at the outlet, as pointed out in [28]. This is due to some "physical" boundary effects, not desired in a truncated domain. In particular, the tangential component of the velocity field at the outlet is non null. To avoid this phenomenon, in [68]

is proposed to prescribe a homogeneous Dirichlet boundary condition for the tangential component, to be included in the space of the variational formulation. In this case we resort to the following conditions:

$$\begin{cases} (-p + \mu(\nabla \boldsymbol{u} + (\nabla \boldsymbol{u})^t)\boldsymbol{n} \cdot \boldsymbol{n})|_{\Gamma_0} = 0 \\ (-p + \mu(\nabla \boldsymbol{u} + (\nabla \boldsymbol{u})^t)\boldsymbol{n} \cdot \boldsymbol{n})|_{\Gamma_i} = -C_i, \quad i = 1, \ldots, m \\ (\boldsymbol{u} \times \boldsymbol{n})|_{\Gamma_i} = \boldsymbol{0}, \quad i = 0, \ldots, m. \end{cases}$$

In Chapter 4 a different, less perturbative strategy is proposed in order to avoid the boundary effects due to the "complete" treatment of the viscous term.

The drawback of the variational formulation-based approach is that with a standard Galerkin-Finite Element approximation (see for example [55]) of Problem 2, we should build a space with null fluxes on the artificial sections and therefore a non standard finite dimensional subspace. This can be somehow problematic in practice.

Remark 1 *Let us consider both Dirichlet and flow rate boundary conditions on the artificial sections Γ_i. In particular, let us suppose to prescribe the following conditions:*

$$\begin{cases} \displaystyle\int_{\Gamma_i} \boldsymbol{u} \cdot \boldsymbol{n}\, d\gamma = Q_i, \quad i = 0, \ldots, m_Q, \\ \boldsymbol{u}|_{\Gamma_i} = \boldsymbol{g}_i, \quad i = m_Q + 1, \ldots, m_Q + m_D = m. \end{cases}$$

In this case, the compatibility condition (1.12) becomes:

$$Q_0 = \int_{\Gamma_0} \boldsymbol{u} \cdot \boldsymbol{n}\, d\gamma = -\sum_{i=1}^{m} \int_{\Gamma_i} \boldsymbol{u} \cdot \boldsymbol{n}\, d\gamma = -\sum_{i=1}^{m_Q} Q_i - \sum_{j=m_Q+1}^{m} \int_{\Gamma_i} \boldsymbol{g}_j \cdot \boldsymbol{n}\, d\gamma$$

and thus we can not impose arbitrarily the flux on Γ_0. Also in this case, without loss of generality, we will refer to condition (1.17) on Γ_0.

Augmented formulation of the steady-Stokes flow rate problem

The *augmented formulation* of the flow rate problem was proposed firstly for the steady-Stokes problem in [14], with the purpose of finding a more suitable approach. The basic idea is to consider the flow rate boundary condition as a constraint for the solution, to be forced through a *Lagrange multiplier approach*. In particular, referring to the computational domain Ω in Figure 1.2 (right) and to the "laplacian' treatment of the viscous term, let us consider the steady-Stokes problem:

$$\begin{cases} -\mu \triangle \boldsymbol{u} + \nabla p = \boldsymbol{f}, \quad \boldsymbol{x} \in \Omega \\ \nabla \cdot \boldsymbol{u} = 0, \quad \boldsymbol{x} \in \Omega \end{cases} \tag{1.19}$$

together with the boundary conditions:

$$\begin{cases} \boldsymbol{u}|_{\Gamma_w} = \boldsymbol{0}, \\ (p\boldsymbol{n} - \mu\nabla\boldsymbol{u}\ \boldsymbol{n})|_{\Gamma_0} = \boldsymbol{0}, \\ \displaystyle\int_{\Gamma_i} \boldsymbol{u}\cdot\boldsymbol{n}\, d\gamma = Q_i, \quad i = 1, 2, \ldots, m. \end{cases} \tag{1.20}$$

The following augmented variational formulation was proposed in [14] for the problem given by (1.19) with (1.20):

Problem 3 *Given $\boldsymbol{f}(t) \in L^2(\Omega)$ and $\boldsymbol{Q} \in \mathbb{R}^m$, find $\boldsymbol{u}(t) \in \boldsymbol{V}$, $p \in L^2(\Omega)$ and $\boldsymbol{\lambda} \in \mathbb{R}^m$ such that*

$$\begin{cases} a_L(\boldsymbol{u}, \boldsymbol{v}) + b(p, \boldsymbol{v}) + \displaystyle\sum_{j=1}^{m} \lambda_j \int_{\Gamma_j} \boldsymbol{v}\cdot\boldsymbol{n}\, d\gamma = (\boldsymbol{f}, \boldsymbol{v}), \quad \boldsymbol{x} \in \Omega \\ b(q, \boldsymbol{u}) = 0, \qquad \boldsymbol{x} \in \Omega \\ \displaystyle\int_{\Gamma_i} \boldsymbol{u}\cdot\boldsymbol{n}\, d\gamma = Q_i \quad \forall i = 1, \ldots, m, \end{cases}$$

for all $\boldsymbol{v} \in \boldsymbol{V}$ and $q \in L^2(\Omega)$.

We point out that a set of Lagrange multipliers, one for each flow rate boundary condition, is introduced. In this way, we have the drawback of solving an augmented problem. However, we observe that the functional space $\boldsymbol{V}$ is "standard", so the definition and implementation of a finite dimensional subspace is quite straightforward. In Section 2.3.1 we present the result of well-posedness of Problem 3. Moreover, we have the following results (see [14]):

Proposition 1 *The Lagrange multiplier λ_i has the physical meaning of normal stress on the artificial section Γ_i, i.e.*

$$(-p\boldsymbol{n} + \mu\nabla\boldsymbol{u}\ \boldsymbol{n})|_{\Gamma_i} = \lambda_i\boldsymbol{n}, \quad i = 1, \ldots, m. \tag{1.21}$$

We point out that the Lagrange multipliers λ_i do coincide with the *a priori* unknown functions of time C_i introduced in the previous section. Nevertheless, with this formulation they are considered as unknowns of the problem, that is augmented in the sense that we have m more unknowns (the Lagrange multipliers) and m more equations (conditions $(1.20)_3$). An augmented formulation with a different treatment of the viscous term has been introduced in [70] and it is presented in Section 2.2.2.

In [14] different numerical algorithms for the resolution of Problem 3 are also suggested. In Section 2.5.2 we review these methods, extending to a more general case some of them in Sections 2.5.3 and 2.5.4.

1.3.2 Mean pressure problem

For what concernes the mean pressure problem, we present the variational formulation-based approach introduced in [28]. This approach is the dual of the one introduced for the flow rate problem. At the best of our knowledge, this was so far the only strategy proposed in literature for this problem.

Let us consider the mean pressure problem, given by (1.2), (1.9) and (1.11) and the following:

Problem 4 *Given* $\boldsymbol{u}_0 \in \boldsymbol{V}^*$, $\boldsymbol{f} \in L^2(0,T;\boldsymbol{L}^2(\Omega))$ *and* $m+1$ *functions* $P_i \in L^2(0,T)$, *find* $\boldsymbol{u} \in L^2(0,T;\boldsymbol{V}) \cap L^\infty(0,T;\boldsymbol{L}^2(\Omega))$ *and* $p \in L^2(0,T;L^2(\Omega))$ *such that:*

$$\begin{cases} \left(\dfrac{\partial \boldsymbol{u}}{\partial t}, \boldsymbol{v}\right) + a_L(\boldsymbol{u},\boldsymbol{v}) + ((\boldsymbol{u}\cdot\nabla)\boldsymbol{u},\boldsymbol{v}) + b(p,\boldsymbol{v}) = (\boldsymbol{f},\boldsymbol{v}) - \displaystyle\sum_{i=0}^{m} P_i \int_{\Gamma_i} \boldsymbol{v}\cdot\boldsymbol{n}\, d\gamma, \\ b(q,\boldsymbol{u}) = 0 \end{cases}$$

for all $\boldsymbol{v} \in \boldsymbol{V}$ *and* $q \in L^(\Omega)$ *and with the initial condition* $\boldsymbol{u}|_{t=0} = \boldsymbol{u}_0$.

In [28] the following results are proven:

Theorem 3 *For* $\sum_{j=0}^{m} |P_j|$ *and* $\|\boldsymbol{u}_0\|_{\boldsymbol{V}}$ *small enough, there exists a positive number* T^* *such that Problem 4 admits an unique solution for all* $t \in (0,T^*]$.

Theorem 4 *Problem 4 is equivalent to the problem given by (1.2), (1.9) and the following conditions:*

$$(-p\boldsymbol{n} + \mu\nabla\boldsymbol{u}\ \boldsymbol{n})|_{\Gamma_i} = -P_i\boldsymbol{n}, \quad i = 0,\dots,m.$$

In other words, the variational formulation in Problem 4 forces implicitely zero tangential stress conditions that in general are not prescribed by conditions (1.11). Therefore, we conclude that Problem 4 is equivalent to the mean pressure problem given by (1.2), (1.9) and (1.11) only for particular geometries, for example for a cylinder. In all the other cases Problem 4 is an approximation of the mean pressure problem. Nevertheless, this approach is very used in the engineering comunity, due to its feasibility. In fact, $\boldsymbol{V}$ is a classical space. This is not the case of Problem 2.

However, in order to complete data (1.11), different boundary conditions related to different variational formulations can be considered as well. In particular, rewriting Problem 4 with the "complete" viscous term, the boundary conditions implicitely assumed on the artificial sections would be

$$(-p\boldsymbol{n} + \mu(\nabla\boldsymbol{u} + (\nabla\boldsymbol{u})^t)\boldsymbol{n})|_{\Gamma_i} = -P_i\boldsymbol{n}, \quad i = 0,\dots,m. \tag{1.22}$$

Also for the mean pressure problem, the observations done in Section 1.3.1 concerning the boundary effects related to the "complete" formulation hold.

Another possibility is to exploit the vector identity

$$-\triangle \boldsymbol{u} = \nabla \times (\nabla \times \boldsymbol{u}) - \nabla(\nabla \cdot \boldsymbol{u}).$$

Recalling the incompressibility constraint $(1.2)_2$ and integrating by parts, we obtain:

$$\begin{aligned} -(\triangle \boldsymbol{u}, \boldsymbol{v}) &= (\nabla \times \boldsymbol{u}, \nabla \times \boldsymbol{v}) - \int_{\partial\Omega} ((\nabla \times \boldsymbol{u}) \times \boldsymbol{n}) \cdot \boldsymbol{v}\, d\gamma = \\ &= (\nabla \times \boldsymbol{u}, \nabla \times \boldsymbol{v}) + \int_{\partial\Omega} (\boldsymbol{v} \times \boldsymbol{n}) \cdot (\nabla \times \boldsymbol{u})\, d\gamma. \end{aligned} \tag{1.23}$$

Let us consider the following space

$$\widetilde{\boldsymbol{V}} = \{\boldsymbol{v} \in \boldsymbol{H}^1_{\Gamma_w}(\Omega) : \boldsymbol{v} \times \boldsymbol{n}|_{\Gamma_i} = \boldsymbol{0},\ \forall i = 0, \ldots, m\}. \tag{1.24}$$

Therefore, we can consider the following (see [3, 28]):

Problem 5 *Given $\boldsymbol{u}_0 \in \widetilde{\boldsymbol{V}}^*$, $\boldsymbol{f} \in L^2(0,T;\boldsymbol{L}^2(\Omega))$ and $m+1$ functions $P_i \in L^2(0,T)$, find $\boldsymbol{u} \in L^2(0,T;\widetilde{\boldsymbol{V}}) \cap L^\infty(0,T;\boldsymbol{L}^2(\Omega))$ and $p \in L^2(0,t;L^2(\Omega))$ such that:*

$$\begin{cases} \left(\dfrac{\partial \boldsymbol{u}}{\partial t}, \boldsymbol{v}\right) + \mu(\nabla \times \boldsymbol{u}, \nabla \times \boldsymbol{v}) + ((\boldsymbol{u} \cdot \nabla)\boldsymbol{u}, \boldsymbol{v}) + b(p, \boldsymbol{v}) = \\ \qquad\qquad = (\boldsymbol{f}, \boldsymbol{v}) - \displaystyle\sum_{i=0}^{m} P_i \int_{\Gamma_i} \boldsymbol{v} \cdot \boldsymbol{n}\, d\gamma, \\ b(q, \boldsymbol{u}) = 0 \end{cases}$$

for all $\boldsymbol{v} \in \widetilde{\boldsymbol{V}}$ and $q \in L^2(\Omega)$ and with the initial condition $\boldsymbol{u}|_{t=0} = \boldsymbol{u}_0$.

The boundary conditions implicitely prescribed by this formulation are:

$$p\boldsymbol{n}|_{\Gamma_i} = P_i \boldsymbol{n}.$$

Therefore for the "laplacian" treatment of the viscous term, we can associate two variational formulation related to the bilinear forms, $a_L(\boldsymbol{w}, \boldsymbol{v})$ and $\mu(\nabla \times \boldsymbol{w}, \nabla \times \boldsymbol{v})$, respectively, leading to different boundary conditions. This could be of some interest in the multiscale modeling of the cardiovascular system (see [70]).

Alternatively, the given average data $P_i(t)$ on the artificial sections Γ_i could refer to the *mean total pressure*:

$$\frac{1}{|\Gamma_i|} \int_{\Gamma_i} \left(p + \frac{1}{2}|\boldsymbol{u}|^2\right) d\gamma = P_i, \quad \forall i = 0, \ldots, m, \quad t \in (0,T].$$

Let us consider the following variational formulation, proposed in [28]:

Problem 6 *Given* $\boldsymbol{u}_0 \in \boldsymbol{V}^*$, $\boldsymbol{f} \in L^2(0,T;\boldsymbol{L}^2(\Omega))$ *and* $m+1$ *functions* $P_i \in L^2(0,T)$, *find* $\boldsymbol{u} \in L^2(0,T;\boldsymbol{V}) \cap L^\infty(0,T;\boldsymbol{L}^2(\Omega))$ *and* $p \in L^2(0,T;L^2(\Omega))$ *such that:*

$$\begin{cases} \left(\dfrac{\partial \boldsymbol{u}}{\partial t}, \boldsymbol{u}\right) + a_L(\boldsymbol{u},\boldsymbol{v}) + ((\boldsymbol{u}\cdot\nabla)\boldsymbol{u},\boldsymbol{v}) - ((\boldsymbol{v}\cdot\nabla)\boldsymbol{u},\boldsymbol{u}) + b(p,\boldsymbol{v}) = \\ \qquad\qquad = (\boldsymbol{f},\boldsymbol{v}) - \displaystyle\sum_{i=0}^{m} P_i \int_{\Gamma_i} \boldsymbol{v}\cdot\boldsymbol{n}\, d\gamma, \\ b(q,\boldsymbol{u}) = 0 \end{cases}$$

for all $\boldsymbol{v} \in \boldsymbol{V}$ *and* $q \in L^2(\Omega)$ *and with the initial condition* $\boldsymbol{u}|_{t=0} = \boldsymbol{u}_0$.

Moreover, it is shown that Problem 6 implicitely assumes the following conditions:

$$\left(-p\boldsymbol{n} - \frac{1}{2}|\boldsymbol{u}|^2\boldsymbol{n} + \mu\nabla\boldsymbol{u}\ \boldsymbol{n}\right)\Big|_{\Gamma_i} = -P_i\boldsymbol{n}, \quad i = 0,\dots,m$$

For the mean total pressure problem, (1.23) and null tangential velocity can be considered as well. In particular, in [68] the following problem is considered:

Problem 7 *Given* $\boldsymbol{u}_0 \in \widetilde{\boldsymbol{V}}^*$, $\boldsymbol{f} \in L^2(0,T;\boldsymbol{L}^2(\Omega))$ *and* $m+1$ *functions* $P_i \in L^2(0,T)$ *find* $\boldsymbol{u} \in L^2(0,T;\widetilde{\boldsymbol{V}}) \cap L^\infty(0,T;\boldsymbol{L}^2(\Omega))$ *and* $p \in L^2(0,T;L^2(\Omega))$ *such that:*

$$\begin{cases} \left(\dfrac{\partial \boldsymbol{u}}{\partial t}, \boldsymbol{v}\right) + (\nabla\times\boldsymbol{u}, \nabla\times\boldsymbol{v}) + ((\nabla\times\boldsymbol{u})\times\boldsymbol{u},\boldsymbol{v}) + b(p,\boldsymbol{v}) = \\ \qquad\qquad = (\boldsymbol{f},\boldsymbol{v}) - \displaystyle\sum_{i=0}^{m} P_i \int_{\Gamma_i} \boldsymbol{v}\cdot\boldsymbol{n}\, d\gamma, \\ b(q,\boldsymbol{u}) = 0 \end{cases}$$

for all $\boldsymbol{v} \in \widetilde{\boldsymbol{V}}$ *and* $q \in L^2(\Omega)$ *and with the initial condition* $\boldsymbol{u}|_{t=0} = \boldsymbol{u}_0$.

In this case the boundary conditions implicitely assumed are:

$$-\left(p\boldsymbol{n} + \frac{1}{2}|\boldsymbol{u}|^2\boldsymbol{n}\right)\Big|_{\Gamma_i} = -P_i\boldsymbol{n}, \quad i = 0,\dots,m$$

Remark 2 *If a mean pressure condition (1.11) or a normal stress condition (1.4) is imposed on at least an artificial section* $\Gamma_i \neq \Gamma_0$, *the constraint on the number of surfaces on which it is possible to prescribe a flow rate condition has not to be enforced anymore. In fact, condition (1.12) is satisfied for any arbitrary chioice of the flow rate* Q_0.

1.4 Summary

Let us give a short summary of the work. In Chapter 2 we consider the flow rate problem, extending to the unsteady-non linear case the augmented approach proposed in [14] (Section 2.2). We analyse the proposed problem, giving a well-posedness analysis and some *a priori* estimates (Section 2.3). Moreover, thanks to the formulation of this problem we prove a result estimating the error introduced in the numerical solution by prescribing an arbitrary velocity profile, rather than the flux (Section 2.4). Then we introduce three algorithms for the numerical resolution (Section 2.5) and we show several numerical results for their validation (Section 2.6).

In Chapter 3, we review the results concerning some bioengineering applications obtained with the proposed strategies. Firstly we give some basic facts about haemodynamics, introducing the mathematical modeling of blood flow (Section 3.1.2). Then, we focus on a first application of these studies. In particular, the right prescription of a flow rate boundary condition allows to collect a set of meaningful numerical results, linking the shape of the computed velocity profile and the pulsatility. In this way it was possible to introduce in current clinical practice an improvement in the estimation of the flow rate measure with a *Doppler* velocimetry technique, otherwise not possible if a selected velocity profile is prescribed (Section 3.2). Moreover, we apply the strategies proposed in Chapter 2 for the resolution of the flow rate problem in a *geometrical multiscale modelization* of the cardiovascular system (Section 3.3) and to a more sophisticated description of the blood flow, including the vessel compliance (Section 3.4).

In Chapter 4, we present a "dual" approach based on the control theory, that can be applied to the mean pressure problem as well. We propose different algorithms and we show some numerical results for the validation of the proposed strategies.

Chapter 2

Augmented Formulation of the Flow Rate Problem

2.1 Introduction

In this chapter we limit our attention to the flow rate problem. As pointed out in Section 1.3.1, two strategies have been actually used in the engineering and mathematical comunities in order to fill the gap introduced by imposing a flow rate boundary condition. Nevertheless, both of them are unsatisfactory. Infact, the prescription *a priori* of the velocity profile (*practical approach*) has the drawback that the numerical solution strongly depends on the arbitrary chosen profile. On the other hand, the *variational formulation-based approach*, has the drawback that in order to obtain a numerical solution we need a non standard finite-dimensional subspace, which might not be easy to construct. As already pointed out, these difficulties have been overcame thanks to the *augmented formulation* of the flow rate problem, proposed firstly for the steady-Stokes case in [14].

Here, we extend this formulation to the unsteady-non linear case. In particular, the outline of this chapter is as follows. In Section 2.2.1 we derive firstly the augmented weak formulation for the unsteady Oseen problem (i.e. the approximation of the Navier-Stokes problem with an assigned convective field) by the constrained minimization of a suitable functional. Then we extend this formulation to the non-linear Navier-Stokes case. Moreover, we point out that the specific boundary problem obtained is related also to the formulation of the viscous term. This issue is discussed in Section 2.2.2. In Section 2.2.3 we extend the proposed approach to different defective boundary informations. In Section 2.3 we show the well posedness of the augmented problems and we give some *a priori* estimates of the solution. In Section 2.4 we present an analysis error of

the *practical approach* shown in Section 1.3.1. In Section 2.5 we propose three algorithms for the numerical solution of the augmented problem. In particular, we refer to algorithms based on the splitting of the augmented problem into the computation of velocity and pressure on one side and of the Lagrange multipliers on the other one. Finally, in Section 2.6 we show the numerical results obtained with these three techniques.

2.2 Derivation of the weak formulations

2.2.1 The unsteady Oseen and Navier-Stokes case

Let us consider the domain $\Omega \subset \mathbb{R}^d$, $d = 2, 3$, represented in Figure 2.1 and the

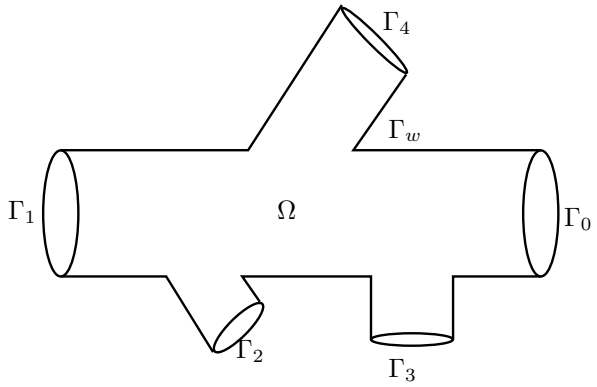

Figure 2.1: Domain Ω of interest in the flow rate problem. In this case we have $m = 4$.

following unsteady Oseen problem, where the viscous term is rappresented by the Laplace operator:

$$\begin{cases} \dfrac{\partial \boldsymbol{u}}{\partial t} - \mu \triangle \boldsymbol{u} + (\boldsymbol{\beta} \cdot \nabla)\boldsymbol{u} + \nabla p = \boldsymbol{f}, \quad (t, \boldsymbol{x}) \in Y_T \\ \nabla \cdot \boldsymbol{u} = 0, \quad (t, \boldsymbol{x}) \in Y_T \\ \boldsymbol{u}|_{t=0} = \boldsymbol{u}_0(\boldsymbol{x}), \quad \boldsymbol{x} \in \Omega \end{cases} \tag{2.1}$$

together with the boundary conditions:

$$\begin{cases} \boldsymbol{u}|_{\Gamma_w} = \boldsymbol{0}, \quad t \in (0, T] \\ (p\boldsymbol{n} - \mu \nabla \boldsymbol{u}\ \boldsymbol{n})|_{\Gamma_0} = \boldsymbol{0}, \quad t \in (0, T] \\ \displaystyle\int_{\Gamma_i} \boldsymbol{u} \cdot \boldsymbol{n}\, d\gamma = Q_i, \quad i = 1, 2, \ldots, m, \quad t \in (0, T]. \end{cases} \tag{2.2}$$

Let us notice that we impose the fluxes on all the artificial sections apart from Γ_0. Let us consider the following functional:

$$F(\boldsymbol{v}) = \Big(\frac{\partial \boldsymbol{v}}{\partial t}, \boldsymbol{v}\Big) + \frac{1}{2} a_L(\boldsymbol{v}, \boldsymbol{v}) + \frac{1}{2}((\boldsymbol{\beta} \cdot \nabla)\boldsymbol{v}, \boldsymbol{v}) - (\boldsymbol{f}, \boldsymbol{v}). \tag{2.3}$$

By minimizing this functional in the space $\boldsymbol{V}^*$ given by (1.13), we obtain a variational formulation of problem (2.1) with the following boundary conditions:

$$\begin{cases} \boldsymbol{u}|_{\Gamma_w} = \boldsymbol{0}, \quad t \in (0, T] \\ (p\boldsymbol{n} - \mu \nabla \boldsymbol{u}\ \boldsymbol{n})|_{\Gamma_0} = \boldsymbol{0}, \quad t \in (0, T] \\ (p\boldsymbol{n} - \mu \nabla \boldsymbol{u}\ \boldsymbol{n})|_{\Gamma_i} = \boldsymbol{0}, \quad i = 1, \ldots, m, \quad t \in (0, T] \end{cases} \tag{2.4}$$

This corresponds to a free minimization of the functional (2.3). On the other hand, if we want take into account the supplementary informations given by the flow rate boundary conditions $(2.2)_3$, we can think to minimize the previous functional with the constraint given by these conditions. With this aim, let us introduce the following definition:

$$< \phi_i, \boldsymbol{v} > := \int_{\Gamma_i} \boldsymbol{v} \cdot \boldsymbol{n}\, d\gamma, \quad \forall i = 1, \ldots, m, \tag{2.5}$$

where $\phi_i \in V'$, $i = 1, \ldots, m$ and $< \cdot, \cdot >$ denotes the duality between V' and $\boldsymbol{V}$. With the previous definition we can formulate the flow rate condition in terms of a continous and linear functional. In particular, let us consider the following constrained minimization problem:

Problem 8 *Find* $\boldsymbol{u} \in \boldsymbol{V}^*$ *such that*

$$\begin{cases} \min_{\{\boldsymbol{w} \in \boldsymbol{V}^*\}} F(\boldsymbol{w}) \\ < \phi_j, \boldsymbol{w} >= Q_j, \quad j = 1, \ldots, m. \end{cases}$$

In order to solve this problem we resort to a *Lagrange multipliers* approach, i.e. we minimize the Lagrangian functional obtained by adding to the functional F the constraints $(2.2)_3$ multiplied by the Lagrange multipliers (see [55]). In this way, the Lagrangian functional associated to Problem 8 becomes:

$$L(\boldsymbol{w}, \xi_1, \ldots, \xi_n) = \frac{1}{2}\Big(\frac{\partial \boldsymbol{w}}{\partial t}, \boldsymbol{w}\Big) + \frac{1}{2} a_L(\boldsymbol{w}, \boldsymbol{w}) + \frac{1}{2}((\boldsymbol{\beta} \cdot \nabla)\boldsymbol{w}, \boldsymbol{w}) +$$

$$-(\boldsymbol{f}, \boldsymbol{w}) + \sum_{j=1}^{m} \xi_j (< \phi_j, \boldsymbol{w} > - Q_j),$$

As usual for constrained minimization problems, we can resort to a saddle point formulation (see [55]):

Problem 9 *Find* $\boldsymbol{u} \in \boldsymbol{V}^*$ *and* $\lambda_1, \ldots, \lambda_n \in \mathbb{R}$ *such that, for each* t*:*

$$L(\boldsymbol{u}, \lambda_1, \ldots, \lambda_m) = \min_{\{\boldsymbol{w} \in \boldsymbol{V}^*\}} \max_{\{\xi_1, \ldots, \xi_m \in \mathbb{R}\}} \{L(\boldsymbol{w}, \xi_1, \ldots, \xi_m)\},$$

where λ_j are the Lagrange multipliers associated to constraints $(2.2)_3$. Let us consider the function Ψ obtained evaluating L in $(\boldsymbol{u}+\varepsilon\boldsymbol{v}, \lambda_j+\alpha_j\eta_j,\ j = 1, \ldots, m)$, with $\boldsymbol{v}$ and η_j the variations (costant in time) from the solution $(\boldsymbol{u}, \lambda_i)$:

$$\Psi(\varepsilon, \alpha_1, \ldots, \alpha_m) = L(\boldsymbol{u} + \varepsilon\boldsymbol{v}, \lambda_1 + \alpha_1\eta_1, \ldots, \lambda_n + \alpha_n\eta_m).$$

Differentiating with the respect to ε, we obtain:

$$\frac{d\Psi(\varepsilon, \alpha_1, \ldots, \alpha_m)}{d\varepsilon} = \Big(\frac{\partial \boldsymbol{u}}{\partial t}, \boldsymbol{v}\Big) + \varepsilon\Big(\frac{\partial \boldsymbol{v}}{\partial t}, \boldsymbol{v}\Big) + a_L(\boldsymbol{u}, \boldsymbol{v}) + \varepsilon a_L(\boldsymbol{v}, \boldsymbol{v}) + ((\boldsymbol{\beta} \cdot \nabla)\boldsymbol{u}, \boldsymbol{v}) +$$

$$+\varepsilon((\boldsymbol{\beta} \cdot \nabla)\boldsymbol{v}, \boldsymbol{v}) - (\boldsymbol{f}, \boldsymbol{v}) + \sum_{j=1}^{m} \lambda_j < \phi_j, \boldsymbol{v} > + \sum_{j=1}^{m} \alpha_j\eta_j < \phi_j, \boldsymbol{v} >$$

and with the respect to α_j:

$$\frac{d\Psi(\varepsilon, \alpha_1, \ldots, \alpha_m)}{d\alpha_j} = \eta_j(< \phi_j, \boldsymbol{u} > -Q_j) + \eta_j\varepsilon < \phi_j, \boldsymbol{v} > .$$

By forcing

$$\begin{cases} \dfrac{d\Psi(0, 0, \ldots, 0)}{d\varepsilon} = 0, \\ \dfrac{d\Psi(0, 0, \ldots, 0)}{d\alpha_j} = 0, \quad j = 1, \ldots, m, \end{cases}$$

we obtain:

$$\begin{cases} \Big(\dfrac{\partial \boldsymbol{u}}{\partial t}, \boldsymbol{v}\Big) + a_L(\boldsymbol{u}, \boldsymbol{v}) + ((\boldsymbol{\beta} \cdot \nabla)\boldsymbol{u}, \boldsymbol{v}) + \displaystyle\sum_{j=1}^{m} \lambda_j < \phi_j, \boldsymbol{v} >= (\boldsymbol{f}, \boldsymbol{v}), \quad \forall \boldsymbol{v} \in \boldsymbol{V}^* \\ \eta_j(< \phi_j, \boldsymbol{u} > -Q_j) = 0, \quad \text{for} \quad j = 1, \ldots, m, \qquad \forall \eta_j \in \mathbb{R}. \end{cases}$$

By proceeding in a similar way, with an explicit treatment of the incompressibility constraint, we obtain the following *augmented* variational formulation for the problem given by (2.1) and (2.2):

Problem 10 *Given* $\boldsymbol{u}_0 \in \boldsymbol{V}^*$, $\boldsymbol{f}(t) \in L^2(0,T;\boldsymbol{L}^2(\Omega))$, $\boldsymbol{\beta} \in L^\infty(0,T;\boldsymbol{L}^\infty(\Omega))$ *and* $\boldsymbol{Q}(t) \in (C^0([0,T]))^m$ *(with* $\int_{\Gamma_j} \boldsymbol{u}_0 \cdot \boldsymbol{n}\, d\gamma = Q_j(0)$*), find* $\boldsymbol{u}(t) \in L^2(0,T;\boldsymbol{V}) \cap L^\infty(0,T;\boldsymbol{L}^2(\Omega))$, $p \in L^2(0,T;L^2(\Omega))$ *and* $\boldsymbol{\lambda} \in (L^2(0,T))^m$ *such that*

$$\begin{cases} \Big(\dfrac{\partial \boldsymbol{u}}{\partial t}, \boldsymbol{v}\Big) + a_L(\boldsymbol{u},\boldsymbol{v}) + ((\boldsymbol{\beta}\cdot\nabla)\boldsymbol{u},\boldsymbol{v}) + b(p,\boldsymbol{v}) + \displaystyle\sum_{j=1}^{m} \lambda_j \int_{\Gamma_j} \boldsymbol{v}\cdot\boldsymbol{n}\, d\gamma = \\ \qquad\qquad = (\boldsymbol{f},\boldsymbol{v}), \quad (t,\boldsymbol{x}) \in Y_T \\ b(q,\boldsymbol{u}) = 0, \qquad (t,\boldsymbol{x}) \in Y_T \\ \boldsymbol{u}|_{t=0} = \boldsymbol{u}_0, \qquad \boldsymbol{x} \in \Omega \\ \displaystyle\int_{\Gamma_i} \boldsymbol{u}\cdot\boldsymbol{n}\, d\gamma = Q_i \quad \forall i = 1,\dots,m, \qquad t \in (0,T] \end{cases} \tag{2.6}$$

for all $\boldsymbol{v} \in \boldsymbol{V}$ *and* $q \in L^2(\Omega)$.

For the Navier-Stokes case, we can not derive an augmented formulation through a constrained minimization problem. Nevertheless, we will consider such a formulation also in this case, by simply setting $\boldsymbol{\beta} = \boldsymbol{u}$ in Problem 10.

Problem 11 *Given* $\boldsymbol{u}_0 \in \boldsymbol{V}^*$, $\boldsymbol{f}(t) \in L^2(0,T;\boldsymbol{L}^2(\Omega))$ *and* $\boldsymbol{Q}(t) \in (C^0([0,T]))^m$ *(with* $\int_{\Gamma_j} \boldsymbol{u}_0 \cdot \boldsymbol{n}\, d\gamma = Q_j(0)$*), find* $\boldsymbol{u}(t) \in L^2(0,T;\boldsymbol{V}) \cap L^\infty(0,T;\boldsymbol{L}^2(\Omega))$, $p \in L^2(0,T;L^2(\Omega))$ *and* $\boldsymbol{\lambda} \in (L^2(0,T))^m$ *such that*

$$\begin{cases} \Big(\dfrac{\partial \boldsymbol{u}}{\partial t}, \boldsymbol{v}\Big) + a_L(\boldsymbol{u},\boldsymbol{v}) + ((\boldsymbol{u}\cdot\nabla)\boldsymbol{u},\boldsymbol{v}) + b(p,\boldsymbol{v}) + \displaystyle\sum_{j=1}^{m} \lambda_j \int_{\Gamma_j} \boldsymbol{v}\cdot\boldsymbol{n}\, d\gamma = \\ \qquad\qquad = (\boldsymbol{f},\boldsymbol{v}), \quad (t,\boldsymbol{x}) \in Y_T \\ b(q,\boldsymbol{u}) = 0, \qquad (t,\boldsymbol{x}) \in Y_T \\ \boldsymbol{u}|_{t=0} = \boldsymbol{u}_0, \qquad \boldsymbol{x} \in \Omega \\ \displaystyle\int_{\Gamma_i} \boldsymbol{u}\cdot\boldsymbol{n}\, d\gamma = Q_i \quad \forall i = 1,\dots,m, \qquad t \in (0,T] \end{cases}$$

for all $\boldsymbol{v} \in \boldsymbol{V}$ *and* $q \in L^2(\Omega)$.

The choice of the space $L^2(0,T)$ for the Lagrange multipliers λ_j will be clear from the *a priori* estimates in Section 2.3.2.

Problem 11 extends the augmented variational formulation, proposed in [14] for the steady-Stokes problem, to the unsteady non-linear Navier-Stokes case. It is easy to check that the result in Proposition 1, Chapter 1, can be extended to Problem 10 and 11. Therefore, also in the general case, equivalence (1.21) holds, i.e the Lagrange multipliers λ_i have the physical meaning of normal stress on the artificial sections. Let us notice that among all the possible Neumann boundary conditions fitting the desired flow rate, the augmented formulation prescribes the

constant one. Moreover, we point out that Problems 10 and 11 share the good property, in view of the numerical simulations, of requiring the discretization of a "standard" space $\boldsymbol{V}$.

2.2.2 Different formulations for the viscous term

In the previous formulation, the boundary conditions implicitely forced by the minimization approach are:

$$\begin{cases} (-p + \mu(\nabla \boldsymbol{u}\ \boldsymbol{n}) \cdot \boldsymbol{n})|_{\Gamma_i} = \lambda_i, \quad i = 1, \ldots, m \\ (\mu(\nabla \boldsymbol{u}\ \boldsymbol{n}) \cdot \boldsymbol{\tau}_j)|_{\Gamma_i} = \boldsymbol{0}, \quad i = 1, \ldots, m, \quad j = 1, d-1, \end{cases}$$

where $\boldsymbol{\tau}_j$, $j = 1, d-1$ are the unit vectors such that $\boldsymbol{\tau}_j \cdot \boldsymbol{n} = 0$ and, if $d = 3$, $\boldsymbol{\tau}_1 \cdot \boldsymbol{\tau}_2 = 0$, and where λ_i are the Lagrange multipliers. These conditions are strictly related to the formulation of the functional to be minimized. In fact, it is possible to refer to different functionals, associated to different boundary conditions. For example, let us consider the following Oseen problem, with a "complete" treatment of the viscous term:

$$\begin{cases} \dfrac{\partial \boldsymbol{u}}{\partial t} - \nabla \cdot \mu(\nabla \boldsymbol{u} + (\nabla \boldsymbol{u})^t) + (\boldsymbol{\beta} \cdot \nabla)\boldsymbol{u} + \nabla p = \boldsymbol{f}, \quad (t, \boldsymbol{x}) \in Y_T \\ \nabla \cdot \boldsymbol{u} = 0, \quad (t, \boldsymbol{x}) \in Y_T \\ \boldsymbol{u}|_{t=0} = \boldsymbol{u}_0(\boldsymbol{x}), \quad \boldsymbol{x} \in \Omega \end{cases} \tag{2.7}$$

together with $(2.2)_1$, $(2.2)_3$ and the following boundary condition:

$$(p\boldsymbol{n} - \mu(\nabla \boldsymbol{u} + (\nabla \boldsymbol{u})^t)\boldsymbol{n})|_{\Gamma_0} = \boldsymbol{0}, \quad t \in (0, T]. \tag{2.8}$$

In order to find an augmented formulation related to problem given by (2.7), $(2.2)_1$, $(2.2)_3$ and (2.8), it is possible to minimize the functional

$$F_C(\boldsymbol{v}) = \left(\frac{\partial \boldsymbol{v}}{\partial t}, \boldsymbol{v}\right) + \frac{1}{2} a_C(\boldsymbol{v}, \boldsymbol{v}) + \frac{1}{2}((\boldsymbol{\beta} \cdot \nabla)\boldsymbol{v}, \boldsymbol{v}) - (\boldsymbol{f}, \boldsymbol{v}), \tag{2.9}$$

with the constraint given by $(2.2)_3$. In this case we obtain a formulation similar to Problem 10 with $a_C(\cdot, \cdot)$ instead of $a_L(\cdot, \cdot)$. The extension to the Navier-Stokes case can be considered as well. In this case the boundary conditions implicitely forced by the minimization approach are:

$$\begin{cases} (-p + \mu(\nabla \boldsymbol{u} + (\nabla \boldsymbol{u})^t)\boldsymbol{n} \cdot \boldsymbol{n})|_{\Gamma_i} = \lambda_i, \quad i = 1, \ldots, m \\ (\mu(\nabla \boldsymbol{u} + (\nabla \boldsymbol{u})^t)\boldsymbol{n} \cdot \boldsymbol{\tau}_j)|_{\Gamma_i} = \boldsymbol{0}, \quad i = 1, \ldots, m, \quad j = 1, d-1. \end{cases}$$

and therefore the Lagrange multipliers λ_i have a different physical meaning on the artificial sections.

Alternatively, refferring to the vector identity (1.23) and to formulation in Problem 5, we can consider the following functional:

$$\widetilde{F}(\boldsymbol{v}) = \Big(\frac{\partial \boldsymbol{v}}{\partial t}, \boldsymbol{v}\Big) + \frac{1}{2}\mu(\nabla \times \boldsymbol{v}, \nabla \times \boldsymbol{v}) + \frac{1}{2}((\boldsymbol{\beta} \cdot \nabla)\boldsymbol{v}, \boldsymbol{v}) - (\boldsymbol{f}, \boldsymbol{v}). \tag{2.10}$$

Thanks to (1.23), it is possible to check that, by minimizing (2.10) in the space $\widetilde{\boldsymbol{V}}^*$ (with $\widetilde{\boldsymbol{V}}$ given by (1.24)), we obtain a variational formulation of problem (2.1) with the following boundary conditions:

$$\begin{cases} \boldsymbol{u}|_{\Gamma_w} = \boldsymbol{0}, \quad t \in (0,T], \\ p|_{\Gamma_0} = 0, \quad t \in (0,T], \\ p|_{\Gamma_i} = 0, \quad i = 1, \dots, m, \quad t \in (0,T], \\ (\boldsymbol{u} \times \boldsymbol{n})|_{\Gamma_0} = \boldsymbol{0}, \quad t \in (0,T], \\ (\boldsymbol{u} \times \boldsymbol{n})|_{\Gamma_i} = \boldsymbol{0}, \quad i = 1, \dots, m, \quad t \in (0,T]. \end{cases} \tag{2.11}$$

This is the result of the unconstrained minimization. On the other hand, in order to take into account the supplementary informations given by the flow rate boundary conditions $(2.2)_3$, we can minimize functional (2.10) with these constraints, obtaining the following minimization problem:

Problem 12 *Find* $\boldsymbol{u} \in \widetilde{\boldsymbol{V}}^*$ *such that*

$$\begin{cases} \min_{\{\boldsymbol{w} \in \widetilde{\boldsymbol{V}}^*\}} \widetilde{F}(\boldsymbol{w}) \\ < \phi_j, \boldsymbol{w} >= Q_j, \quad j = 1, \dots, m \end{cases}$$

Building the Lagrangian functional related to Problem 12 and differenziating as done for Problem 8, we obtain the following augmented formulation for the problem given by (2.1), $(2.11)_1$, $(2.11)_2$, $(2.11)_4$, $(2.11)_5$ and $(2.2)_3$ (see [70]):

Problem 13 *Given* $\boldsymbol{u}_0 \in \widetilde{\boldsymbol{V}}^*$, $\boldsymbol{f}(t) \in L^2(0,T;\boldsymbol{L}^2(\Omega))$, $\boldsymbol{\beta} \in L^\infty(0,T;\boldsymbol{L}^\infty(\Omega))$ *and* $\boldsymbol{Q}(t) \in (C^0([0,T]))^m$ *(with* $\int_{\Gamma_j} \boldsymbol{u}_0 \cdot \boldsymbol{n}\, d\gamma = Q_j(0)$*), find* $\boldsymbol{u}(t) \in L^2(0,T;\widetilde{\boldsymbol{V}}) \cap L^\infty(0,T;\boldsymbol{L}^2(\Omega))$, $p \in L^2(0,T;L^2(\Omega))$ *and* $\boldsymbol{\lambda} \in (L^2(0,T))^m$ *such that*

$$\begin{cases} \Big(\frac{\partial \boldsymbol{u}}{\partial t}, \boldsymbol{v}\Big) + \mu(\nabla \times \boldsymbol{u}, \nabla \times \boldsymbol{v}) + ((\boldsymbol{\beta} \cdot \nabla)\boldsymbol{u}, \boldsymbol{v}) + b(p, \boldsymbol{v}) + \\ \qquad\qquad + \sum_{j=1}^{m} \lambda_j \int_{\Gamma_j} \boldsymbol{v} \cdot \boldsymbol{n}\, d\gamma = (\boldsymbol{f}, \boldsymbol{v}), \quad (t, \boldsymbol{x}) \in Y_T \\ b(q, \boldsymbol{u}) = 0, \qquad (t, \boldsymbol{x}) \in Y_T \\ \boldsymbol{u}|_{t=0} = \boldsymbol{u}_0, \qquad \boldsymbol{x} \in \Omega \\ \int_{\Gamma_i} \boldsymbol{u} \cdot \boldsymbol{n}\, d\gamma = Q_i \quad \forall i = 1, \dots, m, \qquad t \in (0,T] \end{cases} \tag{2.12}$$

for all $\boldsymbol{v} \in \widetilde{\boldsymbol{V}}$ *and* $q \in L^2(\Omega)$.

We have the following result, highlighting the physical role of the Lagrange multipliers (see [70]):

Proposition 2 *The Lagrange multipliers λ_i related to Problem 13 correspond to the pressure on the artificial section Γ_i, i.e.*

$$-p|_{\Gamma_i} = \lambda_i, \quad i = 1, \ldots, m \tag{2.13}$$

Proof
Let us consider $\boldsymbol{v} \in \boldsymbol{D}(\Omega) = \boldsymbol{C}_0^\infty(\Omega)$ in the first of (2.12). By applying the Green formula, we obtain:

$$\left(\frac{\partial \boldsymbol{u}}{\partial t}, \boldsymbol{v}\right) - \mu(\triangle \boldsymbol{u}, \boldsymbol{v}) + ((\boldsymbol{\beta} \cdot \nabla)\boldsymbol{u}, \boldsymbol{v}) + (\nabla p, \boldsymbol{v}) = (\boldsymbol{f}, \boldsymbol{v}), \quad \forall \boldsymbol{v} \in \boldsymbol{D}(\Omega)$$

and therefore we recover the momentum equation $(2.1)_1$. Then, taking $\boldsymbol{v} \in \widetilde{\boldsymbol{V}}$, with the same procedure we obtain:

$$\sum_{j=1}^{m} \lambda_j \int_{\Gamma_j} \boldsymbol{v} \cdot \boldsymbol{n} \, d\gamma + \int_{\partial\Omega} p\boldsymbol{v} \cdot \boldsymbol{n} \, d\gamma = 0, \quad \forall \boldsymbol{v} \in \widetilde{\boldsymbol{V}},$$

i.e. conditions (2.13) and $p|_{\Gamma_0} = 0$. $\diamond$

In this case the Lagrange multipliers play the role of (constant) pressure on the artificial sections. Therefore, this could be of some interest, for instance, in the multiscale modelling of the cardiovascular system (see Section 3.3). Also in this case, we can extend straightforwardly the previous formulation to the non-linear case, by following the same approach presented previously. We do not explicitely repeat this derivation for the sake of brevity.

All these examples highlight the relationship between the treatment of the viscous term and the physical meaning of the Lagrange multipliers.

2.2.3 Different defective boundary problems

It is worth pointing out that the approach previously proposed can be adapted for including any kind of defective boundary conditions. For instance, let us suppose to have also data on the tangential component of the velocity

$$\int_{\Gamma_i} \boldsymbol{u} \cdot \boldsymbol{\tau}_j \, d\gamma = r_{ij}(t), \quad i = 1, \ldots, m, \quad j = 1, d-1 \tag{2.14}$$

Let us introduce the functionals

$$< \psi_{ij}, \boldsymbol{v} >:= \int_{\Gamma_i} \boldsymbol{v} \cdot \boldsymbol{\tau}_j \, d\gamma, \quad \forall i = 1, \ldots, m, \quad j = 1, d-1,$$

where $\psi_{ij} \in V'$. Therefore, problem given by (2.1), (2.2) and (2.14) can be formulated as a constrained minimization problem:

Problem 14 *Find $\boldsymbol{u} \in \boldsymbol{V}^*$ such that*

$$\begin{cases} \min_{\{\boldsymbol{w} \in \boldsymbol{V}^*\}} F(\boldsymbol{w}) \\ < \phi_i, \boldsymbol{w} >= Q_i, \quad i = 1, \ldots, m, \\ < \psi_{ij}, \boldsymbol{w} >= r_{ij}, \quad i = 1, \ldots, m, \quad j = 1, d-1. \end{cases}$$

It is easy to check that this problem leads to the following

Problem 15 *Given $\boldsymbol{u}_0 \in \boldsymbol{V}^*$, $\boldsymbol{f}(t) \in L^2(0,T;\boldsymbol{L}^2(\Omega))$, $\boldsymbol{Q}(t) \in (C^0([0,T]))^m$ (with $\int_{\Gamma_j} \boldsymbol{u}_0 \cdot \boldsymbol{n} \, d\gamma = Q_j(0)$), $r(t) \in (C^0([0,T]))^{m\times(d-1)}$ (with $\int_{\Gamma_j} \boldsymbol{u}_0 \cdot \boldsymbol{\tau}_i \, d\gamma = r_{ji}(0)$) and $\boldsymbol{\beta} \in L^\infty(0,T;\boldsymbol{L}^\infty(\Omega))$, find $\boldsymbol{u}(t) \in L^2(0,T;\boldsymbol{V}) \cap L^\infty(0,T;\boldsymbol{L}^2(\Omega))$, $p \in L^2(0,T;L^2(\Omega))$, $\boldsymbol{\lambda} \in (L^2(0,T))^m$ and $\eta \in (L^2(0,T))^{m\times(d-1)}$ such that*

$$\begin{cases} \Big(\dfrac{\partial \boldsymbol{u}}{\partial t}, \boldsymbol{v}\Big) + a_L(\boldsymbol{u}, \boldsymbol{v}) + ((\boldsymbol{\beta}\cdot\nabla)\boldsymbol{u}, \boldsymbol{v}) + b(p, \boldsymbol{v}) + \displaystyle\sum_{i=1}^{m} \lambda_i \int_{\Gamma_i} \boldsymbol{v} \cdot \boldsymbol{n} \, d\gamma + \\ \qquad + \displaystyle\sum_{j=1}^{d-1} \sum_{i=1}^{m} \eta_{ij} \int_{\Gamma_i} \boldsymbol{v} \cdot \boldsymbol{\tau}_j \, d\gamma = (\boldsymbol{f}, \boldsymbol{v}), \quad (t, \boldsymbol{x}) \in Y_T \\ b(q, \boldsymbol{u}) = 0, \qquad (t, \boldsymbol{x}) \in Y_T \\ \boldsymbol{u}|_{t=0} = \boldsymbol{u}_0, \qquad \boldsymbol{x} \in \Omega \\ \displaystyle\int_{\Gamma_i} \boldsymbol{u} \cdot \boldsymbol{n} \, d\gamma = Q_i \quad \forall i = 1, \ldots, m, \qquad t \in (0, T] \\ \displaystyle\int_{\Gamma_i} \boldsymbol{u} \cdot \boldsymbol{\tau}_j \, d\gamma = r_{ij}, \quad i = 1, \ldots m, \quad j = 1, d-1, \quad t \in (0, T] \end{cases} \tag{2.15}$$

for all $\boldsymbol{v} \in \boldsymbol{V}$ and $q \in L^2(\Omega)$.

Here η_{ij} are the Lagrange multipliers related to the constraints (2.14). It is easy to check that they play the role of constant tangential stress. In fact, let us consider $\boldsymbol{v} \in \boldsymbol{D}(\Omega)$ in the first of (2.15). By applying the Green formula, we recover the momentum equation $(2.1)_1$. Then, taking $\boldsymbol{v} \in \boldsymbol{V}$, with the same procedure we obtain:

$$\sum_{i=1}^{m} \lambda_i \int_{\Gamma_i} \boldsymbol{v}\cdot\boldsymbol{n} \, d\gamma + \sum_{j=1}^{d-1} \sum_{i=1}^{m} \eta_{ij} \int_{\Gamma_i} \boldsymbol{v}\cdot\boldsymbol{\tau}_j \, d\gamma + \int_{\partial\Omega} \Big(p\boldsymbol{n} - \nabla\boldsymbol{u}\ \boldsymbol{n}\Big)\cdot\boldsymbol{v} \, d\gamma = 0, \quad \forall \boldsymbol{v} \in \boldsymbol{V}.$$

By multipling the latter equality with $\boldsymbol{n}$, we obtain

$$(-p + \mu(\nabla \boldsymbol{u}\ \boldsymbol{n}) \cdot \boldsymbol{n})|_{\Gamma_i} = \lambda_i, \quad i = 1, \ldots, m.$$

On the other hand, by multiplying with the tangential unit vector $\boldsymbol{\tau}_j$, we obtain

$$(\mu(\nabla \boldsymbol{u}\ \boldsymbol{n}) \cdot \boldsymbol{\tau}_j)|_{\Gamma_i} = \eta_{ij}\boldsymbol{\tau}_j, \quad i = 1, \ldots, m.$$

2.3 Analysis of the augmented problems

In this Section we present some well-posedness results related to the augmented problems. In particular, in Section 2.3.1 we recall the well posedness analysis of the steady-Stokes augmented problem. This is obtained by a effects superimposition principle based on the steadiness and the linearity of the problem and it is taken from [14]. In Section 2.3.2, we are going to extend these results to the general augmented problem (Problem 11). We point out that in this case it is not possible to resort to a effects superimposition principle. Therefore, we resorted to an abstract result about the augmented problems, based on the fulfilling of an inf-sup condition. Moreover, we show some *a priori* estimates.

From now on in this chapter, for the sake of simplicity, all the problems presented are considered with the "laplacian" treatment of the viscous term and with the bilinear form $a_L(\cdot, \cdot)$. Therefore, since there will be no more ambiguity, we pose

$$a(\cdot, \cdot) = a_L(\cdot, \cdot).$$

Nevertheless, we point out that the results and the algorithms presented from now on could be extended straightforwardly to the other treatments of the viscous terms and therefore to the other formulations of the augmented problems.

2.3.1 Well posedness of the steady-Stokes augmented problem

The well posedness analysis of Problem 3, has been carried out in [14]. In particular, the following result holds:

Theorem 5 *Problem 3 admits an unique solution* $\{\boldsymbol{u}, p, \boldsymbol{\lambda}\}$.

Let us give a trace of the proof. In particular, let us consider the following problems:

1) Find $\boldsymbol{w}_j \in \boldsymbol{V}$ and $p \in L^2(\Omega)$ such that

$$\begin{cases} a(\boldsymbol{w}_j, \boldsymbol{v}) + b(\pi_j, \boldsymbol{v}) = -\displaystyle\int_{\Gamma_j} \boldsymbol{v} \cdot \boldsymbol{n}\, d\gamma, \quad \boldsymbol{x} \in \Omega, \quad j = 1, \ldots, m, \\ b(q, \boldsymbol{w}_j) = 0, \qquad \boldsymbol{x} \in \Omega \end{cases}$$

for all $\boldsymbol{v} \in \boldsymbol{V}$ and $q \in L^2(\Omega)$.

2) Find $\widetilde{\boldsymbol{u}} \in \boldsymbol{V}$ and $\widetilde{p} \in L^2(\Omega)$ such that

$$\begin{cases} a(\widetilde{\boldsymbol{u}}, \boldsymbol{v}) + b(\widetilde{p}, \boldsymbol{v}) = (\boldsymbol{f}, \boldsymbol{v}), \quad \boldsymbol{x} \in \Omega, \\ b(q, \widetilde{\boldsymbol{u}}) = 0, \qquad \boldsymbol{x} \in \Omega \end{cases}$$

for all $\boldsymbol{v} \in \boldsymbol{V}$ and $q \in L^2(\Omega)$.

3) Solve the linear system

$$\sum_{j=1}^{m} \lambda_j \int_{\Gamma_i} \boldsymbol{w}_j \cdot \boldsymbol{n} d\gamma = Q_i - \int_{\Gamma_i} \widetilde{\boldsymbol{u}} \cdot \boldsymbol{n} d\gamma,$$

for the unknowns λ_i, with matrix whose elements are

$$B_{ij} = \int_{\Gamma_i} \boldsymbol{w}_j \cdot \boldsymbol{n} d\gamma. \tag{2.16}$$

4) Build functions $\boldsymbol{u}$ and p such that:

$$\begin{cases} \boldsymbol{u} = \widetilde{\boldsymbol{u}} + \displaystyle\sum_{j=1}^{m} \lambda_j \boldsymbol{w}_j \\ p = \widetilde{p} + \displaystyle\sum_{j=1}^{m} \lambda_j \pi_j. \end{cases} \tag{2.17}$$

The following result holds (see [14]):

Proposition 3 *Matrix B is not singular.*

Therefore, problems at steps 1), 2) and 3) are well-posed. It is easy to check that functions $\boldsymbol{u}$ and p given by (2.17) are the solutions of Problem 3. Let us notice that this technique relies on the linearity and on the steadiness of the problem (in this case the Lagrangian multipliers are constant). Therefore, it can not be extended to a more general case.

2.3.2 Well posedness of the generic augmented problem

The present analysis refers to the unsteady non linear Navier-Stokes augmented problem, yielding a local-in-time well posedness result under suitable regularity hypotheses. Let us denote:
$-$ X and Y two Hilbert spaces,
$-$ $d(\cdot,\cdot)$ a continuous bilinear form defined on $X \times Y$,
$-$ $c(\cdot,\cdot,\cdot)$ a continuous trilinear form defined on $X \times X \times X$ continuous with respect to the last two arguments.
Let us consider the following general abstract problem:

Problem 16 *Given $l \in X'$, find $(z,\gamma) \in X \times Y$ such that*

$$\begin{cases} c(z;z,v) + d(v,\gamma) =< l, v > \\ d(z,\mu) = 0 \end{cases}$$

for all $v \in X$ and $\mu \in Y$.

Let

$$W = \{w \in X : d(w,\mu) = 0,\ \forall \mu \in Y\}$$

be the kernel of the bilinear form $d(\cdot,\cdot)$. We can associate Problem 16 with the following "reduced" problem:

Problem 17 *Given $l \in X'$, find $z \in W$ such that*

$$c(z;z,v) =< l, v >$$

for all $v \in W$.

It is immediate to see that if (z,γ) is a solution of Problem 16, then z is a solution of Problem 17. The converse is true under the following condition (see [7, 24]):

Theorem 6 *If the bilinear form $d(\cdot,\cdot)$ fulfills the following* inf-sup *condition:*

$$\exists \beta > 0 :\ \forall \gamma \in Y,\ \exists v \in X :\ d(v,\gamma) \geq \beta \|\gamma\|_Y \|v\|_X, \tag{2.18}$$

then, for each solution $z \in X$ of Problem 17, there exists $\gamma \in Y$ such that the couple (z,γ) is a solution of Problem 16.

We can now prove the following result, that has been published in [70]:

Proposition 4 *For sufficiently smooth data Q_i with $\sum_i |Q_i|$ and $\|\boldsymbol{u}_0\|_{\boldsymbol{V}}$ small enough, Problem 11 is locally well-posed, i.e. there exists a time $T^* > 0$ such that a solution $(\boldsymbol{u}, p, \{\lambda_i\}_{i=1,\dots,m})$ exists in $[0,T^*]$.*

PROOF

Assume that $Q_i = 0$ for each i. In this case, observe that Problem 2, Section 1 and the augmented Problem 11 play the same role of Problems 17 and 16 in Theorem 6, respectively. In the general case of prescribed non null fluxes, we refer to the velocity field

$$\widetilde{\boldsymbol{u}} = \boldsymbol{u} - \sum_{i=1}^{m} Q_i \boldsymbol{b}_i,$$

with $\boldsymbol{b}_i$ given by (1.14) (lifting). If $\boldsymbol{\nu} \in \mathbb{R}^m$ and $\boldsymbol{w} \in \boldsymbol{V}$, we can introduce the bilinear form

$$e(\boldsymbol{w}, \boldsymbol{\nu}) = \sum_{i=1}^{m} \nu_i \int_{\Gamma_i} \boldsymbol{w} \cdot \boldsymbol{n} \, d\gamma.$$

Theorem 1, Section 1, states that a solution of the reduced problem exists in $[0, T^*]$. In order to prove that also the augmented problem is (locally) well-posed, we need to prove that the inf-sup condition (2.18) is fulfilled for the bilinear form $e(\boldsymbol{w}, \boldsymbol{\nu})$. We fix the time and for any m-dimensional vector $\boldsymbol{\nu}$ we set

$$\|\boldsymbol{\nu}\| = \max_{j=1,\ldots,m} |\nu_j|.$$

Let us denote by $\overline{j}$ ($1 \leq \overline{j} \leq m$) the index for which the maximum is attained (notice that $\overline{j}$ depends on time). Setting

$$\boldsymbol{v} = \text{sign}(\nu_{\overline{j}})(\boldsymbol{b}_{\overline{j}}),$$

we obtain:

$$e(\boldsymbol{v}, \boldsymbol{\nu}) = \sum_{j=1}^{m} \nu_j \int_{\Gamma_j} \text{sign}(\nu_{\overline{j}}) \boldsymbol{b}_{\overline{j}} \cdot \boldsymbol{n} \, d\gamma = \|\boldsymbol{\nu}\| \geq \|\boldsymbol{\nu}\| \frac{\|\boldsymbol{v}\|_{\boldsymbol{V}}}{\max_j \|\boldsymbol{b}_j\|_{\boldsymbol{V}}}.$$

The inf-sup condition is therefore fulfilled with

$$\beta = \frac{1}{\max_j \|\boldsymbol{b}_j\|_{\boldsymbol{V}}},$$

(which is time independent) and the thesis is therefore proven. $\diamond$

Let us prove some *a priori* estimates. Considering Problem 10, for the sake of simplicity with $m = 1$ and $Q_1 = 0$, let us set $\boldsymbol{v} = \boldsymbol{u}$ in the momentum equation and let us integrate in time. We obtain, exploiting that $\int_{\Gamma_1} \boldsymbol{u} \cdot \boldsymbol{n} \, d\gamma = 0$, the classical regularity results (see [67]):

$$\begin{cases} \boldsymbol{u} \in L^2(0, T^*; \boldsymbol{H}^2(\Omega)) \\ \boldsymbol{u}' \in L^2(0, T^*; \boldsymbol{L}^2(\Omega)) \end{cases} \tag{2.19}$$

From the *inf-sup* conditions we obtain (considering free-divergence subspaces):

$$|\lambda_1(t)| \leq \frac{1}{\beta} \sup_{\boldsymbol{v}\in\boldsymbol{V}} \frac{\lambda_1 \int_{\Gamma_1} \boldsymbol{v}\cdot\boldsymbol{n}\, d\gamma}{\|\boldsymbol{v}\|_{\boldsymbol{V}}} =$$

$$= \frac{1}{\beta} \sup_{\boldsymbol{v}\in\boldsymbol{V}} \frac{(\boldsymbol{f},\boldsymbol{v}) - \left(\frac{\partial \boldsymbol{u}}{\partial t},\boldsymbol{v}\right) - a_L(\boldsymbol{u},\boldsymbol{v}) - ((\boldsymbol{\beta}\cdot\nabla)\boldsymbol{u},\boldsymbol{v})}{\|\boldsymbol{v}\|_{\boldsymbol{V}}} \leq$$

$$\leq \frac{1}{\beta} \sup_{\boldsymbol{v}\in\boldsymbol{V}} \frac{\|\boldsymbol{f}\|\,\|\boldsymbol{v}\| + \left\|\frac{\partial \boldsymbol{u}}{\partial t}\right\|\|\boldsymbol{v}\| + \mu\|\boldsymbol{u}\|_{\boldsymbol{V}}\|\boldsymbol{v}\|_{\boldsymbol{V}} + \|\boldsymbol{\beta}\|_{\boldsymbol{L}^\infty(\Omega)}\|\boldsymbol{u}\|_{\boldsymbol{V}}\|\boldsymbol{v}\|}{\|\boldsymbol{v}\|_{\boldsymbol{V}}}$$

Exploiting the Poincaré inequality (with constant C_P), we obtain:

$$|\lambda_1(t)| \leq \frac{1}{\beta}\Big(C_P\|\boldsymbol{f}\| + C_P\left\|\frac{\partial \boldsymbol{u}}{\partial t}\right\| + \mu\|\boldsymbol{u}\|_{\boldsymbol{V}} + C_P\|\boldsymbol{\beta}\|_{\boldsymbol{L}^\infty(\Omega)}\|\boldsymbol{u}\|_{\boldsymbol{V}}\Big).$$

From the regolarity results (2.19) we obtain that all the terms at the right hand side are in $L^2(0,T^*)$ and therefore we conclude that $\lambda_1 \in L^2(0,T^*)$.

Both the well-posedness analysis and the *a priori* estimates could be easily extended to Problem 13 and to its non-linear counterpart.

2.4 Error analysis in imposing Dirichlet boundary conditions

Exploiting the augmented formulations proposed in Section 2.2.1, we prove a result for estimating the error in imposing an arbitrary velocity profile instead of the fluxes (*practical approach*, see Section 1.3.1). The idea is to reformulate also this problem in an augmented way and to give an estimate for the difference between the two problems. This result is reported in [71].

Namely, we want to quantify the error done by imposing the condition

$$\boldsymbol{u}|_{\Gamma_i} = \boldsymbol{g}, \quad i = 1,\dots,m,$$

with an arbitrary function $\boldsymbol{g} \in H^{1/2}(\partial\Omega)$ such that

$$\int_{\Gamma_i} \boldsymbol{g}\cdot\boldsymbol{n}\, d\gamma = Q_i, \quad i = 1,\dots,m,$$

instead of the flow rate boundary condition

$$\int_{\Gamma_i} \boldsymbol{u}\cdot\boldsymbol{n}\, d\gamma = Q_i.$$

Actually, we will develop our analysis in divergence free subspaces, so that we will not deal with the pressure field. For the sake of simplicity, we will refer to the case $m = 1$ and to the Stokes problem. Let us denote by Γ the part of the boundary where the flow rate condition is prescribed. Moreover, let us denote $\hat{\Gamma} = \Gamma_w \cup \Gamma$. In the divergence free subspace, the augmented formulation for this problem reads:

Find $\boldsymbol{u} \in L^2(0,T;\boldsymbol{V}^*) \cap L^\infty(0,T;\boldsymbol{L}^2(\Omega)^*)$ and $\lambda \in L^2(0,T)$ such that for all $\boldsymbol{v} \in \boldsymbol{V}^*$:

$$\begin{cases} \left(\dfrac{\partial \boldsymbol{u}}{\partial t}, \boldsymbol{v}\right) + a\left(\boldsymbol{u}, \boldsymbol{v}\right) + \lambda \displaystyle\int_\Gamma \boldsymbol{v} \cdot \boldsymbol{n} d\gamma = (\boldsymbol{f}, \boldsymbol{v}) \\ \displaystyle\int_\Gamma \boldsymbol{u} \cdot \boldsymbol{n} d\gamma = Q \end{cases}$$

with $\boldsymbol{u}|_{t=0} = \boldsymbol{u}_0$. Let us reformulate the previous problem in an homogeneous form through a lifting procedure. Let us pose

$$\boldsymbol{u}^0 = \boldsymbol{u} - \widetilde{\boldsymbol{g}},$$

with $\widetilde{\boldsymbol{g}} \in H^1(\Omega)$ such that

$$\int_\Gamma \widetilde{\boldsymbol{g}} \cdot \boldsymbol{n}\, d\gamma = Q.$$

In particular, let us choice $\widetilde{\boldsymbol{g}}$ such that

$$\widetilde{\boldsymbol{g}}|_\Gamma = \boldsymbol{g}.$$

In this way, we obtain the following problem:

Find $\boldsymbol{u}^0 \in L^2(0,T;\boldsymbol{V}^*) \cap L^\infty(0,T;\boldsymbol{L}^2(\Omega)^*)$ and $\lambda \in L^2(0,T)$ such that for all $\boldsymbol{v} \in \boldsymbol{V}^*$:

$$\begin{cases} \left(\dfrac{\partial \boldsymbol{u}^0}{\partial t}, \boldsymbol{v}\right) + a\left(\boldsymbol{u}^0, \boldsymbol{v}\right) + \lambda \displaystyle\int_\Gamma \boldsymbol{v} \cdot \boldsymbol{n} d\gamma = (\boldsymbol{f}, \boldsymbol{v}) - \left(\dfrac{\partial \widetilde{\boldsymbol{g}}}{\partial t}, \boldsymbol{v}\right) - a\left(\widetilde{\boldsymbol{g}}, \boldsymbol{v}\right) \\ \displaystyle\int_\Gamma \boldsymbol{u}^0 \cdot \boldsymbol{n} d\gamma = 0 \end{cases} \tag{2.20}$$

with $\boldsymbol{u}^0|_{t=0} = \boldsymbol{u}_0 - \widetilde{\boldsymbol{g}}|_{t=0}$.

Correspondingly, the problem obtained by prescribing the Dirichlet boundary condition

$$\boldsymbol{u}|_\Gamma = \boldsymbol{g}$$

can be formulated, choosing $\widetilde{\boldsymbol{g}}$ as lifting function, as follow:

Find $\hat{\boldsymbol{u}}^0 \in L^2(0,T;\boldsymbol{H}^1_{\hat{\Gamma}}(\Omega)^*) \cap L^\infty(0,T,\boldsymbol{L}^2(\Omega)^*)$ such that for all $\boldsymbol{v} \in \boldsymbol{H}^1_{\hat{\Gamma}}(\Omega)^*$:

$$\left(\frac{\partial \hat{\boldsymbol{u}}^0}{\partial t}, \boldsymbol{v}\right) + a\left(\hat{\boldsymbol{u}}^0, \boldsymbol{v}\right) = (\boldsymbol{f}, \boldsymbol{v}) - \left(\frac{\partial \widetilde{\boldsymbol{g}}}{\partial t}, \boldsymbol{v}\right) - a\left(\widetilde{\boldsymbol{g}}, \boldsymbol{v}\right) \tag{2.21}$$

with the initial condition $\hat{\boldsymbol{u}}^0|_{t=0} = \boldsymbol{u}_0 - \widetilde{\boldsymbol{g}}|_{t=0}$.

In order to compare the two solutions, we reformulate the latter problem in a different way.

Proposition 5 *Problem (2.21) is equivalent to the following "augmented" problem: find* $\hat{\boldsymbol{u}}^0 \in L^2(0,T;\boldsymbol{V}^*) \cap L^\infty(0,T;\boldsymbol{L}^2(\Omega)^*)$ *and* $\boldsymbol{\zeta} \in L^2(0,T;\boldsymbol{H}^{-1/2}(\Gamma))$ *such that for all* $\boldsymbol{v} \in \boldsymbol{V}^*$ *and* $\boldsymbol{\chi} \in \boldsymbol{H}^{-1/2}(\Gamma)$*:*

$$\begin{cases} \left(\dfrac{\partial \hat{\boldsymbol{u}}^0}{\partial t}, \boldsymbol{v}\right) + a\left(\hat{\boldsymbol{u}}^0, \boldsymbol{v}\right) + \displaystyle\int_\Gamma \boldsymbol{\zeta} \cdot \boldsymbol{v} d\gamma = (\boldsymbol{f}, \boldsymbol{v}) - \left(\dfrac{\partial \widetilde{\boldsymbol{g}}}{\partial t}, \boldsymbol{v}\right) - a\left(\widetilde{\boldsymbol{g}}, \boldsymbol{v}\right) \\ \displaystyle\int_\Gamma \boldsymbol{\chi} \cdot \hat{\boldsymbol{u}}^0 d\gamma = 0 \end{cases} \tag{2.22}$$

with $\hat{\boldsymbol{u}}^0|_{t=0} = \boldsymbol{u}_0 - \widetilde{\boldsymbol{g}}|_{t=0}$.

In the previous proposition the terms $\displaystyle\int_\Gamma \boldsymbol{\chi} \cdot \boldsymbol{v}\, d\gamma$ has to be intended as duality between $\boldsymbol{H}^{-1/2}(\Gamma)$ and $\boldsymbol{H}^{1/2}(\Gamma)$ in the general case.

Proof

The implication that the solution $\hat{\boldsymbol{u}}^0$ of (2.22) solves also (2.21) is trivial, since it is enough to select in (2.22) the test functions belonging to $\boldsymbol{H}^1_{\hat{\Gamma}}(\Omega)^* \subset \boldsymbol{V}^*$. The opposite implication can be proven, referring to [7, 24] and to Theorem 6, by showing that the following inequality holds: there exists a $\beta > 0$ such that, for each $\boldsymbol{\chi} \in \boldsymbol{H}^{-1/2}(\Gamma)$, there exists a vector $\boldsymbol{v}$ such that

$$\int_\Gamma \boldsymbol{\chi} \cdot \boldsymbol{v}\, d\gamma \geq \beta ||\boldsymbol{\chi}||_{\boldsymbol{H}^{-1/2}(\Gamma)} ||\boldsymbol{v}||_{\boldsymbol{V}}. \tag{2.23}$$

To this aim, let us introduce the definition of norm in $\boldsymbol{H}^{-1/2}(\Gamma)$:

$$\|\boldsymbol{\chi}\|_{\boldsymbol{H}^{-1/2}(\Gamma)} = \sup_{\|\boldsymbol{w}\|_{\boldsymbol{H}^{1/2}(\Gamma)}=1} \int_\Gamma \boldsymbol{\chi} \cdot \boldsymbol{v}\, d\gamma$$

where $< \cdot, \cdot >$ denotes the duality between $\boldsymbol{H}^{-1/2}(\Gamma)$ and $\boldsymbol{H}^{1/2}(\Gamma)$. Let us choose $\widetilde{\boldsymbol{w}}$ with $\|\widetilde{\boldsymbol{w}}\|_{\boldsymbol{H}^{1/2}(\Gamma)} = 1$, such that

$$\frac{1}{2}\|\boldsymbol{\chi}\|_{\boldsymbol{H}^{-1/2}(\Gamma)} \leq \int_\Gamma \boldsymbol{\chi} \cdot \boldsymbol{v}\, d\gamma.$$

From the definition of norm in $\boldsymbol{H}^{1/2}(\Gamma)$:

$$\|\widetilde{\boldsymbol{w}}\|_{\boldsymbol{H}^{1/2}(\Gamma)} = \inf_{\boldsymbol{z}|_\Gamma=\widetilde{\boldsymbol{w}}} \|\boldsymbol{z}\|_{\boldsymbol{V}}$$

we can choose $\boldsymbol{v}$ with $\boldsymbol{v}|_\Gamma = \widetilde{\boldsymbol{w}}$ such that

$$\|\boldsymbol{v}\|_{\boldsymbol{V}} \leq 2\|\widetilde{\boldsymbol{w}}\|_{\boldsymbol{H}^{1/2}(\Gamma)}.$$

Therefore, we obtain

$$\int_\Gamma \boldsymbol{\chi}\cdot\boldsymbol{v}\, d\gamma \geq \frac{1}{2}\|\boldsymbol{\chi}\|_{\boldsymbol{H}^{-1/2}(\Gamma)} = \frac{1}{2}\|\boldsymbol{\chi}\|_{\boldsymbol{H}^{-1/2}(\Gamma)}\|\widetilde{\boldsymbol{w}}\|_{\boldsymbol{H}^{1/2}(\Gamma)} \geq \frac{1}{4}\|\boldsymbol{\chi}\|_{\boldsymbol{H}^{-1/2}(\Gamma)}\|\boldsymbol{v}\|_{\boldsymbol{V}}$$

i.e. (2.23) with $\beta = \dfrac{1}{4}$. $\quad\diamond$

In the sequel $C_k(t)$ $(k = 1, 2, \ldots)$ will denote a generic function of time (or possibly a constant) dependent on the data and independent of the space coordinate. Observe that as a consequence of Proposition 5, by standard arguments we have that for $t > 0$

$$\int_0^t ||\boldsymbol{\zeta}||^2_{\boldsymbol{H}^{-1/2}(\Gamma)} ds \leq C_1.$$

The error analysis can be now carried out by considering the field $\boldsymbol{\delta} = \boldsymbol{u}^0 - \hat{\boldsymbol{u}}^0$. By subtracting (2.20) and (2.22) we have that for all $\boldsymbol{v} \in \boldsymbol{V}^*$

$$\begin{cases} \left(\dfrac{\partial\boldsymbol{\delta}}{\partial t}, \boldsymbol{v}\right) + a\,(\boldsymbol{\delta}, \boldsymbol{v}) + \displaystyle\int_\Gamma (\lambda\boldsymbol{n} - \boldsymbol{\zeta})\cdot\boldsymbol{v} d\gamma = 0 \\ \displaystyle\int_\Gamma \boldsymbol{\delta}\cdot\boldsymbol{n} d\gamma = 0 \end{cases} \tag{2.24}$$

with $\boldsymbol{\delta}|_{t=0} = \boldsymbol{0}$. We prove the following result.

Theorem 7 *Let $\Omega' \subset\subset \Omega$ be such that $dist(\Omega', \Gamma) \geq \overline{d}$. If the domain Ω is smooth enough, the following inequalities hold for $t > 0$*

$$\begin{cases} \|\boldsymbol{\delta}(t)\|^2 + \alpha\displaystyle\int_0^t ||\boldsymbol{\delta}(s)||^2_{\boldsymbol{V}} ds \leq C_2 \int_0^t ||\boldsymbol{\zeta}(s)||^2_{\boldsymbol{H}^{-1/2}(\Gamma)} ds, \\ \displaystyle\int_0^t ||\boldsymbol{\delta}(s)||^2_{\mathbf{H}^1(\Omega')} ds \leq C(t, \boldsymbol{\zeta}, \Gamma) e^{-\overline{d}}. \end{cases} \tag{2.25}$$

PROOF

Let us set in (2.24) $\boldsymbol{v} = \boldsymbol{\delta}$. Since λ is constant in space and $\int_\Gamma \boldsymbol{\delta} \cdot \boldsymbol{n}\, d\gamma = 0$, we obtain

$$\left(\frac{\partial \boldsymbol{\delta}}{\partial t}, \boldsymbol{\delta}\right) + a\left(\boldsymbol{\delta}, \boldsymbol{\delta}\right) - \int\limits_\Gamma \boldsymbol{\zeta} \cdot \boldsymbol{\delta} d\gamma = 0. \tag{2.26}$$

From the coercivity of the bilinear form $a\left(\cdot, \cdot\right)$, we have

$$\frac{1}{2}\frac{d}{dt}\|\boldsymbol{\delta}\|^2 + \alpha||\boldsymbol{\delta}||^2_{\boldsymbol{V}} \leq \left|\int\limits_\Gamma \boldsymbol{\zeta} \cdot \boldsymbol{\delta} d\gamma\right| \leq \|\boldsymbol{\zeta}\|_{\boldsymbol{H}^{-1/2}(\Gamma)} \|\boldsymbol{\delta}\|_{\boldsymbol{H}^{1/2}(\Gamma)}. \tag{2.27}$$

From this inequality we obtain the first of (2.25) by integrating in time and applying the Young and the trace inequalities in a standard way.

Let us prove the second (2.25). The basic approach is similar to the one followed by Rannacher in the analysis of Chorin-Temam method for Navier-Stokes equations, presented in [58]. Let us denote by $d(\boldsymbol{x})$ the distance of the generic point of the domain Ω from Γ and set $\sigma(\boldsymbol{x}) \equiv \min(e^{d(\boldsymbol{x})}, e^{\overline{d}})$. Since for $\boldsymbol{x} \in \Omega'$ we have $\sigma(\boldsymbol{x}) = e^{\overline{d}}$ and therefore $\nabla(\sqrt{\sigma})|_{\Omega'} = 0$, we obtain:

$$\mu \int\limits_0^t \int\limits_{\Omega'} \nabla \boldsymbol{\delta} : \nabla \boldsymbol{\delta} d\omega ds = e^{-\overline{d}} \mu \int\limits_0^t \int\limits_{\Omega'} \sigma \nabla \boldsymbol{\delta} : \nabla \boldsymbol{\delta} d\omega ds =$$

$$= e^{-\overline{d}} \mu \int\limits_0^t \int\limits_{\Omega'} \nabla(\boldsymbol{\delta}\sqrt{\sigma}) : \nabla(\boldsymbol{\delta}\sqrt{\sigma}) d\omega ds \leq$$

$$\leq e^{-\overline{d}} \mu \int\limits_0^t \int\limits_{\Omega} \nabla(\boldsymbol{\delta}\sqrt{\sigma}) : \nabla(\boldsymbol{\delta}\sqrt{\sigma}) d\omega ds \leq e^{-\overline{d}} C_3 \int\limits_0^t ||\boldsymbol{\delta}\sqrt{\sigma}||^2_{\boldsymbol{V}} ds. \tag{2.28}$$

Now, choose $\boldsymbol{v} = \sigma\boldsymbol{\delta}$ in (2.24). Since on Γ we have that $\sigma = 1$, we obtain

$$\lambda \int\limits_\Gamma \sigma \boldsymbol{\delta} \cdot \boldsymbol{n}\, d\gamma = \lambda \int\limits_\Gamma \boldsymbol{\delta} \cdot \boldsymbol{n}\, d\gamma = 0.$$

Consequently, we have:

$$\frac{1}{2}\frac{d}{dt}||\boldsymbol{\delta}\sqrt{\sigma}||^2 + \mu \int\limits_\Omega \sigma \nabla \boldsymbol{\delta} : \nabla \boldsymbol{\delta} d\omega = -\mu \int\limits_\Omega \boldsymbol{\delta} \cdot (\nabla \boldsymbol{\delta} \nabla \sigma) d\omega + \int\limits_\Gamma \boldsymbol{\zeta} \cdot \boldsymbol{\delta} d\gamma, \tag{2.29}$$

If d is smooth enough, the following identities hold:

$$\begin{cases} \nabla\sigma|_{\Omega'} = \mathbf{0} \\ \nabla\sigma|_{\Omega\setminus\Omega'} = \sigma\nabla d \\ \sqrt{\sigma}|_{\Gamma} = 1 \end{cases}$$

Exploiting this, we obtain from the Young inequality:

$$\left|\mu\int_{\Omega}\boldsymbol{\delta}\cdot(\nabla\boldsymbol{\delta}\nabla\sigma)d\omega\right| \leq \mu||\nabla d||_{\boldsymbol{L}^{\infty}(\Omega)}||\boldsymbol{\delta}\sqrt{\sigma}||\,||\nabla\boldsymbol{\delta}\sqrt{\sigma}|| \leq$$

$$\leq C_4||\boldsymbol{\delta}\sqrt{\sigma}||^2 + C_5||\nabla\boldsymbol{\delta}\sqrt{\sigma}||^2.$$

Consequently, observing that $\nabla(\sqrt{\sigma})|_{\Omega\setminus\Omega'} = 1/2\sqrt{\sigma}\nabla d$, from (2.29) we obtain:

$$\frac{1}{2}\frac{d}{dt}||\boldsymbol{\delta}\sqrt{\sigma}||^2 + \mu\int_{\Omega}\sigma\nabla\boldsymbol{\delta}:\nabla\boldsymbol{\delta}d\omega \leq C_4||\boldsymbol{\delta}\sqrt{\sigma}||^2 + C_5||\nabla\boldsymbol{\delta}\sqrt{\sigma}||^2 + \int_{\Gamma}\boldsymbol{\zeta}\cdot\boldsymbol{\delta}\sqrt{\sigma}d\gamma \leq$$

$$\leq C_4||\boldsymbol{\delta}\sqrt{\sigma}||^2 + C_5||\nabla\boldsymbol{\delta}\sqrt{\sigma}||^2 + C_6\|\boldsymbol{\zeta}\|^2_{\boldsymbol{H}^{-1/2}(\Gamma)} + C_7\|\nabla(\boldsymbol{\delta}\sqrt{\sigma})\|^2 \leq$$

$$\leq C_4||\boldsymbol{\delta}\sqrt{\sigma}||^2 + C_5||\nabla\boldsymbol{\delta}\sqrt{\sigma}||^2 + C_6\|\boldsymbol{\zeta}\|^2_{\boldsymbol{H}^{-1/2}(\Gamma)} + C_7\|\nabla\boldsymbol{\delta}\sqrt{\sigma}\|^2 + C_7\|\nabla d\|_{\boldsymbol{L}^{\infty}(\Omega)}\|\boldsymbol{\delta}\sqrt{\sigma}\|^2$$

and then

$$\frac{1}{2}\frac{d}{dt}||\boldsymbol{\delta}\sqrt{\sigma}||^2 + (\mu - C_5 - C_7)\|\nabla\boldsymbol{\delta}\sqrt{\sigma}\|^2 \leq C_8||\boldsymbol{\delta}\sqrt{\sigma}||^2 + C_6\|\boldsymbol{\zeta}\|^2_{\boldsymbol{H}^{-1/2}(\Gamma)} \quad (2.30)$$

Choosing properly C_5 and C_6, by time integration of (2.30) and application of the Gronwall Lemma, we obtain:

$$||\boldsymbol{\delta}\sqrt{\sigma}||^2 \leq \int_0^t ||\boldsymbol{\zeta}||^2_{\boldsymbol{H}^{-1/2}(\Gamma)}ds\, e^{C_8 t},$$

yielding

$$\int_0^t ||\boldsymbol{\delta}\sqrt{\sigma}||^2_{\boldsymbol{V}} \leq C(\boldsymbol{\zeta}, |\Gamma|, t)$$

where $C(\boldsymbol{\zeta}, |\Gamma|, t)$ is increasing with t and $|\Gamma|$. From (2.28) we finally obtain:

$$\mu\int_0^t\int_{\Omega'}\nabla\boldsymbol{\delta}:\nabla\boldsymbol{\delta}d\omega ds \leq e^{-\overline{d}}C_3C(\boldsymbol{\zeta}, |\Gamma|, t) \quad (2.31)$$

yielding the thesis. $\diamond$

The relevance of the previous result is that at each fixed instant the error in a domain contained in Ω decreases exponentially with the distance from Γ. As pointed out in Section 1.3.1, from the practical viewpoint this implies that the domain of interest has to be extended yielding an increasing in computational costs. However, different Reynolds numbers lead to different enlargement of the domain, as it is evident by the fact that constant C in (2.31) grows up with Re. In Section 2.5.5, we will see an approximate (and however fast) algorithm for solving the flow rate problem that belongs to these categories of approximate strategies, but yielding smaller errors than the ones obtained by choosing arbitrarily the velocity profile.

2.5 Numerical solution of the augmented problem

2.5.1 The discrete problem

We want now to investigate some numerical methods for the approximation of the augmented problems. In the sequel, we refer to a finite element discretization of the Oseen equations, featuring *inf-sup* compatible elements (see [55]). In particular, let us denote by $\boldsymbol{V}_h$ and Q_h the subspaces of $\boldsymbol{V}$ and $L^2(\Omega)$ of dimension N_u and N_p and with basis functions denoted by $\boldsymbol{\psi}_j$ and ζ_k, respectively, such that

$$\exists \beta > 0 : \forall p_h \in Q_h,\ \exists \boldsymbol{v}_h \in \boldsymbol{V}_h :\ b(p_h, \boldsymbol{v}_h) \geq \beta \|p_h\| \, \|\boldsymbol{v}_h\|_{\boldsymbol{V}}. \tag{2.32}$$

Moreover, let us denote with Ω_h the numerical computational domain obtained with a partition τ_h of Ω in elements K_j and let us set $Y_{T,h} = (0,T] \times \Omega_h$. The Galerkin-approximate in space problem related to Problem 10, reads:

Problem 18 *Given $\boldsymbol{u}_{0,h}$ suitable approximation of the initial guess $\boldsymbol{u}_0$ and with the same data of Problem 10, find $\boldsymbol{u}_h(t) \in L^2(0,T;\boldsymbol{V}_h) \cap L^\infty(0,T;\boldsymbol{L}^2(\Omega))$, $p \in L^2(0,T;Q_h)$ and $\boldsymbol{\lambda}_h \in (L^2(0,T))^m$ such that*

$$\begin{cases} \Big(\dfrac{\partial \boldsymbol{u}_h}{\partial t}, \boldsymbol{v}_h\Big) + a(\boldsymbol{u}_h, \boldsymbol{v}_h) + ((\boldsymbol{\beta}\cdot\nabla)\boldsymbol{u}_h, \boldsymbol{v}_h) + b(p_h, \boldsymbol{v}_h) + \\ \qquad\qquad + \displaystyle\sum_{j=1}^{m} \lambda_{j,h} \int_{\Gamma_j} \boldsymbol{v}_h \cdot \boldsymbol{n}\, d\gamma = (\boldsymbol{f}, \boldsymbol{v}_h), \quad (t,\boldsymbol{x}) \in Y_{T,h} \\ b(q_h, \boldsymbol{u}_h) = 0, \qquad (t,\boldsymbol{x}) \in Y_{T,h} \\ \boldsymbol{u}_h|_{t=0} = \boldsymbol{u}_{0,h}, \qquad \boldsymbol{x} \in \Omega \\ \displaystyle\int_{\Gamma_i} \boldsymbol{u}_h \cdot \boldsymbol{n}\, d\gamma = Q_i \quad \forall i = 1,\dots,m, \qquad t \in (0,T] \end{cases}$$

for all $\boldsymbol{v}_h \in \boldsymbol{V}_h$ *and* $q_h \in Q_h$.

In order to discretize also with respect to the time variable, let us introduce a partition of the time interval $[0, T]$ into subintervals. For the sake of simplicity, we refer to a uniform subdivision with size Δt. Among the other methods for the time advancing, we consider a discretization of the time derivatives based on the Backward Difference Formulas (BDF) (see [35]). Setting $t^n = n\Delta t$, for $n = 0, 1, \ldots$, we have the following:

Problem 19 *Given* $\boldsymbol{u}_{0,h}$ *suitable approximation of the initial guess* $\boldsymbol{u}_0$ *and posing* $\boldsymbol{f}^n = \boldsymbol{f}(t^n, \boldsymbol{x})$, $\boldsymbol{\beta}^n = \boldsymbol{\beta}(t^n, \boldsymbol{x})$ *and* $Q_j^n = Q_j(t^n)$, $j = 1, \ldots, m$, *find* $\boldsymbol{u}_h^{n+1}(t) \in \boldsymbol{V}_h$, $p_h^{n+1} \in Q_h$ *and* $\boldsymbol{\lambda}_h^{n+1} \in \mathbb{R}^m$ *such that, for each* n*:*

$$
\begin{cases}
\dfrac{\alpha}{\Delta t}\Big(\boldsymbol{u}_h^{n+1}, \boldsymbol{v}_h\Big) + a(\boldsymbol{u}_h^{n+1}, \boldsymbol{v}_h) + ((\boldsymbol{\beta}^{n+1} \cdot \nabla)\boldsymbol{u}_h^{n+1}, \boldsymbol{v}_h) + b(p_h^{n+1}, \boldsymbol{v}_h) + \\
\quad + \displaystyle\sum_{j=1}^{m} \lambda_{j,h}^{n+1} \int_{\Gamma_j} \boldsymbol{v}_h \cdot \boldsymbol{n}\, d\gamma = (\boldsymbol{f}^{n+1}, \boldsymbol{v}_h) + \sum_{j=0}^{r \le n} \frac{\tau_j}{\Delta t}\Big(\boldsymbol{u}_h^{n-j}, \boldsymbol{v}_h\Big), \ \boldsymbol{x} \in \Omega_h \\
b(q_h, \boldsymbol{u}_h^{n+1}) = 0, \qquad \boldsymbol{x} \in \Omega_h \\
\boldsymbol{u}_h^0 = \boldsymbol{u}_{0,h}, \qquad \boldsymbol{x} \in \Omega_h \\
\displaystyle\int_{\Gamma_i} \boldsymbol{u}_h^{n+1} \cdot \boldsymbol{n}\, d\gamma = Q_i^{n+1} \quad \forall i = 1, \ldots, m,
\end{cases}
$$

for all $\boldsymbol{v}_h \in \boldsymbol{V}_h$ *and* $q_h \in Q_h$ *and where* α *and* τ_j, $j = 0, \ldots, r$, *are the coefficients of the time discretization.*

The algebraic form of the augmented discrete problem is therefore given by:

$$
\begin{bmatrix} K & B^t & \Phi^t \\ B & 0 & 0 \\ \Phi & 0 & 0 \end{bmatrix} \begin{bmatrix} \boldsymbol{U}^{n+1} \\ \boldsymbol{P}^{n+1} \\ \boldsymbol{\Lambda}^{n+1} \end{bmatrix} = \begin{bmatrix} \widetilde{\boldsymbol{F}}^{n+1} \\ \boldsymbol{0} \\ \boldsymbol{Q}^{n+1} \end{bmatrix} \tag{2.33}
$$

where $\boldsymbol{U}^{n+1}$ and $\boldsymbol{P}^{n+1}$ are the vectors of the nodal values of the velocity and of the pressure field respectively and $\boldsymbol{\Lambda}^{n+1}$ is the vector of the approximated Lagrange multipliers at time step $n+1$, $K = K^{n+1} = \dfrac{\alpha}{\Delta t} M + A + C$ sums up the discretization of the time derivative (mass matrix $M = [m_{ij}] = [(\boldsymbol{\psi}_i, \boldsymbol{\psi}_j)]$), of the viscous term (stiffness matrix $A = [a_{ij}] = [a(\boldsymbol{\psi}_i, \boldsymbol{\psi}_j)]$) and of the convective one (matrix $C = C^{n+1} = [c_{ij}] = [((\boldsymbol{\beta}^{n+1} \cdot \nabla)\boldsymbol{\psi}_i, \boldsymbol{\psi}_j)]$. In all these three cases we have $i, j = 1, \ldots, N_u$. Finally, $B = [b_{il}] = [b(\zeta_l, \boldsymbol{\psi}_i)]$, for $l = 1, \ldots, N_p$ and $i = 1, \ldots, N_u$, $\quad \Phi = [\phi_{rj}] = [\int_{\Gamma_r} \boldsymbol{\psi}_j \cdot \boldsymbol{n}\, d\gamma]$, for $r = 1, \ldots, m$ and $j = 1, \ldots, N_u$, and $\widetilde{\boldsymbol{F}}^{n+1} = \boldsymbol{F}^{n+1} + \sum_{j=0}^{r \le n} \dfrac{\tau_j}{\Delta t} M \boldsymbol{U}^{n-j}$, with $\boldsymbol{F} = [F_i] = (\boldsymbol{f}, \boldsymbol{\psi}_i)$. We have the following result:

Proposition 6 *Under the same regularity assumptions of Proposition 4, Problem 18 is locally well-posed, i.e. there exists a time $T^* > 0$ such that a solution $(\boldsymbol{u}_h, p_h, \{\lambda_{i,h}\}_{i=1,\dots,m})$ holds in $[0, T^*]$. Moreover, Problem 19 admits a unique solution if*

$$\Delta t < \min_{\{\boldsymbol{w}_h \neq \boldsymbol{0}\}} \frac{\alpha |\boldsymbol{w}_h^t M \boldsymbol{w}_h|}{|\boldsymbol{w}_h^t C \boldsymbol{w}_h|}. \tag{2.34}$$

PROOF
The well-posedness of Problem 18 is a consequence of Proposition 4 and of the discrete inf-sup condition (2.32). Moreover, in order to prove the well posedness of Problem 19, we prove that under condition (2.34), matrix K is positive definite, i.e. that

$$\boldsymbol{w}_h^t K \boldsymbol{w}_h > 0, \quad \forall \boldsymbol{w}_h \neq \boldsymbol{0}$$

Since A is positive definite (see [55]), we require that:

$$\frac{\alpha}{\Delta t} \boldsymbol{w}_h^t M \boldsymbol{w}_h + \boldsymbol{w}_h^t C \boldsymbol{w}_h > 0, \quad \forall \boldsymbol{w}_h \neq \boldsymbol{0}$$

yielding the thesis. $\diamond$

For the approximation of the augmented Navier-Stokes Problem 11, we consider, if not differently specified, a semi-implicit discretization. In particular, we set

$$\boldsymbol{\beta}^{n+1} = \boldsymbol{u}_h^n$$

in Problem 19 and in (2.33).

In the sequel of this section we recall the numerical methods introduced for the augmented steady-Stokes case in [14]. Then, we illustrate three algorithms for the numerical resolution of Problems 18-19 (Section 2.5.3-2.5.5).

2.5.2 Numercal algorithms for the steady Stokes problem

In this section we present the numerical strategies proposed in [14] for the numerical resolution of Problem 3, whose algebraic counterpart is (2.33) with $K = A$ and $\widetilde{\boldsymbol{F}} = \boldsymbol{F}$.

Reordering + algebraic splitting

The first two algorithms are based on the algebraic factorization of a general system in the form:

$$\begin{bmatrix} D & E^t \\ E & 0 \end{bmatrix} \begin{bmatrix} \boldsymbol{X}_1 \\ \boldsymbol{X}_2 \end{bmatrix} = \begin{bmatrix} \boldsymbol{G} \\ \boldsymbol{0} \end{bmatrix}$$

In particular, let us recall that this linear system can be solved exactly by the following three step algorithm:

i) $D\widetilde{\boldsymbol{X}}_1 = \boldsymbol{G}$

ii) $ED^{-1}E^t\boldsymbol{X}_2 = E\widetilde{\boldsymbol{X}}_1$

iii) $\boldsymbol{X}_1 = \widetilde{\boldsymbol{X}}_1 - D^{-1}E^t\boldsymbol{X}_2$

where $\widetilde{\boldsymbol{X}}_1$ is an intermediate unknown. In this way it is possible to split the computation of the two unknowns $\boldsymbol{X}_1$ and $\boldsymbol{X}_2$. However, in order to obtain reasonable computational costs, a suitable approximation of matrix D^{-1} (inexact algebraic splitting) and a (block) preconditioning are often mandatory (see, for example, for the Navier-Stokes case [53, 69]).

In [14] an application of this algebraic factorization to the augmented steady-Stokes problem is proposed. In particular, system (2.33), with $K = A$ and $\widetilde{\boldsymbol{F}} = \boldsymbol{F}$, can be reordered in a standard form as

$$\begin{bmatrix} \hat{A} & \hat{B}^t \\ \hat{B} & 0 \end{bmatrix} \begin{bmatrix} \hat{\boldsymbol{U}} \\ \boldsymbol{P} \end{bmatrix} = \begin{bmatrix} \hat{\boldsymbol{F}} \\ \boldsymbol{0} \end{bmatrix} \tag{2.35}$$

where

$$\hat{A} = \begin{bmatrix} A & \Phi^t \\ \Phi & 0 \end{bmatrix} \quad \hat{B} = \begin{bmatrix} B & 0 \end{bmatrix}$$
$$\hat{\boldsymbol{U}} = \begin{bmatrix} \boldsymbol{U} \\ \boldsymbol{\Lambda} \end{bmatrix} \qquad \hat{\boldsymbol{F}} = \begin{bmatrix} \boldsymbol{F} \\ \boldsymbol{Q} \end{bmatrix}$$

Alternatively, it can be reordered in a different manner as

$$\begin{bmatrix} A & \hat{B}^t \\ \hat{B} & 0 \end{bmatrix} \begin{bmatrix} \boldsymbol{U} \\ \hat{\boldsymbol{P}} \end{bmatrix} = \begin{bmatrix} \boldsymbol{F} \\ \hat{\boldsymbol{Q}} \end{bmatrix} \tag{2.36}$$

where

$$\hat{B} = \begin{bmatrix} B \\ \Phi \end{bmatrix} \quad \hat{\boldsymbol{P}} = \begin{bmatrix} \boldsymbol{P} \\ \boldsymbol{\Lambda} \end{bmatrix} \quad \hat{\boldsymbol{Q}} = \begin{bmatrix} \boldsymbol{0} \\ \boldsymbol{Q} \end{bmatrix}.$$

Applying the three steps of the algebraic factorizatiom to system (2.35) or to system (2.36), we obtain an exact algebraic splitting of system (2.33) with $K = A$ and $\widetilde{\boldsymbol{F}} = \boldsymbol{F}$. Different inexact algebraic splitting are recovered starting from different approximations of matrix A^{-1} (see [14] for more details). We observe that from the pratical point of view, in each case it is necessary to modify a standard steady-Stokes solver by adding the lines of matrix Φ to A (as in reordering (2.35)) or to B (as in (2.36)).

Schur complement + iterative solver

An alternative algorithm is based on using an iterative solution of a Schur complement system. We rewrite (2.33), with $K = A$ and $\widetilde{\boldsymbol{F}} = \boldsymbol{F}$, in the form

$$\begin{bmatrix} S & \widetilde{\Phi}^t \\ \widetilde{\Phi} & 0 \end{bmatrix} \begin{bmatrix} \boldsymbol{X} \\ \boldsymbol{\Lambda} \end{bmatrix} = \begin{bmatrix} \boldsymbol{H} \\ \boldsymbol{Q} \end{bmatrix} \tag{2.37}$$

where $S = \begin{bmatrix} A & B^t \\ B & 0 \end{bmatrix}$, $\widetilde{\Phi} = \begin{bmatrix} \Phi & 0 \end{bmatrix}$, $\boldsymbol{X} = \begin{bmatrix} \boldsymbol{U} \\ \boldsymbol{P} \end{bmatrix}$ and $\boldsymbol{H} = \begin{bmatrix} \boldsymbol{F} \\ \boldsymbol{0} \end{bmatrix}$. Since the discrete inf-sup condition holds, S is nonsingular, so we can reduce system (2.37) by eliminating $\boldsymbol{X}$ as:

$$\widetilde{\Phi} S^{-1} \widetilde{\Phi}^t \boldsymbol{\Lambda} = \widetilde{\Phi} S^{-1} \boldsymbol{H} - \boldsymbol{Q} \tag{2.38}$$

where with S^{-1} we formally indicate the solution of a steady-Stokes problem. Matrix $R = \widetilde{\Phi} S^{-1} \widetilde{\Phi}^t \in \mathbb{R}^{m \times m}$ is the *Schur complement* associated to (2.37). The following result holds (see [14]):

Proposition 7 *The matrix R is symmetric positive definite.*

Therefore, system (2.38) can be solved by an appropriate iterative method. For example, since R is symmetric, it is possible to resort to the Coniugate Gradient (CG) method. For each iteration a matrix-vector multiplication is required and this implies the solution of a steady-Stokes problem with Neumann conditions on the artificial sections Γ_i. In addition, two extra steady-Stokes problem have to be solved to obtain the initial residual, required to start up the procedure, and the final solution $\boldsymbol{X}$. Therefore, if CG is adopted, the computational cost would be in principle equal to the solution of $m + 2$ steady-Stokes problems. Nevertheless, in Section 2.5.3 we will show that the final differential problem required to obtain the final solution can be skipped.

Continuous splitting algorithms

Finally, a completely different strategy presented in [14] is based on the well posedness analysis carried out for Problem 3. In particular, referring to the splitting recalled in Section 2.3.1, let us consider the following:

Algorithm 1

(See Figure 2.2)

1) Solve for all $i = 1, \ldots, m$

$$\begin{cases} a\left(\boldsymbol{w}_{i,h}, \boldsymbol{v}_h\right) + b\left(\pi_{i,h}, \boldsymbol{v}_h\right) = -\displaystyle\int_{\Gamma_i} \boldsymbol{v}_h \cdot \boldsymbol{n} d\gamma \\ b\left(q_h, \boldsymbol{w}_{i,h}\right) = 0, \end{cases} \tag{2.39}$$

$\forall \boldsymbol{v}_h \in \boldsymbol{V}_h, \forall q_h \in Q_h$.

2) Solve

$$\begin{cases} a\left(\widetilde{\boldsymbol{u}}_h, \boldsymbol{v}_h\right) + b\left(\widetilde{p}_h, \boldsymbol{v}_h\right) = \left(\boldsymbol{f}, \boldsymbol{v}_h\right) \\ b\left(q_h, \widetilde{\boldsymbol{u}}_h\right) = 0 \end{cases} \tag{2.40}$$

$\forall \boldsymbol{v}_h \in \boldsymbol{V}_h, \forall q_h \in Q_h$.

3) Solve the linear system

$$\sum_{j=1}^{m} \lambda_{j,h} \int_{\Gamma_i} \boldsymbol{w}_{j,h} \cdot \boldsymbol{n} d\gamma = Q_i - \int_{\Gamma_i} \widetilde{\boldsymbol{u}}_h \cdot \boldsymbol{n} d\gamma \tag{2.41}$$

in the unknowns $\lambda_{j,h}$.

4) Build the solution:

$$\begin{cases} \boldsymbol{u}_h = \widetilde{\boldsymbol{u}}_h + \displaystyle\sum_{i=1}^{m} \lambda_{i,h}(t) \boldsymbol{w}_{i,h}, \\ p_h = \widetilde{p}_h + \displaystyle\sum_{i=1}^{m} \lambda_{i,h}(t) \pi_{i,h}, \end{cases} \tag{2.42}$$

$\diamond$

We point out that all the differential problems in Algorithm 1 involve standard (natural) boundary conditions on the sections where the flow rates are prescribed. Therefore, if a steady-Stokes solver (possibly a commercial one) is available, it can be effectively used within the framework depicted in Figure 2.2. This algorithm has been investigated and tested in [72].

We observe that in the *Schur complement+iterative solver* and in the *Continuous Splitting* schemes, the Lagrange multipliers computation is split from the computation of the velocity-pressure pair. Furthermore, the steady-Stokes solution is cast in the framework of standard boundary value problems. In this way, the Lagrange multipliers computation can be coded as an external subroutine for a fluid solver that can be considered as a "black-box". Here, extending these

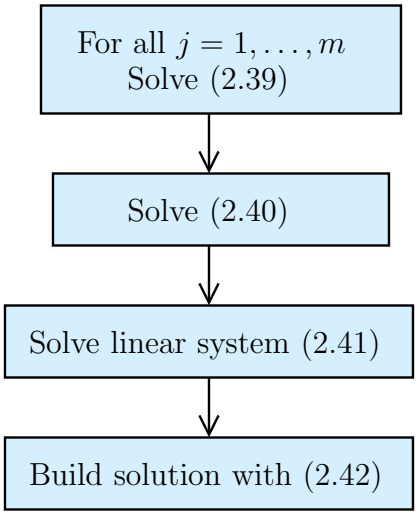

Figure 2.2: Algorithm 1 for the numerical resolution of the steady-Stokes augmented problem.

strategies to the unsteady-non linear case, we basically refer to these two splitting methods. In particular, in the next sections we introduce three algorithms for the resolution of Problem 18 and of its non linear and steady variants. The first two (Section 2.5.3 and 2.5.4) are taken from [70], while the third (Section 2.5.5) is taken from [71]. For the sake of clarity, in Table 2.1 we give a map of the algorithms.

	scheme I	scheme II	scheme III
steady Stokes	Alg. 2 or see [14]	Alg. 1	-
steady Oseen	Alg. 2	Alg. 5	-
steady NS	Alg. 3	Alg. 6	Alg. 8
unsteady Stokes	Alg. 4	Alg. 7	Alg. 8
unsteady Oseen	Alg. 2 (4 if $\boldsymbol{\beta} = \boldsymbol{\beta}(\boldsymbol{x})$)	Alg. 7	Alg. 8
unsteady NS	Alg. 2	Alg. 7	Alg. 8 or 9

Table 2.1: Algorithms for the flow rate problem

2.5.3 Schur complement scheme + GMRes (Scheme I)

General algorithm

Referring to the *Schur complement+iterative solver* scheme introduced above, we rewrite (2.33) in a more compact form:

$$\begin{bmatrix} N & \widetilde{\Phi}^t \\ \widetilde{\Phi} & 0 \end{bmatrix} \begin{bmatrix} \boldsymbol{X}^{n+1} \\ \boldsymbol{\Lambda}^{n+1} \end{bmatrix} = \begin{bmatrix} \boldsymbol{H}^{n+1} \\ \boldsymbol{Q}^{n+1} \end{bmatrix} \tag{2.43}$$

where $N = \begin{bmatrix} K & B^t \\ B & 0 \end{bmatrix}$. Since the discrete inf-sup condition holds, N is nonsingular, so we can reduce system (2.43) by eliminating $\boldsymbol{X}^{n+1}$ as:

$$\widetilde{\Phi} N^{-1} \widetilde{\Phi}^t \boldsymbol{\Lambda}^{n+1} = \widetilde{\Phi} N^{-1} \boldsymbol{H}^{n+1} - \boldsymbol{Q}^{n+1}.$$

where with N^{-1} we formally indicate the solution of a Oseen or of a linearized Navier-Stokes problem. Matrix $R = \widetilde{\Phi} N^{-1} \widetilde{\Phi}^t$ is the *Schur complement* associated to (2.43). The following result extends the one in Proposition 7:

Proposition 8 *Matrix R is positive semidefinite.*

The proof is analogous to the one of Proposition 7. Nevertheless, since N is not symmetric in the general case, we resort to the GMRes method as iterative solver for the computation of $\boldsymbol{\Lambda}^{n+1}$ (see [61]). In particular, we obtain the following (we omit for the sake of clearness the index $n+1$):

Algorithm 2

For each n solve:

$\boldsymbol{\Lambda}_0 = (\lambda_{01}, \ldots, \lambda_{0m})$ is given

a) $N\boldsymbol{X}_1 = \boldsymbol{H} - \widetilde{\Phi}^t \boldsymbol{\Lambda}_0$

$\boldsymbol{r}_0 = \widetilde{\Phi} \boldsymbol{X}_1 - \boldsymbol{Q}$

$\boldsymbol{v}_1 = \dfrac{\boldsymbol{r}_0}{\|\boldsymbol{r}_0\|}$

for $j = 1, \ldots, m$

$\boldsymbol{\eta}_j = \widetilde{\Phi}^t \boldsymbol{v}_j$

b) $N\boldsymbol{\xi}_j = \boldsymbol{\eta}_j$

$\boldsymbol{w}_j = \widetilde{\Phi}\boldsymbol{\xi}_j$

for $i = 1, \ldots, j$

$h_{ij} = (\boldsymbol{w}_j, \boldsymbol{v}_i)$

$\boldsymbol{w}_j = \boldsymbol{w}_j - h_{ij}\boldsymbol{v}_i$

end

$h_{j+1,j} = \|\boldsymbol{w}_j\|$

if $h_{j+1,j} = 0$

$n = j$ go to (*)

else $\boldsymbol{v}_{j+1} = \dfrac{\boldsymbol{w}_j}{h_{j+1,j}}$

end

end

(*) $\boldsymbol{z} = min\|\|\boldsymbol{r}_0\|\boldsymbol{e}_1 - H_n\boldsymbol{z}\|$

$\boldsymbol{\Lambda} = \boldsymbol{\Lambda}_0 + V\boldsymbol{z}$

$\boldsymbol{X} = \boldsymbol{X}_1 - Y\boldsymbol{z}$ $\quad \diamond$

With V we indicate the matrix whose columns are the vectors $\boldsymbol{v}_1, \ldots, \boldsymbol{v}_m$, with Y the matrix whose columns are the vectors $\boldsymbol{Y}_1, \ldots, \boldsymbol{Y}_m$, H_m is the $(m+1) \times m$ matrix whose entries are h_{ij} and where the norm are the Euclidean ones.

We notice that a system in N has to be preliminarily solved for the computation of the initial residual (step a)). Then, since GMRes converges in at most m iterations (recall that m is the number of sections where flow rate conditions are prescribed, so it is usually a small number), further m systems in N are solved to compute the residual at each iteration (step b)). Finally, once $\boldsymbol{\Lambda}$ has been computed, a further system in N should be solved for the computation of the velocity and the pressure fields. However, the residual computation in the last GMRes step on the converged solution already entails the solution of the latter system in N, so that the final velocity-pressure computation actually resorts to an algebraic manipulation of vectors. *This means that $m+1$ systems in N at each time step are required for this scheme.* Moreover, to solve a system for N actually corresponds to the solution of a Oseen or of a linearized Navier-Stokes problem with Neumann conditions on the sections where the flow rate is prescribed. This can be pursued, for example, by means of a given (generic) solver.

The steady Navier-Stokes problem

A specific scheme can be devised for the steady Navier-Stokes problem. In this case we have the problem in building matrix N, whose element ij is $[((\boldsymbol{u}_h \cdot \nabla)\boldsymbol{\psi}_i, \boldsymbol{\psi}_j)]$, if $i, j \leq N_u$, where $\boldsymbol{u}_h = \sum_{j=1}^{N_u} X_j \boldsymbol{\psi}_j$ is the approximated solution related to $\boldsymbol{X}$. In order to linearize the algorithm we resort to a fixed point strategy, obtaining:

Algorithm 3

(See Figure 2.3)
For k=1,... (fixed point iterations)

1) Given an initial guess $\boldsymbol{X}^{(0)}$, until convergence build for each k matrix $N^{(k)}$ whose element ij is $[((\boldsymbol{u}_h^{(k-1)} \cdot \nabla)\boldsymbol{\psi}_i, \boldsymbol{\psi}_j)]$ and solve

$\boldsymbol{\Lambda}_0^{(k)} = (\lambda_{01}^{(k)}, \ldots, \lambda_{0m}^{(k)})$ is given
$N^{(k)} \boldsymbol{X}_1^{(k)} = \boldsymbol{H} - \widetilde{\Phi}^t \boldsymbol{\Lambda}_0^{(k)}$
$\boldsymbol{r}_0^{(k)} = \widetilde{\Phi} \boldsymbol{X}_1^{(k)} - \boldsymbol{Q}$
$\boldsymbol{v}_1^{(k)} = \dfrac{\boldsymbol{r}_0^{(k)}}{\|\boldsymbol{r}_0^{(k)}\|}$
for $j = 1, \ldots, m$
  $\boldsymbol{\eta}_j^{(k)} = \widetilde{\Phi}^t \boldsymbol{v}_j^{(k)}$
  $N^{(k)} \boldsymbol{\xi}_j^{(k)} = \boldsymbol{\eta}_j^{(k)}$
  $\boldsymbol{w}_j^{(k)} = \widetilde{\Phi} \boldsymbol{\xi}_j^{(k)}$
    for $i = 1, \ldots, j$
    $h_{ij}^{(k)} = (\boldsymbol{w}_j^{(k)}, \boldsymbol{v}_i^{(k)})$
    $\boldsymbol{w}_j^{(k)} = \boldsymbol{w}_j^{(k)} - h_{ij}^{(k)} \boldsymbol{v}_i^{(k)}$
    end
  $h_{j+1,j}^{(k)} = \|\boldsymbol{w}_j^{(k)}\|$
  if $h_{j+1,j}^{(k)} = 0$
  $n = j$ go to (*)
  else $\boldsymbol{v}_{j+1}^{(k)} = \dfrac{\boldsymbol{w}_j^{(k)}}{h_{j+1,j}^{(k)}}$
  end
end

$$(*)\ \boldsymbol{z}^{(k)} = min\|\|\boldsymbol{r}_0^{(k)}\|\boldsymbol{e}_1 - H_n^{(k)}\boldsymbol{z}^{(k)}\|$$

$$\boldsymbol{\Lambda}^{(k)} = \boldsymbol{\Lambda}_0^{(k)} + V^{(k)}\boldsymbol{z}^{(k)}$$

$$\boldsymbol{X}^{(k)} = \boldsymbol{X}_1^{(k)} - Y^{(k)}\boldsymbol{z}^{(k)}$$

2) Convergence test

End fixed point iterations. $\diamond$

Obviously, for each iteration k we have to solve $m+1$ linearized Navier-Stokes problems.

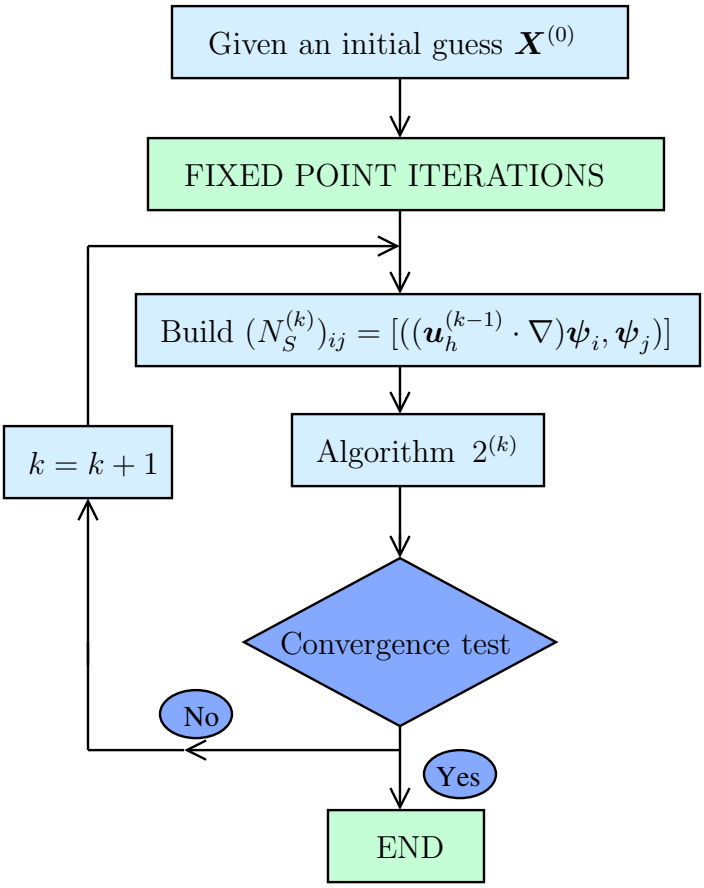

Figure 2.3: Algorithm 3 for the resolution of the steady Navier-Stokes problem - scheme I

The unsteady case with constant in time convective field

Let us consider the unsteady problem with $\boldsymbol{\beta} = \boldsymbol{\beta}(\boldsymbol{x})$ and in particular the unsteady Stokes problem ($\boldsymbol{\beta} = \mathbf{0}$). In this case, we can exploit the fact that matrix N does not depend on time. In particular, we point out that the solution of problems at step b) in Algorithm 2 can be computed outside of the time loop. In fact, if we know the solution of the m problems

$$N\boldsymbol{\theta}_i = \widetilde{\Phi}^t \boldsymbol{\beta}_i, \quad j = i, \ldots, m,$$

being $\boldsymbol{\beta}_1, \ldots, \boldsymbol{\beta}_m$ a basis of $\mathbb{R}^m$, we can construct the unknown $\boldsymbol{\xi}_j$ of problems at step b) by:

$$\boldsymbol{\xi}_j = \sum_{i=1}^{m} v_{ji} \boldsymbol{\theta}_i,$$

with v_{ji} the elements of matrix V definied in Algorithm 2. In particular we have:

Algorithm 4

1) Choose $(\boldsymbol{\beta}_1, \ldots, \boldsymbol{\beta}_m)$ a basis of $\mathbb{R}^m$

   Solve $N\boldsymbol{\theta}_i = \widetilde{\Phi}^t \boldsymbol{\beta}_i, \quad j = i, \ldots, m$

2) Temporal loop. For each n solve:

$\boldsymbol{\Lambda}_0 = (\lambda_{01}, \ldots, \lambda_{0m})$ is given
$N\boldsymbol{X}_1 = \boldsymbol{H} - \widetilde{\Phi}^t \boldsymbol{\Lambda}_0$
$\boldsymbol{r}_0 = \widetilde{\Phi}\boldsymbol{X}_1 - \boldsymbol{Q}$
$\boldsymbol{v}_1 = \dfrac{\boldsymbol{r}_0}{\|\boldsymbol{r}_0\|}$
for $j = 1, \ldots, m$
  $\boldsymbol{\xi}_j = \sum_{i=1}^{m} v_{ji} \boldsymbol{\theta}_i,$
  $\boldsymbol{w}_j = \widetilde{\Phi}\boldsymbol{\xi}_j$
    for $i = 1, \ldots, j$
    $h_{ij} = (\boldsymbol{w}_j, \boldsymbol{v}_i)$
    $\boldsymbol{w}_j = \boldsymbol{w}_j - h_{ij}\boldsymbol{v}_i$
    end
  $h_{j+1,j} = \|\boldsymbol{w}_j\|$
  if $h_{j+1,j} = 0$
  $n = j$ go to (*)

else $\boldsymbol{v}_{j+1} = \dfrac{\boldsymbol{w}_j}{h_{j+1,j}}$

end

end

(*) $\boldsymbol{z} = min\|\|\boldsymbol{r}_0\|\boldsymbol{e}_1 - H_n\boldsymbol{z}\|$

$\boldsymbol{\Lambda} = \boldsymbol{\Lambda}_0 + V\boldsymbol{z}$

$\boldsymbol{X} = \boldsymbol{X}_1 - Y\boldsymbol{z}$ $\quad \diamond$

Therefore, in this particular case, the solution of the augmented problem can be obtained by solving m steady problems out of the temporal loop and 1 unsteady problem, all with standard boundary conditions. We point out that if $\boldsymbol{\beta} = \mathbf{0}$, since matrix R is symmetric, we could resort to the CG method as well, as iterative solver for the computation of the Lagrange multipliers.

2.5.4 Continuous splitting-based scheme (Scheme II)

An alternative method stems from an extension of the splitting presented for the steady Stokes case in Section 2.5.2. The non linearity and the unsteadiness make this extension not trivial. We introduce our proposal by starting from a steady linear Oseen problem and then extending it to the steady non linear and to the unsteady case.

Steady Oseen problem

We refer to the augmented steady Oseen problem:

$$\begin{cases} a(\boldsymbol{u},\boldsymbol{v}) + ((\boldsymbol{\beta}\cdot\nabla)\boldsymbol{u},\boldsymbol{v}) + b(p,\boldsymbol{v}) + \\ \qquad\qquad + \sum_{j=1}^{m} \lambda_j \int_{\Gamma_j} \boldsymbol{v}\cdot\boldsymbol{n}\, d\gamma = (\boldsymbol{f},\boldsymbol{v}), \quad \boldsymbol{x}\in\Omega \\ b(q,\boldsymbol{u}) = 0, \qquad \boldsymbol{x}\in\Omega \\ \displaystyle\int_{\Gamma_i} \boldsymbol{u}\cdot\boldsymbol{n}\, d\gamma = Q_i \quad \forall i = 1,\ldots,m, \end{cases} \tag{2.44}$$

for all $\boldsymbol{v}\in\boldsymbol{V}$ and $q\in L^2(\Omega)$. It is easy to check that the solution of the previous problem is given by

$$\begin{cases} \boldsymbol{u} = \widetilde{\boldsymbol{u}} + \displaystyle\sum_{i=1}^{m} \lambda_i(t)\boldsymbol{w}_i, \\ p = \widetilde{p} + \displaystyle\sum_{i=1}^{m} \lambda_i(t)\pi_i, \end{cases} \tag{2.45}$$

where $(\boldsymbol{w}_i, \pi_i)$, $i = 1, \ldots, m$, are the solutions of the Oseen problems:

$$\begin{cases} a(\boldsymbol{w}_i, \boldsymbol{v}) + (\boldsymbol{\beta} \cdot \nabla)\boldsymbol{w}_i, \boldsymbol{v}) + b(\pi_i, \boldsymbol{v}) = -\displaystyle\int_{\Gamma_i} \boldsymbol{v} \cdot \boldsymbol{n} d\gamma \\ b(q, \boldsymbol{w}_i) = 0, \end{cases} \tag{2.46}$$

$\forall \boldsymbol{v} \in \boldsymbol{V}, \forall q \in L^2(\Omega)$, while $(\widetilde{\boldsymbol{u}}, \widetilde{p})$ is the solution of the Oseen problem:

$$\begin{cases} a(\widetilde{\boldsymbol{u}}, \boldsymbol{v}) + (\boldsymbol{\beta} \cdot \nabla)\widetilde{\boldsymbol{u}}, \boldsymbol{v}) + b(\widetilde{p}, \boldsymbol{v}) = (\boldsymbol{f}, \boldsymbol{v}) \\ b(q, \widetilde{\boldsymbol{u}}) = 0 \end{cases} \tag{2.47}$$

$\forall \boldsymbol{v} \in \boldsymbol{V}, \forall q \in L^2(\Omega)$. Let us notice that (2.46) are standards problems, where natural conditions are prescribed on Γ_i, namely for the $j-$th problem we impose

$$(p\boldsymbol{n} - \mu \nabla \boldsymbol{u}\ \boldsymbol{n})|_{\Gamma_i} = \delta_{ij}\boldsymbol{n}$$

(δ_{ij} is the Kronecker delta), while in (2.47) natural homogeneous conditions are prescribed on Γ_i. To compute the Lagrange multipliers λ_i, we substitute the first of (2.45) in the flow rate boundary conditions $(2.44)_3$, obtaining:

$$\sum_{j=1}^{m} \lambda_j \int_{\Gamma_i} \boldsymbol{w}_j \cdot \boldsymbol{n} d\gamma = Q_i - \int_{\Gamma_i} \widetilde{\boldsymbol{u}} \cdot \boldsymbol{n} d\gamma, \tag{2.48}$$

i.e. the same linear system (2.41) of Algorithm 1. We resort to the following

Algorithm 5

(See Figure 2.4)

1) Solve for all $i = 1, \ldots, m$

$$\begin{cases} a(\boldsymbol{w}_{i,h}, \boldsymbol{v}_h) + ((\boldsymbol{\beta} \cdot \nabla)\boldsymbol{w}_{i,h}, \boldsymbol{v}_h) + b(\pi_{i,h}, \boldsymbol{v}_h) = -\displaystyle\int_{\Gamma_i} \boldsymbol{v}_h \cdot \boldsymbol{n} d\gamma \\ b(q_h, \boldsymbol{w}_{i,h}) = 0, \end{cases} \tag{2.49}$$

$\forall \boldsymbol{v}_h \in \boldsymbol{V}_h, \forall q_h \in Q_h$.

2) Solve

$$\begin{cases} a(\widetilde{\boldsymbol{u}}_h, \boldsymbol{v}_h) + ((\boldsymbol{\beta} \cdot \nabla)\widetilde{\boldsymbol{u}}_h, \boldsymbol{v}_h) + b(\widetilde{p}_h, \boldsymbol{v}_h) = (\boldsymbol{f}, \boldsymbol{v}_h) \\ b(q_h, \widetilde{\boldsymbol{u}}_h) = 0 \end{cases} \tag{2.50}$$

$\forall \boldsymbol{v}_h \in \boldsymbol{V}_h, \forall q_h \in Q_h$.

3) Solve the linear system

$$\sum_{j=1}^{m} \lambda_{j,h} \int_{\Gamma_i} \boldsymbol{w}_{j,h} \cdot \boldsymbol{n} d\gamma = Q_i - \int_{\Gamma_i} \widetilde{\boldsymbol{u}}_h \cdot \boldsymbol{n} d\gamma \tag{2.51}$$

for the unknowns $\lambda_{j,h}$.

4) Build the solution:

$$\begin{cases} \boldsymbol{u}_h = \widetilde{\boldsymbol{u}}_h + \sum_{i=1}^{m} \lambda_{i,h}(t) \boldsymbol{w}_{i,h}, \\ p_h = \widetilde{p}_h + \sum_{i=1}^{m} \lambda_{i,h}(t) \pi_{i,h}, \end{cases} \tag{2.52}$$

◇

Therefore, the solution of the augmented steady Oseen problem is obtained

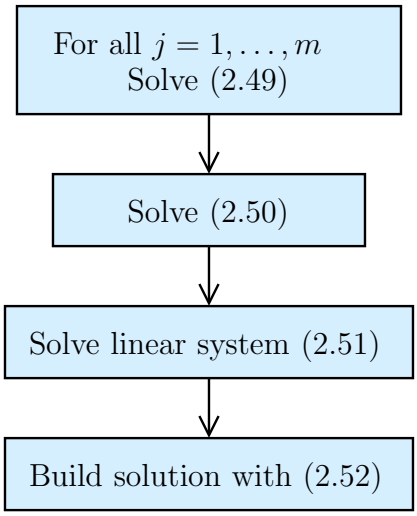

Figure 2.4: Algorithm 5 for the resolution of the steady-Oseen problem - scheme II

by solving $m + 1$ steady Oseen problem with standard boundary conditions. The computational effort of Algorithm 5 is the same of the one of Algorithm 2. Nevertheless, let us notice that if $\boldsymbol{f} = \boldsymbol{0}$, problem at step 2) can be dropped since it admits the unique solution $\boldsymbol{u} = \boldsymbol{0}$, $p = 0$.

Steady Navier-Stokes problem

As in the case of scheme I, in order to linearize the steady Navier-Stokes problem, we can resort to a fixed point strategy. In particular, a procedure similar to Algorithm 5 (with $\boldsymbol{\beta}$ equal to the numerical solution at the previous iteration) should be solved in an iterative framework until convergence. Therefore, we should solve $m+1$ problems for each iteration (as for scheme I). In order to reduce the computational effort, an alternative splitting can be considered. In particular, we resort to the following:

Algorithm 6

(See Figure 2.5)

1) Solve for all $i = 1, \ldots, m$ the standard Stokes problems

$$\begin{cases} a\left(\boldsymbol{w}_{i,h}, \boldsymbol{v}_h\right) + b\left(\pi_{i,h}, \boldsymbol{v}_h\right) = -\displaystyle\int_{\Gamma_i} \boldsymbol{v}_h \cdot \boldsymbol{n} d\gamma \\ b\left(q_h, \boldsymbol{w}_{i,h}\right) = 0, \end{cases} \tag{2.53}$$

$\forall \boldsymbol{v}_h \in \boldsymbol{V}_h, \forall q_h \in Q_h$.

2) For $k = 0, \ldots$ (fixed point iterations)

a) Given an initial guess $\boldsymbol{u}_{h,(0)}$, solve until convergence

$$\begin{cases} a\left(\widetilde{\boldsymbol{u}}_{h,(k+1)}, \boldsymbol{v}_h\right) + \left((\boldsymbol{u}_{h,(k)} \cdot \nabla)\widetilde{\boldsymbol{u}}_{h,(k+1)}, \boldsymbol{v}_h\right) + b\left(\widetilde{p}_{h,(k+1)}, \boldsymbol{v}_h\right) = \\ \qquad = (\boldsymbol{f}, \boldsymbol{v}_h) - \displaystyle\sum_{i=1}^{m} \lambda_{i,h,(k)} \left((\boldsymbol{u}_{h,(k)} \cdot \nabla)\boldsymbol{w}_{i,h}, \boldsymbol{v}_h\right) \\ b\left(q_h, \widetilde{\boldsymbol{u}}_{h,(k+1)}\right) = 0 \end{cases} \tag{2.54}$$

$\forall \boldsymbol{v}_h \in \boldsymbol{V}_h, \forall q_h \in Q_h$.

b) Solve the linear system

$$\sum_{j=1}^{m} \lambda_{j,h,(k+1)} \int_{\Gamma_i} \boldsymbol{w}_{j,h} \cdot \boldsymbol{n} d\gamma = Q_i - \int_{\Gamma_i} \widetilde{\boldsymbol{u}}_{h,(k+1)} \cdot \boldsymbol{n} d\gamma \tag{2.55}$$

for the unknowns $\lambda_{j,h,(k+1)}$.

c) Build the solution:

$$\begin{cases} \boldsymbol{u}_{h,(k+1)} = \widetilde{\boldsymbol{u}}_{h,(k+1)} + \displaystyle\sum_{i=1}^{m} \lambda_{i,h,(k+1)} \boldsymbol{w}_{i,h}, \\ p_{h,(k+1)} = \widetilde{p}_{h,(k+1)} + \displaystyle\sum_{i=1}^{m} \lambda_{i,h,(k+1)} \pi_{i,h}, \end{cases} \tag{2.56}$$

d) Convergence test

End fixed point iterations. $\diamond$

In particular, the convective terms in the problems at step 1) have been moved in (2.54), in order to decouple the computation of $(\boldsymbol{w}_h, p_h)$ on one side and of $(\boldsymbol{u}_h, p_h, \widetilde{\boldsymbol{u}}_h, \widetilde{p}_h)$ on the other. Therefore, with this splitting, the fixed point strategy involves step 2a), 2b) and 2c) and therefore entails only *one* differential problem at each iteration.

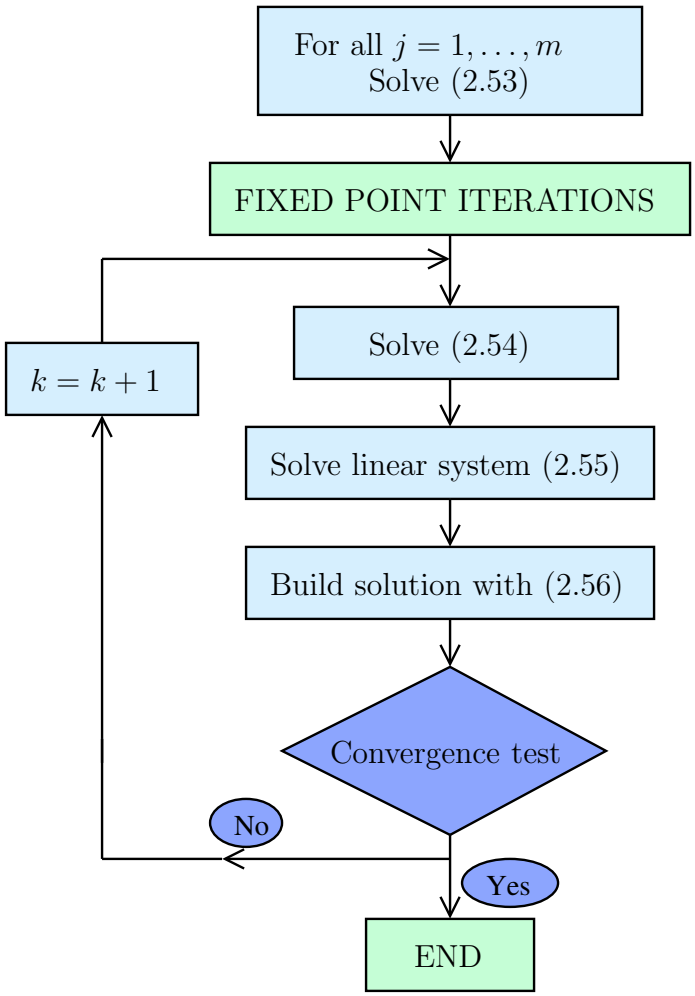

Figure 2.5: Algorithm 6 for the resolution of the steady Navier-Stokes problem - scheme II.

The unsteady problems

Let us consider the augmented Oseen problem (2.6). It is easy to check that the solution of this problem is given by (2.45), where $(\boldsymbol{w}_i, \pi_i)$, $i = 1, \ldots, m$, are the solutions of the steady Stokes problems:

$$\begin{cases} a(\boldsymbol{w}_i, \boldsymbol{v}) + b(\pi_i, \boldsymbol{v}) = -\displaystyle\int_{\Gamma_i} \boldsymbol{v} \cdot \boldsymbol{n} d\gamma \\ \\ b(q, \boldsymbol{w}_i) = 0, \end{cases} \tag{2.57}$$

$\forall \boldsymbol{v} \in \boldsymbol{V}, \forall q \in L^2(\Omega)$, while $(\widetilde{\boldsymbol{u}}, \widetilde{p})$ is the solution of the unsteady Oseen problem:

$$\begin{cases} \left(\dfrac{\partial \widetilde{\boldsymbol{u}}}{\partial t}, \boldsymbol{v}\right) + a(\widetilde{\boldsymbol{u}}, \boldsymbol{v}) + ((\boldsymbol{\beta} \cdot \nabla)\widetilde{\boldsymbol{u}}, \boldsymbol{v}) + b(\widetilde{p}, \boldsymbol{v}) = \\ \qquad\qquad = -\displaystyle\sum_{i=1}^{m} \frac{\partial \lambda_i}{\partial t}(\boldsymbol{w}_i, \boldsymbol{v}) - \sum_{i=1}^{m} \lambda_i ((\boldsymbol{\beta} \cdot \nabla)\boldsymbol{w}_i, \boldsymbol{v}) + (\boldsymbol{f}, \boldsymbol{v}) \\ \\ b(q, \widetilde{\boldsymbol{u}}) = 0 \\ \widetilde{\boldsymbol{u}}|_{t=0} = \boldsymbol{u}_0 \end{cases} \tag{2.58}$$

$\forall \boldsymbol{v} \in \boldsymbol{V}, \forall q \in L^2(\Omega)$. To compute the Lagrange multipliers λ_i, we solve the linear system (2.48).

Since in (2.58) and (2.48) the computations of $\widetilde{\boldsymbol{u}}$ and λ_i are coupled, we can resort to a fixed point strategy to solve them separately. In particular, setting $\boldsymbol{\beta}^{n+1} = \boldsymbol{\beta}(t^{n+1})$ and $\widetilde{\boldsymbol{u}}_h^0 = \boldsymbol{u}_{0,h}$, let us consider the following

Algorithm 7

(See Figure 2.6)

1) Solve for all $i = 1, \ldots, m$ the steady problems (2.53).

2) For $n = 1, \ldots$ (time loop)
   Pose $\lambda_{i,h,(0)}^{n+1} = \lambda_{i,h}^n$, $\forall i = 1, \ldots, m$
   a) For $k = 0, \ldots$ (fixed point subiterations)

i) Find $\widetilde{\boldsymbol{u}}_{h,(k+1)}^{n+1}$ and $\widetilde{p}_{h,(k+1)}^{n+1}$, such that

$$\begin{cases} \dfrac{\alpha}{\Delta t}\left(\widetilde{\boldsymbol{u}}_{h,(k+1)}^{n+1},\boldsymbol{v}_h\right)+a\left(\widetilde{\boldsymbol{u}}_{h,(k+1)}^{n+1},\boldsymbol{v}_h\right)+((\boldsymbol{\beta}^{n+1}\cdot\nabla)\widetilde{\boldsymbol{u}}_{h,(k+1)}^{n+1},\boldsymbol{v}_h)+ \\ +b\left(\widetilde{p}_{h,(k+1)}^{n+1},\boldsymbol{v}_h\right)=-\displaystyle\sum_{i=1}^{m}\frac{\alpha\lambda_{i,h,(k)}^{n+1}-\sum_{j=1}^{r\leq n}\tau_j\lambda_{i,h}^{n-j}}{\Delta t}(\boldsymbol{w}_{i,h},\boldsymbol{v}_h)+ \\ \quad -\displaystyle\sum_{i=1}^{m}\lambda_{i,h,(k)}^{n+1}\left((\boldsymbol{\beta}^{n+1}\cdot\nabla)\boldsymbol{w}_{i,h},\boldsymbol{v}_h\right)+ \\ \quad\quad +\displaystyle\sum_{j=0}^{r\leq n}\frac{\tau_j}{\Delta t}\left(\widetilde{\boldsymbol{u}}_h^{n-j},\boldsymbol{v}_h\right)+\left(\boldsymbol{f}^{n+1},\boldsymbol{v}_h\right) \\ b\left(q_h,\widetilde{\boldsymbol{u}}_{h,(k+1)}^{n+1}\right)=0 \end{cases} \tag{2.59}$$

$\forall\boldsymbol{v}_h\in\boldsymbol{V}_h,\forall q_h\in Q_h$, with $\widetilde{\boldsymbol{u}}_h^0=\boldsymbol{u}_{0,h}$ for $t=0$.

ii) Solve the linear system

$$\sum_{j=1}^{m}\lambda_{j,h,(k+1)}^{n+1}\int_{\Gamma_i}\boldsymbol{w}_{j,h}\cdot\boldsymbol{n}d\gamma=Q_i^{n+1}-\int_{\Gamma_i}\widetilde{\boldsymbol{u}}_{h,(k+1)}^{n+1}\cdot\boldsymbol{n}d\gamma \tag{2.60}$$

for the unknowns $\lambda_{j,h,(k+1)}^{n+1}$.

iii) Convergence test.

End fixed point subiterations (after k_n iterations)
b) Build the solution:

$$\begin{cases} \boldsymbol{u}_h^{n+1}=\widetilde{\boldsymbol{u}}_{h,k_n}^{n+1}+\displaystyle\sum_{i=1}^{m}\lambda_{i,h,k_n}^{n+1}(t)\boldsymbol{w}_{i,h}, \\ p_h^{n+1}=\widetilde{p}_{h,k_n}^{n+1}+\displaystyle\sum_{i=1}^{m}\lambda_{i,h,k_n}^{n+1}(t)\pi_{i,h}, \end{cases} \tag{2.61}$$

End time loop $\diamond$

This approach resorts to the solution of m steady Stokes problems out of the time loop and of *one* Oseen problem with standard boundary conditions for each subiteration of the fixed point algorithm (step (i)). A convergence analysis of this scheme has not been carried out so far. However numerical evidence suggests that it features good convergence properties (see Section 2.6).

In the time discrete Navier-Stokes problem the convective term represents the velocity extrapolated by the previous time steps, i.e. we set

$$\boldsymbol{\beta}^{n+1}=\boldsymbol{u}_h^n.$$

Remark 3 *In the special case in which only one flux is prescribed on the artificial section Γ, an easier modification of splitting (2.57), (2.58), (2.48) and (2.45), can be used. In particular, the solution $(\boldsymbol{u}, p)$ of problem (2.6) is given in this case by*

$$\begin{cases} \boldsymbol{u} = \lambda \widetilde{\boldsymbol{u}}, \\ p = \lambda \widetilde{p}, \end{cases} \tag{2.62}$$

where $(\widetilde{\boldsymbol{u}}, \widetilde{p})$ is the solution of the unsteady Oseen problem:

$$\begin{cases} \left(\dfrac{\partial \widetilde{\boldsymbol{u}}}{\partial t}, \boldsymbol{v}\right) + a\left(\widetilde{\boldsymbol{u}}, \boldsymbol{v}\right) + \left((\boldsymbol{\beta} \cdot \nabla)\widetilde{\boldsymbol{u}}, \boldsymbol{v}\right) + b\left(\widetilde{p}, \boldsymbol{v}\right) + \\ \qquad + \dfrac{1}{\lambda}\dfrac{\partial \lambda}{\partial t}\left(\widetilde{\boldsymbol{u}}, \boldsymbol{v}\right) = -\displaystyle\int_{\Gamma} \boldsymbol{v} \cdot \boldsymbol{n}\, d\gamma + (\boldsymbol{f}, \boldsymbol{v}) \\ b\left(q, \widetilde{\boldsymbol{u}}\right) = 0 \\ \widetilde{\boldsymbol{u}}|_{t=0} = \boldsymbol{u}_0 \end{cases} \tag{2.63}$$

$\forall \boldsymbol{v} \in \boldsymbol{V}, \forall q \in L^2(\Omega)$ and where we choose $\lambda(0) = 1$. In fact, by multiplying equation (2.63) per λ and using (2.62), we obtain $(2.6)_1$. In order to compute the Lagrange multiplier λ, we substitute (2.62) in the flow rate boundary condition $(2.6)_4$, obtaining

$$\lambda = \frac{Q}{\int_{\Gamma} \widetilde{\boldsymbol{u}} \cdot \boldsymbol{n} d\gamma} \tag{2.64}$$

Also in this case a fixed point algorithm is required, since in (2.63) and (2.64) the computation of $\widetilde{\boldsymbol{u}}$ and λ is coupled. Nevertheless, in this case we can avoid the computation of the steady problems (2.57).

2.5.5 Inexact splitting (scheme III)

The drawback of the algorithms presented in Section 2.5.3 and 2.5.4 (schemes I and II) is that in both the cases the computation of the solution is obtained by resorting to an iterative procedure: the iterative solver (GMRes) for the resolution of the linear system in $\boldsymbol{\Lambda}$ in scheme I and the fixed point-based strategy in scheme II. Therefore the computational costs of these strategies could be quite expensive in practical applications. In this section we propose an approximate (inexact) algorithm for the solution of the augmented problem. Since this approach does not require an iterative approach, it yields a significant reduction of the computational costs. This strategy is based on an alternative (exact) continuous splitting of the augmented formulation. In the sequel, we firstly introduce the exact splitting. Then, we propose its approximation that leads to scheme III. In particular, the exact splitting we are going to show is a modification of the one proposed in the previous section (scheme II). We refer firstly to the augmented Oseen problem (2.6). More precisely, consider the following scheme:

1. *Solve the steady Neumann problems (2.57).*

2. *Solve the unsteady Neumann homogeneous problem.* For all $\boldsymbol{v} \in \boldsymbol{V}$, $q \in L^2(\Omega)$, $j = 1, 2, \ldots, m$ find $\boldsymbol{s} \in L^2(0, T, \boldsymbol{V}) \cap L^\infty(0, T, \boldsymbol{L}^2(\Omega))$ and $\xi \in L^2(0, T, L^2(\Omega))$ such that

$$\begin{cases} \left(\dfrac{\partial \boldsymbol{s}}{\partial t}, \boldsymbol{v}\right) + a(\boldsymbol{s}, \boldsymbol{v}) + ((\boldsymbol{\beta} \cdot \nabla)\boldsymbol{s}, \boldsymbol{v}) + b(\xi, \boldsymbol{v}) = (\boldsymbol{f}, \boldsymbol{v}) \\ b(q, \boldsymbol{s}) = 0, \end{cases} \tag{2.65}$$

with the initial condition $\boldsymbol{s}|_{t=0} = \boldsymbol{u}_0$.

3. *Solve the following linear system.* Let B be the matrix given by (2.16), and $\boldsymbol{S}$ the m vector with elements

$$S_i = \int_{\Gamma_i} \boldsymbol{s} \cdot \boldsymbol{n} d\gamma.$$

Let us denote with $\boldsymbol{Q}$ the vector with components Q_i $(i = 1, \ldots, m)$. We find therefore the vector $\boldsymbol{\eta}(t)$ by solving

$$\mathrm{B}\boldsymbol{\eta} = \boldsymbol{Q} - \boldsymbol{S}. \tag{2.66}$$

4. *Solve the following unsteady augmented homogeneous problem.* Find $\boldsymbol{e} \in L^2(0, T, \boldsymbol{V}) \cap L^\infty(0, T, \boldsymbol{L}^2(\Omega))$, $\varepsilon \in L^2(0, T, L^2(\Omega))$ and $\boldsymbol{\nu} \in (L^2(0, T))^m$ such that for all $\boldsymbol{v} \in \boldsymbol{V}$, $q \in L^2(\Omega)$:

$$\begin{cases} \left(\dfrac{\partial \boldsymbol{e}}{\partial t}, \boldsymbol{v}\right) + a(\boldsymbol{e}, \boldsymbol{v}) + ((\boldsymbol{\beta} \cdot \nabla)\boldsymbol{e}, \boldsymbol{v}) + b(\varepsilon, \boldsymbol{v}) + \displaystyle\sum_{i=1}^{m} \nu_i \int_{\Gamma_i} \boldsymbol{v} \cdot \boldsymbol{n} d\gamma = \\ \qquad\qquad = -\displaystyle\sum_{j=1}^{m} \frac{d\eta_j}{dt}(\boldsymbol{w}_j, \boldsymbol{v}) - \sum_{j=1}^{m} \eta_j ((\boldsymbol{\beta} \cdot \nabla)\boldsymbol{w}_j, \boldsymbol{v}) \\ b(q, \boldsymbol{e}) = 0 \\ \displaystyle\int_{\Gamma_i} \boldsymbol{e} \cdot \boldsymbol{n} d\gamma = 0 \qquad i = 1, 2, \ldots m \end{cases}, \tag{2.67}$$

with the initial condition: $\boldsymbol{e}|_{t=0} = \boldsymbol{0}$.

It is possible to verify by linear combination that solution of problem (2.6) can be written as:

$$\begin{cases} \boldsymbol{u} = \boldsymbol{s} + \boldsymbol{e} + \sum_{j=1}^{m} \eta_j \boldsymbol{w}_j, \\ p = \xi + \varepsilon + \sum_{j=1}^{m} \eta_j \pi_j, \\ \lambda_i = \nu_i + \eta_i \quad \forall i = 1, 2, \dots m. \end{cases}$$

It is worth noting that all the subproblems are well posed under suitable assumptions. Namely, (2.57) are standard steady Stokes problems, (2.65) is still a standard unsteady Oseen problem, (2.67) is a homogeneous augmented problem, analyzed in Section 2.3.2. The steady problems are obviously to be solved once at all at the beginning of computations.

Remark 4 *If $\boldsymbol{f} = \boldsymbol{0}$ and $\boldsymbol{u}_0 = \boldsymbol{0}$ problem (2.65) admits the trivial solution $\boldsymbol{s} = \boldsymbol{0}$ and $\xi = 0$. By exploiting this circumstance, in this case numerical solution of (2.65) can be dropped.*

In the previous splitting, we compute separately the contributions to the solution given by the forcing term and the flow rates. The latter still requires the solution of an augmented (homogeneous) problem, and it is expensive to solve, as pointed out in Section 2.5.3 and 2.5.4. We therefore approximate problem (2.67) with the following one. Let us set $\hat{\Gamma} \equiv \Gamma_w \cup \Gamma_1 \cup \ldots \cup \Gamma_m \equiv \partial\Omega \setminus \Gamma_0$.

Problem 20 *Find $\hat{\boldsymbol{e}} \in L^2(0, T, \boldsymbol{H}^1_{\hat{\Gamma}}(\Omega)) \cap L^\infty(0, T, \boldsymbol{L}^2(\Omega))$ and $\hat{\varepsilon} \in L^2(0, T, L^2(\Omega))$ such that for all $\boldsymbol{v} \in \boldsymbol{H}^1_{\hat{\Gamma}}(\Omega)$, $q \in L^2(\Omega)$:*

$$\begin{cases} \left(\dfrac{\partial \hat{\boldsymbol{e}}}{\partial t}, \boldsymbol{v}\right) + a(\hat{\boldsymbol{e}}, \boldsymbol{v}) + ((\boldsymbol{\beta} \cdot \nabla)\hat{\boldsymbol{e}}, \boldsymbol{v}) + b(\hat{\varepsilon}, \boldsymbol{v}) = \\ \qquad\qquad = -\sum_{j=1}^{m} \dfrac{d\eta_j}{dt}(\boldsymbol{w}_j, \boldsymbol{v}) - \sum_{j=1}^{m} \eta_j ((\boldsymbol{\beta} \cdot \nabla)\boldsymbol{w}_j, \boldsymbol{v}) \\ b(q, \hat{\boldsymbol{e}}) = 0 \end{cases} \tag{2.68}$$

with the initial condition: $\hat{\boldsymbol{e}}|_{t=0} = \boldsymbol{0}$.

This is a standard Oseen problem with homogeneous Dirichlet conditions on $\hat{\Gamma}$. Let $\hat{\boldsymbol{V}}_h$ be a *inf-sup* compatible subspace of $\boldsymbol{H}^1_{\hat{\Gamma}}$. Therefore, the outline of the scheme is given by the following:

Algorithm 8

(See Figure 2.7)

1) *Preliminar computations:* Solve the m steady problems (2.53).

2) *Time loop:* Solve the sequence of (standard) problems:

   i) For all $\boldsymbol{v_h} \in \boldsymbol{V_h}$, $q_h \in Q_h$, $j = 1, 2, \ldots, m$, find $\boldsymbol{s_h} \in L^2(0,T,\boldsymbol{V_h}) \cap L^\infty(0,T,\boldsymbol{L}^2(\Omega))$ and $\xi_h \in L^2(0,T;Q_h)$ such that

$$\begin{cases} \dfrac{\alpha}{\Delta t}\Big(\boldsymbol{s}_h^{n+1}, \boldsymbol{v}_h\Big) + a\left(\boldsymbol{s}_h^{n+1}, \boldsymbol{v}_h\right) + \left(\left(\boldsymbol{\beta}^{n+1}\cdot\nabla\right)\boldsymbol{s}_h^{n+1}, \boldsymbol{v}_h\right) + b\left(\xi_h^{n+1}, \boldsymbol{v}_h\right) = \\ \qquad = \left(\boldsymbol{f}^{n+1}, \boldsymbol{v}_h\right) + \displaystyle\sum_{j=0}^{r\le n} \frac{\tau_j}{\Delta t}\Big(\boldsymbol{s}_h^{n-j}, \boldsymbol{v}_h\Big) + \\ b\left(q_h, \boldsymbol{s}_h^{n+1}\right) = 0, \end{cases} \tag{2.69}$$

   with the initial condition $\boldsymbol{s}_h^0 = \boldsymbol{u}_{0,h}$.

   ii) Solve the linear system

$$\sum_{j=1}^{m} \lambda_{j,h}^{n+1} \int_{\Gamma_i} \boldsymbol{w}_{j,h}\cdot\boldsymbol{n}\, d\gamma = Q_i^{n+1} - \int_{\Gamma_i} \boldsymbol{s}_h^{n+1}\cdot\boldsymbol{n}\, d\gamma \tag{2.70}$$

   for the unknowns $\lambda_{j,h}^{n+1}$.

   iii) Find $\hat{\boldsymbol{e}}_h \in L^2(0,T;\hat{\boldsymbol{V}}_h) \cap L^\infty(0,T;\boldsymbol{L}^2(\Omega))$ and $\hat{\varepsilon}_h \in L^2(0,T;Q_h)$ such that for all $\boldsymbol{v}_h \in \hat{\boldsymbol{V}}_h$, $q_h \in Q_h$:

$$\begin{cases} \dfrac{\alpha}{\Delta t}\Big(\hat{\boldsymbol{e}}_h^{n+1}, \boldsymbol{v}_h\Big) + a\left(\hat{\boldsymbol{e}}_h^{n+1}, \boldsymbol{v}_h\right) + \left((\boldsymbol{\beta}^{n+1}\cdot\nabla)\hat{\boldsymbol{e}}_h^{n+1}, \boldsymbol{v}_h\right) + b\left(\hat{\varepsilon}_h^{n+1}, \boldsymbol{v}_h\right) = \\ \qquad = \displaystyle\sum_{j=0}^{r\le n} \frac{\tau_j}{\Delta t}\Big(\hat{\boldsymbol{e}}_h^{n-j}, \boldsymbol{v}_h\Big) - \sum_{i=1}^{m} \frac{\alpha\eta_{i,h}^{n+1} - \sum_{j=1}^{r\le n}\tau_j\eta_{i,h}^{n-j}}{\Delta t}\left(\boldsymbol{w}_{i,h}, \boldsymbol{v}_h\right) + \\ \qquad\quad -\displaystyle\sum_{j=1}^{m} \eta_{j,h}^{n+1}\left(\left(\boldsymbol{\beta}^{n+1}\cdot\nabla\right)\boldsymbol{w}_{j,h}, \boldsymbol{v}_h\right) \\ b\left(q_h, \hat{\boldsymbol{e}}_h^{n+1}\right) = 0 \end{cases} \tag{2.71}$$

   with the initial condition: $\hat{\boldsymbol{e}}_h^0 = \boldsymbol{0}$.

   iv) *Final assembling:* Set:

$$\begin{cases} \hat{\boldsymbol{u}}_h^{n+1} = \boldsymbol{s}_h^{n+1} + \hat{\boldsymbol{e}}_h^{n+1} + \displaystyle\sum_{j=1}^{m} \eta_{j,h}^{n+1}\boldsymbol{w}_{j,h}, \\ \hat{p}_h^{n+1} = \xi_h^{n+1} + \hat{\varepsilon}_h^{n+1} + \displaystyle\sum_{j=1}^{m} \eta_{j,h}^{n+1}\pi_{j,h}. \end{cases} \tag{2.72}$$

2) *End time loop.*

◇

We point out that in this approximation the Lagrange multipliers λ_i are not explicitely computed. Tipically, this is not a problem, since the interest is for the velocity and pressure fields. However, we recall that in the present variational formulation the Lagrangian multiplier has the physical meaning of normal stress (see Proposition 1 in Section 2.2.1) and this can be of some interest in the geometrical multiscale approach for coupling 3D models to 1D or lumped parameters models in the framework of computational haemodynamics (see, for example, [14, 16, 19]). In scheme III, the Lagrange multipliers can be therefore computed as a post-processing step starting from the approximate velocity and pressure fields.

Remark 5 *Observe that in the steady Stokes case, namely for* $\dfrac{d\eta_j}{dt} = 0$ *for each* $j = 1, 2, \ldots, m$*, problem (2.67) and (2.68) both have the unique solution* $\boldsymbol{e} = \hat{\boldsymbol{e}} = \boldsymbol{0}$*. In this case, therefore, scheme III yields the exact solution.*

For what concernes the Navier-Stokes problem, if a semi-implicit treatment of the convective term is chosen, then it is sufficient to set

$$\boldsymbol{\beta}^{n+1} = \boldsymbol{u}_h^n.$$

in Algorithm 8. Let us now consider the case of a genuine Navier-Stokes nonlinear problem solved with an implicit time discretization. For the sake of clarity, we refer to the implicit Euler discretization, even if the same approach can be adopted with every implicit time advancing scheme. In this case, the inexact splitting can be adopted in a fixed point iterative framework.

Algorithm 9

(See Figure 2.8)

1) Solve steady Stokes Neumann problems (2.53).

2) For $n = 1, \ldots$ (temporal loop)
   Pose $\hat{\boldsymbol{u}}_{(0)}^{n+1} = \hat{\boldsymbol{u}}^n$, $\boldsymbol{s}_h^0 = \boldsymbol{u}_{0,h}$ and $\hat{\boldsymbol{e}}_h^0 = \boldsymbol{0}$
   For $k = 0, \ldots$ (fixed point subiterations)

a) Solve the unsteady Neumann homogeneous problem: find $\boldsymbol{s}_{h,(k+1)}^{n+1}$, $\xi_{h,(k+1)}^{n+1}$ such that

$$\begin{cases} \left(\dfrac{\boldsymbol{s}_{h,(k+1)}^{n+1}-\boldsymbol{s}_h^n}{\Delta t},\boldsymbol{v}_h\right)+a\left(\boldsymbol{s}_{h,(k+1)}^{n+1},\boldsymbol{v}_h\right)+ \\ \qquad +\left((\hat{\boldsymbol{u}}_{h,(k)}^{n+1}\cdot\nabla)\boldsymbol{s}_{h,(k+1)}^{n+1},\boldsymbol{v}_h\right)+b\left(\xi_{h,(k+1)}^{n+1},\boldsymbol{v}_h\right)=\left(\boldsymbol{f}^{n+1},\boldsymbol{v}_h\right) \\ b\left(q_h,\boldsymbol{s}_{h,(k+1)}^{n+1}\right)=0, \end{cases} \tag{2.73}$$

b) Linear system:

$$\mathrm{B}\boldsymbol{\eta}_{h,(k+1)}^{n+1}=\boldsymbol{Q}^{n+1}-\boldsymbol{S}_{h,(k+1)}^{n+1} \tag{2.74}$$

c) Homogeneous Dirichlet problem: as for problem (2.71), solve:

$$\begin{cases} \left(\dfrac{\hat{\boldsymbol{e}}_{h,(k+1)}^{n+1}-\hat{\boldsymbol{e}}_h^n}{\Delta t},\boldsymbol{v}_h\right)+a\left(\hat{\boldsymbol{e}}_{h,(k+1)}^{n+1},\boldsymbol{v}_h\right)+\left((\hat{\boldsymbol{u}}_{h,(k)}^{n+1}\cdot\nabla)\hat{\boldsymbol{e}}_{h,(k+1)}^{n+1},\boldsymbol{v}_h\right)+ \\ \qquad +b\left(\hat{\varepsilon}_{h,(k+1)}^{n+1},\boldsymbol{v}_h\right)=-\displaystyle\sum_{j=1}^{m}\frac{\eta_{j,h,(k+1)}^{n+1}-\eta_{j,h}^n}{\Delta t}\left(\boldsymbol{w}_{j,h},\boldsymbol{v}_h\right)+ \\ \qquad\qquad -\displaystyle\sum_{j=1}^{m}\eta_{j,h,(k+1)}^{n+1}\left((\hat{\boldsymbol{u}}_{h,(k)}^{n+1}\cdot\nabla)\boldsymbol{w}_{j,h},\boldsymbol{v}_h\right) \\ b\left(q_h,\hat{\boldsymbol{e}}_{h,(k+1)}^{n+1}\right)=0 \end{cases} \tag{2.75}$$

d) Final assembling: for θ real parameter, set:

$$\begin{cases} \hat{\boldsymbol{u}}_{h,(k+1)}^{n+1}=\theta\left(\hat{\boldsymbol{e}}_{h,(k+1)}^{n+1}+\boldsymbol{s}_{h,(k+1)}^{n+1}+\displaystyle\sum_{j=1}^{m}\eta_{j,h,(k+1)}^{n+1}\boldsymbol{w}_{j,h}\right)+(1-\theta)\hat{\boldsymbol{u}}_{h,(k)}^{n+1} \\ p_{h,(k+1)}^{n+1}=\theta\left(\hat{\varepsilon}_{h,(k+1)}^{n+1}+\xi_{h,(k+1)}^{n+1}+\displaystyle\sum_{j=1}^{m}\eta_{j,h,(k+1)}^{n+1}\pi_{j,h}\right)+(1-\theta)\hat{p}_{h,(k)}^{n+1} \end{cases} \tag{2.76}$$

e) Convergence test

End fixed point subiterations

End temporal loop. $\diamond$

Numerical evidence (see Section 2.6) suggests that with an appropriate selection of the relaxation parameter θ, this algorithm converges in a few iterations to the

fixed point, yielding the desired approximate solution of the augmented problem with an implicit time advancing scheme.

We point out that in the exact version of scheme III a null flux problem is solved instead of (2.58) in scheme II. In this way, this problem gives a null contribution when introduced in the flow rate equations $(2.6)_4$ in order to build the linear system in the unknown λ_i. Therefore, the computation of the Lagrange multipliers and of the intermediate velocity are decoupled and it is not necessary anymore to resort to a fixed point algorithm. The price to pay is the following: the null flux problem is still an augmented problem and therefore, in solving it approximatively, we introduce an error in a small neighborhood of the artificial sections where the flow rate is prescribed. From the practical viewpoint, this means that correct numerical results can be obtained in the region of interest by working in a slightly extended computational domain. Even when working with a larger domain, in fact, the computational times of the present method are significantly reduced with respect to the "exact" Lagrange multiplier approaches (scheme I and II), yielding comparable numerical results in the region of interest (see Section 2.6).

Observe that since the error in scheme III has been introduced by forcing a null velocity profile (Dirichlet condition) in (2.68) instead of a null flow rate, as a matter of fact, we are prescribing a "wrong" velocity profile. Therefore the error analysis can be based on the result proven in Theorem 7. Nevertheless, as the numerical results in Section 2.6 highlight, the errors made with this strategy are less than the ones done by imposing directly a parabolic or a flat profile fitting the desired flow rate (as in the *practical approach*). The reasons of this improvement is double. On one hand, we point out that the (inexact) contribution on the solution of scheme III at the artificial sections is given only by the preliminar computations (2.57), since problem (2.68) gives a null contribution. The velocity profile arising from (2.57) takes into account the computational domain and therefore it should be more accurate than an arbitrary one (as in the *practical approach*). On the other hand, in problem (2.68) we are imposing a null Dirichlet boundary condition, i.e. we are considering a problem with small Reynolds number near the boundary. Therefore, the error is smaller than the one made imposing directly a non-null velocity profile (as in the *practical approach*), where Re could be very big.

The present proposal could therefore be considered as an intermediate and reliable approach between the engineering one (*practical approach*), requiring a relevant expansion of the domain for loosing the effects of the arbitrary velocity profile selection, and the exact one based on the augmented reformulation.

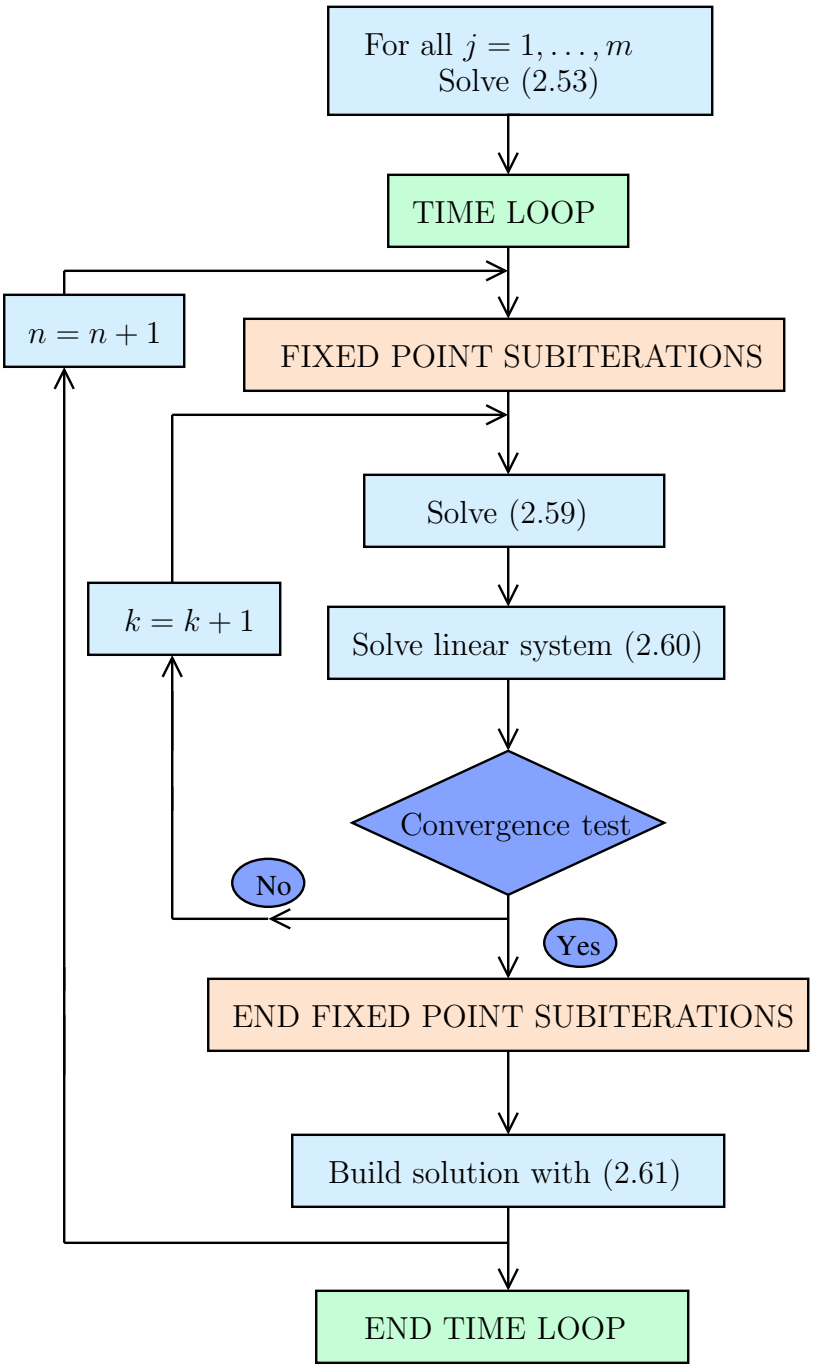

Figure 2.6: Algorithm 7 for the resolution of the unsteady Oseen problem - scheme II

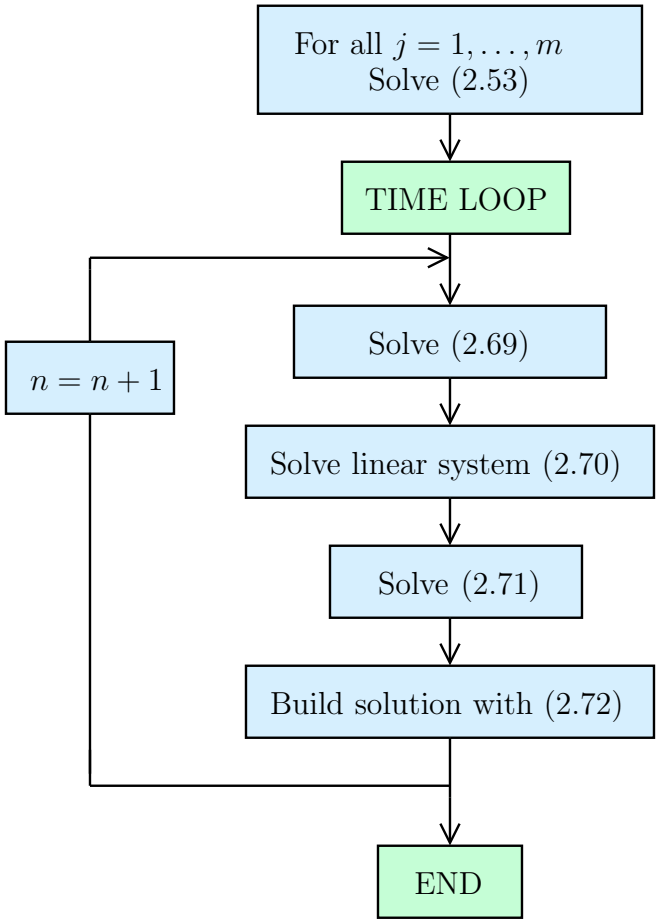

Figure 2.7: Algorithm 8 for the resolution of the unsteady Oseen problem - scheme III

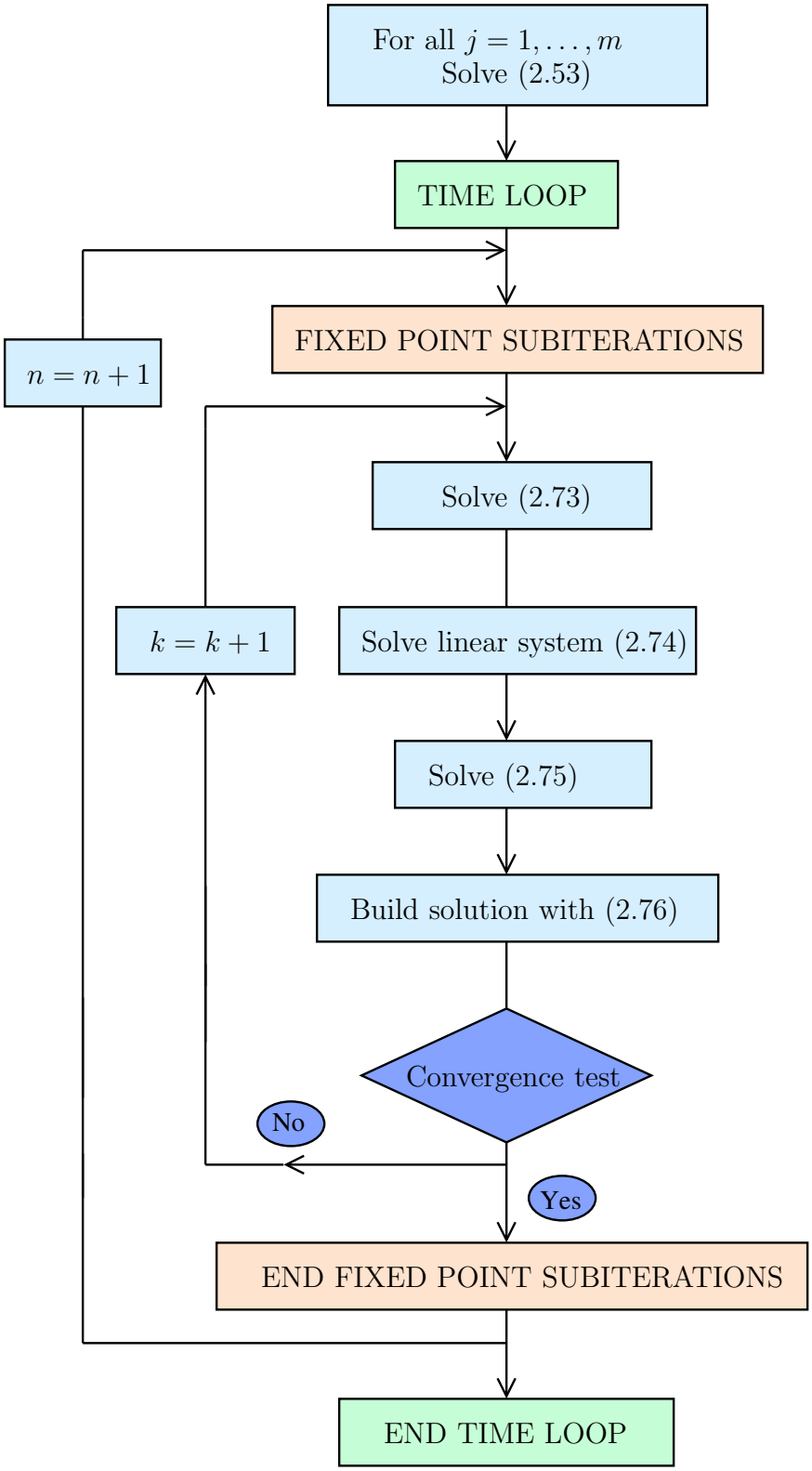

Figure 2.8: Algorithm 9 for the resolution of the unsteady Navier-Stoke problem with an implicit scheme- scheme III

2.6 Numerical results

In this section we present several numerical results concerning the three schemes presented in Section 2.5. In particular, in Section 2.6.1 and 2.6.2 the 2-dimensional and the 3-dimensional cases are considered, respectively. For each one of these sections, firstly validation simulations on accademic cases where an analytical solution is available are shown. Then, we focus on the error using scheme III and finally on simulations concerning realistic geometries.

2.6.1 2D simulations

Validation test case - Poiseuille problem

In the first set of simulations we aim at validating the three algorithms proposed in Section 2.5 in the 2d case, considering two cases where the analytical solution of the Navier-Stokes equation is known: the *Poiseuille* solution when a steady flow rate is imposed and the *Womersley* solution when a sinusoidal (or in general a sum of sinus and cosinus) flow rate is prescribed (see [68]). With this purpose, we use the 2d Finite Element code *Freefem++* (see [21]). The simulations done with this code have got also the aim of showing that the proposed schemes could be implemented even with a standard finite element package.

The computational domain Ω is a rectangular whose size is $6 \times 1\, cm$ and the viscosity is $\mu = 0.035\, cm^2/sec$. In the first test case we consider the steady Stokes problem and we impose a flux $Q = 1\, cm^2/sec$ at the inlet Γ of Ω. In Figures 2.9

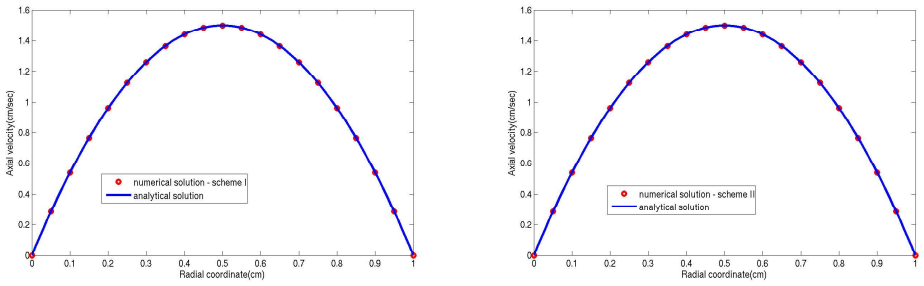

Figure 2.9: Axial velocity at the inlet section Γ in the steady Stokes simulation obtained with scheme I (left) and with scheme II (right), $h = 0.05\, cm$.

and 2.10 the axial velocity and the pressure, respectively, obtained with scheme I (left) and with scheme II (right) are shown. We point out that in this case scheme II and scheme III coincide, since the latter in the steady Stokes case gives the exact solution (see Remark 5). Both the algorithms recover the well known

Poiseuille solution

$$p(x) = 2.52\Big(1 - \frac{1}{6}x\Big)$$

and

$$u(y) = 6y(1-y),$$

where u is the axial component of the velocity field and x and y are the axial and the radial coordinates, respectively. In Table 2.2 is shown that the error in both the cases is neglegible and that it does not depend on the space discretization h.

	scheme I	scheme II
$h = 0.1$	$1.1542 \cdot 10^{-7}$	$1.1537 \cdot 10^{-7}$
$h = 0.05$	$1.1839 \cdot 10^{-7}$	$1.1809 \cdot 10^{-7}$

Table 2.2: Errors in the $L^2(\Gamma)$ norm for different values of the space discretization h for the Stokes steady simulation.

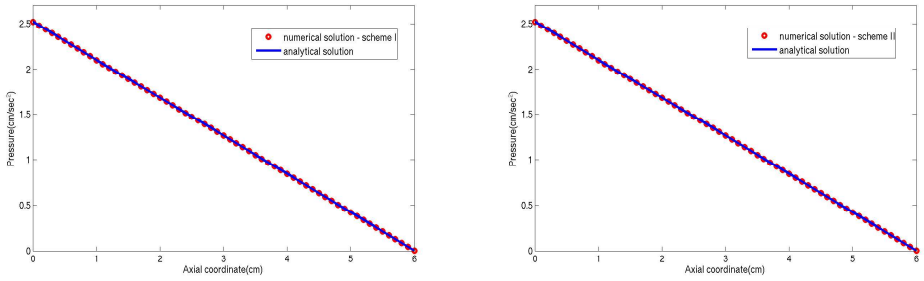

Figure 2.10: Pressure for a fixed y in the steady Stokes simulation obtained with scheme I (left) and with scheme II (right), $h = 0.1\,cm$.

In the second test case we consider the steady Navier-Stokes case, with the same data of the previous simulation. We point out that in this case scheme II and scheme III do not coincide, since problems (2.67) and (2.68) do not have as solution the trivial one and therefore they could differ near the boundary. In all the three cases, a fixed point strategy is required for managing the non-linear term (see Section 2.5 and Table 2.4). In Figure 2.11, 2.12 and 2.13 the axial velocity and the pressure obtained with the three strategies are shown. Also in this case the Poiseuille solution is recovered.

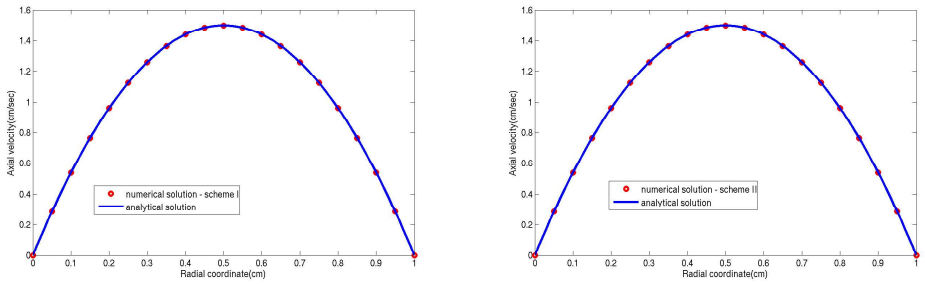

Figure 2.11: Axial velocity at the inlet section Γ in the steady Navier-Stokes simulation obtained with scheme I (left) and with scheme II (right), $h = 0.05\,cm$.

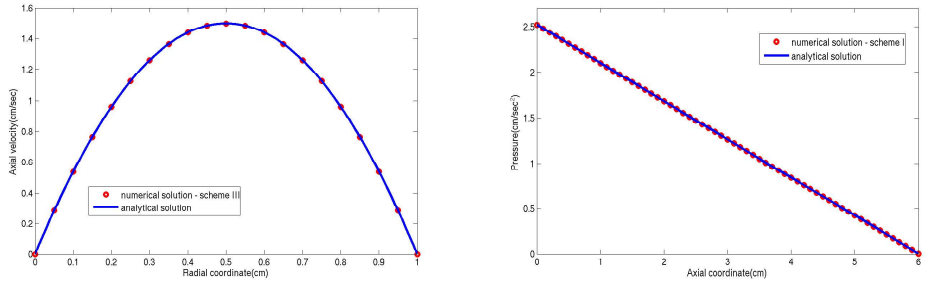

Figure 2.12: Axial velocity at the inlet section Γ obtained with scheme III (left, $h = 0.05\,cm$) and pressure for a fixed y obtained with scheme I (right, $h = 0.1\,cm$) in the steady Navier-Stokes simulation.

Validation test case - Womersley problem

The next simulations refer to the unsteady case. In particular, we prescribe a flux $Q = 0.15\cos(2\pi t)\,cm^2/sec$ and we compare the numerical solution with the Womersley one (see [68]). In Figure 2.14, 2.15 and 2.16 the comparision between the numerical solution obtained with three schemes and the analytical one are shown at different instants for the case of the Stokes problem. In Figure 2.17, 2.18 and 2.19 the same is done for the Navier-Stokes problem. We notice that in both the cases the two solutions are in good agreement for each of the three algorithms. The numerical solution obtained with scheme III highlights an error in the neighborhood of the boundary Γ. In practice, as already pointed out in Section 2.5.5, an affordable approach consists of enlarging the computational domain in order to confine the boundary error induced by the inexact splitting out of the region of interest. However, we point out that a small increase of the computational domain is enough. As a matter of fact, in our case it is sufficient to increase the lenght of the domain of $1cm$. In Figure 2.16 and 2.19 we report the numerical solution obtained with this strategy on a section sufficiently far

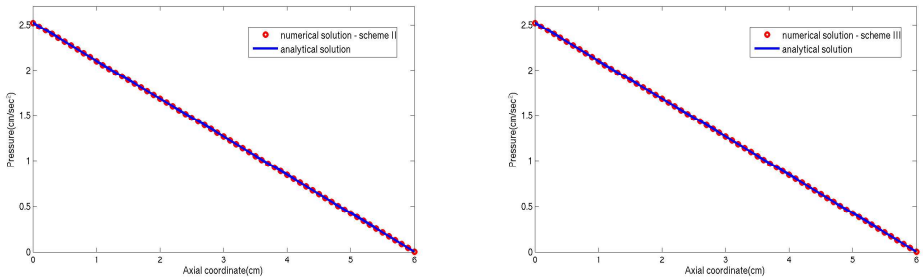

Figure 2.13: Pressure for a fixed y in the steady Navier-Stokes simulation obtained with scheme II (left) and with scheme III (right), $h = 0.1\,cm$.

from the boundary, in order to compare it with the analytical solution. The next Section is devoted to a deeper discussion of the error of the numerical solution computed with scheme III.

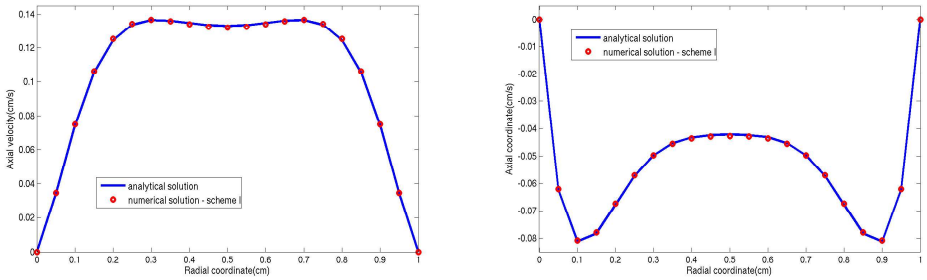

Figure 2.14: Womersely test case - Stokes problem. Axial velocity compared with the Womersley solution, $t = 2.1\,s$ (left) and $t = 2.3\,s$ (right) - scheme I. - $\Delta t = 0.01$, $h = 0.05$

In Table 2.3 we report the errors obtained with the three algorithms for the Stokes problem for different values of the space discretization h and of the time step Δt, at $t = 2.1s$ (up) and $t = 2.3s$ (bottom).

In Table 2.4 we report the number of the differential problems n_d involved in the three strategies (for the unsteady simulations we consider only the differential problems for each time step, neglecting those out of the temporal loop) and the CPU times. When a fixed point strategy is required, let us indicate with n_k the number of subiterations (in the unsteady cases, this number is the mean on the temporal cycle). In these cases, we indicate in the brackets the value $n_d \times n_k$. Moreover, we point out that for scheme III in the unsteady case, the CPU times refer to an enlarged domain.

Table 2.4 suggests the following considerations. For the steady case, scheme II seems to be the fastest. For the unsteady Stokes problem, scheme I is cer-

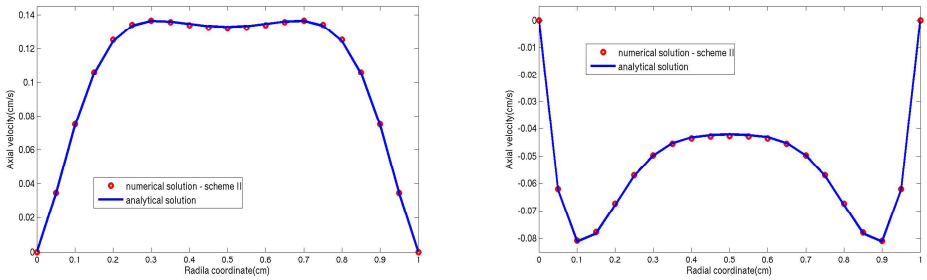

Figure 2.15: Womersely test case - Stokes problem. Axial velocity compared with the Womersley solution, $t = 2.1\,s$ (left) and $t = 2.3\,s$ (right) - scheme II. - $\Delta t = 0.01$, $h = 0.05$

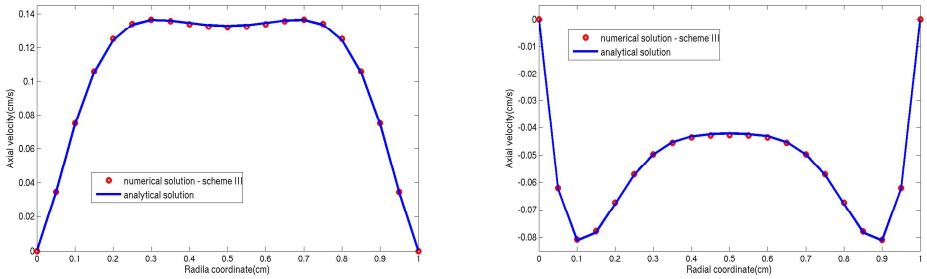

Figure 2.16: Womersely test case - Stokes problem. Axial velocity, sufficiently far from the boundary, compared with the Womersley solution, $t = 2.1\,s$ (left) and $t = 2.3\,s$ (right) - scheme III. - $\Delta t = 0.01$, $h = 0.05$

tainly the best strategy, ensuring reasonably low computational costs with good accuracy properties. In the unsteady Navier-Stokes case, scheme III gives best performances in terms of computational costs, with a good accuracy. Nevertheless, as we point out in the following sections, numerical simulations performed with scheme III in realistic geometries are less accurate. Therefore, we can state that, for general computational domains and physiological data, scheme I gives best performances in terms of accuracy; on the other hand, as was to be expected, scheme III features still the best properties in term of computational costs.

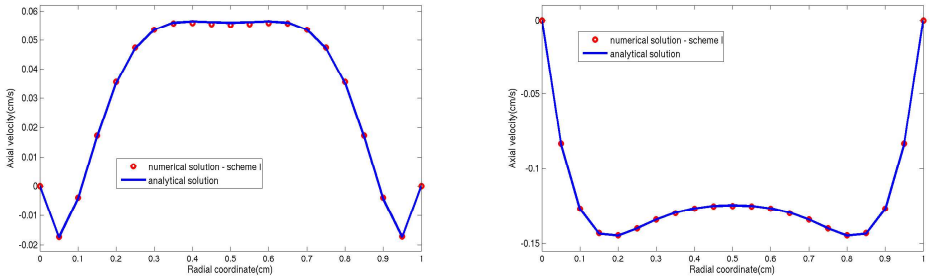

Figure 2.17: Womersely test case - Navier-Stokes problem. Axial velocity compared with the Womersley solution, $t = 2.2\,s$ (left) and $t = 2.4\,s$ (right) - scheme I. - $\Delta t = 0.01$, $h = 0.05$

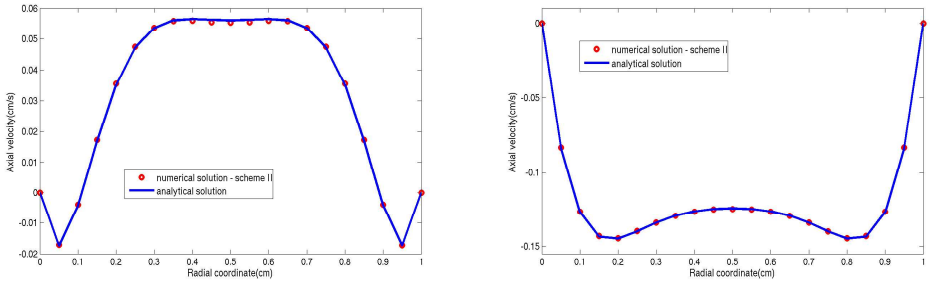

Figure 2.18: Womersely test case - Navier-Stokes problem. Axial velocity compared with the Womersley solution, $t = 2.2\,s$ (left) and $t = 2.4\,s$ (right) - scheme II. - $\Delta t = 0.01$, $h = 0.05$

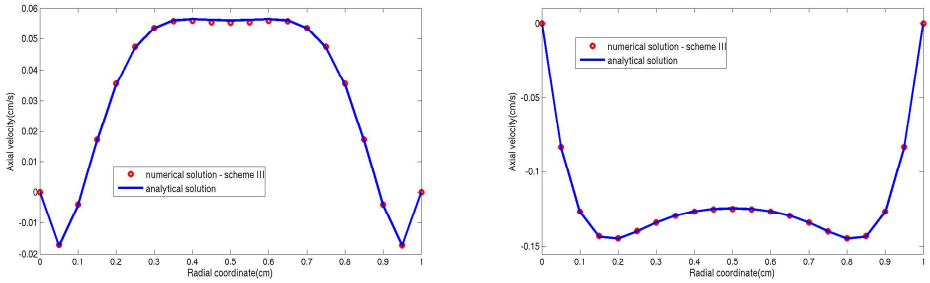

Figure 2.19: Womersely test case - Navier-Stokes problem. Axial velocity, sufficiently far from the boundary, compared with the Womersley solution, $t = 2.2\,s$ (left) and $t = 2.4\,s$ (right) - scheme III. - $\Delta t = 0.01$, $h = 0.05$

		scheme I	scheme II	scheme III
$\Delta t = 0.01$	$h = 0.1$	$6.277 \cdot 10^{-4}$	$5.932 \cdot 10^{-4}$	$5.630 \cdot 10^{-4}$
		$3.688 \cdot 10^{-4}$	$4.178 \cdot 10^{-4}$	$3.464 \cdot 10^{-4}$
	$h = 0.05$	$6.132 \cdot 10^{-4}$	$5.987 \cdot 10^{-4}$	$6.054 \cdot 10^{-4}$
		$3.450 \cdot 10^{-4}$	$5.813 \cdot 10^{-4}$	$3.217 \cdot 10^{-4}$
$\Delta t = 0.005$	$h = 0.1$	$5.995 \cdot 10^{-4}$	$6.127 \cdot 10^{-4}$	$5.356 \cdot 10^{-4}$
		$3.391 \cdot 10^{-4}$	$4.237 \cdot 10^{-4}$	$3.522 \cdot 10^{-4}$
	$h = 0.05$	$5.973 \cdot 10^{-4}$	$6.241 \cdot 10^{-4}$	$5.926 \cdot 10^{-4}$
		$3.375 \cdot 10^{-4}$	$4.361 \cdot 10^{-4}$	$3.297 \cdot 10^{-4}$

Table 2.3: Errors in the $L^2(\Gamma)$ norm for different values of the space discretization h and of the time step Δt for the Stokes unsteady simulation - $t = 2.1\,s$ (up) and $t = 2.3\,s$ (bottom).

		scheme I	scheme II	scheme III
Number of differential problems	steady Stokes	2	1	1
	steady NS	4(=2×2)	2(=2×1)	2(=2×1)
	unsteady Stokes	1	7(=7×1)	1
	unsteady NS	2	7(=7×1)	1
CPU times	steady Stokes	12.73s	6.84s	6.84s
	steady NS	25.12s	13.25s	15.02s
	unsteady Stokes	11min 04s	75min 54s	11min 42s
	unsteady NS	21min 42s	76min 28s	11min 52s

Table 2.4: Number of differential problems and CPU times involving in the three algorithms, for different problems, with $h = 0.1$. We point out the high computational costs of scheme II. For the unsteady simulations, we refer to a whole period $T = 1s$, with $\Delta t = 0.01$.

Error using scheme III

In this section we investigate the error made using scheme III. In Figure 2.20 we illustrate the results obtained by prescribing a sinusoidal-in-time flow ($Q(t) = 0.1 \cdot \cos(2\pi t) cm^2/s$) at the inlet Γ of a rectangular Ω with size $4 \times 1\, cm$. It is possible to observe the difference between the solutions obtained with scheme I and with scheme III. In particular, as expected from the analysis of Section 2.4, we observe that the error significantly reduces far away from the boundary Γ, as pointed out also in Figure 2.22 and 2.21. Moreover, the latter highlights that the error is proportional to the measure of Γ (i.e. to the *Reynolds number*), as expected from the error analysis in Section 2.4.

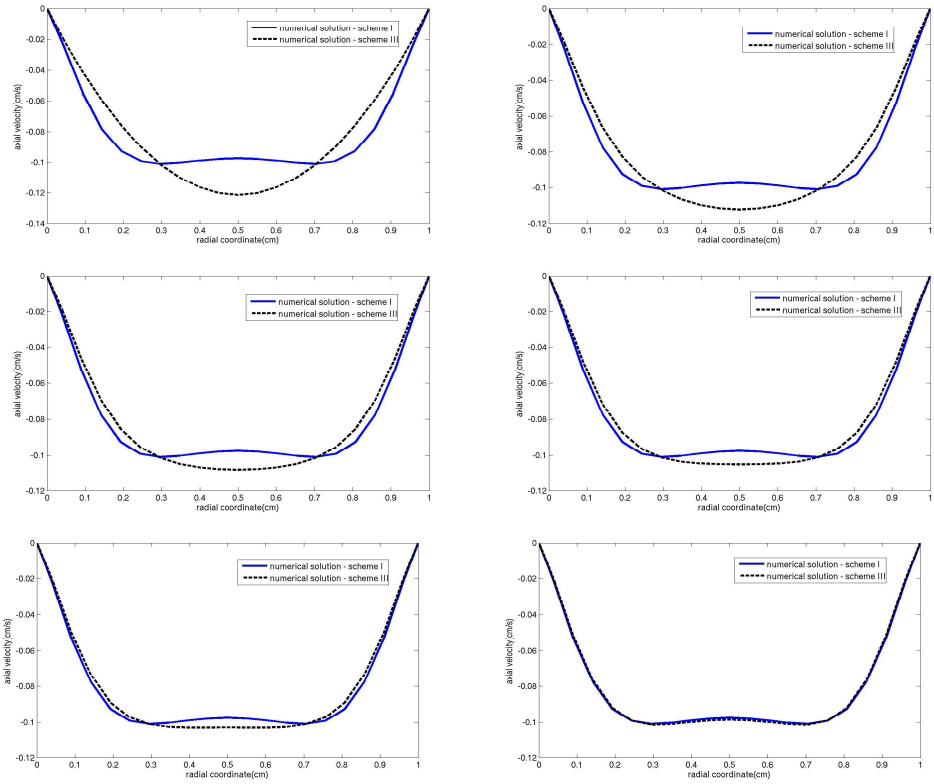

Figure 2.20: Comparison between the solution computed using scheme I (solid line) and scheme III (dashed line) in the Womersley test case - $h = 0.025$, $\Delta t = 0.01$, $t = 1.6\, s$. The difference between the two solutions reduces when the distance from the boundary increases. (Top, left: distance=0cm; Top, right: 0.2cm; Middle, left: 0.3cm; Middle, right 0.4cm; Bottom, left: 0.5cm; Bottom, right: 1cm).

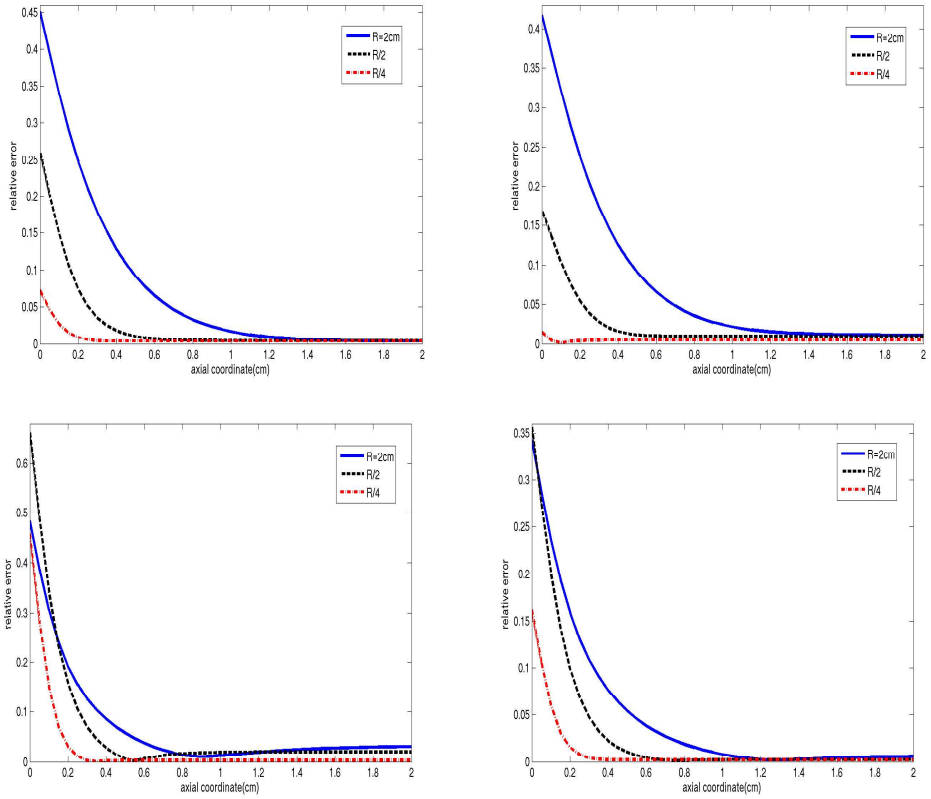

Figure 2.21: Womersley test case - scheme III. Errors along the axial coordinate at different instants for different values of the pipe radius - $h = 0.1$, $\Delta t = 0.01$, $t = 1.5\,s$ (top, left), $t = 1.6\,s$ (top, right), $t = 1.7\,s$ (bottom, left), $t = 1.8\,s$ (bottom, right).

In Figure 2.23 the error of scheme III for different values of the time step is shown. We notice that the boundary error does not depend on the time step. Moreover, in Figure 2.24 and 2.25 the dependence of the error on the fluid viscosity and on the Womersley number respectively is shown. We notice that the smaller the viscosity (i.e. the bigger the Womersley number), the bigger is the error near the boundary. This is confirmed by the fact that increasing the pulsatility (i.e. the Womersley number) the error in solving equation (2.68) instead of (2.67) grows up.

Figure 2.26 shows that the boundary error does not depend on the spatial discretization step, as expected. Finally, in Figure 2.27 the pressure solution and the pressure error are shown with $\Delta t = 0.01s$ (left) and $\Delta t = 0.005s$ (right), pointing out that also the pressure error is localized near the boundary, independently of the discretization.

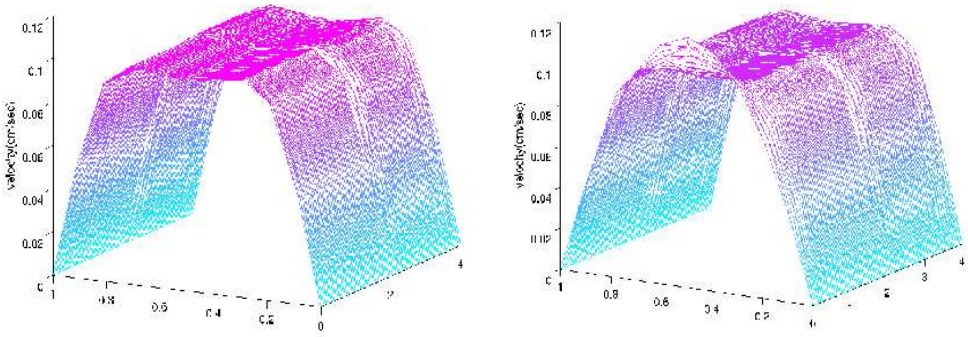

Figure 2.22: Womersley test case. Comparison between the velocity fields computed using scheme I (left) and scheme III (right).

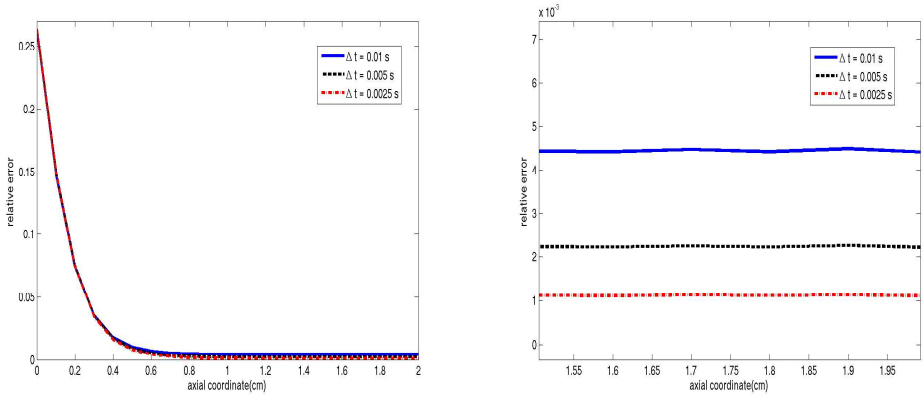

Figure 2.23: Womersley test case. Errors using scheme III for different values of the time steps. On the right a detail of the errors in the centre of the domain, where the error is essentially due to the time discretization - $h = 0.1$, $t = 1.5\,s$.

Then, we solved the same Navier-Stokes problem by using the implicit Euler scheme following the iterative procedure proposed in Algorithm 9, Section 2.5.5, for the treatment of the convective term. In Table 2.5 the mean number of subiterations per time step is shown. The convergence of the scheme can be strongly improved by an appropriate selection of θ.

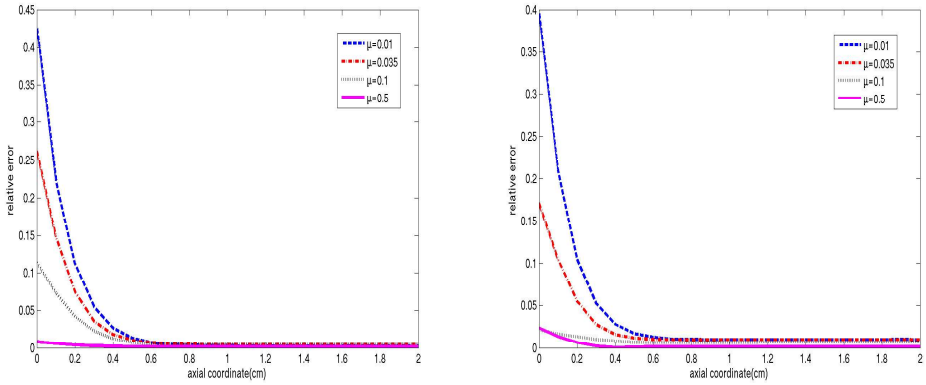

Figure 2.24: Womersley test case. Dependence of the error using scehem III on the fluid viscosity - $h = 0.1$, $\Delta t = 0.01$, $t = 1.5\,s$ (left) and $t = 1.6\,s$ (right).

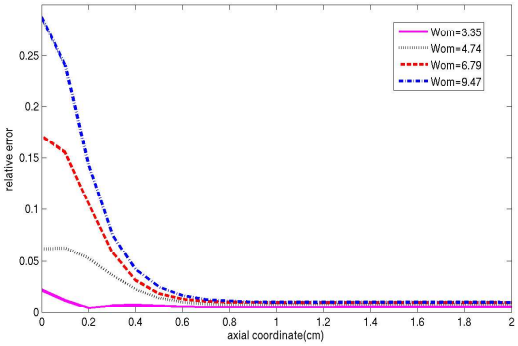

Figure 2.25: Womersley test case. Dependence of the error using scheme III on the Womersley number - $h = 0.1$, $\Delta t = 0.01$, $t = 1.6\,s$.

	$\theta = 0.1$	$\theta = 0.5$	$\theta = 0.9$
# subiterations	70	13	5

Table 2.5: Mean number of subiterations per time step using the implicit scheme III for the treatment of the convective term for different values of θ.

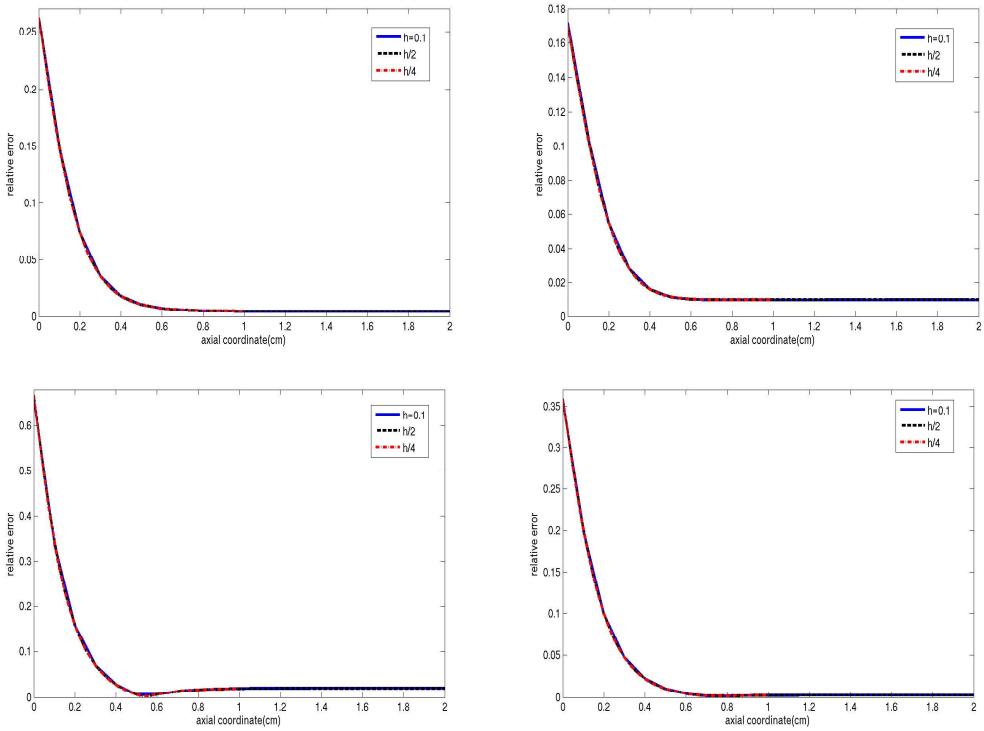

Figure 2.26: Womersley test case. Dependence of the error using scheme III on the space discretization - $\Delta t = 0.01$, $t = 1.5\,s$ (top, left), $t = 1.6\,s$ (top, right), $t = 1.8\,s$ (bottom, left), $t = 1.9\,s$ (bottom, right),

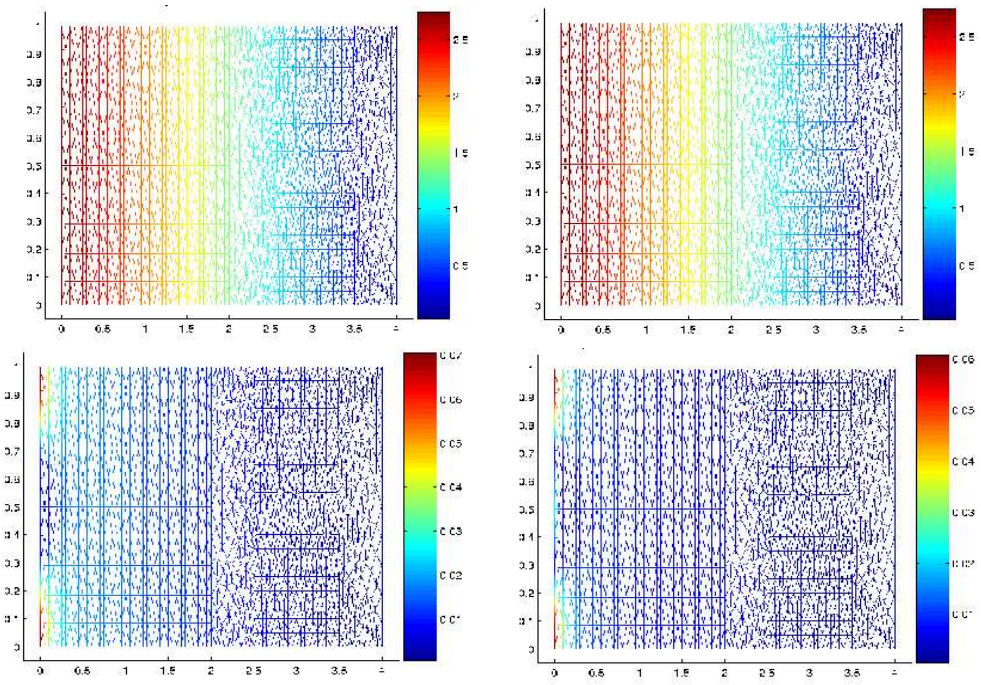

Figure 2.27: Womersley test case - scheme III. Top: Pressure solution with $\Delta t = 0.01s$ (left) and $\Delta t = 0.005s$ (right). Bottom: Pressure splitting error. The time steps is the same of the pictures at the top - $h = 0.05$, $t = 1.8\,s$

We compare now the error done with scheme III with the one obtained imposing a parabolic velocity profile. In particular, let Ω be the domain in Figure 2.28, modeling the *extracorporeal membrane oxygenator of Bellhouse* (see [4, 65]). This is a high-efficiency membrane oxygenatore which utilizes pulsatile flow through furrowed channels to achieve high mass transer rates. In particular, blood is pumped back and forth through the channels with a small mean flow component. Since there is a large mean pressure difference between the blood side and the oxygen side of the channel, small transient pressure fluctuations that would occur during the flow cycle would not be expected to cause significant movement of the membrane. The simplest approximation for a 2d model is to assume that between the struts supporting the membrane the shape of the furrow is the arc of a circle. This particular device is important for blood because it is able to significantly reduce the fluid resistance without using turbolent flow. Let us set $\Omega_j \subset \Omega$ the domains:

$$\Omega_j = \{(x, y) \in \Omega : \, x \geq j\}.$$

In Figures 2.29-2.34 the $L^2(\Omega_j)$ norm errors for different instants of the temporal

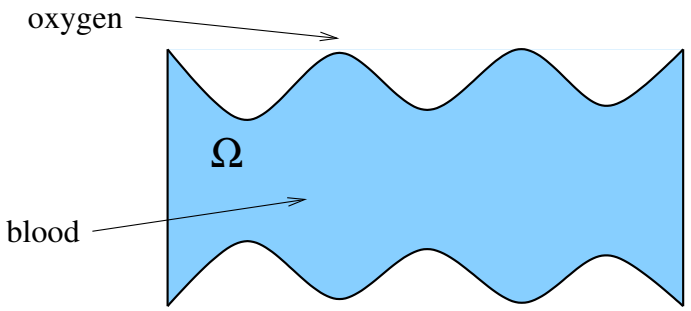

Figure 2.28: 2d domain for a Bellhouse oxygenator (see [4, 65].

cycle (left) and the $L^2(kT, (k+1)T; L^2(\Omega_j))$ norm errors for different cycles k (right) are shown. We notice that the numerical solution computed with scheme III is invariably more accurate than the one obtained by imposing a selected velocity profile. Therefore, we conclude that using scheme III the enlargement of the domain is smaller than the one required by the most used approach introduced in Section 1.3.1. This is in agreement with the observations done in Section 2.5.5.

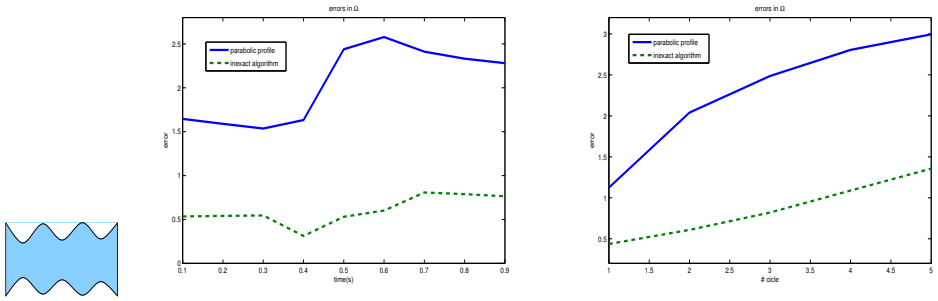

Figure 2.29: $L^2(\Omega)$ norm errors in the second cycle (left) and $L^2(L^2)$ norm errors for different cycles (right) using scheme III and practical approach. In abscissa the time (left) and the number of the cycles (right).

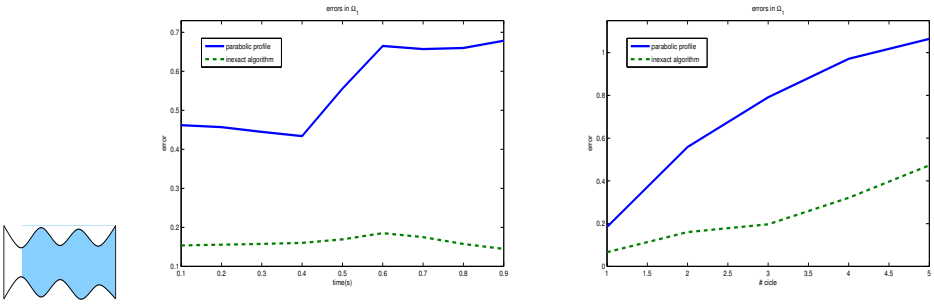

Figure 2.30: $L^2(\Omega_1)$ norm errors in the second cycle (left) and $L^2(L^2)$ norm errors for different cycles (right) using scheme III and practical approach. In abscissa the time (left) and the number of the cycles (right).

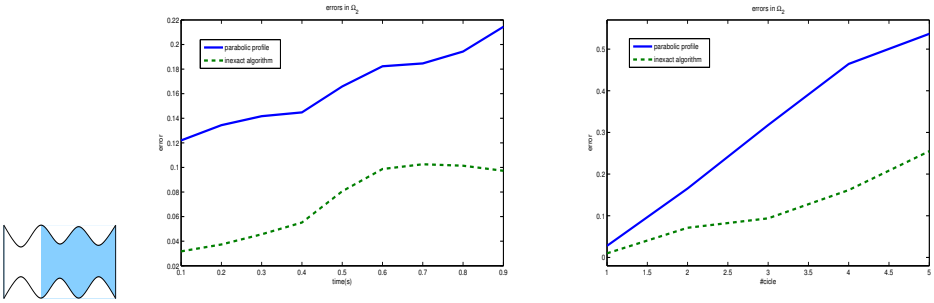

Figure 2.31: $L^2(\Omega_2)$ norm errors in the second cycle (left) and $L^2(L^2)$ norm errors for different cycles (right) using scheme III and practical approach. In abscissa the time (left) and the number of the cycles (right).

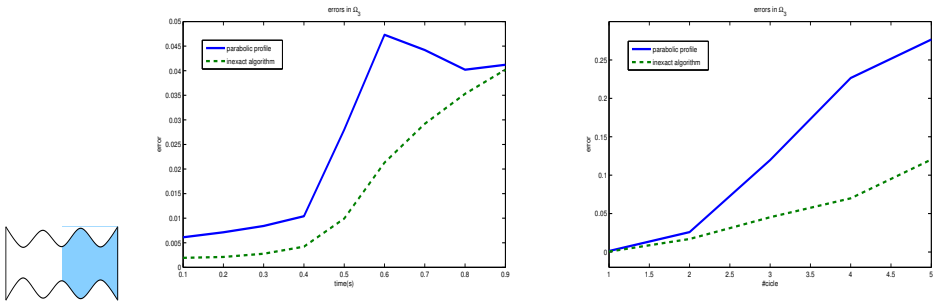

Figure 2.32: $L^2(\Omega_3)$ norm errors in the second cycle (left) and $L^2(L^2)$ norm errors for different cycles (right) using scheme III and practical approach. In abscissa the time (left) and the number of the cycles (right).

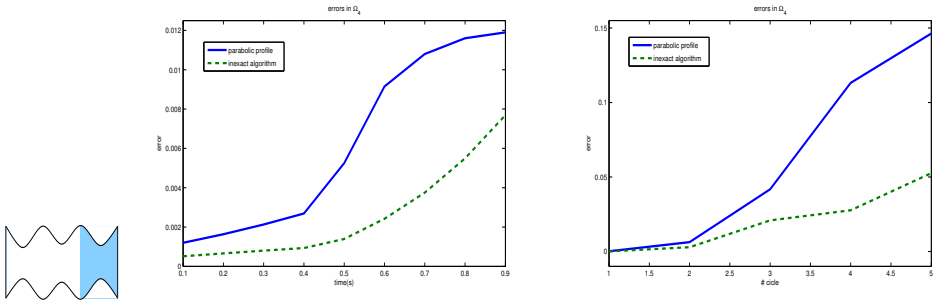

Figure 2.33: $L^2(\Omega_4)$ norm errors in the second cycle (left) and $L^2(L^2)$ norm errors for different cycles (right) using scheme III and practical approach. In abscissa the time (left) and the number of the cycles (right).

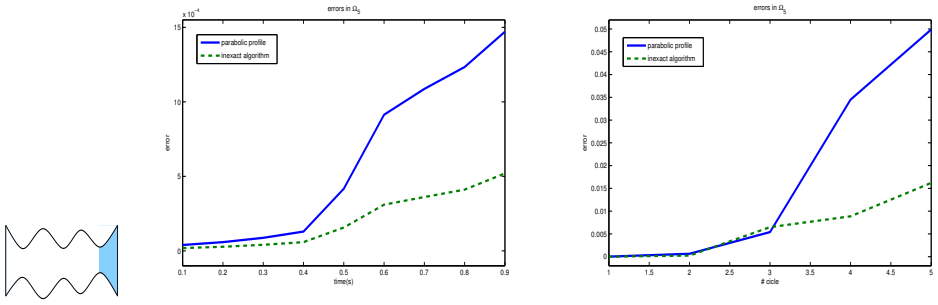

Figure 2.34: $L^2(\Omega_5)$ norm errors in the second cycle (left) and $L^2(L^2)$ norm errors for different cycles (right) using scheme III and practical approach. In abscissa the time (left) and the number of the cycles (right).

Computations in realistic cases

We focus now our attention on more realistic cases. Firstly, let us continue the error analysis of scheme III. In particular, we simulate the flow of the fluid in an anastomosis of a by-pass, whose sections have measure equal to $1cm$ and whose lenght is equal to $10cm$. We prescribed the physiological flux shown in Figure 2.35 (right) both at the bottom and at the top inlet (with $50cm^2/s$ and $25cm^2/s$ as peak value respectively). Figures 2.35 (left) and 2.36 show that the error is localized near the boundaries. Figure 2.37 points out again the dependence of the boundary error on the measure of Γ. Moreover, in Figure 2.38 the pressure field (left) and the pressure error (right) are shown.

In order to have a comparision between the computational efforts of scheme I and scheme III, we use the latter in a domain extended of $0.5cm$ at both the inlet. Nevertheless, the CPU time (see Table 2.6) is about one half of the one requested by scheme I when the flow rate is prescribed at one inlet. The CPU time reduction is even more evident when the flow rates are prescribed on both the inlets. Therefore, differently from scheme I, as expected the computational effort of scheme III does not depend on the number of the sections where we prescribe the flow rate.

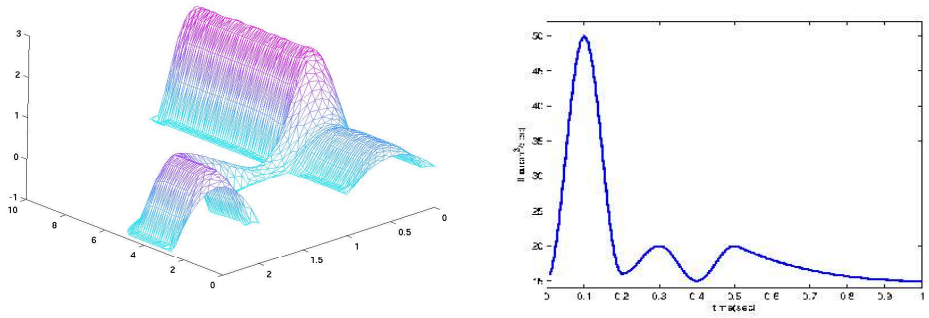

Figure 2.35: Anastomosis solution and physiological flux imposed at the two inlets - scheme III.

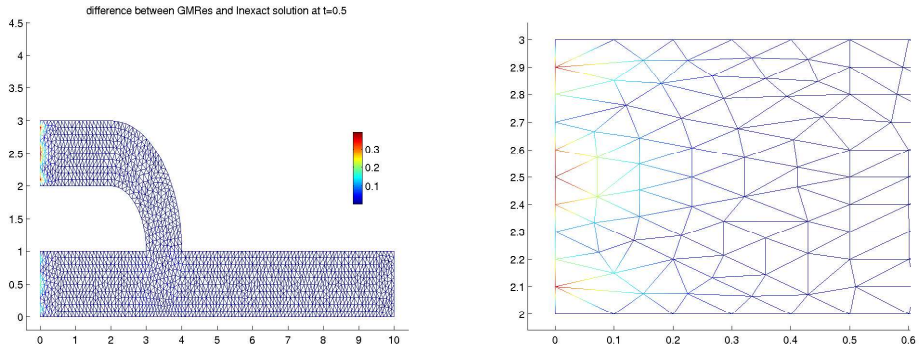

Figure 2.36: Solution in the anastomosis case: difference of the velocity computed using scheme I and scheme III. On the right a zoom of the figure on the upper inlet - $h = 0.1$, $\Delta t = 0.01$, $t = 1.5\,s$.

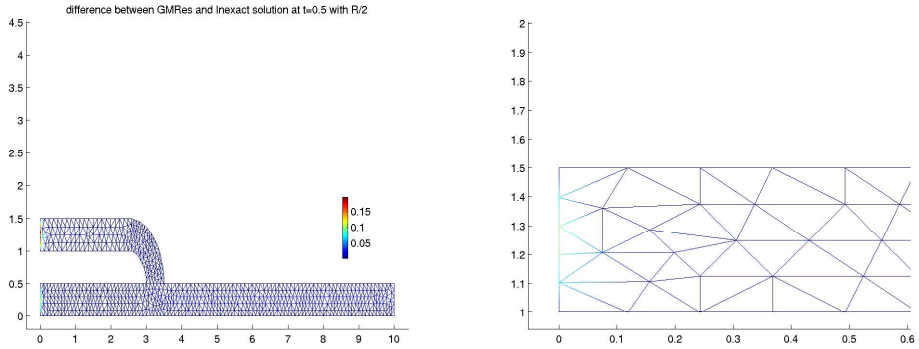

Figure 2.37: The same as in Figure 2.36 with an inlet radius one half of the case plotted above.

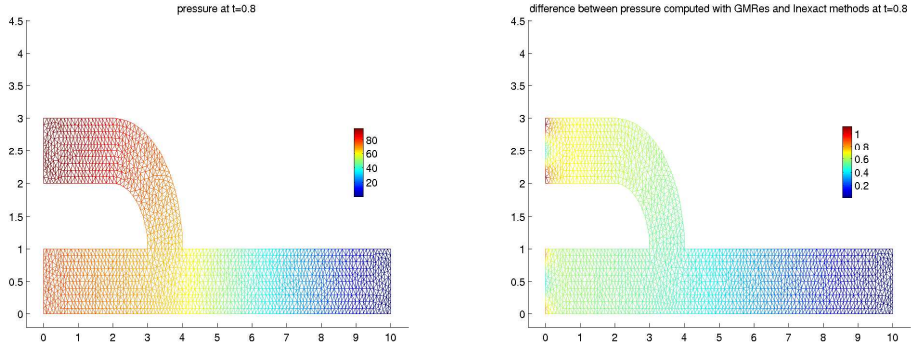

Figure 2.38: Pressure solution (left) and difference between the solutions obtained with scheme I and scheme III (right) for the anastomosis computation - $h = 0.1$, $\Delta t = 0.01$, $t = 1.8\,s$

Test Case	scheme I	scheme III	CPU sch.I/ CPU sch.III
Anastomosis $m = 1$	7min 58s	4min 27s	0.56
Anastomosis $m = 2$	11min 3s	4min 33s	0.41

Table 2.6: CPU times in the anastomosis test case. The final time was $1s$, using for both the simulations $\Delta t = 0.01s$. The inexact splitting computations have been performed on a extended domain, so that the two solutions in the domain of interest covered by the exact solver coincide up to the discretization errors.

In the sequel we report the numerical solutions obtained applying scheme I in two academic code for 2d realistic domains. In the first we consider the Finite element library *Life II* developed at *M.O.X - Dipartimento di Matematica - Politecnico di Milano* and written in *Fortran 77* and *90*. The solver in this code is based on an inexact algebraic splitting of the Navier-Stokes equations (see for example [53]). In particular, a block factorized preconditioner based on the *Yosida* scheme is implemented (see [69]).

As pointed out, different variational formulations can be associated with the prescribed flux problem with different "implicit boundary conditions". Here we compare the numerical results obtained with the two formulations provided in Section 2.2, the one in Problem 11 (*grad-grad* formulation), and the one in Problem 13 (*curl-curl* formulation), on a bypass anastomosis. In particular, we impose two sinusoidal flow rates at both the inlet. Figure 2.39 and 2.40 show the axial velocity at two different instant and Figure 2.41 the modulus of the velocity at the upper inlet. Moreover, in Figure 2.42 the pressure at the upper inlet is shown. As expected, we have some differences between the two solutions, in particular for the pressure (see Tab. 2.7).

$\|\boldsymbol{u}_{\text{grad}} - \boldsymbol{u}_{\text{curl}}\|_{L^\infty L^2}$	$\int_{\Gamma_{up}} \|p_{\text{grad}} - p_{\text{curl}}\|$
$2.16 \cdot 10^{-4}$	$5.31 \cdot 10^{-1}$

Table 2.7: Differences between "grad-grad" and "curl-curl" formulations - scheme I.

The next results are obtained with the Spectral/hp elements code *Nektar*, developed at the *Aeronautic Department - Imperial College* and written in *C* (see [64]). This code is based on a differential splitting of the Navier-Stokes equations (see for example [8, 26]), in particular on a high-order splitting, featured in [31]. These strategies split the computation of the velocity and of the pressure resorting to a projection step. In particular, they introduce an intermediate differential problem (for the unknown velocity or pressure) in order to reduce the computational costs. One of the limit of the differential splitting is the introduction of an inaccuracy near the boundary due to the prescription of non-physical boundary conditions for the intermediate problems (see [58]). In particular, this phenomenon grows up if a Dirichlet boundary condition is imposed at the outlet or a Neumann condition is imposed at the inlet of the domain in the original problem.

In our case, we consider the problem of the flow division in a bifurcation. In particular we would like to impose the flow rates in Figure 2.43 (left) at the inlet and at the upper outlet of the bifurcation. Therefore, in this case we can prescribe

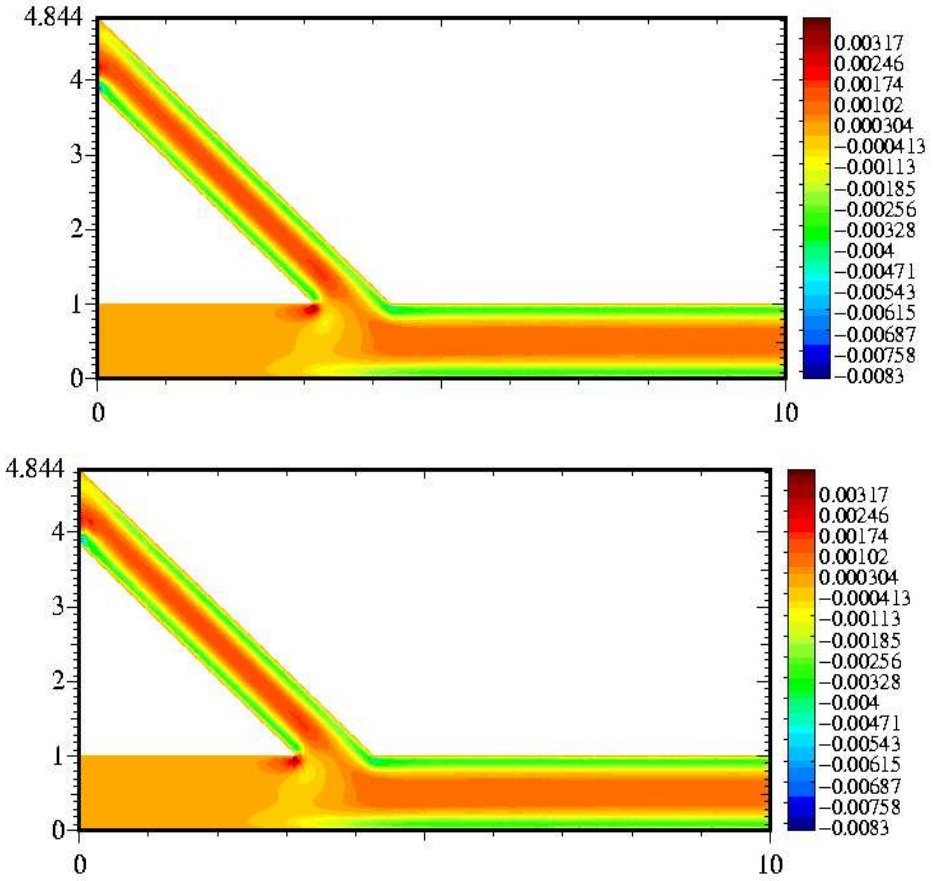

Figure 2.39: Axial velocity in the anastomosis - Sinusoidal fluxes imposed - Grad-grad (up) vs Curl-curl formulation (bottom) - $t = 1.26\,s$ - scheme I.

at the inlet an arbitrary velocity profile fitting the desired flow rate, extending the domain in order to confine the error due to the imposition of a wrong profile out of the zone of interest. Nevertheless, in order to reduce the error due to the splitting, at the upper outlet we should impose a natural condition. A classical choice is to resort to a null natural condition. Therefore, with this choice it is not possible to recover the desired flow division. On the contrary, this problem is avoided by using scheme I. In fact, we remind that the augmented formulation resort to a (unknown) natural condition in order to prescribe the flow rate. In Figure 2.43 (right) the percentage of flow rate passing through the upper outlet is shown for both the choice of boundary conditions. In Figure 2.44 and 2.45 the velocity field is shown at the peak instant and at the middle of the cicle. It is evident that by imposing a null stress condition at the upper outlet, we are underestimating the flow rate passing through this section.

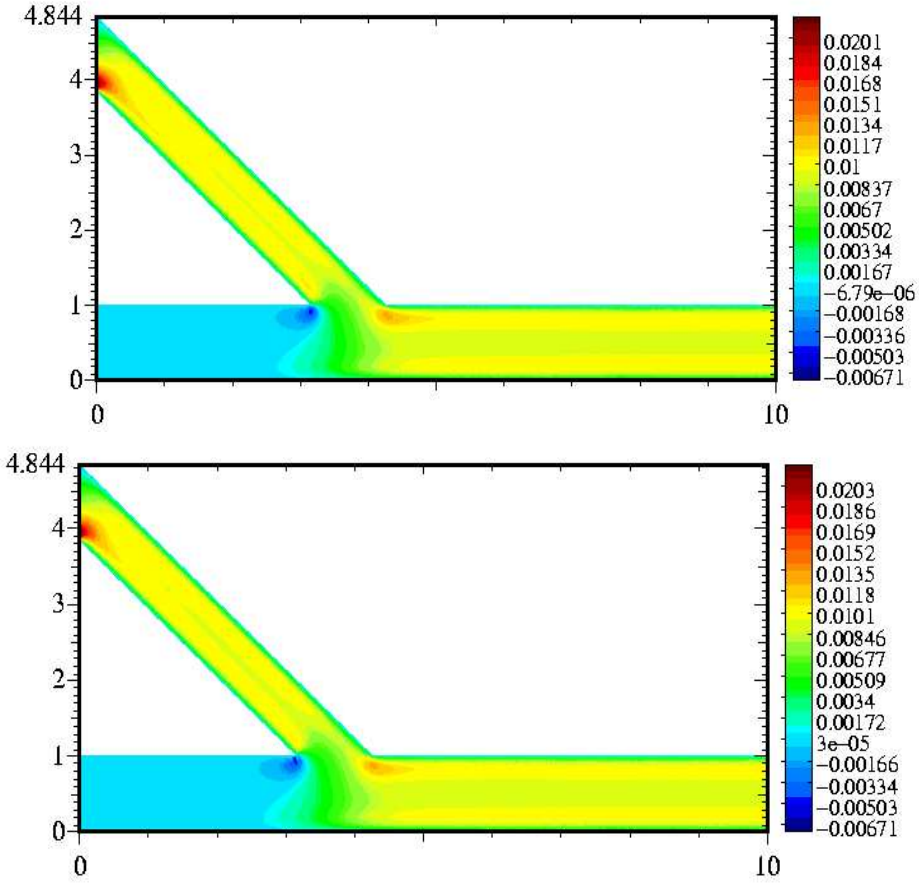

Figure 2.40: Axial velocity in the anastomosis - Sinusoidal fluxes imposed - Grad-grad (up) vs Curl-curl formulation (bottom) - $t = 1.92\,s$ - scheme I.

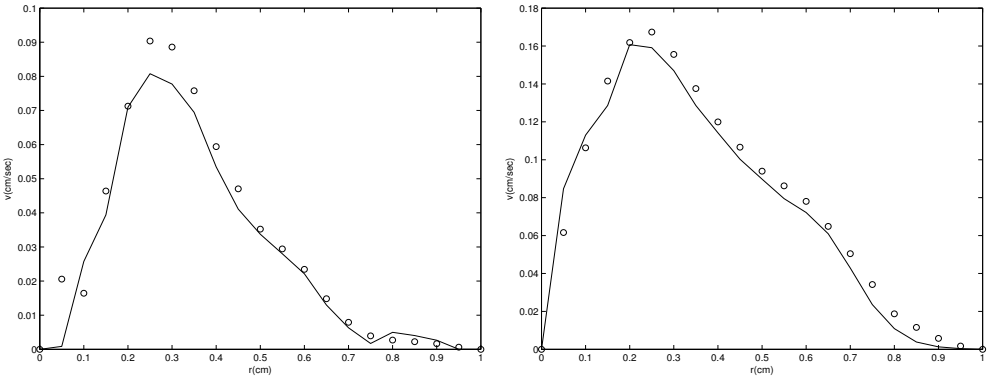

Figure 2.41: Inlet velocity modulus at the beginning of the time period (left) and at the half period (right) in a bypass simulation with sinusoidal prescribed flux - Grad-grad (markers) vs Curl-curl (solid line) formulation - scheme I.

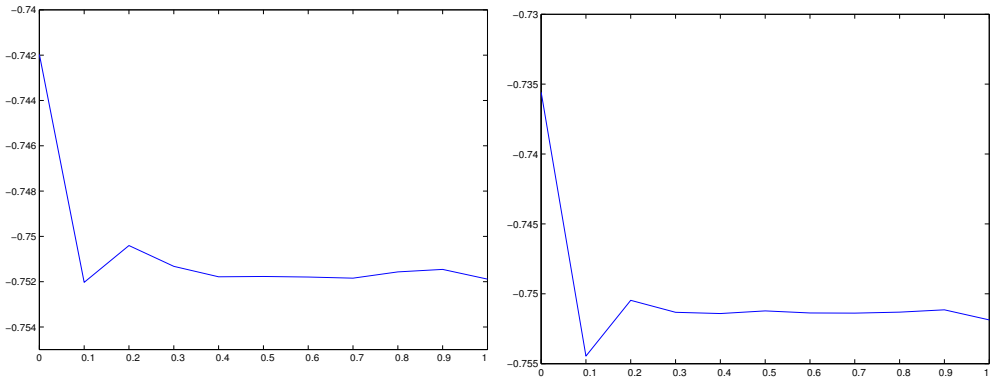

Figure 2.42: Pressure at the upper inlet of the anastomosis - Sinusoidal fluxes imposed - Grad-grad (left) vs Curl-curl formulation (right) - $t = 1.37\,s$ - scheme I.

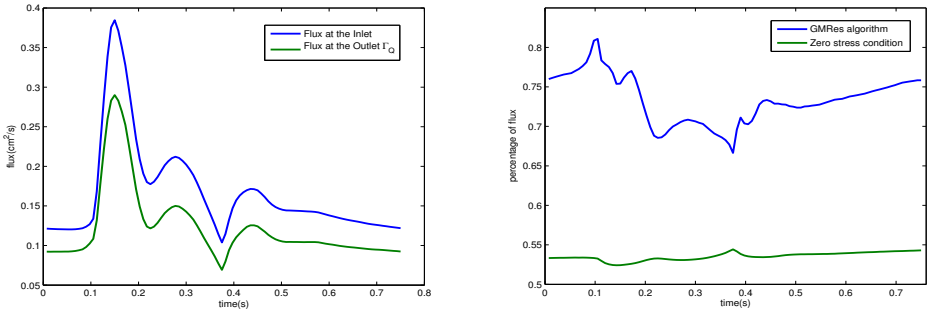

Figure 2.43: Imposed physiological fluxes (left) and ratio between the fluxes at the upper outlet and at the inlet using scheme I (blue line) and a zero stress condition (green line) (right).

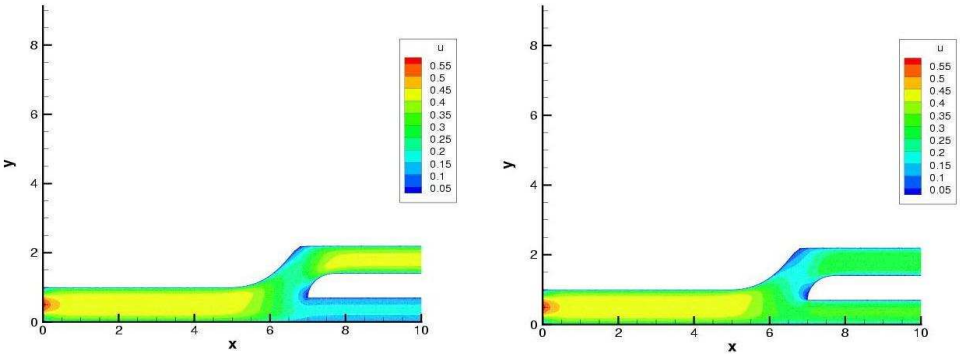

Figure 2.44: Velocity field prescribing the physiological flux with scheme I (left) and imposing zero stress (right) on the upper outlet at the peak instant.

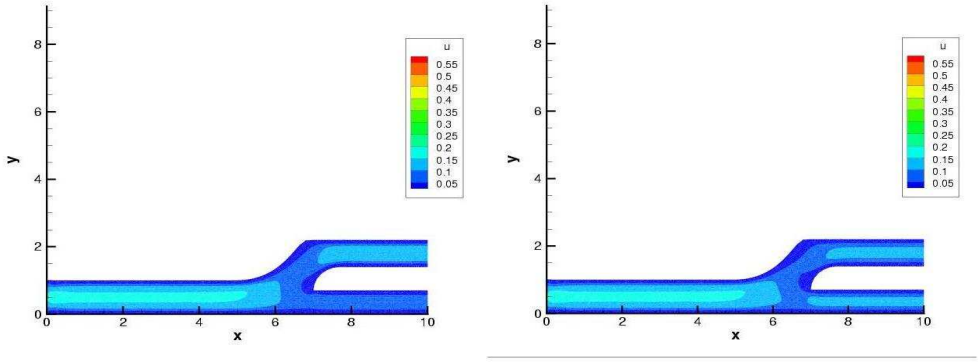

Figure 2.45: Velocity field prescribing the physiological flux with scheme I (left) and imposing zero stress (right) on the upper outlet at the middle of the cicle.

2.6.2 3D simulations

2D axi-symmetric simulations

In this section, we consider the numerical simulations performed with the *axi-symmetric* version of the code *LifeII*, developed at *MOX - Politecnico di Milano* and at *Institute of Analysis and Scientific Computing - EPFL*. Thanks to this, it is possible to obtain numerical results on a 3d/axi-symmetric geometry by solving a 2d problem. In particular, we aim at validating scheme I and the scheme II on analytical test cases. We simulate the flow in an axi-symmetric cylindrical rigid domain with a prescribed flow rate ($Q = 1\, cm^3/sec$, $\nu = 0.035\, cm^2/sec.$). We recover the well known Poiseuille profile (see Fig. 2.46, left). Then, we prescribe a sinusoidal-in-time flow ($Q(t) = 1 \cdot \cos(2\pi t)\, cm^3/sec$), thus recovering the Womersley solution (Fig. 2.46, middle and right and Table 2.8, see [78]).

In Tab. 2.9 we compare the numerical performances of the two numerical schemes proposed. As pointed out, in the unsteady case the coupling between the velocity and the Lagrange multipliers, due to the time derivative, makes scheme II more expensive. Nevertheless, it seems more stable in time, as far as it works with larger time steps.

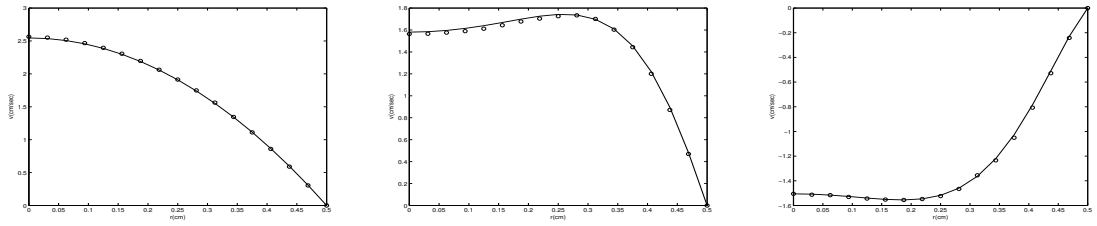

Figure 2.46: Axial velocity on a radius with a constant flux (on the left) and with periodic flux at the beginning of the period (middle) and at a half period (right) - scheme I - The markers refer to the numerical solution, continuous line being the analytical one - $h = 0.03125$, $\Delta t = 0.01$.

	$h = 1/16$	$h = 1/32$
$\Delta t = 0.001$	$1.043 \cdot 10^{-4}$	$1.211 \cdot 10^{-4}$
$\Delta t = 0.0005$	$4.063 \cdot 10^{-5}$	$3.679 \cdot 10^{-5}$

Table 2.8: Errors (in $L^2(L^2)$ norm) between the numerical and the analytical solutions for the pulsatile flow simulation (scheme I).

	scheme I	sscheme II
CPU time(sec)	20.97	486.35
error ($L^\infty(L^\infty)$)	0.005	0.011
Δt	≤ 0.01	≤ 0.05

Table 2.9: scheme I vs. scheme II in the unsteady simulations.

3d validation test cases

In this set of simulations we studied the efficency of scheme I and of scheme III for 3d simulations, using the 3d Finite Element Library *LifeV* (see [36]), developed at *M.O.X - Dipartimento di Matematica - Politecnico di Milano*, at *Institute of Analysis and Scientific Computing - EPFL* and at *INRIA - Paris* and written in *C++*. In this, the Navier-Stokes solver is based on a preconditioned pressure matrix method (see [23]).

Firstly, we simulate the flow of the fluid in a cylinder Ω with radius $r = 0.5\,cm$ and lenght $l = 1\,cm$ by prescribing a constant flow $Q = 1\,cm^3/s$ and we solve the Navier-Stokes equations using scheme I. Figures 2.47 show the axial velocity field (left) and the comparision between the numerical and the analytical solution on a radius of a section (right). We point out that the numerical solution differs from the analytical one, in particular it is bigger. The reason is that the numerical section $\Gamma_h \subset \Gamma$ where we are prescribing the flow rate is such that

$$|\Gamma_h| \leq |\Gamma|.$$

Since the flow rate prescribed on a section Σ is given by

$$Q = \widetilde{V}|\Sigma|,$$

with $\widetilde{V}$ the mean velocity, in order to impose the desired flux we obtain

$$\widetilde{u}_h \geq \widetilde{u},$$

where with $\widetilde{u}_h$ and $\widetilde{u}$ we indicate the mean numerical and the mean analytical velocity, respectively. We expect that, with a better space discretization, section Γ_h fits better with the real section Γ and hence that the numerical solution is in better agreement with the analytical one. This is confirmed by Figures 2.48. Therefore, when a flow rate is prescribed on a 3d domain, a pre-process operation would be mandatory if the computational domain does not coincide with the analytical one. Moreover in Figure 2.49 the pressure field is shown. These results are in good agreement with the Poiseuille solution:

$$\begin{cases} p(z) = 1.426(1-x) \\ u(x,y) = 2.546(1-4(x^2+y^2)), \end{cases}$$

where x and y are the radial coordinate and z is the axial coordinate.

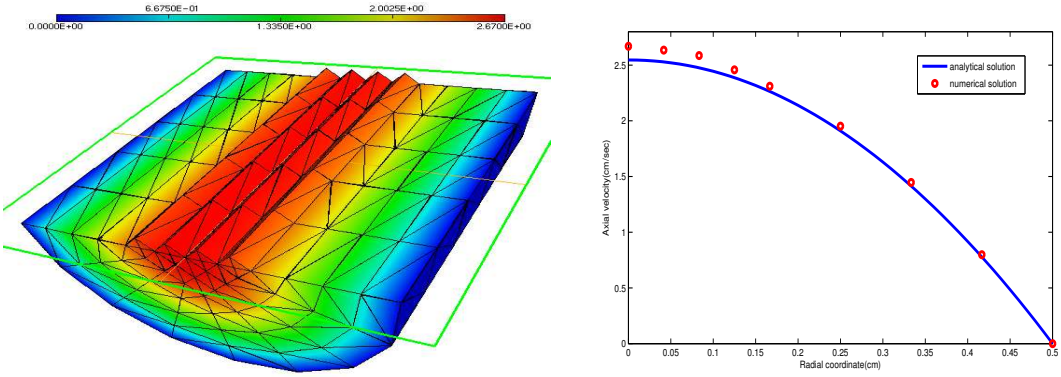

Figure 2.47: Steady simulation - Axial velocity field (left) and axial velocity on a radius of a section (right) - $h = 0.1$ - scheme I.

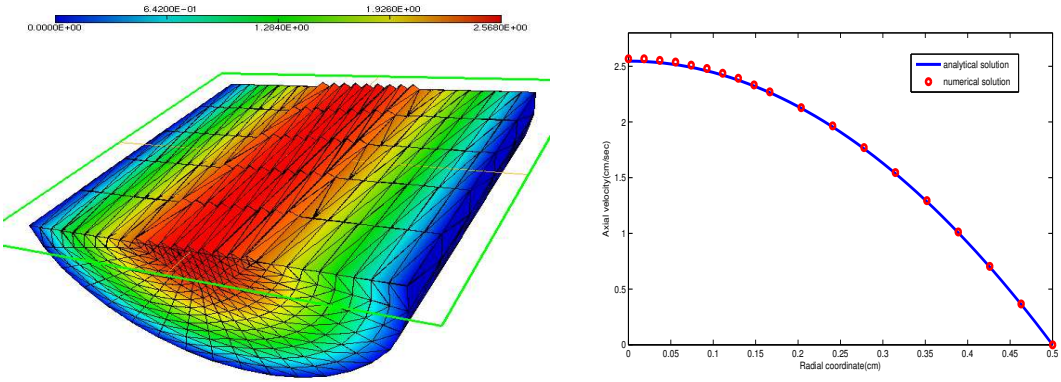

Figure 2.48: Steady simulation - Axial velocity field (left) and axial velocity on a radius of a section (right) - $h = 0.05$ - scheme I.

Secondly, we prescribe the sinusoidal flow rate $Q(t) = 1 \cdot \cos(2\pi t)\, cm^3/sec$ at the inlet of Ω. Figures 2.50 show the comparision between the numerical and the analytical (Womersley) axial velocity.

In the next simulation we prescribe the physiological flow rate in Figure 2.35 (right) with peak value $0.2\, m^3/s$ and a period $T = 0.84\, s$. Figures 2.51 show the comparision between the numerical solutions obtained with the 2d/axi-symmetric library *LifeII* and with the 3d library *LifeV*. These solutions seem to be in good qualitative agreement with the experimental measures (see [38]). We point out that the 2d axi-symmetric code is not affected by the error on the measure of Γ_h,

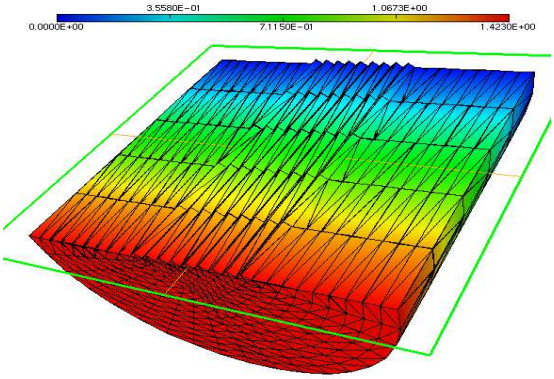

Figure 2.49: Steady simulation - Pressure field - $h = 0.05$ - scheme I.

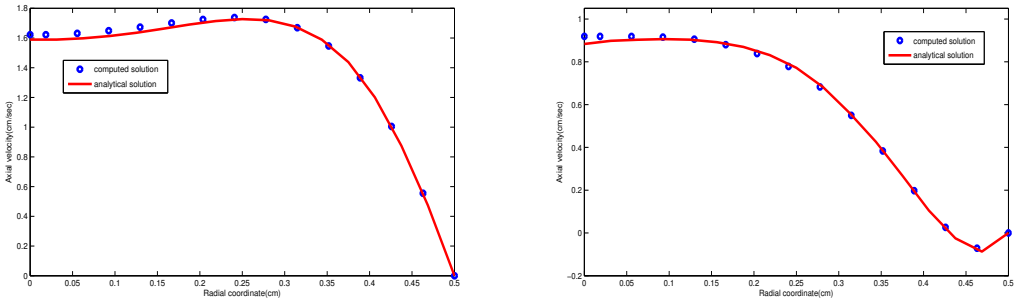

Figure 2.50: Womersley simulation - Axial velocity on a section at $t = 2.0\,s$ (left) and $t = 2.2\,s$ (right) - $h = 0.05$ - scheme I

since $\Gamma_h = \Gamma$ in this case. This is confirmed by the numerical results, showing that in the case of 2d axi-symmetric simulation the mean velocity is less than the one performed by the 3d code.

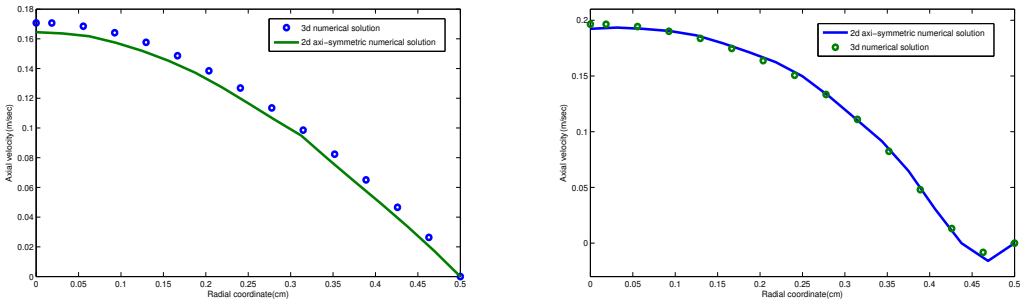

Figure 2.51: Physiological simulation - Axial velocity on a section at $t = 0.85\,s$ (left) and $t = 1.01\,s$(right) - $h = 0.05$ - scheme I

We want now to investigate the error made with scheme III. In particular, we refer to the Womersley simulation. In Figures 2.52 and 2.53 the differences of the numerical solution obtained prescribing a parabolic velocity profile (left) and using scheme III (right) with the analytical solutions are plotted. We observe that also in the 3d computations the enlarged zone needed in order to obtain a meaningful solution with scheme III is smaller then the one requested by the *practical approach*.

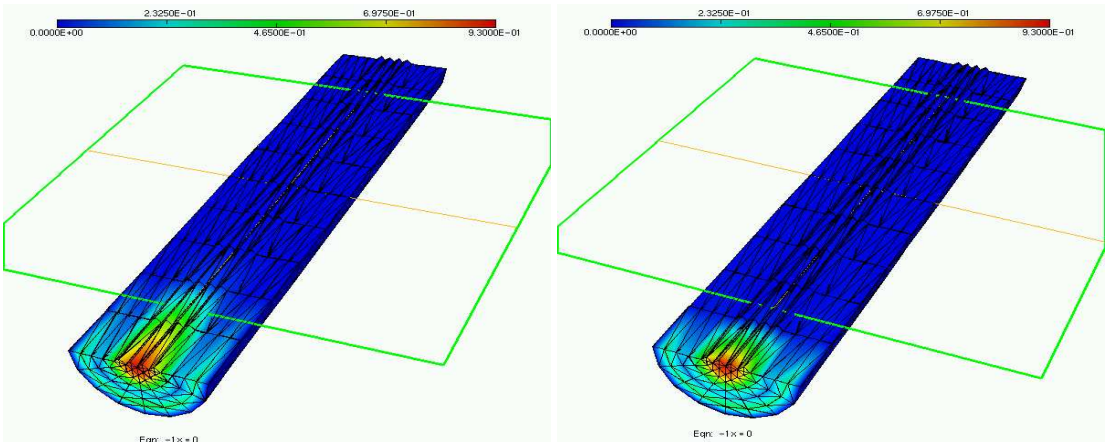

Figure 2.52: Womersley simulation - Differences between the numerical (practical approach, left - scheme III, right) and the analytical solution, $h = 0.05$, $\Delta t = 0.01$, $t = 2.32\,s$

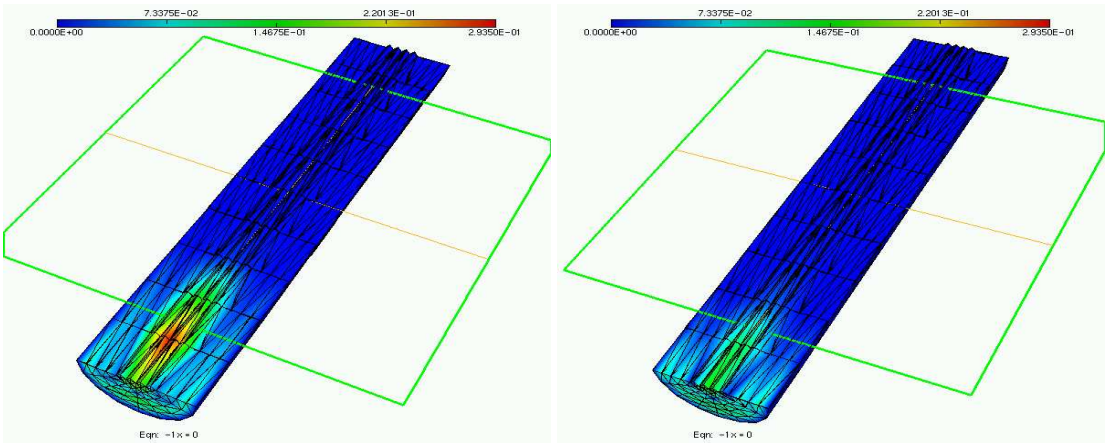

Figure 2.53: Womersley simulation - Differences between the numerical (practical approach, left - scheme III, right) and the analytical solution, $h = 0.05$, $\Delta t = 0.01$, $t = 2.34\,s$

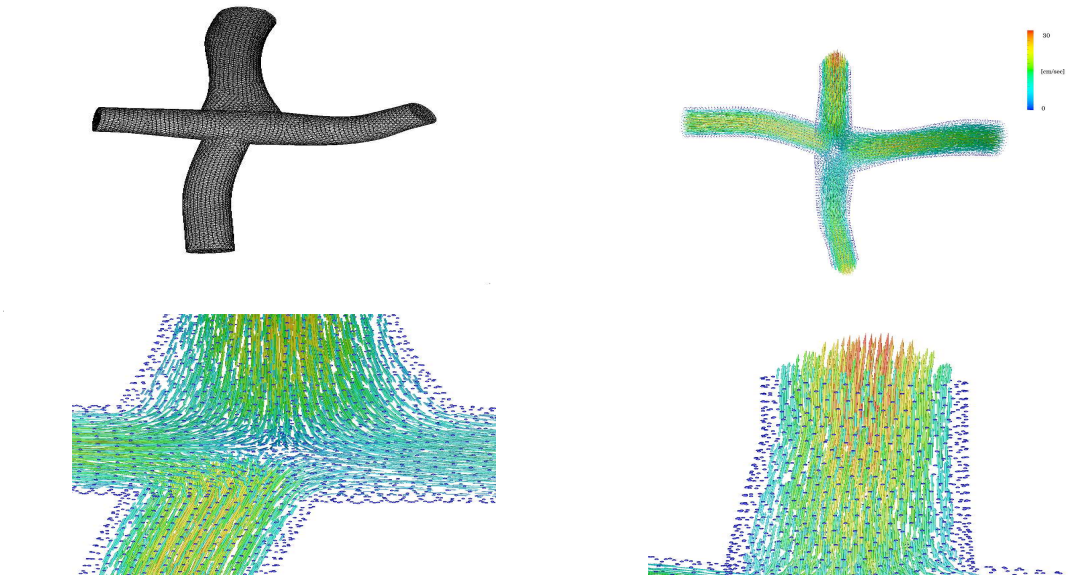

Figure 2.54: Cavo-pulmonary connection: the vertical vessel is the Inferior Vena Cava, the horizontal one is the Pulmonary Artery. Computational 3D grid (top, left), velocity field (top, right, bottom left) and velocity field on Inferior Vena Cava (bottom, right) - scheme II.

Computations in realistic cases

We want now to illustrate the solution of an augmented problem resorting to the commercial package FIDAP as Navier-Stokes solver. For the sake of simplicity, we refer to the solution of a steady Stokes solver by means of scheme II. In particular, we refer to the problem of the *total cavopulmonary connection*, which is a surgical operation sometimes needed in pediatric pathologies in which only the right ventricle works (see [39]). In this case, the pulmonary artery and the vena cava are connected, leading to a cross-shape domain, as illustrated in Fig. 2.54 top-left, obtained starting from RNM data. The multiscale approach in this case is mandatory to have realistic boundary data accounting for the whole vascular network (see [51, 56]). Here we present some results obtained by prescribing phisiological defective flow rate data on two of the four artificial sections. Observe from Figure 2.54 bottom-right, how the expected quasi-parabolic profile is obtained as a numerical result of the augmented approach (without prescribing it).

Finally, we apply scheme I and scheme III in a carotid domain obtained from real data of a patient through a cast produced by D. Liepsch - FH Munich (see Figure 1.3) . We impose physiological flow rates in Figure 2.43 (left) at the inlet and at the internal outlet of the domain, with a peak value equal to 20.31 cm^3/s and 17.39 cm^3/s, respectively. Figures 2.55-2.60 show the velocity fields obtained with scheme I, with scheme III and imposing a parabolic velocity profile at the inlet and a flat velocity profile at the internal outlet (both fitting the prescribed flow rates), respectively. We use LifeV as solver. Moreover, we refer to the solution obtained with scheme I as the "exact" solution, in order to amount the error made with scheme III and with the *pratical approach*. Also in this case it is evident that the error made with scheme III is confined near the boundary and that the enlarged zone requested by the latter is smaller than the one needed by the *practical approach*. Moreover, the latter approach seems to give a numerical solution that does not agree very well with the one obtained using scheme I. In particular, we point out big differences also far from the artificial sections, in particular at the bifurcation near the wall (see Figure 2.60).

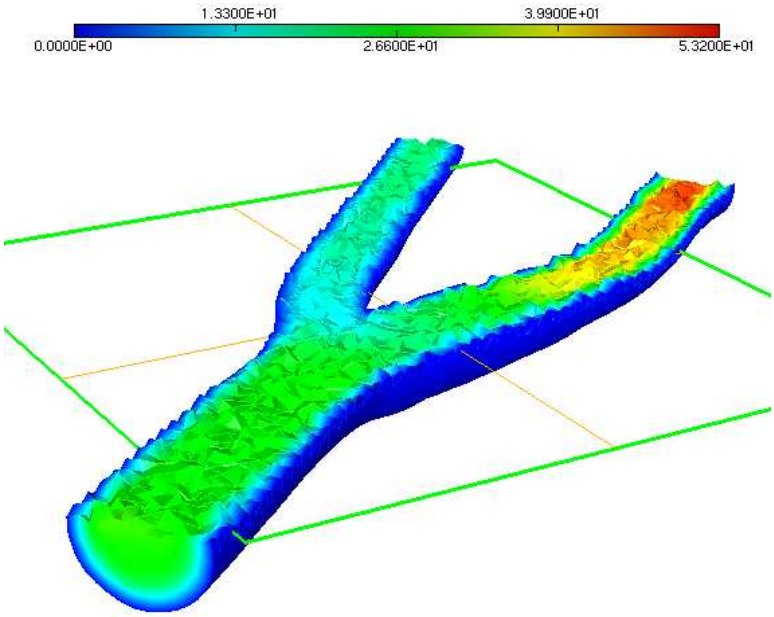

Figure 2.55: Computations in 3D: carotid solution. Velocity field obtained with scheme I, $t = 0.195\,s$, $\Delta t = 0.0075\,s$.

We point out the influence of the geometry on the solution of the Navier-Stokes problem. In Figure 2.61 and 2.62 the velocity field at the inlet of the carotid bifurcation computed with scheme I and imposed as parabolic, respec-

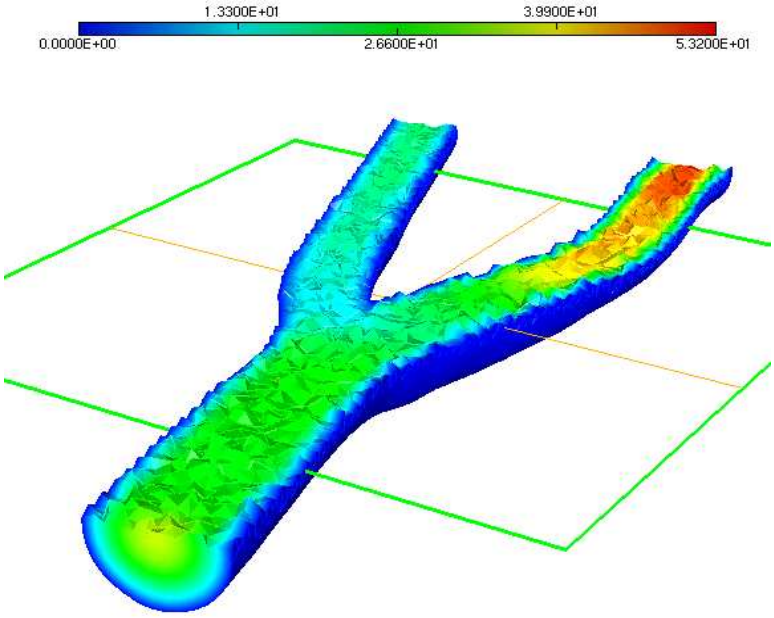

Figure 2.56: Computations in 3D: carotid solution. Velocity field obtained with scheme III, $t = 0.195\,s$, $\Delta t = 0.0075\,s$.

tively, are shown. Let us notice the asymmetry of the velocity profile recovered without prescribing it using scheme I. Therefore, for a non-cylindrical domain, the prescription of a parabolic velocity profile or even of the Womersley solution as Dirichlet boundary condition, as suggested in [79], leads anyway to an error due to the effect of the geometry.

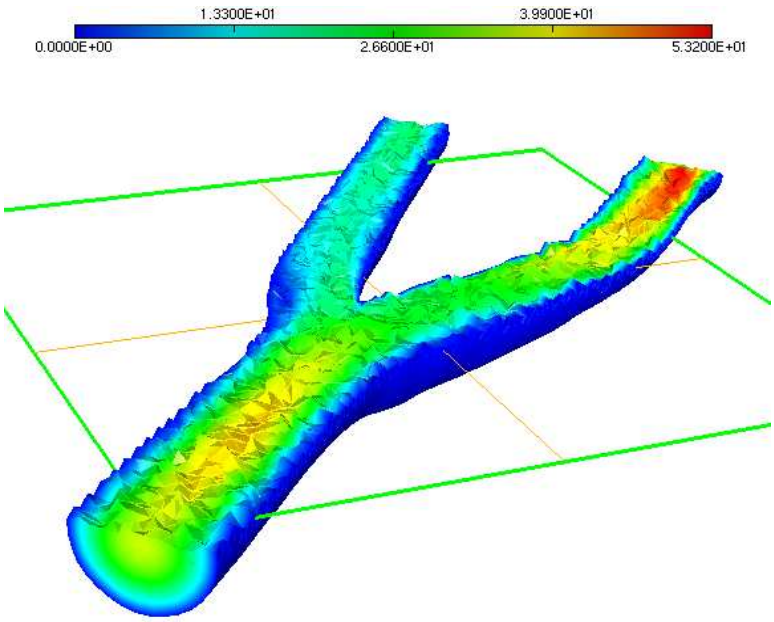

Figure 2.57: Computations in 3D: carotid solution. Velocity field obtained with the *practical approach*, $t = 0.195\,s$, $\Delta t = 0.0075\,s$

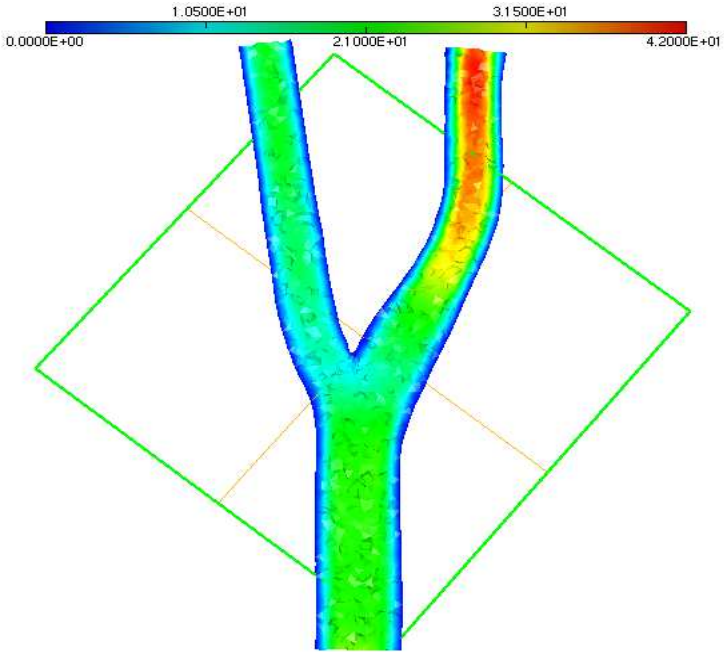

Figure 2.58: Computations in 3D: carotid solution. Velocity field obtained with scheme I, $t = 0.225\,s$, $\Delta t = 0.0075\,s$.

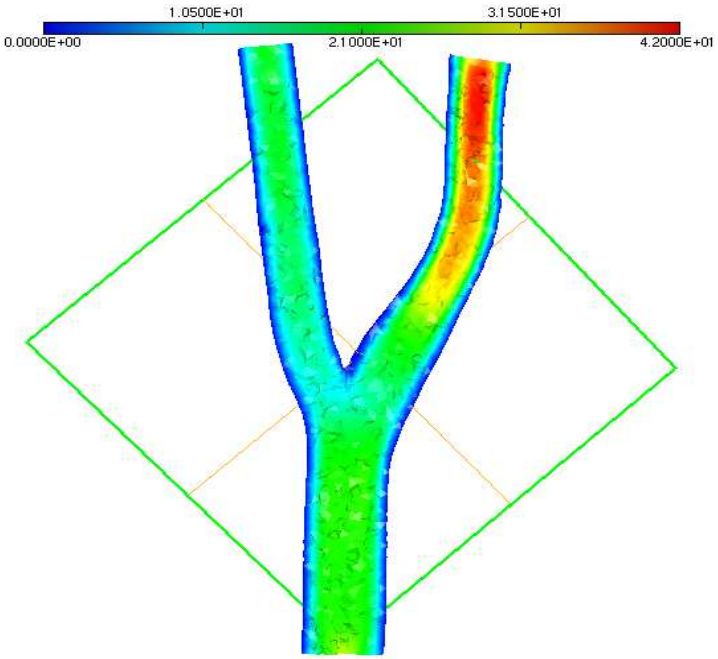

Figure 2.59: Computations in 3D: carotid solution. Velocity field obtained with scheme III, $t = 0.225\,s$, $\Delta t = 0.0075\,s$.

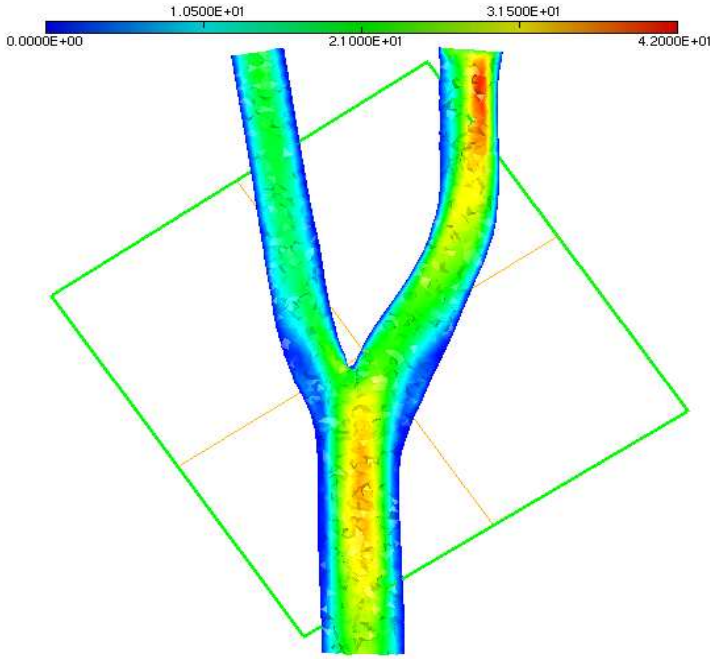

Figure 2.60: Computations in 3D: carotid solution. Velocity field obtained with the *practical approach*, $t = 0.225\,s$, $\Delta t = 0.0075\,s$

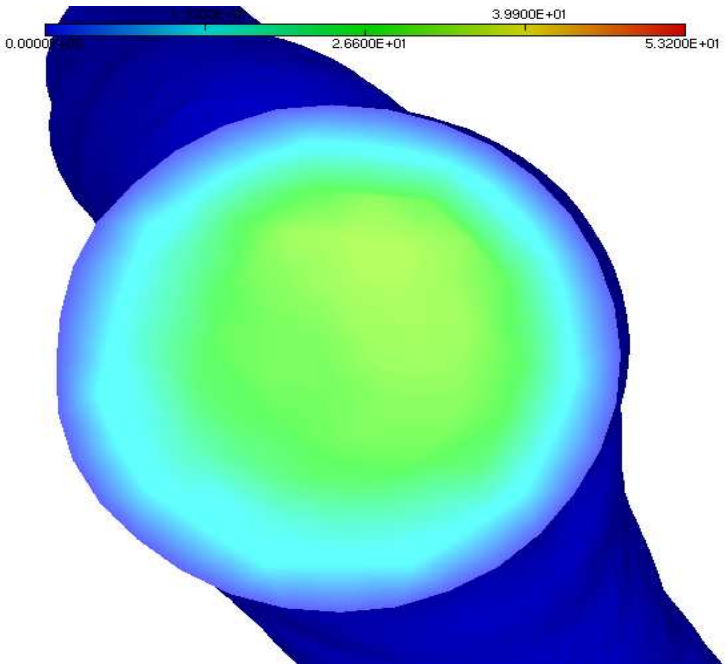

Figure 2.61: Computations in 3D: carotid solution. Velocity field at the inlet obtained with scheme I, $t = 0.195\,s$, $\Delta t = 0.0075\,s$.

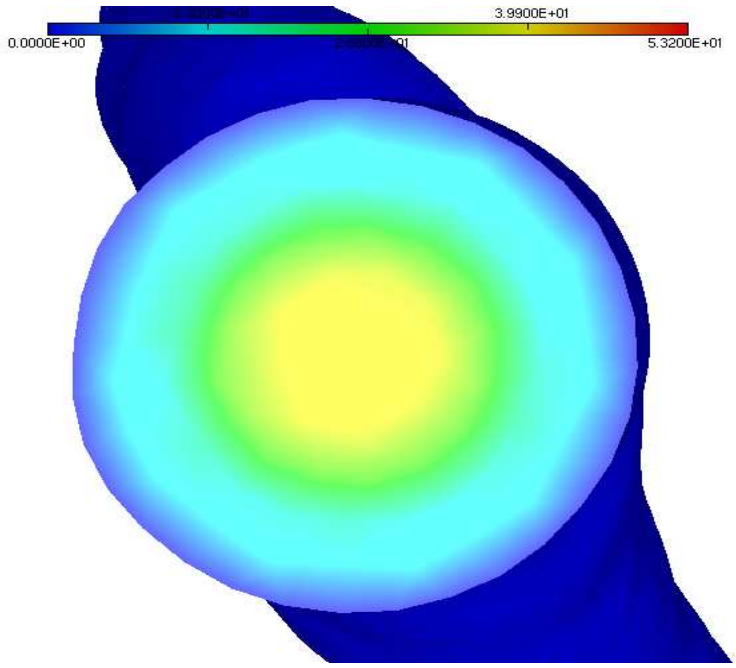

Figure 2.62: Computations in 3D: carotid solution. Velocity field at the inlet prescribed with the *practical approach*, $t = 0.195\,s$, $\Delta t = 0.0075\,s$.

Chapter 3

Applications to Haemodynamics

3.1 Introduction

3.1.1 Outline of the chapter

In this chapter we present three applications of some of the algorithms proposed in Chapter 2 to computational haemodynamics. As already pointed out, this field has mainly inspired and justified the research of new techniques for the prescription of a flow rate boundary condition.

In Section 3.1.2 we present a brief introduction to the computational haemodynamics, pointing out the role it has played in the last years in the bioengineering comunity. Moreover, we give some basic facts about the modeling of blood in rigid domains.

In Section 3.2, we present a first application. In particular, in the clinical practice the non-invasive measure techniques estimate indirectly the flow rate through a direct measure of the maximum velocity. In fact, thanks to some haemodynamics hypotheses (based on the assumption of parabolic velocity profile) it is possible to compute the flux starting from the maximum velocity. Nevertheless, these hypotheses lead to large measurements errors in many haemodynamics conditions. Thanks to the right prescription of a flow rate boundary condition on a surface Γ, it was possible to collect a set of numerical results linking the shape of the computed velocity profile on Γ to the pulsatility of the hearth action. In this way, we could estimate the relationship between the flow rate, the maximum velocity and the pulsatility. By resorting to a least square approach, we could propose formulae for the estimation of the flow rate starting from the maximum velocity that highlight a better fitting with the real value. It is clear that this improvement is possible only thanks to the right prescription of a flow rate boundary condition. Otherwise, the linking between the flux and the maximum velocity

would be faked.

In Section 3.3 we consider the flow rate problem in a multiscale simulation of the cardiovascular system. In this context, different models with different spatial detail are matched together in order to obtain a description of the whole cardiovascular net. In particular, a *three* (or *two*) dimensional domain in which we are interested to compute the pointwise velocity or pressure field, is coupled with *one* or *zero*-dimensional models that deals only average informations. It is clear that at the interface of this coupling, the exchange of information between the three (two) dimensional and the reduced model allows to prescribe suitable boundary conditions in both the directions. However, the reduced model could give only an average datum (like the flow rate). In particular, we propose the numerical results obtained by coupling a cylindrical domain with two zero-dimensional models of the cardiovascular system.

Finally, in Section 3.4 we consider the motion of the blood in compliant domains. In particular, we propose a new strategy in order to couple the Navier-Stokes equations with a simple law for the vascular wall, leading to very good performances in terms of CPU times. Moreover, we propose the prescription of suitable outflow boundary conditions that allows to reduce the reflexions induced by the ondulatory movements of the wall. Finally, we present numerical results obtained applying the scheme I, proposed in the previous chapter for the prescription of a flow rate, to the simulation of a case in which the vascular wall is assumed to be compliant.

3.1.2 Basic facts in haemodynamics

In recent years there has been a growing interest in medical and bioengineering community in using of numerical simulations of biological systems and devices (see e.g. [66, 17, 18, 54]). In particular, cardiovascular pathologies have a relevant socio-economic impact in Western countries and this has motivated extensive investigations in haemodynamics by means of *Computational Fluid Dynamics* (CFD). This tool can give some important informations about the fluid-dynamics of the blood, in particular about some meaningful physical and clinical quantities hardly measurable so far. For instance, while the flow rate in a vessel is a quantity quite easy to be measured in standard clinical practice, the velocity field can be obtained only by application of expensive techniques, like the *nuclear magnetic resonance* (NMR). Not to mention specific quantities like the shear stress, which is practically impossible to be measured directly. These quantities can now be calculated by numerical simulations carried out on real geometries obtained by three-dimensional reconstruction.

To be more precise, there are different levels of impact of numerical simulations

in haemodynamics. Firstly, computational haemodynamics aims at supporting the understanding of the on-rise and the development of pathologies. For example, numerical simulations of the different pulmonary artery bandings in new born babies affected by left ventricule hypoplasia have clarified the impact of the banded vessel profile on the shear stress and provided a quantitative explanation of the observed follow up on the patients (see [9]). Another issue is the design of medical devices. For example, since 30 years it is a common practice in cardiology to use stents in order to open a stenosis of a vessel. A stent is a small, lattice-shaped, metal tube that, inserted permanently into an artery, helps hold open it so that blood can flow through it. In particular, drug-eluting stents contain drugs that potentially reduce the possible inflammatory reaction of the vascular walls. In the design of drug-eluting stents, the role of numerical simulations in setting up a coating film ensuring a correct drug delivery is relevant (see [57, 80]). Another example is given by numerical simulations for comparing different possibilities of a surgical intervention in pediatric heart diseases, providing practical indications for the surgeon (see [33]). A third kind of task for the computational haemodynamics is the identifications and the optimization of some physical parameters. Thanks to the possibility to solve inverse problems, it is possible to devise a numerical solution which fulfills some prescribed optimality criteria. For example, shape optimization techniques are applied to coronary bypass anastomosis in order to choose the post-surgery configuration which reduces the risk of operation failure (see [52]). For a more complete and detailed review of the applications of computational haemodynamics, see [18].

From the physical point of view, blood is a complex suspension of several particles such *red* and *white cells* and *platelets* in an acqueos solution called *plasma* (see Figure 3.1). Its motion has a *pulsatile* nature, due to the action of the heart, in deformable domains. The basic time scale in this context is given by the heart beat (about $0.8\,s$), in which we may recognise an initial phase called *systole* (about $0.3\,s$) when the aortic valve is open and the blood is thrusted into the arterial system, followed by the *diastole* initiated by the closure of the aortic valve. Fast transient are therefore a relevant feature of blood flow (see Figure 3.2). Moreover, vascular walls have complex and variable mechanic characteristics (e.g. inelasticity, anisotropy, etc). Due to these complexities, the mathematical-numerical modeling of the blood needs some simplifying assumptions. First of all, blood can be considered as an incompressible homogeneous fluid. Moreover, if we restrict our attention to large vessels ($\text{radius} \geq 0.1\,cm$) and in non-pathological situations, the rheology of the blood can be assumed to be Newtonian, i.e. the constitutive law between internal stress and deformation is linear (see Section 1.2). In fact, only in small vessels as the *capillaries* the dimensions of the particles are such to modify the rheology (see e.g. [17, 54]). Under

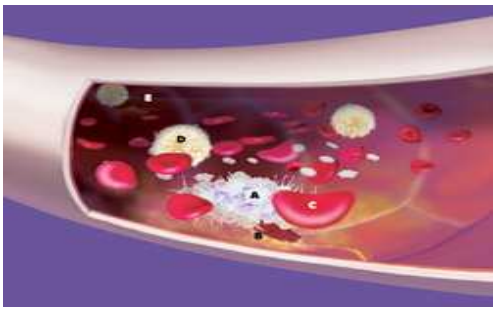

Figure 3.1: Red and white cells and platelets in plasma.

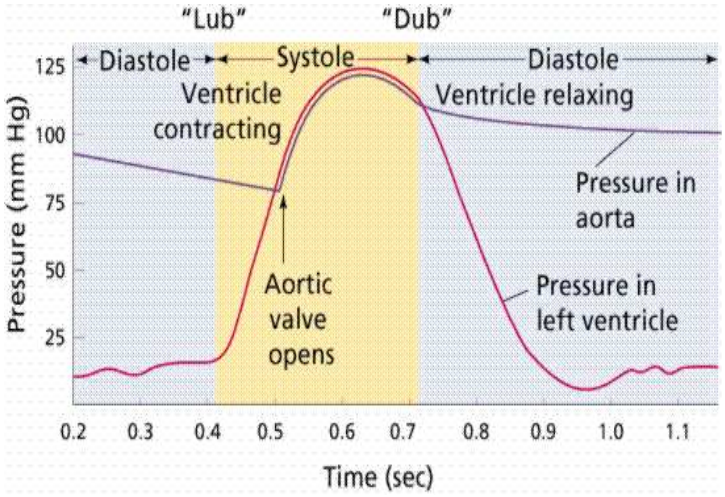

Figure 3.2: Pressure in left ventricle and in aorta: we detect the systole and the diastole.

these hypotesis, the behaviour of the blood can be modeled starting from the mass and momentum conservation laws, leading to the *Navier-Stokes equations* for an incompressible Newtonian fluid (see Section 1.2). In particular, in Section 3.2 and 3.3 we consider blood flow in *rigid* domains. This assumption is quite acceptable in many applications (see [48]), even if in the last year a lot of work investigated numerical techniques for the fluid-structure interaction problem (see [42],[12]). Following these lines, in Section 3.4 we consider compliant vessels.

3.2 Estimation of flow rate in haemodynamics measures

In this section, we present an application of the methodology described in Chapter 2 for the prescription of a flow rate boundary condition to a case of clinical

interest. These results have been presented in [50].

The correct knowledge of the blood flow rate Q in a vascular district is a major issue in many clinical situations for estimating the perfusion state of a certain tissue and for decision-making when a cardiovascular disease occurs. For example, the evaluation of the *flow reserve*, which is the ratio between the maximal flow obtained in vasodilation conditions and the baseline conditions, is one of the most important parameters used to characterize the haemodynamics impact of a luminal obstruction. In principle the knowledge of the whole velocity field is needed for the computation of the flow rate Q on a section Γ, since

$$Q = \int_\Gamma \boldsymbol{u} \cdot \boldsymbol{n} \, d\gamma. \tag{3.1}$$

However, this information cannot be obtained in ordinary Doppler velocimetry analysis. A different way for representing Q is to resort to a *mean velocity* value $\widetilde{V}$ such that

$$Q(t) = \widetilde{V}(t)A(t), \tag{3.2}$$

where A is the measure of Γ. The problem with this formulation is still that $\widetilde{V}$ cannot be directly measured, therefore it is currently estimated by the measure of the maximum value of velocity V_M on Γ by means of an appropriate relation linking V_M to $\widetilde{V}$. In particular, it is usually assumed (see [10]) that

$$\widetilde{V} = \frac{1}{2} V_M. \tag{3.3}$$

This equation stems from the hypothesis of a *parabolic* spatial profile for the velocity. According to this assumption, blood is considered a steady, laminar Newtonian fluid in a cylindrical vessel. As also pointed out in Section 2.6, in real situations, blood flow is far from fulfilling these features. Several works (see e.g. [60, 47, 63, 49]) pointed out that a non parabolic profile can be computed in simulating realistic conditions even when the considered morphologies were the same of those studied in the validation protocol of the Doppler guide wire (see e.g. [10, 62]).

In particular, the relevance of blood pulsatility on velocity profiles has been clearly pointed out since a long time by [78] and among the others, we quote [27, 41]. These works highlight that the hypothesis that blood is quasi-static (i.e. that at each instant the velocity profile is the same as for a steady fluid featuring the flow rate prescribed at that instant) is not realistic, in particular when the *Womersley number*

$$W = r\sqrt{2\pi f/\mu} = \sqrt{2Af/\mu}$$

increases. In the previous definition $r = \sqrt{A/\pi}$ is the vessel radius, f the frequency of blood impulse and μ the blood viscosity

In order to obtain a more realistic relation linking V_M to $\widetilde{V}$ taking into account the pulsatility of the blood flow rate, a first possibility is to utilize the analytical relationship that [29] proposed for a cylindrical domain for a sinusoidal signal. This approach can be extended to general physiological waveforms by application of the effects superimposition principle that holds for linear problems. However, this approach has two major drawbacks. On one hand it has been devised for cylindrical morphologies and its extension to more realistic geometries seems not trivial and somehow problematic. On the other one, the problem at hand is driven by the non-linear Navier-Stokes equations, so the effects superimposition is strictly non applicable. When the Reynolds number increases, i.e. when the non linear convective term becomes more relevant, this can induce some inaccuracies.

For these reasons, alternatively some works developed different relations between the maximum and the mean velocity for specific cases, using Computational Fluid Dynamics (CFD). In this context, approximations have been found in [45, 46] for the case of the venosus ductus and in [49] for coronary Y-graft bypass.

In [50], we propose a general CFD-based approach for improving blood flow estimates from maximum velocity measures, generalizing formula (3.3). In principle, we could think to extend this formula by introducing a relation of the form

$$\widetilde{V} = g(V_M, r, f, \mu, \ldots),$$

where all significant parameters (such as the vessel curvature or torsion) can be included for improving the accuracy of the mean velocity. The specific features of the flow patterns in a vascular district, once boundary conditions have been assigned, are basically the morphology, the pulsatility and the rheology. On one hand, one would set up an accurate equation linking the mean and the maximum velocities, taking into account all these aspects. On the other hand, the usage of this equation is subordinated to the possibility of getting reliable estimates of all these features in the clinical practice. As a reasonable compromise between the accuracy and the feasibility, we summarize the dependence on all these features by resorting to the Womersley number W. As a matter of fact, we introduce the relation

$$\widetilde{V} = g(V_M, W), \tag{3.4}$$

establishing a link between the $\widetilde{V}$ (and then the flow rate) and V_M as a function of the Womersley number W. In this way, we synthetically account for the radius of the vessel, the blood viscosity and in particular for the *pulsatility*. W can be in practice estimated on the basis of available clinical measures. We actually are assuming that it is possible to define locally a *vessel radius*. This will be the only geometrical parameter in our equation. More complex (and more difficult

to implement) equations could be considered as possible future development.

Function g will be fixed by specifying some parameters, depending on its specific functional form. The quantitative determination of these parameters can be carried out by fitting available data with a least squares approach. These data could be provided by "in vitro" measures taken in realistic experimental set up. Alternatively, fitting can be carried out by exploiting numerical simulations (see [46, 49]). The direct derivation of a unique, exhaustive formula for the estimation of the flow rate in the whole Womersley number physiological range, would be optimal from the operative point of view. Nevertheless, we found that the fitting procedure brought to an inaccurate unique formula. Therefore, for the sake of accuracy, we decided to consider two different situations representative for small and medium/large vessels (see Figure 3.3) and to devise for each one a different equation (3.4). We address separately one computational protocol in each case.

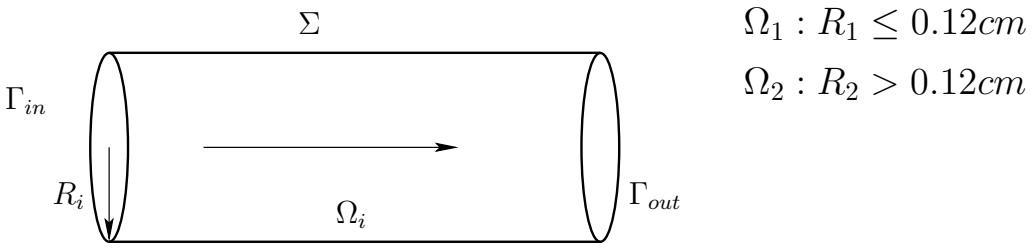

Figure 3.3: Reference domains Ω_i.

1) *Small vessels.* Small vessels are represented by a cylindrical domain Ω_1 with $R_1 \leq 0.12cm$. In this class of vessels, a physiological range for the Womersley number is (see [41, 75, 6, 77]):

$$W \leq 3.1.$$

A possible general formulation for the equation (3.4) to be used in the case of small vessels is:

$$\widetilde{V} = g_1(V_M, W) = \frac{1}{2} V_M \left(1 + a_1 W^{b_1}\right), \tag{3.5}$$

where a_1 and b_1 are the parameters to be fitted. This parametric representation has been selected as a power law generalization of the steady ($W = 0$) equation (3.3). In the numerical simulations carried out for fitting a_1 and b_1, we distinguished two situations that can be referred to "small vessels":

a) small arteries

b) coronaries.

The two cases are considered separately because the flow rate waveform in the coronaries is by far different than the one in the other small arteries due to the heart squeezing. This actually means that in the fitting procedure we selected two different set of test cases adopting two different flow rate waveforms. In particular, for small arteries we choose the profile reported in Figure 3.4, left, representing the flow rate in the *vertebral artery*, following [73]. For the coronary fitting, waveform is reported in Figure 3.4, right, taken from [47].

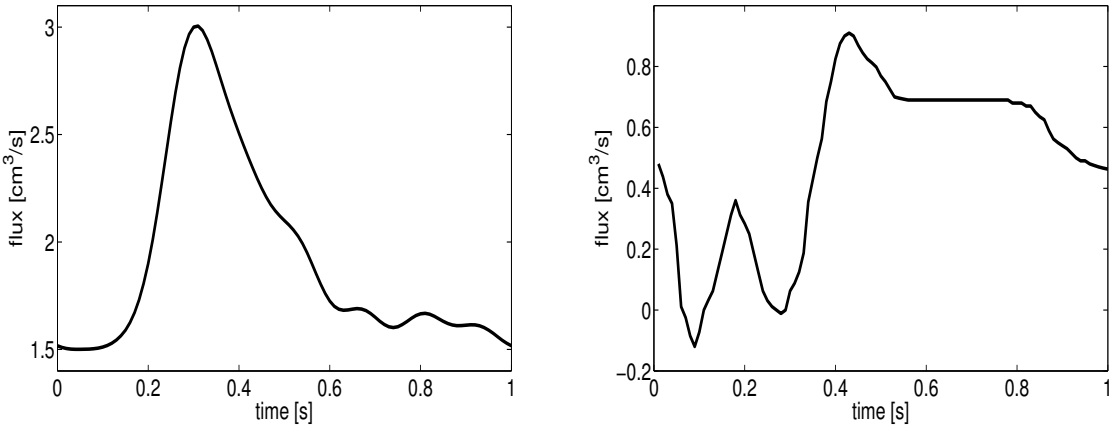

Figure 3.4: Vertebral (left) and coronaric (right) flow waves with $f = 1\,Hz$ imposed in Ω_1

2) *Medium/Large vessels.* Medium and large vessels are represented by a value of radius $R_2 > 0.12$ cm in the Womersley number range (see [41, 75, 6, 77]):

$$2.70 \leq W \leq 15.$$

In this case, we found that an appropriate parametric representation of (3.4) is:

$$\widetilde{V} = g_2(V_M, W) = \frac{1}{2} V_M b_2 \arctan(a_2 W), \tag{3.6}$$

being a_2 and b_2 the parameters again. In order to fit them, we used the flow rates in Figure 3.5, representing the flux in the *iliac* and in the *aortic* artery respectively (see [44]).

For each of the considered situations (small and medium/large vessels), parameters can be fitted if several numerical estimates of data in the form $(\widetilde{V}, V_M, W)$ are available. Since we aim at setting up a computational protocol similar to the clinical one, in which V_M is the maximum velocity in space and in time, we focus our attention on the peak velocity instant (see Figure 3.6). Data for the fitting are taken at that instant.

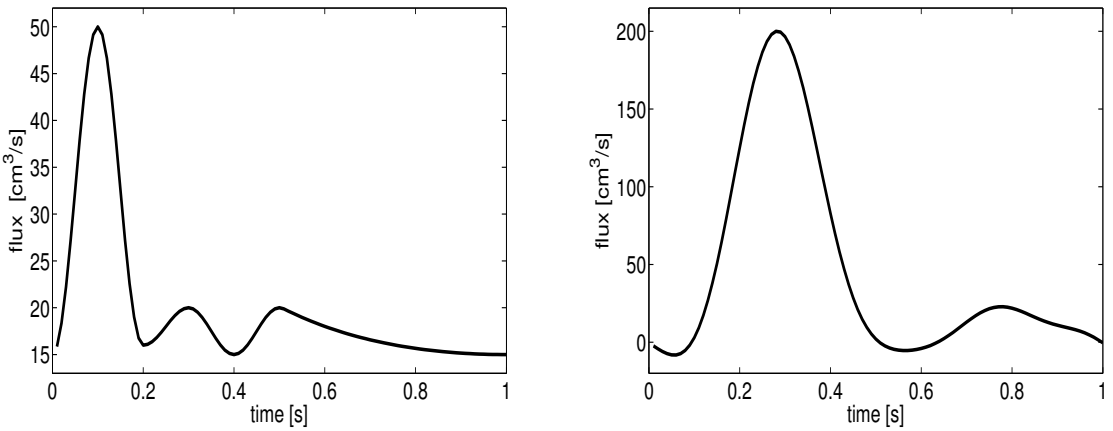

Figure 3.5: Iliac (left) and aortic (right) flow waves with $f = 1\,Hz$ imposed in Ω_2

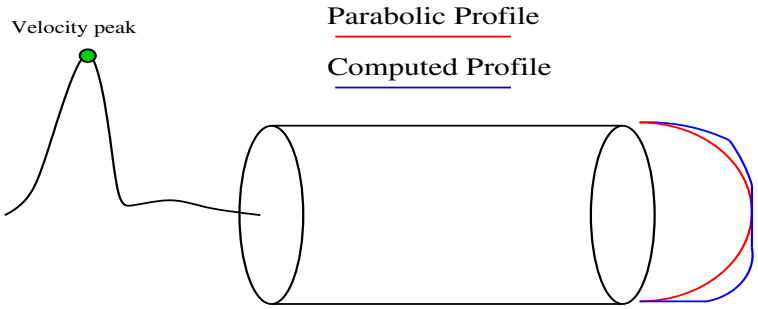

Figure 3.6: Overall vision of the computational protocol: at the peak instant the comparison between the parabolic profile and the computed is done in order to evaluate and correct the flux estimation.

We solved the Navier Stokes equations in a computational domain like the one showed in Figure 3.3 (using $R_1 = 0.06, 0.12$ cm and $R_2 = 0.24, 0.4, 0.5, 0.7$ cm) for a total of 182 simulations in the range of W illustrated in Figure 3.7. In particular, we impose a *no-slip* condition on the physical wall Σ (i.e. $\boldsymbol{u}|_\Sigma = \mathbf{0}$), corresponding to the assumption of rigid walls, and null normal stress on the outlet Γ_{out}. At the inlet, we would like to prescribe the flow rate (3.1) specified by the waveforms reported in Figures 3.4 and 3.5. In the context of the present work, the prescription of a velocity profile would be equivalent to select *a priori* for each value of W a functional relation like (3.4) and this would reduce the significance of numerical simulations and definitely the accuracy of (3.4) in recovering the flow rate from the maximum velocity. Therefore, we resort to scheme I for the numerical resolution (see Section 2.5.3). The potential bias in using numerical simulations specifying the velocity profile can be therefore avoided. Simulation

parameters (viscosity and frequency) have been varied in order to perform two simulation for each imposed flow rate at each W; in particular the blood viscosity changes in the discrete set $(0.022, 0.03, 0.035, 0.04)$ Poise according to [6, 75], while the frequency in the range $(0.6, 3)$ Hz according to [77]. Once large data set made of vectors of evaluations $(\widetilde{V}, V_M, W)$ for the prescribed Q are available from numerical simulations, parameters in (3.5), (3.6) are obtained by means of a non-linear least-square fitting optimization. In particular, we have used the Least Squares module present in the package Scientific-Python. We do not dwell here with further mathematical details. The interested reader is referred to [34].

More data can be included in tuning parameters in (3.4) and more accurate will be the estimates obtained. In particular, this means that if we restrict the range of validity of (3.4) to specific situations and perform specific parametric fittings, we will obtain a set of equations very accurate for the situations they are devised for. The two formulae (3.5) and (3.6) will be therefore very accurate in the appropriate range of Womersley numbers. In principle, more accuracy could be achieved by furtherly specializing the validity of each formula. For instance, by separating the fitting for small arteries and coronaries, two set of parameters would be obtained for equation (3.5), each of them seemingly very accurate for the case of small arteries and coronaries respectively. The drawback is however that, in practice, it could be difficult to manage three, four (or even more) different equations for estimating the flow rate. A unique formula will be less accurate but easier to use in the clinical practice. For this reason, after considering the two cases presented above seprately, we devised a unique formula spanning the whole range of physiological Womersley numbers. The set up of a unique formula can be achieved in different ways. Here we simply decided to introduce a suitable weighted linear combination of the two functions $g_1(V_M, W)$ and $g_2(V_M, W)$. More precisely, in presenting the two cases considered we introduced an overlapping subdivision of the range of Womersley numbers (see Figure 3.7). Hereafter, we will say that a function g_i $(i = 1, 2)$ is "active" on an interval of this subdivision, if it has been set up in a Womersley numbers range including that interval. We have therefore the following subdivision:

Interval 1 For $W < 2.70$ the only active function is g_1;

Interval 2 For $2.70 \leq W < 3.1$ the active functions are both g_1 and g_2;

Interval 3 For $3.1 < W \leq 15$ only g_2 is active.

A unified function g can be therefore obtained by forcing g to be equal to the only active function in the Intervals 1, 3 and to a linear convex combination of

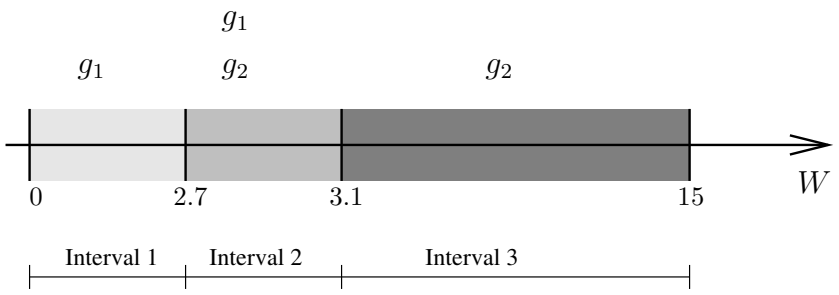

Figure 3.7: Subdivision of the whole range of Womersley numbers into intervals with the specification of the different active g_i $(i = 1, 2)$.

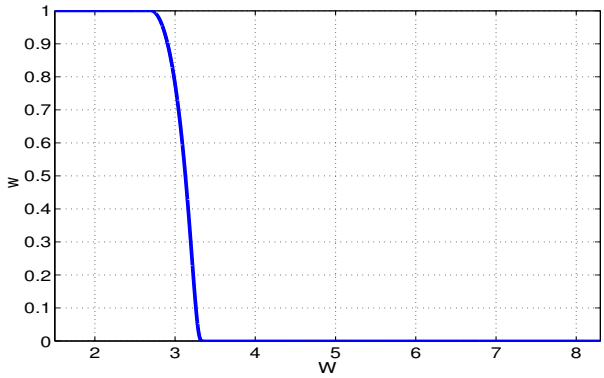

Figure 3.8: Weight function w

the two active functions on the Interval 2. This means that we set:

$$\widetilde{V} = g(V_M, W) = \begin{cases} g_1 & W \leq 2.7 \\ wg_1 + (1-w)g_2 & 2.7 < W \leq 3.1 \\ g_2 & 3.1 < W \leq 15 \end{cases} \tag{3.7}$$

The weight function $w(W)$ is represented in Figure 3.8: it is infinitely smooth function equal to 1 on the left end point of Interval 2 and 0 on the right one, given by:

$$w = e^{\frac{(W-2.7)^2}{(W-2.7)^2-(3.1-2.7)^2}}.$$

Equation (3.7) is the formula of the class (3.4) we are going to validate in the next Section.

The fitting procedure for the two cases considered leads to the following estimates of the parameters in (3.5) and (3.6):

$$\begin{cases} a_1 = 0.00417, & b_1 = 2.95272 \\ a_2 = 1.00241, & b_2 = 0.94973 \end{cases} \tag{3.8}$$

The performances of the proposed formulae have been tested in three cases. In each case, we compare the mean velocity estimated by (3.5), (3.6) or (3.7) with (3.8), starting from the maximum velocity computed with CFD, with the exact prescribed value and with the parabolic estimate (3.3).

In the first test, we referred to the same conditions used for fitting the parameters, as a consistency test of the least square approach adopted for the parameters estimation. In Figures 3.9 and 3.10 we report the relative errors on the flow rates estimated by (3.5), (3.6), (3.7) with (3.8) and by (3.3). As was to be expected in this favorable case, in which the haemodynamics conditions do actually coincide with the one used for the fitting, the improvement induced by the new formulae is relevant for all the cases considered. It is worth pointing out that the accuracy of the estimate based on (3.7) reduces in the Interval 2 (see Figure 3.7) where the two functions g_1 and g_2 are both active, in particular with respect to the corresponding estimate given by the g_i alone in the associated intervals. This is still to be expected, since for the specific case in which a function g_i has been devised it works obviously better. In fact, the unified formula in this range does not show a significant improvement with the respect to (3.3).

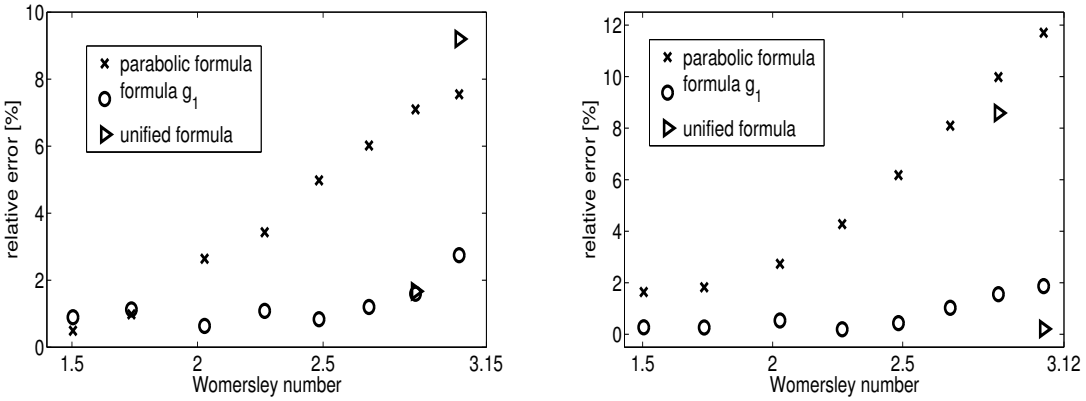

Figure 3.9: Relative errors between the estimated fluxes and the imposed ones for the geometry Ω_1 with the vertebral (left) and the coronary (right) flow waves.

In the second test cases set, we retained the same geometries used for the parameters fitting and changed the flow rate waveforms prescribed at the inlet. In particular, we compare the fluxes estimated by (3.7) with (3.8) and by (3.3) with the exact prescribed flow rate. In particular, we firstly imposed the flow wave reported in Figure 3.11, found in a proximal LITA (Left Interior Thoracic Artery) used as an aorto-coronary by-pass, at the inlet of a domain Ω_1 with radius equal to 0.12 cm (see [49]). Secondly, we imposed the physiological flow rate perfusing the *renal artery* reported in Figure 3.12, left, at the inlet of a domain Ω_2 with radius

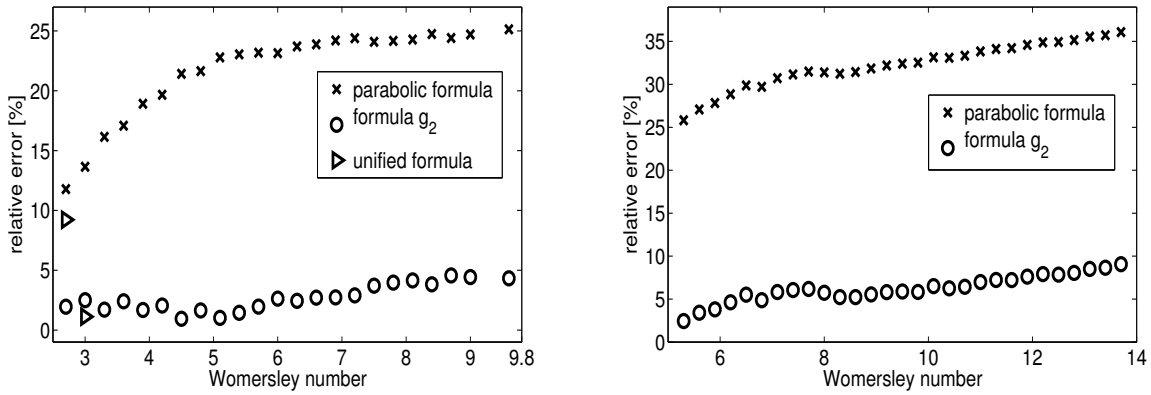

Figure 3.10: Relative errors between the estimated fluxes and the imposed ones for the geometries Ω_2 with iliac (left) and by the aortic (right) flow rate.

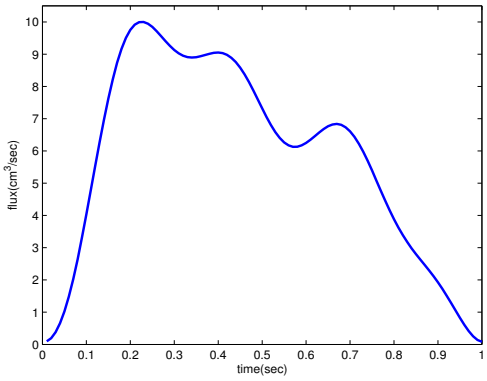

Figure 3.11: Proximal LITA inlet flow rate waveform

equal to 0.4 cm (see [41]). Then, we imposed the physiological flow rate perfusing the *brachialis artery* reported in Figure 3.12, right, at the inlet of a domain Ω_2 with radius equal to 0.24 cm (see [44]). In Table 1 we report the relative errors introduced by the two formulae in these three cases. We point out that in four of the eleven cases the Womersely number is in Interval 2, Figure 3.7, where the unified formula differs from g_1 and g_2. The improvement introduced by the new formula is still relevant.

In the last class of benchmarks, we applied (3.7) to completely different geometries and flow rate waveforms. In particular, we refer to the numerical results performed with scheme I presented in Section 2.6.2 and obtained in the realistic carotid model reported in Figure 1.3. This geometry is by far different from the cylindrical morphologies used for the parameters assessment. We prescribe the

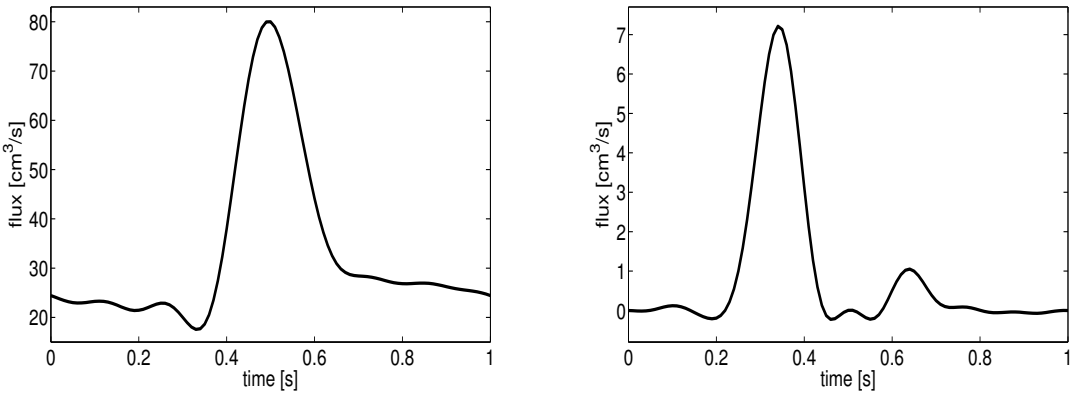

Figure 3.12: Renal and brachialis inlet flow rate waveforms

physiological flow rate shown in Figure 2.43 (left) both at the inlet and at the internal outlet of the carotid. The results in Table 2 show that the relative errors in estimating the flux from the maximum velocity using (3.7) with (3.8) are really less than the estimates based on (3.3).

The relative error associated with the prediction formula (3.7) in these validation test cases, is bounded in a very small range as a consequence of the accounting for the pulsatile nature of blood (mean = 3.73%, stdv = 2.51%, versus mean = 22.01%, stdv = 11.08% using (3.3)). Moreover, we point out that the magnitude of the error using (3.3) depends on the shape of the waveform perfusing the vessel. The same does not seem to hold for (3.7) (see Figure 3.9 and 3.10). Hence, formula (3.7) seems to be robust with respect to the shape of the flow rate.

The choice of cylindrical domain for building formula (3.7) and for testing its validity versus (3.3) has been done in order to isolate the effect of pulsatility on the velocity profile. However, we point out that this approach can be extended in order to build new formulae taking into account different (realistic) geometries. In particular, on one side, we can remove some simplifying assumptions made in order to build a formula like (3.4); for instance, simulations in curved pipes or with compliant walls could be carried out for a finer or more specific formula. Another possibility is to introduce new independent variables in the relation between the maximum and the mean velocities, beyond the Womersley number. For instance, one could account here for the possible curvature k or other morphological features, by devising a formula in the form:

$$\widetilde{V} = g(V_M, W, k, ...).$$

Other, more complicates, independent variables can be chosen in this context,

	W	Estimate based on (3.3)	Estimate based on (3.7)
Proximal LITA	1.7366	1.24%	0.86%
	2.2673	4.20%	0.28%
	2.868	9.09%	3.64%
	3.0419	9.64%	6.68%
Renal	5.3594	18.34%	4.12%
	7.5793	23.64%	4.43%
	8.8676	25.38%	3.38%
Brachialis	2.868	18.42%	9.29%
	3.0419	18.17%	1.32%
	5.3594	32.50%	11.09%
	7.5793	38.34%	15.67%

Table 3.1: Relative errors for the proximal LITA, renal and brachialis flow wave test case.

	Inlet	Outlet I	Outlet II
W	7.74	5.21	4.90
Radius (cm)	0.5	0.337	0.317
$V_{peak}\,(cm/sec)$	204.47	339.55	132.15
Imposed flux (cm^3/sec)	115.33	86.97	28.36
Relative error with parabolic formula (%)	31.27	30.56	26.69
Relative error with correction formula (%)	4.61	8.88	4.62

Table 3.2: Application of (3.7) in a numerical model of carotid bifurcation

with the constraint that they should be (easily) measurable in order to be used for a real-time estimates of the flow rate.

An extensive "in vitro" and "in vivo" validation activity is now mandatory as a necessary phase for confirming the strong improvements found here, before incorporating this formula into clinical devices.

3.3 Multiscale simulation of the cardiovascular system

Prescribed flux problems arise also in the (geometrical) multiscale modelling of the circulatory system. In fact, the cardiovascular system has a multiscale nature, since local phenomena, such as the perturbation of flow pattern in a specific

vascular region, are strictly related to the global features of the whole circulation. Nevertheless, a global 3d description of the cardiovascular system is computationally impossible. Therefore, we focus on a 3d domain of interest, embedded in a reduced model (easy to solve) of the cardiovascular system. In this way, a local, accurate, 3D description of blood flow by means of the Navier-Stokes equations in a specific artery is coupled with a systemic, 0D, lumped model of the remainder of circulation (see [16, 56, 51, 33]).

To this aim, the arterial tree is split into elementar districts. For each one of these, starting from the 3-dimensional Navier-Stokes equations in moving domains, simplified equations can be deduced for the beahviour of blood. In particular, an appropriate average over the space variables is considered. We point out that the reduced model is strictly related to the boundary conditions on the artficial sections for the original 3d problem. For example, for a vascular vessels it is a common practice to consider a compliant cylinder as elementar district (see Figure 3.13). To be more concrete, let us prescribe the velocity field at the inlet Γ_{in} and the normal stress on Γ_{out}. Therefore, let us write the Navier-Stokes equations in moving domains and let us integrate in space both in the radial and in the axial direction. We obtain the reduced model in Figure 3.14 (see [51]). We point out the analogy between the electrical and fluid-dynamics global quantities. In particular, the electrical counterpart of the flow rate and of the pressure are the current and the voltage, respectively. This reduced model is described by a system of two Ordinary Differential Equations (ODE) for the unknowns pressure P_1 and flow rate Q_2, while P_2 and Q_1 are known from the prescribed boundary conditions in the 3d original problem. Therefore, since P_1 and Q_2 are the state variables of the electric net, it is necessary for the well posedness of the ODE system that a compliance is at the interface with P_1 and an inductance at the interface with Q_2. If we start from different boundary conditions, we obtain different state variables and therefore different reduced models (see Figures 3.15-3.17).

A possible set of approximate values for amounting the electrical/geometrical

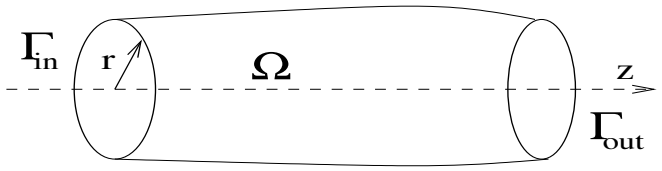

Figure 3.13: Reference cylinder Ω

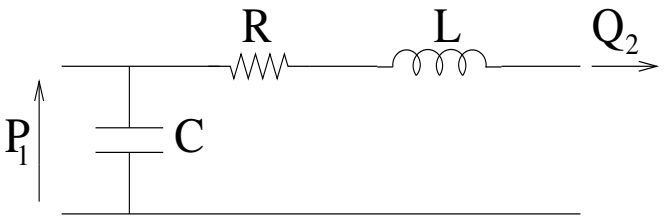

Figure 3.14: LP model of a cylinder when a Dirichlet boundary condition is prescribed on Γ_{in} and a Neumann boundary condition is prescribed on Γ_{out}

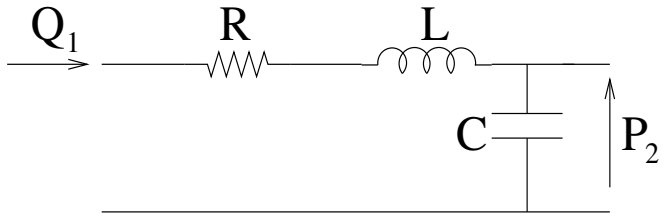

Figure 3.15: LP model of a cylinder when a Neumann boundary condition is prescribed on Γ_{in} and a Dirichlet boundary condition is prescribed on Γ_{out}

component of the four reduced model, is (see [51]):

$$\begin{cases} R = \dfrac{8\mu l}{\pi r^4} \\ L = \dfrac{\rho l}{\pi r^2} \\ C = \dfrac{2\pi r^3 (1-\sigma^2) l}{Eh}, \end{cases} \tag{3.9}$$

where l is the length of the cylinder, σ is the *Poisson ratio*, E is the *Young modulus* and h is the thickness of the external wall. Nevertheless, different authors proposed different values.

Moreover, in order to describe the heart action, in the electric/hydraulic analogy every valve beahviour is suitable modelled by a diode for the current according to the value of the applied voltage drop. Moreover, its pulsatile action is modelled with a pressure generator and the variable properties of the heart wall with an elastance changing in time (see Figure 3.18 and [30]).

Collecting the LP models of various districts and compartments, we obtain an electrical net, that, from the mathematical point of view, could be written as a system of ODE:

$$\begin{cases} \dfrac{d\boldsymbol{y}}{dt} = A(\boldsymbol{y}, t)\boldsymbol{y} + \boldsymbol{r}_H(\boldsymbol{y}, t) + \boldsymbol{c}(t) \\ \boldsymbol{y}(0) = \boldsymbol{y}_0, \end{cases} \tag{3.10}$$

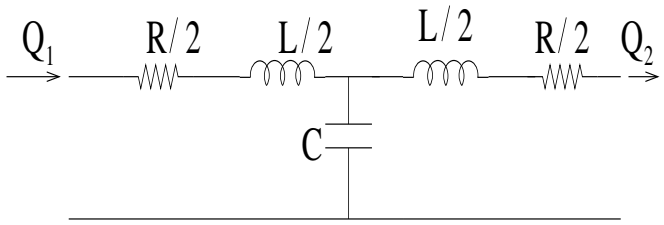

Figure 3.16: LP model of a cylinder when Neumann boundary conditions are prescribed on both the artificial sections

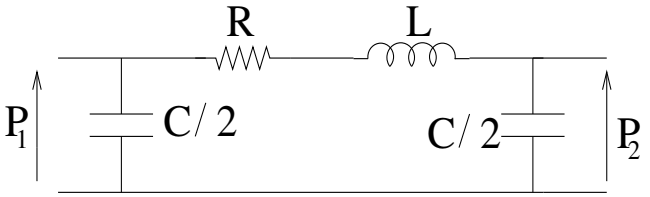

Figure 3.17: LP model of a cylinder when Dirichlet boundary conditions are prescribed on both the artificial sections

where $\boldsymbol{y}$ is the vector of the state variables, A the matrix that takes into account the relations between the state variables and the electrical components (resistances, compliances, etc), $\boldsymbol{r}_H$ and $\boldsymbol{c}(t)$ the vectors that take into account the heart action and the boundary conditions, respectively.

As pointed out, in the multiscale framework a 3d (or 2d) Navier-Stokes (NS) solver is coupled with a 0d lumped parameter (LP) model of the whole (or a part of) arterial network. From the numerical point of view, it is a common practice to resort to a domain decomposition technique, in which the 3d and the reduced models are solved alternatively and the matching conditions become boundary conditions for the two models. In particular, the LP model provides the boundary data to the NS solver and receives from the latter a forcing term. In this way, at each artificial section linked with the LP model, the 3d solver receives the flux (i.e. the current) or the mean pressure (i.e. the voltage) from the 0d model and it prescribes to the latter the mean pressure or the flux, respectively (see [16, 13]). Coupling a 3d solver with a suitable electrical net is the only way to prescribe realistic (global) boundary conditions on the artificial sections, if no data from medical measurements are available (see [33]). For a mathematical analysis of the 3d-0d coupling see [56].

In the sequel we present the numerical results of two multiscale simulations

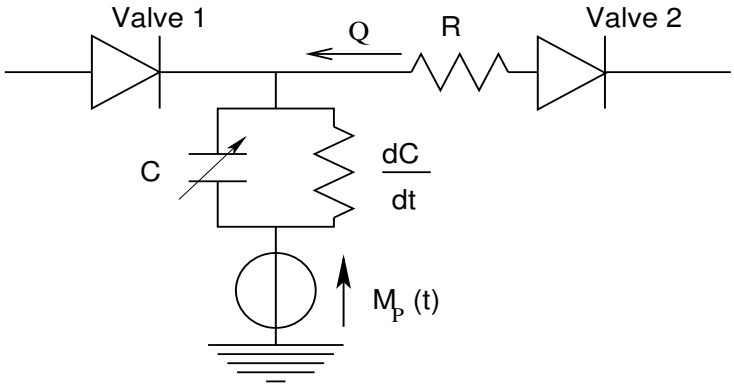

Figure 3.18: LP model of heart

involving flow rate boundary conditions for the 3d solver.

The scheme shown in Figure 3.19 represents a simplified circulatory system, where the pressure generator describes the action of the heart. The boxed part is solved by a NS axi-symmetric solver (LifeII). In this scheme, the LP model computes the flow rate to be assigned as boundary condition at the inlet of the NS solver and the latter prescribes the computed pressure drop to the net. As a validation, we solve a case in which the heart pumps a periodic pressure both in the multiscale framework (with both the treatment of the viscous term, see Section 2.2) and in the complete LP model, where the NS model is replaced by its LP analogous thanks to (3.9), featuring $C = 0$ since we are considering rigid wall (see Fig. 3.19). We observe that from the viewpoint of systemic simulations the results are in good agreement (see Table in Figure 3.19), having the possibility in the multiscale framework of detailing the local blood flow features with the 3D model (see [70]). In particular, the results seem to be slightly better for the Curl-curl formulation.

In the second simulation we consider a more realistic representation of the cardiovascular system, taken from [11] and shown in Figure 3.21. This lumped network includes the two ventricles, the systemic tree and the lungs and it is coupled with a 3d model of a part of the discending aortic compartment. In particular, the lumped parameters $R_5, C_4, R_6, L_3, C_5, L_4, R_7, C_6$ and R_8 are related to the pulmonary tree, S_1, S_2, S_3 and S_4 represent the aortic, tricuspid, pulmonary and mitral valves, respectively. Moreover, a pressure source is related to both the ventricles:

$$\begin{cases} U_L(t) = U_{L0}A(t) \\ U_R(t) = U_{R0}A(t) \end{cases}$$

where U_{L0} and U_{R0} are suitable constants and $A(t)$ is the periodic activation

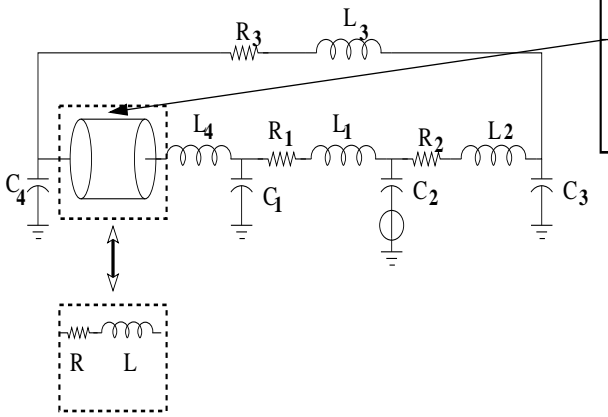

	Multiscale (grad)	Multiscale (curl)	LP
Flux	0.0570	0.0569	0.0593
Pressure	0.1274	0.1234	0.1246

Figure 3.19: Simplify electrical net modelling the cardiovascular system. In the dotted boxes the geometry for the NS solver (up) and its analogous in term of LP model (down). In the table, the maximum values of flux and pressures in the three cases.

function shown in Figure 3.20. The elastances related to each ventricles are defined as

$$\begin{cases} E_L(t) = E_{LD} + E_{LS}A(t) \\ E_R(t) = E_{RD} + E_{RS}A(t) \end{cases}$$

with E_{LD}, E_{LS}, E_{RD} and E_{RS} suitable constants. The other lumped parameters correspond to the systemic part of the cardiovascular system.

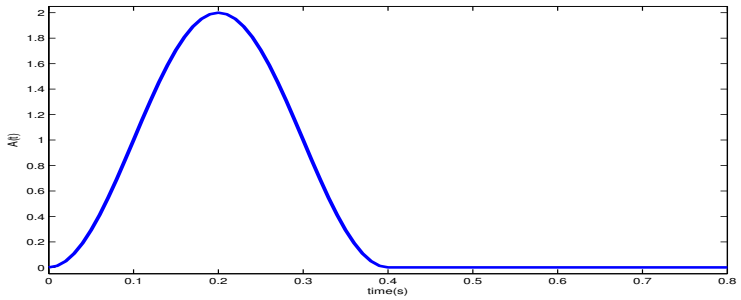

Figure 3.20: Activation function $A(t)$.

As in the previous multiscale simulation, the LP model computes the flow rate to be assigned as boundary condition at the inlet of the NS solver (LifeV) and the latter prescribes the computed pressure drop to the net. Figures 3.22 show a

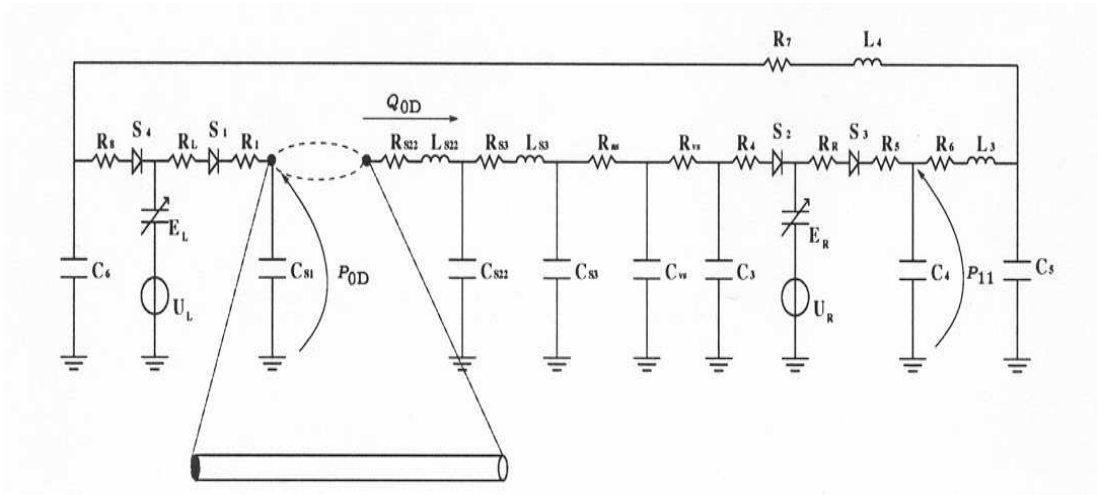

Figure 3.21: Electrical net modelling the cardiovascular system

comparision between the pressure in correspondance of the compliance C_{s1} (left, indicated in Figure 3.21 as P_{0D}) and of the vascular vessel (right) computed in the multiscale framework, with the ones obtained in a whole 0d simulations. We point

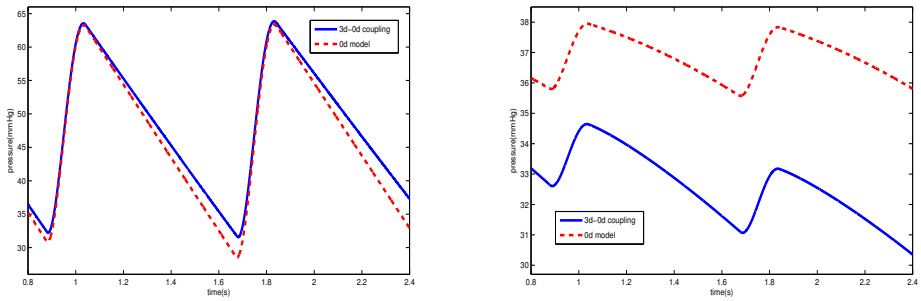

Figure 3.22: Comparision between the numerical results obtained in the multiscale and in the 0d simulations. Pressure in correspondance of the compliance C_{s1} (left) and of the vascular vessel (right).

out that the numerical results are in good agreement in the case of the pressure in correspondance of the compliance C_{s1}. On the contrary, the results concerning the pressure in correspondance of the vascular vessel are quite different. This means that, in order to obtain matching numerical results, the parameters of the electrical net need to be calibrated in more suitable way. This is a possible future work starting from the present one.

3.4 Fluid-structure interaction problem

In this section we remove the hypothesis of rigidity of the wall of the vascular vessel. In particular, we consider the problem of prescribing the flow rate in a 2d compliant domain, where the blood dynamics is described by coupling the Navier-Stokes equations with a model for the structure. The vascular wall has a very complex nature and devising an accurate model for its mechanical behaviour is quite difficult. Its structure is indeed formed by many layers with different mechanical characteristics (see e.g. [22]). Some simplifying hypotheses are therefore mandatory. In particular, arterial tissue is quite often assumed to be homogeneous. Moreover, since the displacements could often be considered small, we assume that its beahviour can be described in terms of linear elasticity (see [17]). In particular, in this context, we consider an algebraic one-dimensional law. Regarding the fluid problem, we can not use an *Eulerian* approach, as done in the previous cases. In fact, referring to Figure 3.23, since *no slip* conditions

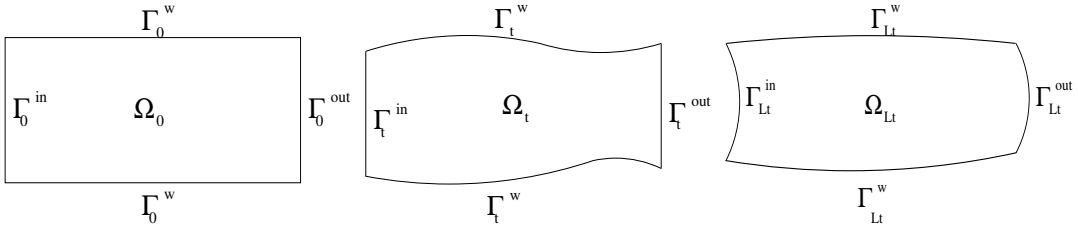

Figure 3.23: Reference (left), ALE (center) and Lagrangian (right) fluid domain.

are prescribed on the physical boundary Γ_t^w, we would like to use Lagrangian coordinates near the wall. In this way the velocity of the fluid and of the structure are equal on Γ_t^w. However, a fully Lagrangian approach is not suitable, since we would like that, far from the wall, the points of the fluid domain do not move, so that the domain does not warp (see Figure 3.23, right). In order to merge these requirements, we resort to the *Arbitrary Lagrangian Eulerian* (ALE) approach (see [42, 17]), that we are going to introduce briefly. The idea is based on moving the points of the fluid domain in an arbitrary way, with the constraint that the points on Γ_t^w move with the structure and the points on Γ_t^{in} and Γ_t^{out} do not move in the normal direction. This can be done, for instance, by solving a Laplace equation (*harmonic extension*):

$$\begin{cases} -\triangle \boldsymbol{w} = \boldsymbol{0} \qquad \text{in} \quad \Omega_t \\ \boldsymbol{w}|_{\Gamma_t^w} = \dfrac{\partial \boldsymbol{\eta}}{\partial t} \\ (\boldsymbol{w} \cdot \boldsymbol{n})|_{\Gamma_0^{in} \cup \Gamma_t^{out}} = 0 \\ (\nabla \boldsymbol{w}\ \boldsymbol{\tau})|_{\Gamma_0^{in} \cup \Gamma_t^{out}} = \boldsymbol{0}, \end{cases} \tag{3.11}$$

being $\boldsymbol{w}$ the velocity of the points of the domain and $\boldsymbol{\eta}$ the structure displacement. The problem given by (3.11) allows one to build the domain Ω_t, for all $t > 0$ (Figure 3.23, center) and, at the discrete level, it allows to map the initial mesh onto the current configuration. Similarly to the Lagrangian case, the *ALE time derivative* of a scalar quantity f is given by

$$\frac{D^A f}{Dt} = \frac{\partial f}{\partial t} + \boldsymbol{w} \cdot \boldsymbol{\nabla} f.$$

It is now possible to write the Navier-Stokes equations in Ω_t in ALE coordinates (see [42]):

$$\begin{cases} \dfrac{D^A \boldsymbol{u}}{Dt} - \nabla \cdot \sigma + [(\boldsymbol{u} - \boldsymbol{w}) \cdot \nabla]\boldsymbol{u} = \boldsymbol{0} \quad \text{in} \quad \Omega_t \\ \nabla \cdot \boldsymbol{u} = 0 \quad \text{in} \quad \Omega_t. \end{cases} \tag{3.12}$$

where

$$\sigma = \mu(\nabla \boldsymbol{u} + (\nabla \boldsymbol{u})^t) - pI$$

is the Cauchy stress tensor and where I the 3×3 identity tensor. We point out that for $\boldsymbol{w} \simeq \boldsymbol{0}$, i.e. far from the wall, we recover the Eulerian formulation, while for $\boldsymbol{w} = \boldsymbol{u}$, i.e. on the wall, we get the Lagrangian formulation. Problem given by (3.12) has to be completed with suitable initial and boundary conditions:

$$\begin{cases} \boldsymbol{u}|_{t=0} = \boldsymbol{u}_0(\boldsymbol{x}) \\ \boldsymbol{u}|_{\Gamma_t^w} = \dfrac{\partial \boldsymbol{\eta}}{\partial t} \\ \displaystyle\int_{\Gamma_t^{in}} \boldsymbol{u} \cdot \boldsymbol{n} \, d\gamma = Q \\ (\sigma \boldsymbol{n})|_{\Gamma_t^{out}} = \boldsymbol{h}, \end{cases} \tag{3.13}$$

where $\boldsymbol{h}$ is a suitable outflow condition.

Concerning the structure model, for the sake of simplicity, we consider the one-dimensional algebraic law

$$\beta \boldsymbol{\eta} = -(\sigma \boldsymbol{n})|_{\Gamma_t^w} = (p\boldsymbol{n} - \mu(\nabla \boldsymbol{u} + (\nabla \boldsymbol{u})^t)\boldsymbol{n})|_{\Gamma_t^w}, \tag{3.14}$$

with β a parameter depending on the elasticity property of the vascular vessel.

The non-linear fluid-structure interaction problem is given by (3.11), (3.12), (3.13) and (3.14). At the discrete level, it is usually solved in an iterative framework, where the fluid and the structure equations are solved separately (see e.g. [42, 12] and references therein). We point out that $(3.13)_2$ and (3.14) are the matching conditions at the fluid-structure interface. In particular, the structure prescribes the velocity as Dirichlet boundary condition to the fluid and the latter gives the stress at the interface as forcing term to the structure. Let us notice

that in this context we utilize the "complete" formulation of the viscous term, so that the forcing term passed to the structure is the physical stress (3.14).

Here, we propose an alternative strategy that does not need to subiterate (see [43]). In the sequel, we present this new approach for the augmented flow rate problem, but we observe that it can be applied to standard boundary value problems as well. In particular, let us write $(3.13)_2$ and (3.14) after time discretization (see Section 2.5.1):

$$\begin{cases} \beta \boldsymbol{\eta}^{n+1} = -(\sigma^{n+1}\boldsymbol{n})|_{\Gamma_t^w} \\ \boldsymbol{u}^{n+1}|_{\Gamma_t^w} = \dfrac{\boldsymbol{\eta}^{n+1} - \boldsymbol{\eta}^n}{\Delta t} \end{cases} \tag{3.15}$$

We point out the use of an implicit Euler formula in (3.15). Combining these two relations, we obtain:

$$(\sigma^{n+1}\boldsymbol{n})|_{\Gamma_t^w} = -\beta(\Delta t \boldsymbol{u}^{n+1}|_{\Gamma_t^w} + \boldsymbol{\eta}^n). \tag{3.16}$$

Let us set

$$\boldsymbol{V}_t = \boldsymbol{H}^1(\Omega_t).$$

Therefore, writing the augmented variational formulation of problem given by (3.12) and (3.13) (see Chapter 2), we obtain, for all $\boldsymbol{v} \in \boldsymbol{V}_t$:

$$\frac{1}{\Delta t}(\boldsymbol{u}^{n+1}, \boldsymbol{v}) + (\sigma^{n+1}, \nabla \boldsymbol{v}) + (((\boldsymbol{u}^{n+1} - \boldsymbol{w}^{n+1}) \cdot \nabla)\boldsymbol{u}^{n+1}, \boldsymbol{v}) + \lambda^{n+1} \int_{\Gamma_t^{in}} \boldsymbol{v} \cdot \boldsymbol{n}\, d\gamma =$$

$$= \int_{\partial\Omega} (\sigma^{n+1}\boldsymbol{n}) \cdot \boldsymbol{v}\, d\gamma - \int_{\Gamma_t^{out}} \boldsymbol{h}^{n+1} \cdot \boldsymbol{v}\, d\gamma + \frac{1}{\Delta t}(\boldsymbol{u}^n, \boldsymbol{v}).$$

Using (3.15) and introducing the notation (1.7), we have

$$\frac{1}{\Delta t}(\boldsymbol{u}^{n+1}, \boldsymbol{v}) + a_C(\boldsymbol{u}^{n+1}, \boldsymbol{v}) + (((\boldsymbol{u}^{n+1} - \boldsymbol{w}^{n+1}) \cdot \nabla)\boldsymbol{u}^{n+1}, \boldsymbol{v}) +$$

$$+ b(p^{n+1}, \boldsymbol{v}) + \lambda^{n+1} \int_{\Gamma_t^{in}} \boldsymbol{v} \cdot \boldsymbol{n}\, d\gamma = -\int_{\Gamma_t^w} \beta(\Delta t \boldsymbol{u}^{n+1} + \boldsymbol{\eta}^n) \cdot \boldsymbol{v}\, d\gamma +$$

$$- \int_{\Gamma_t^{out}} \boldsymbol{h}^{n+1} \cdot \boldsymbol{v}\, d\gamma + \frac{1}{\Delta t}(\boldsymbol{u}^n, \boldsymbol{v}).$$

Therefore, setting

$$\begin{cases} \boldsymbol{W}_t = \{\boldsymbol{v} \in \boldsymbol{H}^1(\Omega_t) : \boldsymbol{v}|_{\Gamma_t^w} = \boldsymbol{0} \text{ and } (\boldsymbol{v} \cdot \boldsymbol{n})|_{\Gamma_t^{in} \cup \Gamma_t^{out}} = 0\} \\ Q_t = L^2(\Omega_t) \end{cases}$$

we obtain the following problem:

Problem 21 *Solve, for each n:*

$$1) \quad (\nabla \boldsymbol{w}^{n+1}, \nabla \boldsymbol{s}) = -(\boldsymbol{R}_g^{n+1}, \boldsymbol{s}) \quad \forall \boldsymbol{s} \in \boldsymbol{W}_t$$

$$\begin{cases} 2) \quad \Big(\dfrac{\boldsymbol{u}^{n+1}}{\Delta t}, \boldsymbol{v}\Big) + \displaystyle\int_{\Gamma_t^w} \beta \Delta t \boldsymbol{u}^{n+1} \cdot \boldsymbol{v}\, d\gamma + a_C(\boldsymbol{u}^{n+1}, \boldsymbol{v}) + \\ \qquad + (((\boldsymbol{u}^{n+1} - \boldsymbol{w}^{n+1}) \cdot \nabla)\boldsymbol{u}^{n+1}, \boldsymbol{v}) + b(p^{n+1}, \boldsymbol{v}) + \lambda^{n+1} \displaystyle\int_{\Gamma_t^{in}} \boldsymbol{v} \cdot \boldsymbol{n}\, d\gamma = \\ \qquad\qquad = -\displaystyle\int_{\Gamma_t^w} \beta \boldsymbol{\eta}^n \cdot \boldsymbol{v}\, d\gamma - \displaystyle\int_{\Gamma_t^{out}} \boldsymbol{h}^{n+1} \cdot \boldsymbol{v}\, d\gamma + \Big(\dfrac{\boldsymbol{u}^n}{\Delta t}, \boldsymbol{v}\Big) \quad \forall \boldsymbol{v} \in \boldsymbol{V}_t \\ b(q, \boldsymbol{u}^{n+1}) = 0 \quad \forall q \in Q_t \\ \displaystyle\int_{\Gamma_t^w} \boldsymbol{u}^{n+1} \cdot \boldsymbol{n}\, d\gamma = Q^{n+1} \end{cases}$$

where $\boldsymbol{R}_g^{n+1}$ is a $\boldsymbol{H}^1(\Omega_t)$ function such that $\boldsymbol{R}_g^{n+1}|_{\Gamma_t^w} = \boldsymbol{u}^n|_{\Gamma_t^w}$. Then $\boldsymbol{\eta}^n$ is updated thanks to $(3.15)_2$. Observe that, with this strategy, the coupling resorts to a *Robin* condition for the fluid problem.

One of the most relevant issues in solving a fluid-structure interaction coupling is due to the outlet boundary condition. In fact, an arbitrary stress prescribed at the outlet could produce some *non-physical* reflections of the waves propagating in the vessel (see e.g. [42, 15]). In order to avoid this phenomenon, it is possible to prescribe a suitable *absorbing* stress condition. A possibility is to couple the 3d model with a 1d reduced model related to a compliant vessel (multiscale approach). In this case, the reduced model could act as a suitable, non-reflecting boundary condition (see e.g. [42, 15]). Here we propose to use the 1d model in another way. In particular, referring to the compliant cylinder in Figure 3.13, whose length is L, a simplified 1d model can be obtained integrating at each time t the Navier-Stokes equations over each section S normal to the axis z of the cylinder. The 1d model reads, for each $t > 0$ and $0 < z < L$, (see [15, 16]):

$$\begin{cases} \dfrac{\partial A}{\partial t} + \dfrac{\partial Q}{\partial z} = 0 \\ \dfrac{\partial Q}{\partial t} + \dfrac{\partial}{\partial z}\Big(\alpha \dfrac{Q^2}{A}\Big) + A\dfrac{\partial \widetilde{p}}{\partial z} + K_R \dfrac{Q}{A} = 0 \end{cases} \tag{3.17}$$

where Q is the flow rate through S, A is the area of S, $\widetilde{p}$ the mean pressure over S, the constant K_R is a resistance parameter which accounts for fluid viscosity, while α is definied as

$$\alpha = A\Big(\int_S u_z^2\, d\gamma\Big)\Big(\int_S u_z\, d\gamma\Big)^{-2}$$

and accounts for the velocity profile over S. For example if $\alpha = 1$ we are assuming a flat velocity profile. System (3.17) is a system of two equations in three

unknowns $(\widetilde{p}, Q, A)$. For its closure, a third equation is provided by a suitable wall model relating the radial displacement (and therefore the area A) to the mean pressure $\widetilde{p}$. In particular, here we consider a simple algebraic relation (see [19]):

$$\widetilde{p} = \beta(\sqrt{A} - \sqrt{A_0}) \tag{3.18}$$

where A_0 is the area of the surface S at $t = 0$. Observe that (3.18) is an algebraic law linking the pressure to the wall displacement, analogous to (3.14). Then, system (3.17) turns out to be hyperbolic and posseses two distinct eigenvalues

$$\zeta_{1,2} = \frac{Q}{A} \pm c$$

where

$$c(A) = \frac{\beta\sqrt{A}}{2}$$

The hyperbolic nature of this system allows to capture the ondulatory component of the axial propagation of the blood in a moving vessel. The corresponding eigenfunctions are the characteristic variables, given by

$$W_{1,2} = \frac{Q}{A} \pm \int_{A_0}^{A} \frac{c(\tau)}{\tau} d\tau.$$

We can reduce the reflection's phenomenon imposing that the characteristic variable coming back is zero on the outflow section (see [42, 43] for more details). In particular, we obtain the following *absorbing boundary condition*:

$$\boldsymbol{h}^{n+1} = \Big[\Big(\sqrt{\frac{1}{2}}\frac{\int_{\Omega_t} \boldsymbol{u}^n \cdot \boldsymbol{n}\, d\gamma}{2A^n_{out}} + \sqrt{\beta\sqrt{A_{out,0}}}\Big)^2 - \beta\sqrt{A_{out,0}}\Big]\boldsymbol{n}, \tag{3.19}$$

where A^n_{out} and $A_{out,0}$ are the measure of Γ^{out}_t at $t = t^n$ and at the initial instant, respectively.

In the sequel we present the numerical results, obtained with *Freefem++*, concerning two test cases. We point out that in both cases, the numerical simulations highlight that Problem 21 does not need to be solved in an iterative framework. Therefore, the CPU times related to this approach seem to be very good, even if further numerical tests are mandatory.

In the first test case, we aim at validating the effect of the absorbing condition. The computational domain is a rectangle Ω_t, whose size in the reference configuration Ω_0 is $15 \times 2\, cm$. Moreover, we set $\beta = 10^5\, cm/s^2$. We impose at the inlet of Ω_t a pressure impulse

$$P = \begin{cases} 10^4\, cm^2/s^2 \quad \text{for} \quad t \leq 0.005\, s \\ 0 \quad \text{for} \quad t > 0.005\, s. \end{cases}$$

In Figure 3.24-3.27 we compare the numerical solutions obtained with (left) and without (right) prescribing the absorbing condition (3.19). We notice the relevant reflections of the solution once the wave reaches the end of the domain if a non-absorbing condition is forced. On the contrary, by imposing condition (3.19), the effect of spurious reflections is significantly damped.

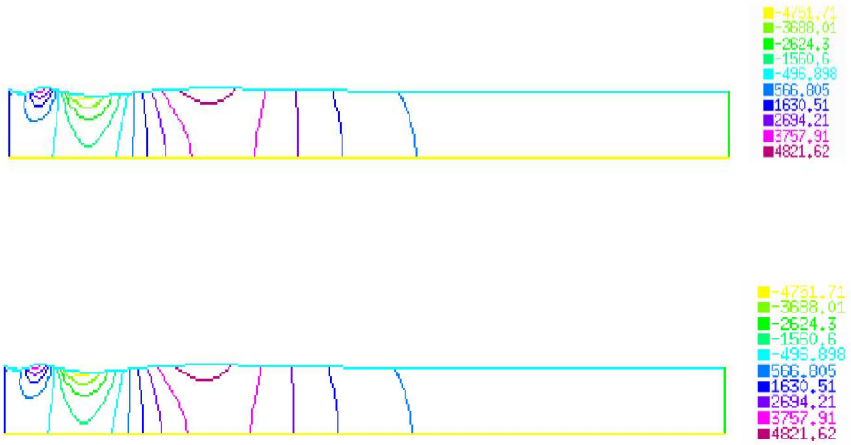

Figure 3.24: Pressure wave propagation in the half upper domain with (up) and without (bottom) prescribing an absorbing condition. Before the wave has reached the outlet of the domain there are no reflections and the two solutions coincide - $t = 0.02\,s$ - $\Delta t = 10^{-3}, h = 0.1$.

In the second test case, we impose the flow rate $Q = 1 \cdot \sin(2\pi t)\, cm^2/s$ at the inlet of Ω_t and we compare the numerical results on different sections with the Womersley solution in Ω_0. In Figures 3.28 the flow rate at different distances from the inlet of Ω_t is shown. In particular, we chose two instants of the period, such that in the rigid case the flow rates are the same. We point out that the flux is not the same on all sections in the compliant case. In particular, at $t = 1.1\,s$ (i.e. at the beginning of the cicle, when the flow rate grows up) the flux decreases moving along the domain. On the contrary, at $t = 1.4\,s$ (i.e. when the flow rate begins to decrease after the peak) the flux increases moving along the domain. This is due to the fact that the propagation of the flow rate is not instantaneous as in the rigid case. Figures 3.29-3.33 confirm that the axial velocity profile in the compliant case features a delay with respect to the Womersley solution for rigid pipes. In particular, we find a delay of $0.007s$ at distance $2\,cm$ from the inlet. Moreover, these figures highlight that the displacment of the vessel wall is negligible (about 0.2% of the radius).

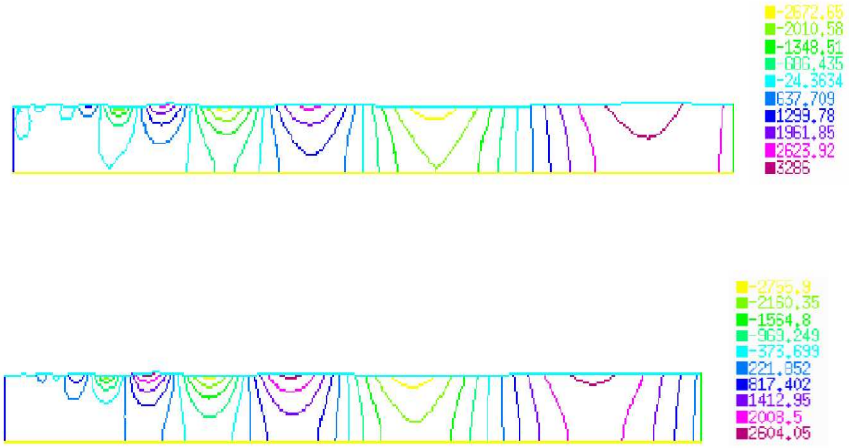

Figure 3.25: Pressure wave propagation in the half upper domain with (up) and without (bottom) prescribing an absorbing condition. - The pressure wave has reached the outlet of the domain and the reflections start - $t = 0.05\,s$ - $\Delta t = 10^{-3}, h = 0.1$.

Let us notice in Figure 3.31, left, the difference between the solutions computed at the inlet. This is due to the boundary effects obtained with the "complete" formulation of the viscous term. This phenomenon is due to the fact that the natural boundary conditions associated to (1.7) implicitely prescribe a non-null tangential velocity at the inlet and at the outlet (see [68] and Chapter 4 for more details). In Figure 3.34 we compare the solutions obtained in a compliant and in a rigid domain using (1.7) with the solution in a rigid domain using the "laplacian" viscous term $-\mu\triangle\boldsymbol{u}$, in particular using (1.6). Observe that the differences between the rigid and the compliant solutions at the inlet are mainly due to the different formulations of the viscous term.

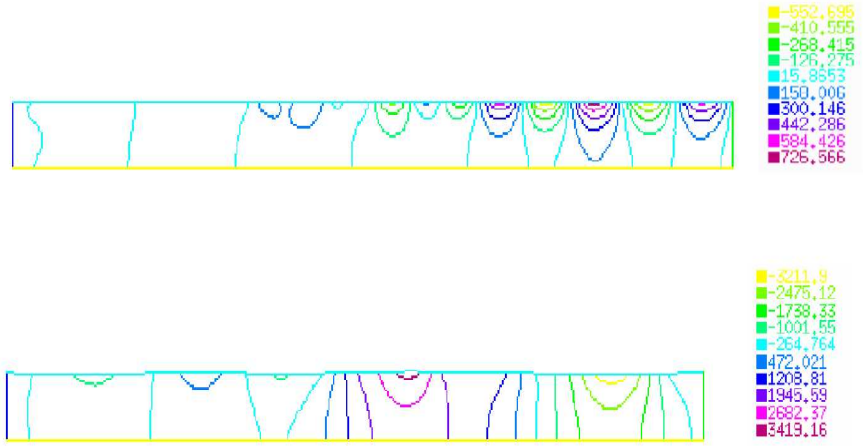

Figure 3.26: Pressure wave propagation in the half upper domain with (up) and without (bottom) prescribing an absorbing condition. - $t = 0.20\,s$ - $\Delta t = 10^{-3}, h = 0.1$.

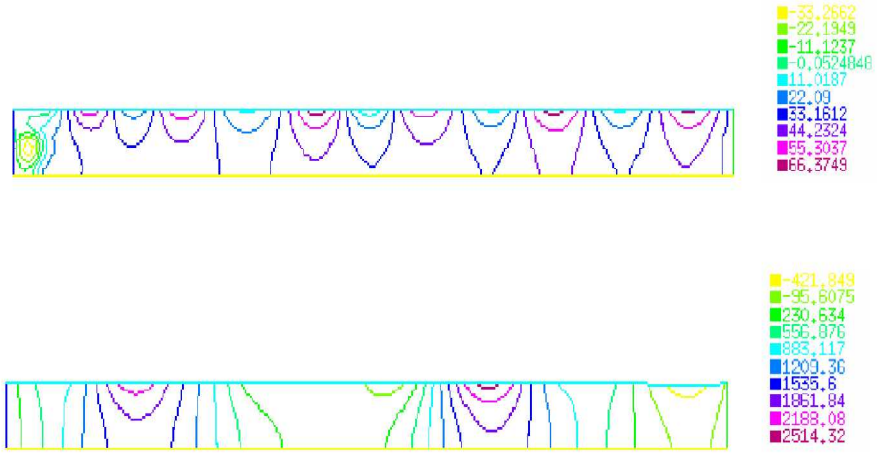

Figure 3.27: Pressure wave propagation in the half upper domain with (up) and without (bottom) prescribing an absorbing condition. - $t = 0.50\,s$ - $\Delta t = 10^{-3}, h = 0.1$.

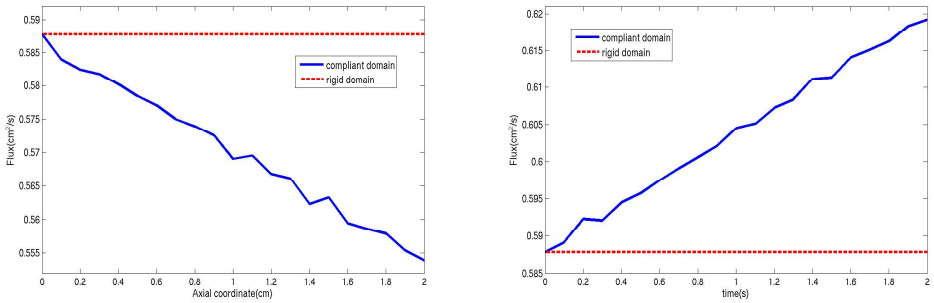

Figure 3.28: Flow rate at different sections of Ω_t - $t = 1.1\,s$ (left) and $t = 1.4\,s$ (right). We point out that the flow rate is the same at these two instants in the rigid case.

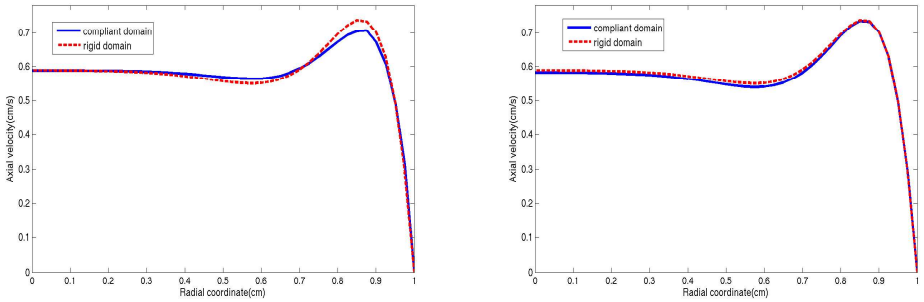

Figure 3.29: Sinusoidal flow rate: axial velocity on a radius - distance from the inlet: $0.0\,cm$ (left) and $0.4\,cm$ (right) - $t = 1.1\,s$ - $\Delta t = 10^{-3}, h = 0.025$.

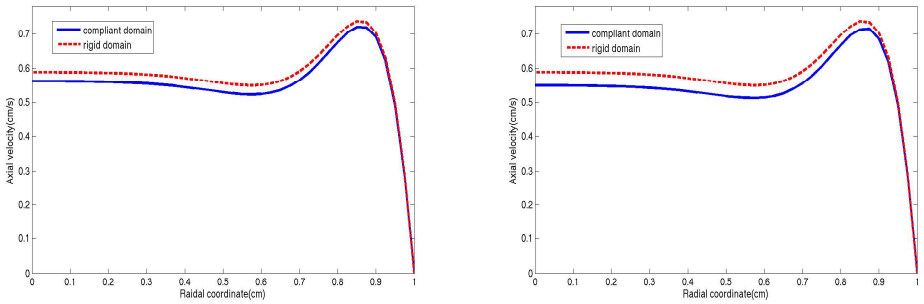

Figure 3.30: Sinusoidal flow rate: axial velocity on a radius - distance from the inlet: $1.4\,cm$ (left) and $2.0\,cm$ (right) - $t = 1.1\,s$ - $\Delta t = 10^{-3}, h = 0.025$.

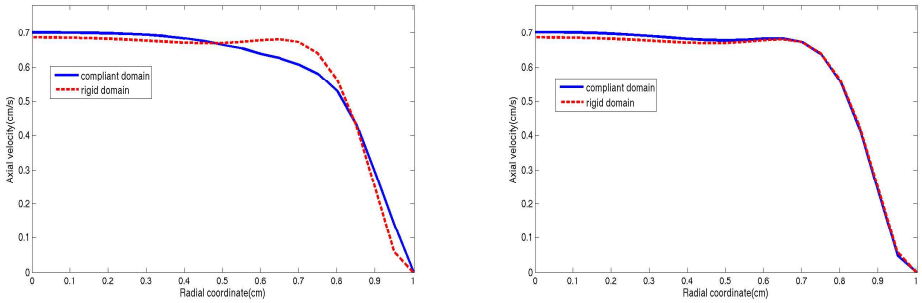

Figure 3.31: Sinusoidal flow rate: axial velocity on a radius - distance from the inlet: $0.0\,cm$ (left) and $0.4\,cm$ (right) - $t = 1.4\,s$ - $\Delta t = 10^{-3}, h = 0.1$.

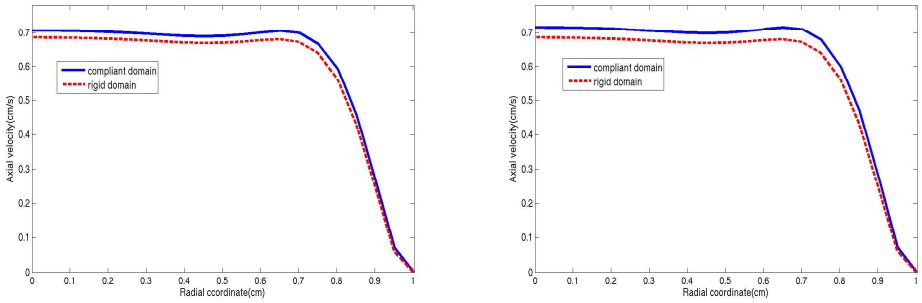

Figure 3.32: Sinusoidal flow rate: axial velocity on a radius - distance from the inlet: $1.4\,cm$ (left) and $2.0\,cm$ (right) - $t = 1.4\,s$ - $\Delta t = 10^{-3}, h = 0.1$.

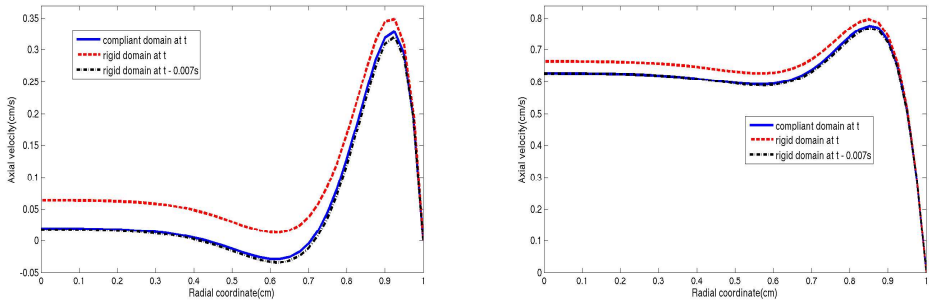

Figure 3.33: Sinusoidal flow rate: axial velocity on a radius - comparision between the compliant and the rigid case at the current instant t with the Womersley solution at $t - 0.007s$ - distance from the inlet: $2.0\,cm$ - $t = 1.015\,s$ (left), $t = 1.113\,s$ (right) - $\Delta t = 10^{-3}, h = 0.025$.

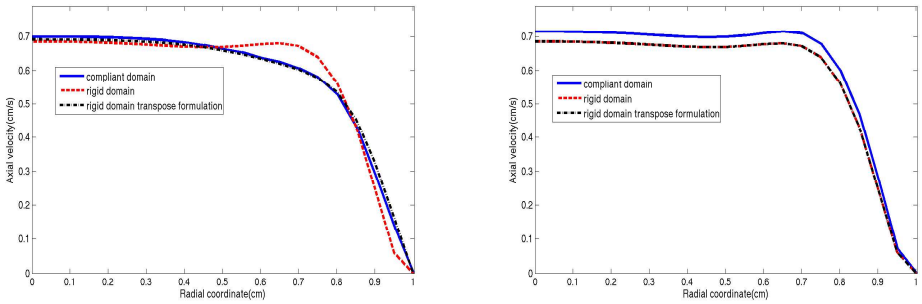

Figure 3.34: Sinusoidal flow rate imposed: axial velocity on a radius - distance from the inlet: $0.0\,cm$ (left) and $2.0\,cm$ (right) - comparision with the solution of the "complete" viscous term in the rigid case - $t = 1.4\,s$ - $\Delta t = 10^{-3}, h = 0.1$.

Chapter 4

A "Dual" Approach based on the Control Theory

4.1 Introduction

In this chapter we present a new approach for managing the defective boundary problems that will be presented in [20]. In particular, it is based on the *control theory* (see e.g. [2, 37, 1]) and can be considered as the "dual" of the augmented formulation presented in Chapter 2. In fact, both these strategies resort to a Lagrange multipliers approach. In particular, in the augmented formulation the flux conditions are treated as constraints for the Navier-Stokes equations. Conversely, with the new approach, the Navier-Stokes equations are considered as the constraint to be forced on the defective boundary conditions, formulated on a minimization problem.

In Chapter 2, we have obtained the augmented formulation for the flow rate problem. It is worth pointing out that it is possible to find such a formulation for the mean pressure problem, as well. Nevertheless, it shows a fundamental problem. In this case the Lagrange multiplier has the physical meaning of constant normal velocity on the artificial section where the mean pressure is prescribed. This contrasts the choice of the functional spaces for which the boundary conditions force null velocity on the physical wall. On the contrary, due to the exchange of the roles between the fluid equations and the defective boundary conditions, the proposed approach can manage the mean pressure problem as well. In this sense, the new approach can be considered as a more general strategy for the implementation of the defective boundary problems.

The outline of this chapter is as follows. In Section 4.2 we give a short introduction of the control theory applied to partial differential equations. In Section 4.3 we present the flow rate problem case. In particular, we introduce

the linear steady case (Section 4.3.1), the linear unsteady case (Section 4.3.2) and the steady non-linear case (Section 4.3.3). In Section 4.4 the mean pressure problem case is treated. In particular, we present the linear steady case treating separately the "laplacian" (Section 4.4.1) and the "complete" (Section 4.4.2) formulation of the viscous term. Moreover, in Section 4.4.3 a different approach based on the flow rates as control variables is shown. In Section 4.5, we introduce some numerical algorithms for solving the proposed problem. Finally, in Section 4.6 we present some numerical results.

4.2 General settings of the control problems

The general problem we are going to consider has the form:

$$\begin{cases} \text{minimize} \quad J(w) \\ A(w(g)) = f + D(g), \end{cases} \tag{4.1}$$

where $A : W \to W'$ is an elliptic differential operator for the *state variable* w, $D : Q \to W'$ an impact operator for the *control variable* g, W and Q two Hilbert spaces and J is a *cost functional*. Observe that we highlight the dependence of the state variable w on the control variable g. In order to treat the problem given by (4.1), two approaches have been considered in the literature. The first is based on the introduction of the adjoint operators related to A and D (see [1, 37]). The second relies on the classical Lagrange multiplier framework. In this work we chose to follow the latter approach and we refer in particular to [2] for a short review. The idea is based on reformulating the optimal control problem (4.1) as a boundary value problem for stationary points of the associated first-order necessary optimality condition. Let us introduce the Lagrangian functional related to problem (4.1):

$$L(w, \lambda_w, g) = J(w, g) + < A(w, g) - D(g) - f, \lambda_w >, \tag{4.2}$$

where with $\lambda_w \in W$ we indicate the Lagrange multiplier (*adjoint variable*) related to the constraint given by $(4.1)_2$ and $< \cdot, \cdot >$ denotes the duality between W' and W. Therefore, the solution of (4.1) is among the stationary points of L and it is determinated by the system of equations

$$\nabla L(w, \lambda_w, g) = \mathbf{0}. \tag{4.3}$$

In the latter equation the derivatives are to be intended in the Frechet sense. In particular, we recall that the Frechet differential with the respect of the variable x of a functional F computed in y is $dF_x(y) \in W'$, such that:

$$F(y + h) - F(y) = dF_x(y)\, h + o(\|h\|_W), \quad \forall h \in W,$$

where a quantity $R(h) \in \mathbb{R}$ is $o(\|h\|_W)$ if

$$\lim_{h \to 0} \frac{|R(h)|}{\|h\|_W} = 0.$$

Observe that the differential of F with respect to x computed in y ($dF_x(y)$) is an element of the dual of W. Therefore it can be evaluated in a function $w \in W$, obtaining $dF_x(y)\, w \in \mathbb{R}$. In particular, in searching a stationary point of L using (4.3), we evaluate the differentials on a set of test functions. Then the fulfillment of (4.3) is written in the form:

$$\begin{cases} < dL_w, v >=< dL_w(w), v >= 0, \quad \forall v \in W \\ < dL_{\lambda_w}, v >=< dL_{\lambda_w}(\lambda_w), v >= 0, \quad \forall v \in W \\ < dL_g, q >=< dL_g(g), q >= 0, \quad \forall q \in Q \end{cases} \tag{4.4}$$

In the sequel, as in (4.4), for the sake of simplicity we omit to specify where the differential is computed, when it is clear from the context. Problem (4.1) can be reformulated as a system of three boundary value problems.

4.3 Flow rate boundary problems

Referring to Figure 4.1, we recall that the flow rate boundary problem for an incompressible Newtonian homogeneous fluid is given by

$$\begin{cases} \dfrac{\partial \boldsymbol{u}}{\partial t} - \mu \triangle \boldsymbol{u} + (\boldsymbol{u} \cdot \nabla)\boldsymbol{u} + \nabla p = \boldsymbol{f}, \quad (t, \boldsymbol{x}) \in Y_T \\ \nabla \cdot \boldsymbol{u} = 0, \quad (t, \boldsymbol{x}) \in Y_T \end{cases} \tag{4.5}$$

together with the initial and boundary conditions:

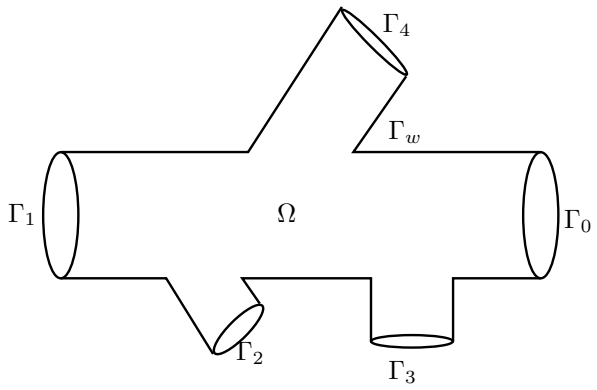

Figure 4.1: Domain Ω of interest for the defective boundary problems.

$$\begin{cases} \boldsymbol{u}|_{t=0} = \boldsymbol{u}_0(\boldsymbol{x}), \quad \boldsymbol{x} \in \Omega \\ \boldsymbol{u}|_{\Gamma_w} = \boldsymbol{0}, \quad t \in (0,T] \\ (p\boldsymbol{n} - \mu \nabla \boldsymbol{u}\ \boldsymbol{n})|_{\Gamma_0} = \boldsymbol{0}, \quad t \in (0,T] \\ \displaystyle\int_{\Gamma_i} \boldsymbol{u} \cdot \boldsymbol{n}\, d\gamma = Q_i, \quad i = 1,2,\ldots,m, \quad t \in (0,T]. \end{cases} \tag{4.6}$$

For the sake of simplicity, here and in the sequel of this Section we consider the "laplacian" treatment of the viscous term and the bilinear form

$$a_L(\boldsymbol{v}, \boldsymbol{w}) = \mu(\nabla \boldsymbol{v}, \nabla \boldsymbol{w})$$

in the variational formulation. In addition, we will first consider semplifications of problem (4.5) and (4.6). Let us start with the linear steady case, i.e. an Oseen problem.

4.3.1 Linear steady case

Let us consider the following steady Oseen problem:

$$\begin{cases} -\mu \triangle \boldsymbol{u}(k_j) + (\boldsymbol{\beta} \cdot \nabla)\boldsymbol{u}(k_j) + \nabla p(k_j) = \boldsymbol{f}, \qquad \boldsymbol{x} \in \Omega \\ \nabla \cdot \boldsymbol{u}(k_j) = 0, \qquad \boldsymbol{x} \in \Omega \\ \boldsymbol{u}(k_j)|_{\Gamma_w} = \boldsymbol{0} \\ (-p(k_j)\boldsymbol{n} + \mu \nabla \boldsymbol{u}(k_j)\, \boldsymbol{n})|_{\Gamma_0} = \boldsymbol{0}, \\ (-p(k_j)\boldsymbol{n} + \mu \nabla \boldsymbol{u}(k_j)\, \boldsymbol{n})|_{\Gamma_i} = -k_i \boldsymbol{n}, \quad i = 1,\ldots,m, \end{cases} \tag{4.7}$$

where $\boldsymbol{f} \in \boldsymbol{L}^2(\Omega)$ and $\boldsymbol{\beta} \in \boldsymbol{L}^\infty(\Omega)$ are given and $k_j \in \mathbb{R}$ are unknowns. This problem states a relation between the k_j and $(\boldsymbol{u}, p)$. The key step of our procedure is to consider the Neumann boundary values k_j as *control variables* to be set such that $\boldsymbol{u}$ fulfills the constraint:

$$\int_{\Gamma_j} \boldsymbol{u}(k_j) \cdot \boldsymbol{n}\, d\gamma = Q_j, \quad j = 1,\ldots,m. \tag{4.8}$$

To this aim we introduce the following functional:

$$J_Q(\boldsymbol{u}) = \frac{1}{2} \sum_{i=1}^{m} \Big(\int_{\Gamma_i} \boldsymbol{u} \cdot \boldsymbol{n}\, d\gamma - Q_i \Big)^2. \tag{4.9}$$

Referring to the general case shown in Section 4.2, in this case we have

$$\begin{cases} W = \boldsymbol{W}_Q = \boldsymbol{V} \times L^2(\Omega) \\ Q = \mathbb{R}^m \\ J = J_Q \\ A = A_Q : \boldsymbol{W}_Q \to (V')^2 \text{ such that} \\ \quad < A\boldsymbol{y}, \boldsymbol{v} >=< A(\boldsymbol{z}, q), \boldsymbol{v} >= a_L(\boldsymbol{z}, \boldsymbol{v}) + ((\boldsymbol{\beta} \cdot \nabla)\boldsymbol{z}, \boldsymbol{v}) + b(q, \boldsymbol{v}), \\ \qquad\qquad \forall \boldsymbol{y} = (\boldsymbol{z}, q) \in \boldsymbol{W}_Q \quad \text{and} \quad \boldsymbol{v} \in \boldsymbol{V} \\ D = D_Q : \mathbb{R}^m \to V' \text{ such that} \\ \quad < D_Q(\boldsymbol{k}), \boldsymbol{v} >= \Big(\displaystyle\int_{\Gamma_1} k_1 \boldsymbol{v} \cdot \boldsymbol{n} \, d\gamma, \ldots, \int_{\Gamma_m} k_m \boldsymbol{v} \cdot \boldsymbol{n} \, d\gamma \Big), \ \forall \boldsymbol{v} \in \boldsymbol{V} \text{ and } \boldsymbol{k} \in \mathbb{R}^m. \end{cases}$$

Following [2] and recalling (4.2), we build the associated Lagrange functional where equations (4.7) play the role of *constraints* for the functional (4.9):

$$L((\boldsymbol{u}, p), (\boldsymbol{\lambda}_u, \lambda_p), k_j) = \frac{1}{2} \sum_{i=1}^{m} \Big(\int_{\Gamma_i} \boldsymbol{u} \cdot \boldsymbol{n} \, d\gamma - Q_i \Big)^2 + a_L(\boldsymbol{u}, \boldsymbol{\lambda}_u) +$$

$$+((\boldsymbol{\beta} \cdot \nabla)\boldsymbol{u}, \boldsymbol{v}) + b(p, \boldsymbol{\lambda}_u) + \sum_{i=1}^{m} \int_{\Gamma_i} k_i \boldsymbol{\lambda}_u \cdot \boldsymbol{n} \, d\gamma - (\boldsymbol{f}, \boldsymbol{\lambda}_u) + b(\lambda_p, \boldsymbol{u}).$$

Here, $\boldsymbol{\lambda}_u$ and λ_p are the *adjoint* variables associated to $\boldsymbol{u}$ and p respecively. In order to solve this stationary point problem, we impose that in correspondance of the solution the Frechet differentials of L are null if evaluated in the test functions, so that we get the:

Problem 22 *Given $\boldsymbol{f} \in \boldsymbol{L}^2(\Omega)$, $\boldsymbol{\beta} \in \boldsymbol{L}^\infty(\Omega)$ and $\boldsymbol{Q} \in \mathbb{R}^m$, find $\boldsymbol{u}(k_j) \in \boldsymbol{V}, p(k_j) \in L^2(\Omega), \boldsymbol{\lambda}_u \in \boldsymbol{V}, \lambda_p \in L^2(\Omega)$ and $k_j \in \mathbb{R}$, $j = 1, \ldots, m$, such that, for all $\boldsymbol{v} \in \boldsymbol{V}$, $q \in L^2(\Omega)$ and $\nu \in \mathbb{R}$*

$$\begin{cases} (P) \begin{cases} < dL_{\boldsymbol{\lambda}_u}, \boldsymbol{v} >= a_L(\boldsymbol{u}(k_j), \boldsymbol{v}) + ((\boldsymbol{\beta} \cdot \nabla)\boldsymbol{u}(k_j), \boldsymbol{v}) + b(p(k_j), \boldsymbol{v}) + \\ \qquad\qquad + \displaystyle\sum_{i=1}^{m} \int_{\Gamma_i} k_i \boldsymbol{v} \cdot \boldsymbol{n} \, d\gamma - (\boldsymbol{f}, \boldsymbol{v}) = 0, \\ < dL_{\lambda_p}, q >= b(q, \boldsymbol{u}(k_j)) = 0, \end{cases} \\ (A) \begin{cases} < dL_{\boldsymbol{u}}, \boldsymbol{v} >= a_L(\boldsymbol{\lambda}_u, \boldsymbol{v}) + ((\boldsymbol{\beta} \cdot \nabla)\boldsymbol{v}, \boldsymbol{\lambda}_u) + b(\lambda_p, \boldsymbol{v}) + \\ \qquad\qquad - \displaystyle\sum_{i=1}^{m} \Big(\int_{\Gamma_i} \boldsymbol{u}(k_j) \cdot \boldsymbol{n} \, d\gamma - Q_i \Big) \int_{\Gamma_i} \boldsymbol{v} \cdot \boldsymbol{n} \, d\gamma = 0, \\ < dL_p, q >= b(q, \boldsymbol{\lambda}_u) = 0, \end{cases} \\ (C_j) \quad < dL_{k_j}, \nu >= \displaystyle\int_{\Gamma_j} \nu \boldsymbol{\lambda}_u \cdot \boldsymbol{n} \, d\gamma = 0. \end{cases}$$

From the mathematical viewpoint, this system couples a steady Oseen problem (P) with its adjoint (A) (both with standard boundary conditions on the artificial sections) and m scalar equations (*optimality conditions*, denoted by (C_j)). To solve it we need to resort to iterative techniques, as we will see in Section 4.5. It is worth noting that when the convergence of the iterative process is reached, the fulfillment of (A) and (C_j) implies $\boldsymbol{\lambda}_u = \mathbf{0}$ and $\lambda_p = 0$. This is promptly verified by selecting $\boldsymbol{v} = \boldsymbol{\lambda}_u$ and $q = \lambda_p$ in (A) and taking into account the (C_j).

We point out that the optimality conditions (C_j) are equivalent to impose that:

$$\int_{\Gamma_j} \boldsymbol{\lambda}_u \cdot \boldsymbol{n}\, d\gamma = 0, \quad j = 1, \ldots, m$$

i.e. a null flux on the artificial sections for the adjoint solution.

Observe in particular that if $\boldsymbol{\beta} = \mathbf{0}$, the coupling is between two steady Stokes problems and the strong formulation of the adjoint problem (A) reads:

$$\begin{cases} -\mu \triangle \boldsymbol{\lambda}_u + \nabla \lambda_p = \mathbf{0}, & \boldsymbol{x} \in \Omega \\ \nabla \cdot \boldsymbol{\lambda}_u = 0, & \boldsymbol{x} \in \Omega \\ \boldsymbol{\lambda}_u|_{\Gamma_w} = \mathbf{0} \\ (-\lambda_p \boldsymbol{n} + \mu \nabla \boldsymbol{\lambda}_u\, \boldsymbol{n})|_{\Gamma_0} = \mathbf{0}, \\ (-\lambda_p \boldsymbol{n} + \mu \nabla \boldsymbol{\lambda}_u\, \boldsymbol{n})|_{\Gamma_i} = \Big(\displaystyle\int_{\Gamma_i} \boldsymbol{u}(k_j) \cdot \boldsymbol{n}\, d\gamma - Q_i \Big) \boldsymbol{n}, & i = 1, \ldots, m. \end{cases}$$

4.3.2 Linear unsteady case

Let us consider now a similar framework for the following unsteady Oseen problem:

$$\begin{cases} \dfrac{\partial \boldsymbol{u}(k_j)}{\partial t} - \mu \triangle \boldsymbol{u}(k_j) + (\boldsymbol{\beta} \cdot \nabla)\boldsymbol{u}(k_j) + \nabla p(k_j) = \boldsymbol{f}, & (t, \boldsymbol{x}) \in Y_T \\ \nabla \cdot \boldsymbol{u}(k_j) = 0, & (t, \boldsymbol{x}) \in Y_T \\ \boldsymbol{u}(k_j)|_{t=0} = \boldsymbol{u}_0(\boldsymbol{x}), & \boldsymbol{x} \in \Omega \\ \boldsymbol{u}(k_j)|_{\Gamma_w} = \mathbf{0}, & t \in (0, T) \\ (-p(k_j)\boldsymbol{n} + \mu \nabla \boldsymbol{u}(k_j)\, \boldsymbol{n})|_{\Gamma_0} = \mathbf{0}, & t \in (0, T), \\ (-p(k_j)\boldsymbol{n} + \mu \nabla \boldsymbol{u}(k_j)\, \boldsymbol{n})|_{\Gamma_i} = -k_i(t)\boldsymbol{n}, \quad i = 1, \ldots, m, & t \in (0, T), \end{cases} \tag{4.10}$$

with $\boldsymbol{f} \in L^\infty(0, T; \boldsymbol{L}^2(\Omega))$, $\boldsymbol{\beta} \in L^\infty(0, T; \boldsymbol{L}^\infty(\Omega))$, $\boldsymbol{u}_0 \in \boldsymbol{L}^2(\Omega)$ and $\nabla \cdot \boldsymbol{u}_0 = 0$. Again, here we consider the (constant in space) Neumann boundary data k_j as control variables in minimizing the functional (4.9) for each $t \in (0, T)$. To this aim, we consider first a discretization of the time derivative by a BDF scheme. Equation $(4.10)_1$ becomes:

$$\frac{\alpha}{\Delta t} \boldsymbol{u}^{n+1}(k_j^{n+1}) - \mu \triangle \boldsymbol{u}^{n+1}(k_j^{n+1}) + (\boldsymbol{\beta}^{n+1} \cdot \nabla)\boldsymbol{u}^{n+1}(k_j^{n+1}) + \tag{4.11}$$

$$+\nabla p^{n+1}(k_j^{n+1}) = \boldsymbol{f}^{n+1} + \sum_{i=0}^{r\leq n} \frac{\tau_i}{\Delta t}\boldsymbol{u}^{n-i},$$

where $t^n = n\Delta t$, $\boldsymbol{f}^n = \boldsymbol{f}(t^n, \boldsymbol{x})$, $\boldsymbol{\beta}^n = \boldsymbol{\beta}(t^n, \boldsymbol{x})$, $k_j^n = k_j(t^n)$, $\boldsymbol{u}^{n-i}$ is an approximation of the unknown $\boldsymbol{u}(t^{n-i})$ and α and τ_i are the coefficients of the time discretization. Furthermore, we require that $J_Q(\boldsymbol{u})$ is minimized, where here Q_j is replaced by $Q_j^n = Q_j(t^n)$. The Lagrangian functional at time $t = t^{n+1}$ is then given by:

$$L^{n+1}((\boldsymbol{u}, p), (\boldsymbol{\lambda}_u, \lambda_p), k_j) = \frac{1}{2}\sum_{i=1}^{m}\int_{\Gamma_i}(\boldsymbol{u}\cdot\boldsymbol{n}\,d\gamma - Q_i^{n+1})^2 + \frac{\alpha}{\Delta t}(\boldsymbol{u}, \boldsymbol{\lambda}_u) +$$

$$+a_L(\boldsymbol{u}, \boldsymbol{\lambda}_u) + ((\boldsymbol{\beta}^{n+1}\cdot\nabla)\boldsymbol{u}, \boldsymbol{\lambda}_u) + b(p, \boldsymbol{\lambda}_u) + \sum_{i=1}^{m}\int_{\Gamma_i} k_i\boldsymbol{\lambda}_u\cdot\boldsymbol{n}\,d\gamma +$$

$$-(\boldsymbol{f}^{n+1}, \boldsymbol{\lambda}_u) - \sum_{i=0}^{r\leq n}\frac{\tau_i}{\Delta t}(\boldsymbol{u}^{n-i}, \boldsymbol{\lambda}_u) + b(\lambda_p, \boldsymbol{u}).$$

Now, we seek the stationary point $(\boldsymbol{u}^{n+1}(k^{n+1}), p^{n+1}(k^{n+1}), \boldsymbol{\lambda}_u^{n+1}, \lambda_p^{n+1}, k_j^{n+1})$ of the Lagrangian L^n. By imposing (4.3) we obtain

Problem 23 *Given $\boldsymbol{f}^{n+1} \in \boldsymbol{L}^2(\Omega)$, $\boldsymbol{\beta}^{n+1} \in \boldsymbol{L}^\infty(\Omega)$, $\boldsymbol{u}^{n-i} \in \boldsymbol{V}$, $\forall i = 0, \ldots, r$ and Q_j^{n+1}, $j = 1\ldots, m$, find $\boldsymbol{u}^{n+1}(k_j^{n+1}) \in \boldsymbol{V}, p^{n+1}(k_j^{n+1}) \in L^2(\Omega), \boldsymbol{\lambda}_u^{n+1} \in \boldsymbol{V}, \lambda_p^{n+1} \in L^2(\Omega)$ and $k_j^{n+1} \in \mathbb{R}$, $j = 1, \ldots, m$, such that, for all $\boldsymbol{v} \in \boldsymbol{V}$, $q \in L^2(\Omega)$ and $\nu \in \mathbb{R}$:*

$$\begin{cases}
(P)\begin{cases}
< dL_{\boldsymbol{\lambda}_u^{n+1}}, \boldsymbol{v} >= \dfrac{\alpha}{\Delta t}(\boldsymbol{u}^{n+1}(k_j^{n+1}), \boldsymbol{v}) + a_L(\boldsymbol{u}^{n+1}(k_j^{n+1}), \boldsymbol{v}) + \\
\qquad +((\boldsymbol{\beta}^{n+1}\cdot\nabla)\boldsymbol{u}^{n+1}(k_j^{n+1}), \boldsymbol{v}) + b(p^{n+1}(k_j^{n+1}), \boldsymbol{v}) + \\
\quad + \displaystyle\sum_{i=1}^{m}\int_{\Gamma_i} k_i^{n+1}\boldsymbol{v}\cdot\boldsymbol{n}\,d\gamma - (\boldsymbol{f}^{n+1}, \boldsymbol{v}) - \sum_{i=0}^{r\leq n}\frac{\tau_i}{\Delta t}(\boldsymbol{u}^{n-i}, \boldsymbol{v}) = 0, \\
< dL_{\lambda_p^{n+1}}, q >= b(q, \boldsymbol{u}^{n+1}(k_j^{n+1})) = 0,
\end{cases} \\
(A)\begin{cases}
< dL_{\boldsymbol{u}^{n+1}}, \boldsymbol{v} >= \dfrac{\alpha}{\Delta t}(\boldsymbol{\lambda}_u^{n+1}, \boldsymbol{v}) + a_L(\boldsymbol{\lambda}_u^{n+1}, \boldsymbol{v}) + ((\boldsymbol{\beta}^{n+1}\cdot\nabla)\boldsymbol{v}, \boldsymbol{\lambda}_u^{n+1}) + \\
\quad + b(\lambda_p^{n+1}, \boldsymbol{v}) - \displaystyle\sum_{i=1}^{m}\Big(\int_{\Gamma_i}\boldsymbol{u}^{n+1}(k_j^{n+1})\cdot\boldsymbol{n}\,d\gamma - Q_i^{n+1}\Big)\int_{\Gamma_i}\boldsymbol{v}\cdot\boldsymbol{n}\,d\gamma = 0, \\
< dL_{p^{n+1}}, q >= b(q, \boldsymbol{\lambda}_u^{n+1}) = 0,
\end{cases} \\
(C_j) \quad < dL_{k_j^{n+1}}, \nu >= \displaystyle\int_{\Gamma_j}\nu\boldsymbol{\lambda}_u^{n+1}\cdot\boldsymbol{n}\,d\gamma = 0, \quad j = 1, \ldots, m
\end{cases}$$

Also in this case, Problem 23 will be solved with an iterative technique and the adjoint problem (A) admits as (unique) solution the trivial one.

In the Stokes case ($\boldsymbol{\beta} = \mathbf{0}$), the adjoint problem associated to problem (A) is now:

$$\begin{cases} -\mu\triangle\boldsymbol{\lambda}_u^{n+1} + \dfrac{\alpha}{\Delta t}\boldsymbol{\lambda}_u^{n+1} + \nabla\lambda_p^{n+1} = \mathbf{0} \qquad \boldsymbol{x} \in \Omega \\ \nabla\cdot\boldsymbol{\lambda}_u^{n+1} = 0 \qquad \boldsymbol{x} \in \Omega \\ \boldsymbol{\lambda}_u^{n+1}|_{\Gamma_w} = \mathbf{0} \\ (-\lambda_p^{n+1}\boldsymbol{n} + \mu\nabla\boldsymbol{\lambda}_u^{n+1}\ \boldsymbol{n})|_{\Gamma_0} = \mathbf{0}, \\ (-\lambda_p^{n+1}\boldsymbol{n} + \mu\nabla\boldsymbol{\lambda}_u^{n+1}\ \boldsymbol{n})|_{\Gamma_i} = \Big(\displaystyle\int_{\Gamma_i}\boldsymbol{u}(k_j^{n+1})\cdot\boldsymbol{n}\,d\gamma - Q_i^{n+1}\Big)\boldsymbol{n}, \quad i = 1,\dots,m. \end{cases}$$

4.3.3 Non linear case

We focus on the problem arising when a non-linear term is present in the equations. With this aim, we consider the technique applied to the steady Navier-Stokes problem. We have in this case:

$$\begin{cases} -\mu\triangle\boldsymbol{u}(k_j) + (\boldsymbol{u}(k_j)\cdot\nabla)\boldsymbol{u}(k_j) + \nabla p(k_j) = \boldsymbol{f}, \qquad \boldsymbol{x} \in \Omega \\ \nabla\cdot\boldsymbol{u}(k_j) = 0, \qquad \boldsymbol{x} \in \Omega \\ \boldsymbol{u}(k_j)|_{\Gamma_w} = \mathbf{0} \\ (-p(k_j)\boldsymbol{n} + \mu\nabla\boldsymbol{u}(k_j)\,\boldsymbol{n})|_{\Gamma_0} = 0, \\ (-p(k_j)\boldsymbol{n} + \mu\nabla\boldsymbol{u}(k_j)\,\boldsymbol{n})|_{\Gamma_i} = -k_i\boldsymbol{n}, \quad i = 1,\dots,m. \end{cases} \tag{4.12}$$

In order to minimize (4.9) with the constraint given by (4.12), we consider the following Lagrangian functional:

$$L((\boldsymbol{u},p),(\boldsymbol{\lambda}_u,\lambda_p),k_j) = \frac{1}{2}\sum_{i=1}^{m}\int_{\Gamma_i}\Big(\boldsymbol{u}\cdot\boldsymbol{n}\,d\gamma - Q_i\Big)^2 + a_L(\boldsymbol{u},\boldsymbol{\lambda}_u) +$$

$$+((\boldsymbol{u}\cdot\nabla)\boldsymbol{u},\boldsymbol{\lambda}_u) + b(p,\boldsymbol{\lambda}_u) + \sum_{i=1}^{m}\int_{\Gamma_i}k_i\boldsymbol{\lambda}_u\cdot\boldsymbol{n}\,d\gamma - (\boldsymbol{f},\boldsymbol{\lambda}_u) + b(\lambda_p,\boldsymbol{u}),$$

and this leads to the following:

Problem 24 *Given $\boldsymbol{f} \in \boldsymbol{L}^2(\Omega)$ and $\boldsymbol{Q} \in \mathbb{R}^m$ find $\boldsymbol{u}(k_j) \in \boldsymbol{V}, p(k_j) \in L^2(\Omega), \boldsymbol{\lambda}_u \in \boldsymbol{V}, \lambda_p \in L^2(\Omega)$ and $k_j \in \mathbb{R}$, $j = 1,\dots,m$, such that, for all $\boldsymbol{v} \in \boldsymbol{V}$, $q \in L^2(\Omega)$*

and $\nu \in \mathbb{R}$*:*

$$\begin{cases} \begin{cases} < dL_{\boldsymbol{\lambda}_u}, \boldsymbol{v} >= a_L(\boldsymbol{u}(k_j), \boldsymbol{v}) + ((\boldsymbol{u}(k_j) \cdot \nabla)\boldsymbol{u}(k_j), \boldsymbol{v}) + \\ \qquad\qquad +b(p(k_j), \boldsymbol{v}) + \displaystyle\sum_{i=i}^{m} \int_{\Gamma_i} k_i \boldsymbol{v} \cdot \boldsymbol{n}\, d\gamma - (\boldsymbol{f}, \boldsymbol{v}) = 0, \\ < dL_{\lambda_p}, q >= b(q, \boldsymbol{u}(k_j)) = 0, \end{cases} \quad (P) \\ \begin{cases} < dL_{\boldsymbol{u}}, \boldsymbol{v} >= a_L(\boldsymbol{\lambda}_u, \boldsymbol{v}) + ((\boldsymbol{u}(k_j) \cdot \nabla)\boldsymbol{v}, \boldsymbol{\lambda}_u) + ((\boldsymbol{v} \cdot \nabla)\boldsymbol{u}(k_j), \boldsymbol{\lambda}_u) + \\ \qquad\qquad +b(\lambda_p, \boldsymbol{v}) - \displaystyle\sum_{i=1}^{m} \Big(\int_{\Gamma_i} \boldsymbol{u}(k_j) \cdot \boldsymbol{n}\, d\gamma - Q_i \Big) \int_{\Gamma_i} \boldsymbol{v} \cdot \boldsymbol{n}\, d\gamma = 0, \\ < dL_p, q >= b(q, \boldsymbol{\lambda}_u) = 0, \end{cases} \quad (A) \\ (C) \quad < dL_{k_j}, \nu >= \displaystyle\int_{\Gamma_j} \nu \boldsymbol{\lambda}_u \cdot \boldsymbol{n}\, d\gamma = 0, \quad j = 1, \ldots, m. \end{cases}$$

In this case the adjoint problem is given by (see [5]):

$$\begin{cases} -\mu \triangle \boldsymbol{\lambda}_u + (\nabla \boldsymbol{u}(k_j))^T \boldsymbol{\lambda}_u - (\boldsymbol{u}(k_j) \cdot \nabla)\boldsymbol{\lambda}_u + \nabla \lambda_p = \boldsymbol{0}, \qquad \boldsymbol{x} \in \Omega \\ \nabla \cdot \boldsymbol{\lambda}_u = 0, \qquad \boldsymbol{x} \in \Omega \\ \boldsymbol{\lambda}_u|_{\Gamma_w} = \boldsymbol{0} \\ (-\lambda_p \boldsymbol{n} + \mu \nabla \boldsymbol{\lambda}_u\ \boldsymbol{n})|_{\Gamma_0} = \boldsymbol{0}, \\ (-\lambda_p \boldsymbol{n} + \mu \nabla \boldsymbol{\lambda}_u\ \boldsymbol{n})|_{\Gamma_j} = \Big(\displaystyle\int_{\Gamma_j} \boldsymbol{u}(k_j) \cdot \boldsymbol{n}\, d\gamma - Q_j \Big) \boldsymbol{n}, \qquad j = 1, \ldots, m. \end{cases}$$

4.4 Mean pressure boundary problems

As pointed out in Chapter 1, another defective boundary data problem sometimes considered in the applications refers to the mean pressure. As a matter of fact, referring to Figure 4.1, we recall that the mean pressure problem for an incompressible Newtonian homogeneous fluid is given by (4.5) together with the initial and boundary conditions $(4.6)_1$,$(4.6)_2$ and the following defective condition on the artficial sections Γ_j:

$$\frac{1}{|\Gamma_j|} \int_{\Gamma_j} p\, d\gamma = P_j, \quad j = 0, 1, \ldots, m, \quad t \in (0, T], \tag{4.13}$$

where P_j are given. Let us notice that if $\boldsymbol{f} \in \boldsymbol{L}^2(\Omega)$ and if the boundary $\partial\Omega$ of the domain is twice continuously differentiable, the trace of p is well defined, since $p \in H^1(\Omega)$ (see [32]).

As already pointed out in Section 1.3.2, the approach based on the implicit forcing of natural boundary conditions associated to the choice of a variational formulation leads to Problem 4 (proposed in [28]), which is an approximation of

the mean pressure problem. In fact, this formulation actually forces the following boundary conditions

$$(-p\boldsymbol{n} + \mu\nabla\boldsymbol{u}\ \boldsymbol{n})|_{\Gamma_j} = -P_j\boldsymbol{n} \quad j = 0, \ldots, m.$$

More precisely, these conditions are exact if the tangential viscous stress are null, i.e.

$$(\mu(\nabla\boldsymbol{u}\ \boldsymbol{n}) \cdot \boldsymbol{\tau}_i)|_{\Gamma_j} = 0, \quad j = 0, \ldots, m, \quad i = 1, d-1.$$

Moving from the proposal of the previous section, it is possible to generalize this formulation in terms of a control problem. Let us still consider the constant normal stresses k_j as control variable for achieving the constraint minimization of a suitable functional. We start again by considering the linear steady case.

4.4.1 Linear steady case

Let us consider the steady Oseen problem given by $(4.7)_1$, $(4.7)_2$, $(4.7)_3$ togheter with the following boundary conditions:

$$(-p(k_j)\boldsymbol{n} + \mu\nabla\boldsymbol{u}(k_j)\ \boldsymbol{n})|_{\Gamma_j} = -k_j\boldsymbol{n} \quad j = 0, \ldots, m. \tag{4.14}$$

where we stress the dependence of the solution $(\boldsymbol{u}, p)$ on the constant k_j. The latter are determined in order to minimize the following functional:

$$J_P(p) = \frac{1}{2}\Big(\sum_{i=0}^{m} \frac{1}{|\Gamma_i|}\int_{\Gamma_i} p\, d\gamma - P_i\Big)^2. \tag{4.15}$$

In particular, we refer to the following Lagrangian functional:

$$L((\boldsymbol{u}, p), (\boldsymbol{\lambda}_u, \lambda_p), k_j) = \frac{1}{2}\sum_{i=0}^{m}\Big(\frac{1}{|\Gamma_i|}\int_{\Gamma_i} p\, d\gamma - P_i\Big)^2 + a_L(\boldsymbol{u}, \boldsymbol{\lambda}_u) +$$

$$+((\boldsymbol{\beta}\cdot\nabla)\boldsymbol{u}, \boldsymbol{\lambda}_u) + b(p, \boldsymbol{\lambda}_u) + \sum_{i=0}^{m}\int_{\Gamma_i} k_i\boldsymbol{\lambda}_u \cdot \boldsymbol{n}\, d\gamma - (\boldsymbol{f}, \boldsymbol{\lambda}_u) + b(\lambda_p, \boldsymbol{u})$$

The search of a stationary point for L leads

Problem 25 *Given $\boldsymbol{f} \in \boldsymbol{L}^2(\Omega)$ and $P_j \in \mathbb{R}$, $j = 0, \ldots, m$, find $\boldsymbol{u} \in \boldsymbol{V}, p \in H^1(\Omega), \boldsymbol{\lambda}_u \in \boldsymbol{V}, \lambda_p \in L^2(\Omega)$ and $k_j \in \mathbb{R}$, $j = 0, \ldots, m$, such that, for all $\boldsymbol{v} \in$*

$\boldsymbol{V}$, $q \in L^2(\Omega)$ *and* $\nu \in \mathbb{R}$*:*

$$\begin{cases} (P) \begin{cases} < dL_{\boldsymbol{\lambda}_u}, \boldsymbol{v} >= a_L(\boldsymbol{u}(k_j), \boldsymbol{v}) + ((\boldsymbol{\beta}\cdot\nabla)\boldsymbol{u}(k_j), \boldsymbol{v}) + b(p(k_j), \boldsymbol{v}) + \\ \qquad\qquad + \displaystyle\sum_{i=0}^{m} \int_{\Gamma_i} k_i \boldsymbol{v}\cdot\boldsymbol{n}\, d\gamma - (\boldsymbol{f}, \boldsymbol{v}) = 0, \\ < dL_{\lambda_p}, q >= b(q, \boldsymbol{u}(k_j)) = 0, \end{cases} \\ (A) \begin{cases} < dL_{\boldsymbol{u}}, \boldsymbol{v} >= a_L(\boldsymbol{\lambda}_u, \boldsymbol{v}) + ((\boldsymbol{\beta}\cdot\nabla)\boldsymbol{v}, \boldsymbol{\lambda}_u) + b(\lambda_p, \boldsymbol{v}) = 0, \\ < dL_p, q >= \displaystyle\sum_{i=0}^{m} \Big(\frac{1}{|\Gamma_i|}\int_{\Gamma_i} p(k_j)\, d\gamma - P_i\Big) \frac{1}{|\Gamma_i|}\int_{\Gamma_i} q\, d\gamma + b(q, \boldsymbol{\lambda}_u) = 0, \end{cases} \\ (C_j) \quad < dL_{k_i}, \nu >= \displaystyle\int_{\Gamma_i} \nu \boldsymbol{\lambda}_u\cdot\boldsymbol{n}\, d\gamma = 0, \quad i = 0, \ldots, m. \end{cases}$$

In this case, we obtain a system coupling an Oseen (P) and a steady-compressible problem (A). In the particular case $\boldsymbol{\beta} = \boldsymbol{0}$, the adjoint problem is given by:

$$\begin{cases} -\mu\triangle\boldsymbol{\lambda}_u + \nabla\lambda_p = \boldsymbol{0}, \qquad \boldsymbol{x} \in \Omega \\ \nabla\cdot\boldsymbol{\lambda}_u = \displaystyle\sum_{i=0}^{m} \Big(\frac{1}{|\Gamma_i|}\int_{\Gamma_i} p(k_j)\, d\gamma - P_i\Big), \qquad \boldsymbol{x} \in \Omega \\ \boldsymbol{\lambda}_u|_{\Gamma_w} = \boldsymbol{0} \\ (-\lambda_p\boldsymbol{n} + \mu\nabla\boldsymbol{\lambda}_u\ \boldsymbol{n})|_{\Gamma_j} = \boldsymbol{0}, \qquad j = 0, \ldots, m \end{cases}$$

In correspondence of the solution of Problem 25 it admits as unique solution the trivial one.

It is worth pointing out that the previous approach can be straightforwardly extended to the unsteady and to the non-linear case, in analogy with Section 4.3.

We note that the computed velocity on an artificial section Γ_i is, in general, not aligned with the normal to the section (see Figures 4.10 in Section 4.6). This is due to the fact that Problem 25 forces zero tangential stresses on Γ_i as natural boundary condition. This is indeed not corresponding to the physical problem. In order to overcome this, we need to add more control variables in order to control also the tangential components of the stress. Therefore, in order to treat the more general case, we set:

$$(-p(k_j)\boldsymbol{n} + \mu\nabla\boldsymbol{u}(k_j)\ \boldsymbol{n})|_{\Gamma_j} = -\boldsymbol{k}_j(\boldsymbol{x}), \quad j = 0, \ldots, m. \tag{4.16}$$

where the values of the $\boldsymbol{k}_j$ are chosen in order to minimize the functional:

$$J_P(p) = \frac{1}{2}\sum_{i=0}^{m} \Big(\frac{1}{|\Gamma_i|}\int_{\Gamma_i} p\, d\gamma - P_i\Big)^2 + \frac{1}{2}\sum_{i=0}^{m} \int_{\Gamma_i} \|\nabla\boldsymbol{u}\, \boldsymbol{a}_i\|^2_{\mathbb{R}^d}\, d\gamma, \tag{4.17}$$

where $\|\cdot\|_{\mathbb{R}^d}$ is the Euclidean norm and $\boldsymbol{a}_i$ is the axial direction over Γ_i. Building the Lagrangian functional obtained from (4.17) constrained by $(4.7)_1$, $(4.7)_2$, $(4.7)_3$ and (4.16), we obtain the following:

Problem 26 *Given* $\boldsymbol{f} \in \boldsymbol{L}^2(\Omega)$ *and* $P_j \in \mathbb{R}$, $j = 0, \ldots, m$, *find* $\boldsymbol{u} \in \boldsymbol{V}, p \in H^1(\Omega), \boldsymbol{\lambda}_u \in \boldsymbol{V}, \lambda_p \in L^2(\Omega)$ *and* $\boldsymbol{k}_j \in \boldsymbol{L}^2(\Gamma_j)$, $j = 0, \ldots, m$, *such that, for all* $\boldsymbol{v} \in \boldsymbol{V}$, $q \in L^2(\Omega)$ *and* $\boldsymbol{\nu} \in \boldsymbol{L}^2(\Gamma_i)$, $i = 0, \ldots, m$*:*

$$
\begin{cases}
(P) \begin{cases} < dL_{\boldsymbol{\lambda}_u}, \boldsymbol{v} >= a_L(\boldsymbol{u}(\boldsymbol{k}_j), \boldsymbol{v}) + ((\boldsymbol{\beta} \cdot \nabla)\boldsymbol{u}, \boldsymbol{v}) + b(p(\boldsymbol{k}_j), \boldsymbol{v}) + \\ \qquad + \sum_{i=0}^{m} \int_{\Gamma_i} \boldsymbol{k}_i \cdot \boldsymbol{v}\, d\gamma - (\boldsymbol{f}, \boldsymbol{v}) = 0, \\ < dL_{\lambda_p}, q >= b(q, \boldsymbol{u}(\boldsymbol{k}_j)) = 0, \end{cases} \\
(A) \begin{cases} < dL_{\boldsymbol{u}}, \boldsymbol{v} >= \sum_{i=0}^{m} \int_{\Gamma_i} (\nabla \boldsymbol{u}(\boldsymbol{k}_j)\, \boldsymbol{a}_i) \cdot (\nabla \boldsymbol{v}\ \boldsymbol{a}_i)\, d\gamma + a_L(\boldsymbol{\lambda}_u, \boldsymbol{v}) + \\ \qquad + ((\boldsymbol{\beta} \cdot \nabla)\boldsymbol{v}, \boldsymbol{\lambda}_u) + b(\lambda_p, \boldsymbol{v}) = 0, \\ < dL_p, q >= \sum_{i=0}^{m} \Big(\frac{1}{|\Gamma_i|} \int_{\Gamma_i} p(\boldsymbol{k}_j)\, d\gamma - P_i \Big) \frac{1}{|\Gamma_i|} \int_{\Gamma_i} q\, d\gamma + b(q, \boldsymbol{\lambda}_u) = 0, \end{cases} \\
(C_i) \quad < dL_{\boldsymbol{k}_i}, \boldsymbol{\nu} >= \int_{\Gamma_i} \boldsymbol{\nu} \cdot \boldsymbol{\lambda}_u\, d\gamma = 0, \quad i = 0, \ldots, m
\end{cases}
$$

Let us notice that the optimality conditions (C_i) imply that:

$$\boldsymbol{\lambda}_u|_{\Gamma_i} = \boldsymbol{0}, \quad i = 0, \ldots, m$$

and so they are no more scalar but vectorial function conditions. Therefore, the conditions of fulfilment of the optimal state are more restrictive of the previous ones. Let us also notice that, since

$$\int_{\Gamma_i} (\nabla \boldsymbol{u}(\boldsymbol{k}_j)\, \boldsymbol{a}_i) \cdot (\nabla \boldsymbol{v}\ \boldsymbol{a}_i)\, d\gamma = -\int_{\Gamma_i} \frac{\partial^2 \boldsymbol{u}(\boldsymbol{k}_j)}{\partial \boldsymbol{a}_i^2} \cdot \boldsymbol{v}\, d\gamma + \int_{\partial\Gamma_i} \frac{\partial \boldsymbol{u}(\boldsymbol{k}_j)}{\partial \boldsymbol{a}_i} \cdot \boldsymbol{v} dl,$$

and since $\partial\Gamma_i \subset \Gamma_w$, the adjoint problem, if $\boldsymbol{\beta} = \boldsymbol{0}$, is now:

$$
\begin{cases}
-\mu \triangle \boldsymbol{\lambda}_u + \nabla \lambda_p = \sum_{i=0}^{m} \frac{\partial^2 \boldsymbol{u}(\boldsymbol{k}_j)}{\partial \boldsymbol{a}_i^2}\Big|_{\Gamma_i}, & \boldsymbol{x} \in \Omega \\
\nabla \cdot \boldsymbol{\lambda}_u = \sum_{i=1}^{m} \Big(\frac{1}{|\Gamma_i|} \int_{\Gamma_i} p(\boldsymbol{k}_j)\, d\gamma - P_i \Big), & \boldsymbol{x} \in \Omega \\
\boldsymbol{\lambda}_u|_{\Gamma_w} = \boldsymbol{0} \\
(-\lambda_p \boldsymbol{n} + \mu \nabla \boldsymbol{\lambda}_u\ \boldsymbol{n})|_{\Gamma_j} = \boldsymbol{0}, \quad j = 0, \ldots, m
\end{cases}
$$

In order that the trace of $\partial^2 \boldsymbol{u}(\boldsymbol{k}_j)/\partial \boldsymbol{a}_i^2$ on Γ_i is well definied it is necessary to ask that $\boldsymbol{f} \in \boldsymbol{H}^1(\Omega)$ (assuming that Ω is smooth enough). Infact, in this case $\boldsymbol{u} \in \boldsymbol{H}^3(\Omega)$ and therefore $\partial^2 \boldsymbol{u}(\boldsymbol{k}_j)/\partial \boldsymbol{a}_i^2 \in \boldsymbol{H}^1(\Omega)$ (see [32]).

4.4.2 A more appropriate description of the viscous term

As already pointed out in Chapter 1, we refer to the "complete" formulation when we consider the full viscous term,

$$\nabla \cdot (\mu(\nabla \boldsymbol{u} + (\nabla \boldsymbol{u})^t)).$$

We are interested in this formulation since it is the correct formulation to be considered for several applications, e.g. the fluid-structure interaction problem (see Section 3.4). The natural boundary conditions associated to this treatment of the viscous term are (1.8). Therefore, imposing null tangential stresses is equivalent in this case to:

$$(\mu(\nabla \boldsymbol{u} + (\nabla \boldsymbol{u})^t)\boldsymbol{n} \cdot \boldsymbol{\tau}_j)|_{\Gamma_i} = \boldsymbol{0}, \quad i = 0, \ldots, m, \quad j = 1, d-1.$$

This condition in general implies that

$$\frac{\partial(\boldsymbol{u} \cdot \boldsymbol{\tau}_j)}{\partial \boldsymbol{n}}\Big|_{\Gamma_i} \neq \boldsymbol{0}, \quad i = 0, \ldots, m, \quad j = 1, d-1$$

and consequently

$$(\boldsymbol{u} \cdot \boldsymbol{\tau}_j)|_{\Gamma_i} \neq \boldsymbol{0}, \quad i = 0, \ldots, m, \quad j = 1, d-1.$$

It means that in this case the imposition of null tangential stress on an artificial section Γ_i, brings about a non null tangential component of the velocity (see [28]). This "boundary effect" would be physical if the artificial section was at the inteface with an external pressure (as in a tube from which water flows). Nevertheless, it is undesiderable in a truncated domain, where Γ_i represents just an artificial "cut" of a larger domain. To treat this problem in [68] it has been proposed to prescribe directly

$$(\boldsymbol{u} \cdot \boldsymbol{\tau}_j)|_{\Gamma_i} = \boldsymbol{0}, \quad i = 0, \ldots, m, \quad j = 1, d-1,$$

in the variational formulation of the problem. However, this is a very strong statement. Therefore, in order to introduce a less perturbative strategy, here we introduce a new approach, based again on the control theory. In particular, let us consider the following linear steady problem:

$$\begin{cases} -\nabla \cdot (\mu(\nabla \boldsymbol{u}(\boldsymbol{k}_j) + (\nabla \boldsymbol{u}(\boldsymbol{k}_j))^t)) + (\boldsymbol{\beta} \cdot \nabla)\boldsymbol{u}(\boldsymbol{k}_j) + \nabla p(\boldsymbol{k}_j) = \boldsymbol{f}, & \boldsymbol{x} \in \Omega \\ \nabla \cdot \boldsymbol{u}(\boldsymbol{k}_j) = 0, & \boldsymbol{x} \in \Omega \\ \boldsymbol{u}(\boldsymbol{k}_j)|_{\Gamma_w} = \boldsymbol{0} \\ (-p(\boldsymbol{k}_j)\boldsymbol{n} + \mu(\nabla \boldsymbol{u}(\boldsymbol{k}_j) + (\nabla \boldsymbol{u}(\boldsymbol{k}_j))^t)\boldsymbol{n})|_{\Gamma_j} = -\boldsymbol{k}_j(\boldsymbol{x}), \quad j = 0, \ldots, m \end{cases} \tag{4.18}$$

In this case, due to the boundary effects, we consider conditions (4.16) and functional (4.17) also for a rectangular/cylindrical domain. Minimizing functional (4.17) constrained by equations (4.18), we obtain the following

Problem 27 *Given* $\boldsymbol{f} \in \boldsymbol{L}^2(\Omega)$ *and* $P_j \in \mathbb{R}$, $j = 0, \ldots, m$, *find* $\boldsymbol{u} \in \boldsymbol{V}, p \in H^1(\Omega), \boldsymbol{\lambda}_u \in \boldsymbol{V}, \lambda_p \in L^2(\Omega)$ *and* $\boldsymbol{k}_j \in \boldsymbol{L}^2(\Gamma_j)$, $j = 0, \ldots, m$, *such that, for all* $\boldsymbol{v} \in \boldsymbol{V}$, $q \in L^2(\Omega)$ *and* $\boldsymbol{\nu} \in \boldsymbol{L}^2(\Gamma_i)$, $i = 0, \ldots, m$*:*

$$
\begin{cases}
(P) \begin{cases} < dL_{\boldsymbol{\lambda}_u}, \boldsymbol{v} >= a_C(\boldsymbol{u}(\boldsymbol{k}_j), \boldsymbol{v}) + ((\boldsymbol{\beta} \cdot \nabla)\boldsymbol{u}(\boldsymbol{k}_j), \boldsymbol{v}) + b(p(\boldsymbol{k}_j), \boldsymbol{v}) + \\ \qquad + \displaystyle\sum_{i=0}^{m} \int_{\Gamma_i} \boldsymbol{k}_i \cdot \boldsymbol{v} \, d\gamma - (\boldsymbol{f}, \boldsymbol{v}) = 0, \\ < dL_{\lambda_p}, q >= b(q, \boldsymbol{u}(\boldsymbol{k}_j)) = 0, \end{cases} \\
(A) \begin{cases} < dL_{\boldsymbol{u}}, \boldsymbol{v} >= \displaystyle\sum_{i=0}^{m} \int_{\Gamma_i} (\nabla \boldsymbol{u}(\boldsymbol{k}_j) \, \boldsymbol{a}_i) \cdot (\nabla \boldsymbol{v} \ \boldsymbol{a}_i) \, d\gamma + a_C(\boldsymbol{v}, \boldsymbol{\lambda}_u) + \\ \qquad + ((\boldsymbol{\beta} \cdot \nabla)\boldsymbol{v}, \boldsymbol{\lambda}_u) + b(\lambda_p, \boldsymbol{v}) = 0, \\ < dL_p, q >= \displaystyle\sum_{i=0}^{m} \Big(\frac{1}{|\Gamma_i|} \int_{\Gamma_i} p(\boldsymbol{k}_j) \, d\gamma - P_i \Big) \frac{1}{|\Gamma_i|} \int_{\Gamma_i} q \, d\gamma + b(q, \boldsymbol{\lambda}_u) = 0, \end{cases} \\
(C_i) \quad < dL_{\boldsymbol{k}_i}, \boldsymbol{\nu} >= \displaystyle\int_{\Gamma_i} \boldsymbol{\nu} \cdot \boldsymbol{\lambda}_u \, d\gamma = \boldsymbol{0}, \quad i = 0, \ldots, m
\end{cases}
$$

where $a_C(\cdot, \cdot)$ is given by (1.7).

Alternatively, we could look for the condition (4.16) that minimize directly the tangential velocity, for example minimizing the following functional:

$$
J_P(p) = \frac{1}{2} \sum_{i=0}^{m} \Big(\frac{1}{|\Gamma_i|} \int_{\Gamma_i} p \, d\gamma - P_i \Big)^2 + \frac{1}{2} \sum_{l=1}^{d-1} \sum_{i=0}^{m} \int_{\Gamma_i} |\boldsymbol{u} \cdot \boldsymbol{\tau}_l|^2 \, d\gamma \tag{4.19}
$$

This leads to the following Lagrangian functional:

$$
L((\boldsymbol{u}, p), (\boldsymbol{\lambda}_u, \lambda_p), \boldsymbol{k}_j) = \frac{1}{2} \sum_{i=0}^{m} \Big(\frac{1}{|\Gamma_i|} \int_{\Gamma_i} p \, d\gamma - P_i \Big) +
$$

$$
+ \frac{1}{2} \sum_{l=1}^{d-1} \sum_{i=0}^{m} \int_{\Gamma_i} |\boldsymbol{u} \cdot \boldsymbol{\tau}_l|^2 \, d\gamma + a_C(\boldsymbol{u}, \boldsymbol{\lambda}_u) + ((\boldsymbol{\beta} \cdot \nabla)\boldsymbol{u}, \boldsymbol{\lambda}_u) +
$$

$$
+ b(p, \boldsymbol{\lambda}_u) + \sum_{i=0}^{m} \int_{\Gamma_i} \boldsymbol{k}_i \cdot \boldsymbol{\lambda}_u \, d\gamma - (\boldsymbol{f}, \boldsymbol{\lambda}_u) + b(\lambda_p, \boldsymbol{u})
$$

and to the following

Problem 28 *Given* $\boldsymbol{f} \in \boldsymbol{L}^2(\Omega)$ *and* $P_j \in \mathbb{R}$, $j = 0, \ldots, m$, *find* $\boldsymbol{u} \in \boldsymbol{V}, p \in H^1(\Omega), \boldsymbol{\lambda}_u \in \boldsymbol{V}, \lambda_p \in L^2(\Omega)$ *and* $\boldsymbol{k}_j \in \boldsymbol{L}^2(\Gamma_j)$, $j = 0, \ldots, m$, *such that,* $\forall \boldsymbol{v} \in$

$\boldsymbol{V},\, q \in L^2(\Omega)$ *and* $\boldsymbol{\nu} \in \boldsymbol{L}^2(\Gamma_i)$, $i = 0, \ldots, m$*:*

$$
\begin{cases}
(P) \begin{cases} < dL_{\boldsymbol{\lambda}_u}, \boldsymbol{v} >= a_C(\boldsymbol{u}(\boldsymbol{k}_j), \boldsymbol{v}) + ((\boldsymbol{\beta}\cdot\nabla)\boldsymbol{u}(\boldsymbol{k}_j), \boldsymbol{v}) + b(p(\boldsymbol{k}_j), \boldsymbol{v}) + \\ \qquad\qquad + \displaystyle\sum_{i=0}^{m} \int_{\Gamma_i} \boldsymbol{k}_i \cdot \boldsymbol{v}\, d\gamma - (\boldsymbol{f}, \boldsymbol{v}) = 0, \\ < dL_{\lambda_p}, q >= b(q, \boldsymbol{u}(\boldsymbol{k}_j)) = 0, \end{cases} \\
(A) \begin{cases} < dL_{\boldsymbol{u}}, \boldsymbol{v} >= \displaystyle\sum_{l=1}^{d-1} \sum_{i=0}^{m} \int_{\Gamma_i} \boldsymbol{u} \cdot \boldsymbol{\tau}_l(\boldsymbol{k}_j)\, \boldsymbol{v} \cdot \boldsymbol{\tau}_j\, d\gamma + a_C(\boldsymbol{v}, \boldsymbol{\lambda}_u) + \\ \qquad\qquad + ((\boldsymbol{\beta}\cdot\nabla)\boldsymbol{v}, \boldsymbol{\lambda}_u) + b(\lambda_p, \boldsymbol{v}) = 0, \\ < dL_p, q >= \displaystyle\sum_{i=0}^{m} \Big(\frac{1}{|\Gamma_i|} \int_{\Gamma_i} p(\boldsymbol{k}_j)\, d\gamma - P_i \Big) \frac{1}{|\Gamma_i|} \int_{\Gamma_i} q\, d\gamma + b(q, \boldsymbol{\lambda}_u) = 0, \end{cases} \\
(C) \quad < dL_{\boldsymbol{k}_i}, \boldsymbol{\nu} >= \displaystyle\int_{\Gamma_i} \boldsymbol{\nu} \cdot \boldsymbol{\lambda}_u\, d\gamma = 0, \quad i = 0, \ldots, m
\end{cases}
$$

Also in this case we can extend the previous control problems to the unsteady and to the non linear cases.

4.4.3 Flow rates as control variables

In the formulation of the flow rates problem, we introduced a set of control variables associated to the normal component of the stress tensor. For solving the mean pressure problem, we can also pursue a sort of "dual" approach, in which the control variables are given by the flow rates on Γ_j, $j = 1, \ldots, m$. More precisely, we consider the linear steady problem

$$
\begin{cases}
-\mu \triangle \boldsymbol{u}(Q_j) + (\boldsymbol{\beta}\cdot\nabla)\boldsymbol{u}(Q_j) + \nabla p(Q_j) = \boldsymbol{f}, \qquad \boldsymbol{x} \in \Omega \\
\nabla \cdot \boldsymbol{u}(Q_j) = 0 \qquad \boldsymbol{x} \in \Omega \\
\boldsymbol{u}(Q_j)|_{\Gamma_w} = \boldsymbol{0} \\
\Big(- p(Q_j)\boldsymbol{n} + \mu \nabla \boldsymbol{u}(Q_j)\, \boldsymbol{n}) |_{\Gamma_0} = -P_0 \boldsymbol{n}, \\
\displaystyle\int_{\Gamma_j} \boldsymbol{u}(Q_j) \cdot \boldsymbol{n}\, d\gamma = Q_j, \quad j = 1, \ldots, m
\end{cases}
\tag{4.20}
$$

Condition on Γ_0 is explicitly prescribed in order to avoid compatibility conditions on the flow rate data induced by the incompressibility (see (1.12)).

Let us now formulate the problem in terms of constrained minimization of the functional given by (4.15), with the constraint given by (4.20). We point out that the latter is a flow rate problem and therefore we introduce the related augmented formulation. In particular, the Lagrangian functional reads

$$
L((\boldsymbol{u}, p, \eta_i), (\boldsymbol{\lambda}_u, \lambda_p, \lambda_{\eta_j}), Q_j) = \frac{1}{2} \Big(\sum_{i=1}^{m} \frac{1}{|\Gamma_i|} \int_{\Gamma_i} p\, d\gamma - P_i \Big)^2 +
$$

$$+a_L(\boldsymbol{u},\boldsymbol{\lambda}_u)+((\boldsymbol{\beta}\cdot\nabla)\boldsymbol{u},\boldsymbol{\lambda}_u)+b(p,\boldsymbol{\lambda}_u)+\sum_{i=1}^{m}\eta_i\int_{\Gamma_i}\boldsymbol{\lambda}_u\cdot\boldsymbol{n}\,d\gamma+$$

$$-(\boldsymbol{f},\boldsymbol{\lambda}_u)+b(\lambda_p,\boldsymbol{u})+\sum_{i=1}^{m}\lambda_{\eta_i}\Big(\int_{\Gamma_i}\boldsymbol{u}\cdot\boldsymbol{n}\,d\gamma-Q_i\Big).$$

Let us point out that η_j are the Lagrange multipliers of the augmented formulation (see Chapter 2) and that $\boldsymbol{\lambda}_u, \lambda_p$ and λ_{η_j} are the adjoint variables related to $\boldsymbol{u}, p$ and η_j respectively. By forcing the vanishing of the derivatives of L with respect all the variables in correspondance of the solution, we obtain the following problem.

Problem 29 *Given* $\boldsymbol{f}\in\boldsymbol{L}^2(\Omega)$ *and* $P_j\in\mathbb{R}$, $j=1,\dots,m$, *find* $\boldsymbol{u}\in\boldsymbol{V}, p\in H^1(\Omega), \eta_j\in\mathbb{R}$, $j=1,\dots,m$, $\boldsymbol{\lambda}_u\in\boldsymbol{V}, \lambda_p\in L^2(\Omega), \lambda_{\eta_j}\in\mathbb{R}$, $j=1,\dots,m$, *and* $\boldsymbol{Q}\in\mathbb{R}^m$ *such that, for all* $\boldsymbol{v}\in\boldsymbol{V}$, $q\in L^2(\Omega)$ *and* $\nu\in\mathbb{R}$*:*

$$\begin{cases}
(P)\begin{cases}
< dL_{\boldsymbol{\lambda}_u},\boldsymbol{v}>=a_L(\boldsymbol{u}(Q_j),\boldsymbol{v})+((\boldsymbol{\beta}\cdot\nabla)\boldsymbol{u}(Q_j),\boldsymbol{v})+b(p(Q_j),\boldsymbol{v})+\\
\qquad\qquad+\sum_{i=1}^{m}\eta_i(Q_j)\int_{\Gamma_i}\boldsymbol{v}\cdot\boldsymbol{n}\,d\gamma-(\boldsymbol{f},\boldsymbol{v})=0,\\
< dL_{\lambda_p},q>=b(q,\boldsymbol{u}(Q_j))=0,\\
< dL_{\lambda_{\eta_i}},\nu>=\Big(\int_{\Gamma_i}\boldsymbol{u}(Q_j)\cdot\boldsymbol{n}\,d\gamma-Q_i\Big)\nu=0,
\end{cases}\\
(A)\begin{cases}
< dL_{\boldsymbol{u}},\boldsymbol{v}>=a_L(\boldsymbol{\lambda}_u,\boldsymbol{v})+((\boldsymbol{\beta}\cdot\nabla)\boldsymbol{v},\boldsymbol{\lambda}_u)+b(\lambda_p,\boldsymbol{v})+\\
\qquad\qquad+\sum_{i=1}^{m}\lambda_{\eta_i}\int_{\Gamma_i}\boldsymbol{v}\cdot\boldsymbol{n}\,d\gamma=0,\\
< dL_p,q>=\sum_{i=1}^{m}\Big(\frac{1}{|\Gamma_i|}\int_{\Gamma_i}p(Q_j)\,d\gamma-P_i\Big)\frac{1}{|\Gamma_i|}\int_{\Gamma_i}q\,d\gamma+b(q,\boldsymbol{\lambda}_u)=0,\\
< dL_{\eta_i},\nu>=\Big(\int_{\Gamma_i}\boldsymbol{\lambda}_u\cdot\boldsymbol{n}\,d\gamma\Big)\nu=0,
\end{cases}\\
(C_i)\quad < dL_{Q_i},\nu>=-\lambda_{\eta_i}\nu=0,\quad j=1,\dots,m
\end{cases}$$

Conditions (C_i) are equivalent to

$$\lambda_{\eta_i}=0,\quad i=1,\dots,m.$$

Therefore, recalling the physical meaning of the Lagrange multipliers in the augmented formulation (see Proposition 1, Section 1.3.1) we have to check that the normal stress of the adjoint problem is zero on each artificial section. This is in perfect analogy with the problems proposed in Section 4.3, for which we have to check that the fluxes of the adjoint problem were zero.

In this case, if $\boldsymbol{\beta} = \mathbf{0}$, the adjoint problem is:

$$\begin{cases} -\mu\triangle\boldsymbol{\lambda}_u + \nabla\lambda_p = \mathbf{0}, & \boldsymbol{x} \in \Omega \\ \nabla\cdot\boldsymbol{\lambda}_u = \displaystyle\sum_{i=1}^{m}\Big(\frac{1}{|\Gamma_i|}\int_{\Gamma_i} p(Q_j)\,d\gamma - \widetilde{P}_i\Big), & \boldsymbol{x} \in \Omega \\ \boldsymbol{\lambda}_u|_{\Gamma_w} = \mathbf{0} \\ (-\lambda_p\boldsymbol{n} + \mu\nabla\boldsymbol{\lambda}_u\ \boldsymbol{n})|_{\Gamma_0} = \mathbf{0}, \\ \displaystyle\int_{\Gamma_i}\boldsymbol{\lambda}_u\cdot\boldsymbol{n}\,d\gamma = 0, & i = 1,\dots,m. \end{cases}$$

and it admits as (unique) solution the trivial one.

4.5 Numerical methods

In this section we present some numerical methods for the resolution of the problems introduced in the previous sections. In particular, in Section 4.5.1 we investigate the flow rate problem, introducing firstly a particular algorithm for the imposition of one flow rate and then a general strategy applied, by way of example, to Problem 22. In Section 4.5.2 we apply this strategy to Problem 25 as well, as example for the mean pressure problems.

4.5.1 Flow rate problems

A particular case: prescription of one flow rate condition

The first kind of algorithm we are going to show is not based on the control problems introduced in Section 4.3, but directly on the weak formulation of (4.7), (4.10) or (4.12). Nevertheless, this is valid only if one flux is imposed.

Firstly, let us consider problem given by (4.7) and (4.8), with $m = 1$. The weak formulation is: find $\boldsymbol{u}(k) \in \boldsymbol{V}$ and $p(k) \in L^2(\Omega)$ such that for all $\boldsymbol{v} \in \boldsymbol{V}$, $q \in L^2(\Omega)$

$$\begin{cases} a_L(\boldsymbol{u}(k),\boldsymbol{v}) + ((\boldsymbol{\beta}\cdot\nabla)\boldsymbol{u}(k),\boldsymbol{v}) + b(p(k),\boldsymbol{v}) + \displaystyle\int_\Gamma k\boldsymbol{v}\cdot\boldsymbol{n}\,d\gamma = (\boldsymbol{f},\boldsymbol{v}) \\ b(q,\boldsymbol{u}(k)) = 0 \end{cases} \tag{4.21}$$

Setting $\boldsymbol{v} = \boldsymbol{u}(k)$ in the first, we obtain:

$$a_L(\boldsymbol{u}(k),\boldsymbol{u}(k)) + ((\boldsymbol{\beta}\cdot\nabla)\boldsymbol{u}(k),\boldsymbol{u}(k)) + \int_\Gamma k\boldsymbol{u}(k)\cdot\boldsymbol{n}\,d\gamma = (\boldsymbol{f},\boldsymbol{u}(k)),$$

and then:

$$k = \frac{(\boldsymbol{f}, \boldsymbol{u}(k)) - \mu \|\nabla \boldsymbol{u}(k)\|^2 - ((\boldsymbol{\beta} \cdot \nabla)\boldsymbol{u}(k), \boldsymbol{u}(k))}{Q} = \phi(k).$$

This is a fixed point equation that could be solved with the following iterative procedure (we have denoted with l the subiteration index and with $\boldsymbol{V}_h$ and Q_h the subspaces of $\boldsymbol{V}$ and $L^2(\Omega)$ respectively):

Algorithm 10

(See Figure 4.2) `Given` k_h^1 `and` ε, `do until convergence`

- `Solve`

$$\begin{cases} a_L(\boldsymbol{u}_h^l(k_h^l), \boldsymbol{v}_h) + ((\boldsymbol{\beta} \cdot \nabla)\boldsymbol{u}_h^l(k_h^l), \boldsymbol{v}_h) + b(p_h^l(k_h^l), \boldsymbol{v}_h) + \displaystyle\int_\Gamma k_h^l \boldsymbol{v}_h \cdot \boldsymbol{n}\, d\gamma = \\ \qquad\qquad = (\boldsymbol{f}, \boldsymbol{v}_h), \qquad \forall \boldsymbol{v}_h \in \boldsymbol{V}_h, \\ b(q_h, \boldsymbol{u}_h^l(k_h^l)) = 0, \qquad \forall q_h \in Q_h. \end{cases} \tag{4.22}$$

- `Compute`

$$k_h^{l+1} = \frac{(\boldsymbol{f}, \boldsymbol{u}_h^l(k_h^l)) - \mu \|\nabla \boldsymbol{u}_h^l(k^l)\|^2 - ((\boldsymbol{\beta} \cdot \nabla)\boldsymbol{u}_h^l(k_h^l), \boldsymbol{u}_h^l(k_h^l))}{Q} \tag{4.23}$$

- `if` $|k_h^{l+1} - k_h^l| < \varepsilon$

  `exit`

- `else` $l = l + 1$

`end` $\diamond$

In the Navier-Stokes case, it is possible to set

$$\boldsymbol{\beta} = \boldsymbol{u}_h^{l-1}$$

in Algorithm 10.

In the particular case $\boldsymbol{f} = \boldsymbol{0}$, the velocity $\boldsymbol{u}$ depends linearly on k. Therefore, denoting with $\widetilde{\boldsymbol{u}}$ the solution of problem (4.21), with $\boldsymbol{f} = \boldsymbol{0}$ and $k = 1$, the solution $\boldsymbol{u}$ is given by

$$\boldsymbol{u} = k\widetilde{\boldsymbol{u}}. \tag{4.24}$$

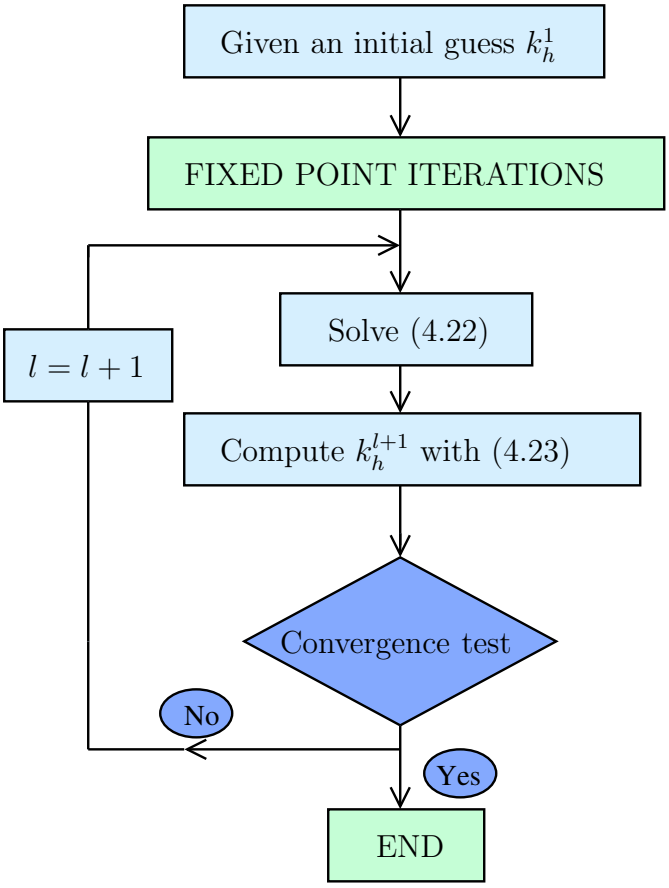

Figure 4.2: Algorithm 10 for the prescription of one flow rate conditions, steady case.

Posing $\boldsymbol{v} = \boldsymbol{u}$ in (4.21), with $\boldsymbol{f} = \boldsymbol{0}$, we obtain:

$$\mu\|\nabla\boldsymbol{u}\|^2 + ((\boldsymbol{\beta}\cdot\nabla)\boldsymbol{u},\boldsymbol{u}) + kQ = 0.$$

Substituting (4.24) in the latter equation we obtain

$$\mu k^2\|\nabla\widetilde{\boldsymbol{u}}\|^2 + k^2((\boldsymbol{\beta}\cdot\nabla)\widetilde{\boldsymbol{u}},\widetilde{\boldsymbol{u}}) + kQ = 0$$

and therefore the following explicit expression for k:

$$k = -\frac{Q}{(\mu\|\nabla\widetilde{\boldsymbol{u}}\|^2 + ((\boldsymbol{\beta}\cdot\nabla)\widetilde{\boldsymbol{u}},\widetilde{\boldsymbol{u}}))}.$$

Therefore, in this case we do not need to resort to a fixed point strategy.

In the unsteady case, let us consider the time discretized problem (4.11) together with $(4.10)_{2-6}$. The related weak formulation at time $t = t^{n+1}$ reads:

$$\frac{\alpha}{\Delta t}(\boldsymbol{u}^{n+1}(k^{n+1}),\boldsymbol{v}) + a_L(\boldsymbol{u}^{n+1}(k^{n+1}),\boldsymbol{v}) + ((\boldsymbol{\beta}^{n+1}\cdot\nabla)\boldsymbol{u}^{n+1}(k^{n+1}),\boldsymbol{v}) +$$

$$+\int_\Gamma k^{n+1}\boldsymbol{v}\cdot\boldsymbol{n}\,d\gamma=(\boldsymbol{f}^{n+1},\boldsymbol{v})+\sum_{i=0}^{r\le n}\frac{\tau_i}{\Delta t}(\boldsymbol{u}^{n-i},\boldsymbol{v}).$$

Posing $\boldsymbol{v}=\boldsymbol{u}^{n+1}$, we obtain for all n:

$$\frac{\alpha}{\Delta t}(\boldsymbol{u}^{n+1}(k^{n+1}),\boldsymbol{u}^{n+1}(k^{n+1}))+\mu(\nabla\boldsymbol{u}^{n+1}(k^{n+1}),\nabla\boldsymbol{u}^{n+1}(k^{n+1}))+$$

$$((\boldsymbol{\beta}^{n+1}\cdot\nabla)\boldsymbol{u}^{n+1}(k^{n+1}),\boldsymbol{u}^{n+1}(k^{n+1}))+\int_\Gamma k^{n+1}\boldsymbol{u}^{n+1}(k^{n+1})\cdot\boldsymbol{n}\,d\gamma=$$

$$=(\boldsymbol{f}^{n+1},\boldsymbol{u}^{n+1}(k^{n+1}))+\sum_{i=0}^{r\le n}\frac{\tau_i}{\Delta t}(\boldsymbol{u}^{n-i},\boldsymbol{u}^{n+1}(k^{n+1}))=0,$$

and then:

$$k^{n+1}=\frac{(\boldsymbol{f}^{n+1},\boldsymbol{u}^{n+1}(k^{n+1}))+\sum_{i=0}^{r\le n}\frac{\tau_i}{\Delta t}(\boldsymbol{u}^{n-i},\boldsymbol{u}^{n+1}(k^{n+1}))}{Q^{n+1}}+$$

$$-\frac{\frac{\alpha}{\Delta t}(\boldsymbol{u}^{n+1}(k^{n+1}),\boldsymbol{u}^{n+1}(k^{n+1}))+\mu(\nabla\boldsymbol{u}^{n+1}(k^{n+1}),\nabla\boldsymbol{u}^{n+1}(k^{n+1}))}{Q^{n+1}}+$$

$$-\frac{((\boldsymbol{\beta}^{n+1}\cdot\nabla)\boldsymbol{u}^{n+1}(k^{n+1}),\boldsymbol{u}^{n+1}(k^{n+1}))}{Q^{n+1}}=\phi^{n+1}(k^{n+1})$$

that could be solved with a fixed point algorithm like the previous one.

The general case

Let us consider Problem 22 as our model. For its numerical resolution, we can think to use an iterative method such that at each iteration we solve separately the single problems (P) and (A) and we check condition (C_j) until convergence. Indipendently from the algorithm chosen, let us notice that the adjoint problem (A) in Problem 22 (and also in Problem 23 and 24) depends linearly on the values of the natural boundary condition $(\int_{\Gamma_j}\boldsymbol{u}(k_j)\cdot\boldsymbol{n}\,d\gamma-Q_j)$ on Γ_j. Therefore, if for all $i=1,\dots,m$, $(\boldsymbol{\lambda}_{u,i},\,\boldsymbol{\lambda}_{p,i})$ is solution of:

$$\begin{cases} a_L(\boldsymbol{\lambda}_{u,i},\boldsymbol{v})+((\boldsymbol{\beta}\cdot\nabla)\boldsymbol{v},\boldsymbol{\lambda}_{u,i})+b(\lambda_{p,i},\boldsymbol{v})-\displaystyle\int_{\Gamma_i}\boldsymbol{v}\cdot\boldsymbol{n}\,d\gamma=0, \quad \forall\boldsymbol{v}\in\boldsymbol{V},\\ b(\boldsymbol{\lambda}_{u,i},q)=0, \quad \forall q\in L^2(\Omega), \end{cases} \tag{4.25}$$

the solution of (A) in Problem 22 is given by

$$\begin{cases} \boldsymbol{\lambda}_u = \displaystyle\sum_{i=1}^{m} \Big(\int_{\Gamma_i} \boldsymbol{u}(k_j) \cdot \boldsymbol{n}\, d\gamma - Q_i \Big) \boldsymbol{\lambda}_{u,i} \\ \lambda_p = \displaystyle\sum_{i=1}^{m} \Big(\int_{\Gamma_i} \boldsymbol{u}(k_j) \cdot \boldsymbol{n}\, d\gamma - Q_i \Big) \lambda_{p,i}. \end{cases}$$

Hence, instead of the adjoint problem we can solve m problems (4.25) out of the iterative cycle.

In order to obtain an algorithm to solve Problem 22, we could think to look for the zeros of dL_{k_j}, i.e. to find the values k_j satisfying the conditions of fulfilment of the optimal state

$$< dL_{k_j}, \nu >= 0, \quad \forall \nu \in \mathbb{R}.$$

Then, starting from some initial guesses k_j^0, we can utilize the residuals of this equations (i.e. dL_{k_j} itself) to update the values of k_j. In particular, let us consider the following:

Algorithm 11

(See Figure 4.3)

- `Solve for` $j = 1, \ldots, m$ `the problems`

$$\begin{cases} a_L(\boldsymbol{\lambda}_{u,j,h}, \boldsymbol{v}_h) + ((\boldsymbol{\beta} \cdot \nabla)\boldsymbol{v}_h, \boldsymbol{\lambda}_{u,j,h}) + b(\lambda_{p,j,h}, \boldsymbol{v}_h) - \displaystyle\int_{\Gamma_j} \boldsymbol{v}_h \cdot \boldsymbol{n}\, d\gamma = 0, \\ \qquad\qquad\qquad\qquad\qquad\qquad\qquad\qquad \forall \boldsymbol{v}_h \in \boldsymbol{V}_h, \\ b(\boldsymbol{\lambda}_{u,j,h}, q_h) = 0, \qquad \forall q_h \in Q_h, \end{cases} \tag{4.26}$$

- `Given` $k_{j,h}^1$, $j = 1, \ldots, m$ `and` ε, `do until convergence`

  - `Solve`

$$\begin{cases} a_L(\boldsymbol{u}_h^l(k_{j,h}^l), \boldsymbol{v}_h) + ((\boldsymbol{\beta} \cdot \nabla)\boldsymbol{u}_h^l(k_{j,h}^l), \boldsymbol{v}_h) + b(p_h^l(k_{j,h}^l), \boldsymbol{v}_h) + \\ \qquad + \displaystyle\sum_{i=1}^{m} \int_{\Gamma_i} k_{i,h}^l \boldsymbol{v}_h \cdot \boldsymbol{n}\, d\gamma - (\boldsymbol{f}, \boldsymbol{v}_h) = 0, \qquad \forall \boldsymbol{v}_h \in \boldsymbol{V}_h \\ b(q_h, \boldsymbol{u}_h^l(k_{j,h}^l)) = 0, \qquad \forall q_h \in Q_h \end{cases} \tag{4.27}$$

  - `Compute the adjoint solutions`

$$\begin{cases} \boldsymbol{\lambda}_{u,h}^l = \displaystyle\sum_{i=1}^{m} \Big(\int_{\Gamma_i} \boldsymbol{u}_h^l(k_{j,h}^l) \cdot \boldsymbol{n}\, d\gamma - Q_i \Big) \boldsymbol{\lambda}_{u,i,h}^l \\ \lambda_{p,h}^l = \displaystyle\sum_{i=1}^{m} \Big(\int_{\Gamma_i} \boldsymbol{u}_h^l(k_{j,h}^l) \cdot \boldsymbol{n}\, d\gamma - Q_i \Big) \lambda_{p,i,h}^i. \end{cases} \tag{4.28}$$

- if

$$\int_{\Gamma_j} \boldsymbol{\lambda}_{u,h}^l \cdot \boldsymbol{n}\, d\gamma < \varepsilon,\ \forall j = 1, \ldots, m \tag{4.29}$$

  exit

- else

$$k_{j,h}^{l+1} = k_{j,h}^l + \tau_j^l \int_{\Gamma_j} \boldsymbol{\lambda}_{u,h}^l \cdot \boldsymbol{n}\, d\gamma \tag{4.30}$$

$$l = l + 1.$$

- end

A possible expression for the coefficient τ_j^l is:

$$\tau_j^l = -\frac{J(\boldsymbol{u}_h^l)}{|L^2_{k_{j,h}^l}|}.$$

that leads to a steepest descent algorithm. For example, for Problem 22 we obtain the update rule:

$$k_{j,h}^{l+1} = k_{j,h}^l - \frac{\dfrac{1}{2}\displaystyle\sum_{j=1}^{m} \Big(\int_{\Gamma_j} \boldsymbol{u}_h^l \cdot \boldsymbol{n}\, d\gamma - Q_j \Big)^2}{\displaystyle\int_{\Gamma_j} \boldsymbol{\lambda}_{u,h}^l \cdot \boldsymbol{n}\, d\gamma}.$$

This strategy could be extended over all the other proposed problems.

Algorithm 11 allows us to prove that Problem 22 is well posed (for the sake of simplicity, we refer to the case $m = 1$). We have the following:

Proposition 9 *If $\|\boldsymbol{\beta}\|_{\boldsymbol{L}^\infty} \leq \mu/C_P^2$, Problem 22 admits an unique solution $(\boldsymbol{u}(k), p(k), \boldsymbol{\lambda}_u, \lambda_p, k)$.*

Proof

Let us consider the solenoidal space $\boldsymbol{V}^*$ and let us introduce the following operators:

- $P_{\boldsymbol{f}} : \mathbb{R} \to \boldsymbol{V}^*$, that associate to a scalar k the solution $\boldsymbol{u}$ of the following steady Oseen problem:

$$a_L(\boldsymbol{u}, \boldsymbol{v}) + ((\boldsymbol{\beta} \cdot \nabla)\boldsymbol{u}, \boldsymbol{v}) = -\int_\Gamma k\boldsymbol{v} \cdot \boldsymbol{n}\, d\gamma + (\boldsymbol{f}, \boldsymbol{v}) \tag{4.31}$$

  for all $\boldsymbol{v} \in \boldsymbol{V}^*$.

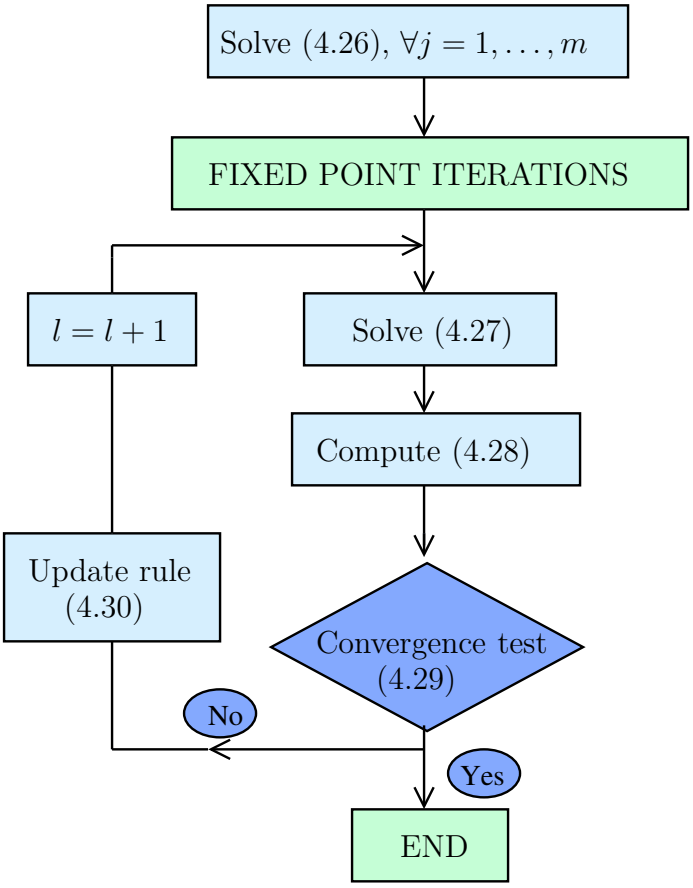

Figure 4.3: Algorithm 11 for the prescription of flow rates conditions, steady case.

- $S_\tau : (\mathbb{R} \times \mathbb{R}) \to \mathbb{R}$ such that $S_\tau(k, j) = k + \tau j$, with τ given.
- $A : \boldsymbol{V}^* \to \mathbb{R}$ such that $A(\boldsymbol{v}) = \displaystyle\int_\Gamma \boldsymbol{v} \cdot \boldsymbol{n}\, d\gamma$.

Let us notice that all the operators introduced are linear. Problem 22 can be reformulated as a fixed point problem: *find the fixed point k of the operator* $T : \mathbb{R} \to \mathbb{R}$:

$$T(k) = S_\tau(k, A(P_{\boldsymbol{0}}(A(P_{\boldsymbol{f}}(k)) - Q)))$$

From (4.31), posing $\boldsymbol{v} = \boldsymbol{u}$, $\|\boldsymbol{v}\|_{\boldsymbol{V}^*} = \|\nabla \boldsymbol{v}\|$, with $\|\cdot\|$ the $\boldsymbol{L}^2$ norm and with C_T and C_p the trace and Poincaré inequalities constant respectively, we obtain:

$$\mu \|\nabla \boldsymbol{u}\|^2 \leq \|\boldsymbol{\beta}\|_{\boldsymbol{L}^\infty} \|\boldsymbol{u}\|^2 + |k| C_T \|\boldsymbol{u}\|_{\boldsymbol{H}^1(\Omega)} + \|\boldsymbol{f}\| \, \|\boldsymbol{u}\| \leq$$

$$\leq |k| C_T \sqrt{C_P^2 + 1} \|\nabla \boldsymbol{u}\| + \frac{1}{2\varepsilon} \|\boldsymbol{f}\|^2 + \left(\|\boldsymbol{\beta}\|_{\boldsymbol{L}^\infty} + \frac{\varepsilon}{2} \right) \|\boldsymbol{u}\|^2 \leq$$

$$\leq \frac{|k|^2 C_T^2 (C_P^2+1)}{2\varepsilon} + \frac{\varepsilon}{2}\|\nabla \boldsymbol{u}\|^2 + \frac{1}{2\varepsilon}\|\boldsymbol{f}\|^2 + C_P^2\Big(\|\boldsymbol{\beta}\|_{\boldsymbol{L}^\infty} + \frac{\varepsilon}{2}\Big)\|\nabla \boldsymbol{u}\|^2,$$

and then the following estimate holds:

$$\|\boldsymbol{u}\|_{\boldsymbol{V}^*} \leq \sqrt{\frac{1}{C_1}\Big(\|\boldsymbol{f}\|^2 + C_2|k|^2\Big)} \leq \frac{1}{\sqrt{C_1}}\|\boldsymbol{f}\| + \sqrt{\frac{C_2}{C_1}}|k|, \tag{4.32}$$

with

$$\begin{cases} C_1 = \Big(\mu - \Big(\frac{\varepsilon}{2} + C_P^2\Big(\|\boldsymbol{\beta}\|_{\boldsymbol{L}^\infty} + \frac{\varepsilon}{2}\Big)\Big)\Big) \\ C_2 = C_T^2(1+C_p^2) \end{cases}$$

Let us notice that from the arbitrariety of ε follows that $C_1 > 0$ if

$$\|\boldsymbol{\beta}\|_{\boldsymbol{L}^\infty} \leq \frac{\mu}{C_P^2}$$

Let us prove that, under suitable assumptions, T is a contraction:

$$|T(k_1) - T(k_2)| = |k_1 + \tau A(P_{\mathbf{0}}(A(P_{\boldsymbol{f}}(k_1)) - Q)) - k_2 - \tau A(P_{\mathbf{0}}(A(P_{\boldsymbol{f}}(k_2)) - Q))| =$$

$$= |(k_1 - k_2) + \tau A(P_{\mathbf{0}}(A(P_{\mathbf{0}}(k_1 - k_2))))| \leq$$

$$|(k_1 - k_2) + \tau C_T \|P_{\mathbf{0}}(A(P_{\mathbf{0}}(k_1 - k_2)))\|_{\boldsymbol{H}^1(\Omega)}| \leq$$

$$\leq |(k_1 - k_2) + \tau C_T \sqrt{C_p^2+1}\|P_{\mathbf{0}}(A(P_{\mathbf{0}}(k_1 - k_2)))\|_{\boldsymbol{V}^*}| \leq$$

$$\leq |(k_1 - k_2) + \tau C_T \sqrt{C_p^2+1}\sqrt{\frac{C_2}{C_1}}|A(P_{\mathbf{0}}(k_1 - k_2))| \leq$$

$$\leq |(k_1 - k_2) + \tau C_T \sqrt{C_p^2+1}\sqrt{\frac{C_2}{C_1}} C_T \sqrt{C_p^2+1}\|P_{\mathbf{0}}(k_1 - k_2)\|_{\boldsymbol{V}^*}| \leq$$

$$\leq \Big||k_1 - k_2| + \tau C_T^2 (C_p^2+1)\sqrt{\frac{C_2}{C_1}}\sqrt{\frac{C_2}{C_1}}|k_1 - k_2|\Big| \leq \Big|1 + \tau C_T^2 (C_p^2+1)\frac{C_2}{C_1}\Big||k_1 - k_2| \tag{4.33}$$

Therefore T is a contraction if

$$\frac{-2C_1}{C_T^2(C_p^2+1)C_2} < \tau < 0.$$

$\diamond$

4.5.2 Mean pressure problems

We can extend Algorithm 11 to the problems shown in Section 4.4. Let us notice that if the control variable is a set of scalar (i.e. for Problem 25 and 29), the adjoint problem could be solved out of the iterative cicle. In particular, referring to Problem 25 by way of example, if $(\widetilde{\boldsymbol{\lambda}}_u, \widetilde{\lambda}_p)$ is solution of the following problem

$$\begin{cases} a_L(\widetilde{\boldsymbol{\lambda}}_u, \boldsymbol{v}) + ((\boldsymbol{\beta}\cdot\nabla)\boldsymbol{v}, \widetilde{\boldsymbol{\lambda}}_u) + b(\widetilde{\lambda}_p, \boldsymbol{v}) = 0, \quad \forall \boldsymbol{v} \in \boldsymbol{V}, \\ b(\widetilde{\boldsymbol{\lambda}}_u, q) = -\displaystyle\int_\Omega q\, d\omega, \quad \forall q \in L^2(\Omega) \end{cases}$$

we can build the solution of the adjoint problem (A) in the iterative cycle by:

$$\begin{cases} \boldsymbol{\lambda}_u = \Big[\displaystyle\sum_{i=1}^m \Big(\frac{1}{|\Gamma_i|}\int_{\Gamma_i} p(k_j)\, d\gamma - P_i\Big)\Big]\widetilde{\boldsymbol{\lambda}}_u \\ \lambda_p = \Big[\displaystyle\sum_{i=1}^m \Big(\frac{1}{|\Gamma_i|}\int_{\Gamma_i} p(k_j)\, d\gamma - P_i\Big)\Big]\widetilde{\lambda}_p \end{cases}$$

Therefore, we obtain the following algorithm for the resolution of Problem 25:

Algorithm 12

(See Figure 4.4)

- `Solve`

$$\begin{cases} a_L(\widetilde{\boldsymbol{\lambda}}_{u,h}, \boldsymbol{v}_h) + ((\boldsymbol{\beta}\cdot\nabla)\boldsymbol{v}_h, \widetilde{\boldsymbol{\lambda}}_{u,h}) + b(\widetilde{\lambda}_{p,h}, \boldsymbol{v}_h) = 0, \quad \forall \boldsymbol{v}_h \in \boldsymbol{V}_h, \\ b(\widetilde{\boldsymbol{\lambda}}_{u,h}, q_h) = -\displaystyle\int_\Omega q_h\, d\omega, \quad \forall q_h \in Q_h \end{cases} \tag{4.34}$$

- `Given` k_j^1, $j = 0, \ldots, m$ `and` ε, `do until convergence`

  - `Solve`

$$\begin{cases} a_L(\boldsymbol{u}_h^l(k_{j,h}^l), \boldsymbol{v}_h) + ((\boldsymbol{\beta}\cdot\nabla)\boldsymbol{u}_h^l(k_{j,h}^l), \boldsymbol{v}_h) + b(p_h^l(k_{j,h}^l), \boldsymbol{v}_h) + \\ \qquad + \displaystyle\sum_{i=0}^m \int_{\Gamma_i} k_{i,h}^l \boldsymbol{v}_h \cdot \boldsymbol{n}\, d\gamma - (\boldsymbol{f}, \boldsymbol{v}_h) = 0, \qquad \forall \boldsymbol{v}_h \in \boldsymbol{V}_h \\ b(q_h, \boldsymbol{u}_h^l(k_{j,h}^l)) = 0, \qquad \forall q_h \in Q_h \end{cases} \tag{4.35}$$

  - `Compute the adjoint solutions`

$$\begin{cases} \boldsymbol{\lambda}_{u,h}^l = \Big[\displaystyle\sum_{i=1}^m \Big(\frac{1}{|\Gamma_i|}\int_{\Gamma_i} p_h^l(k_{j,h}^l)\, d\gamma - P_i\Big)\Big]\widetilde{\boldsymbol{\lambda}}_{u,h} \\ \lambda_{p,h}^l = \Big[\displaystyle\sum_{i=1}^m \Big(\frac{1}{|\Gamma_i|}\int_{\Gamma_i} p_h^l(k_{j,h}^l)\, d\gamma - P_i\Big)\Big]\widetilde{\lambda}_{p,h} \end{cases} \tag{4.36}$$

- if

$$\int_{\Gamma_j} \boldsymbol{\lambda}_{u,h}^l \cdot \boldsymbol{n}\, d\gamma < \varepsilon, \quad \forall j = 0, \ldots, m$$

  exit

- else

$$k_{j,h}^{l+1} = k_{j,h}^l + \tau_j^l \int_{\Gamma_j} \boldsymbol{\lambda}_{u,h}^l \cdot \boldsymbol{n}\, d\gamma \quad \forall j = 0, \ldots, m$$

$$l = l + 1$$

- end

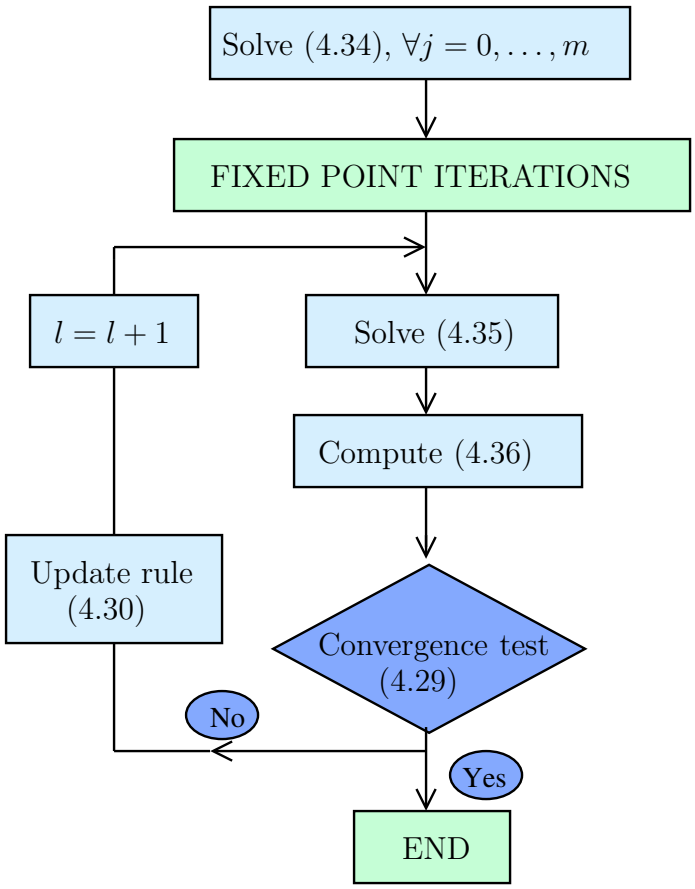

Figure 4.4: Algorithm 12 for the prescription of mean pressure conditions, steady case.

4.6 Numerical results

In this section we present some numerical results for the validation of the algorithms introduced in Section 4.5. In particular, in Section 4.6.1 we focus on the flow rate problems, while in Section 4.6.2 on the mean pressure problems. In all the simulations we used the 2D Finite Elements library *Freefem++* (see [21]).

4.6.1 Flow rate problems

In the simulation we are going to present, the computational domain is a rectangular R, whose size is $6 \times 1cm$, with viscosity $\mu = 0.035cm^2/s$.

In order to validate the algorithms proposed in Section 4.5.1, we imposed both a steady ($Q = 0.1cm^2/s$) and a pulsatile ($Q = 0.15 + 0.1cos(2\pi t)cm^2/s$ for Algorithm 10 and $Q = 0.1cos(2\pi t)cm^2/s$ for Algorithm 11) flow rate at the inlet of R. Algorithm 10 (with an *Aitken* procedure) converges in 21 iterations in the steady case (Figure 4.5, left) and in 3 (average) iterations in the unsteady case (Figure 4.6), with tollerance 10^{-6}. Also with Algorithm 11 the numerical results are in good agreement with the analytical ones (see Figures 4.5, right, and Figure 4.7). The number of iterations in this case is shown in Table 4.1.

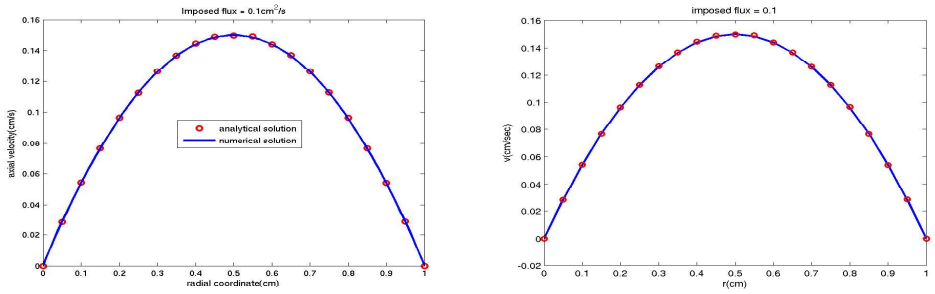

Figure 4.5: Axial velocity computed with Algorithm 10 (left - toll = 10^{-6}) and Algorithm 11 (right - toll = 10^{-7}) - steady flux imposed - o numerical solution, - analitical solution

Number of iterations	$\tau = -1$	$\tau_n = -J(u^n)/L^2_{k^n}$	$\tau_n = -J(u^n)/L^2_{k^n}$+Aitken
Steady case	87	22	4
Unsteady case	-	7	3

Table 4.1: Number of iterations for the convergence of Algorithm 11 (in average for the unsteady case) - toll = 10^{-7}

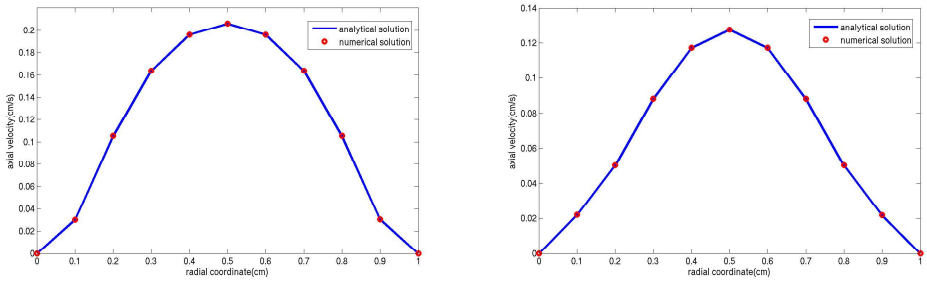

Figure 4.6: Axial velocity computed with Algorithm 10 - cosinusoidal flux imposed - $t = 0.3s$ on the left and $t = 0.6s$ on the right - toll $= 10^{-6}$

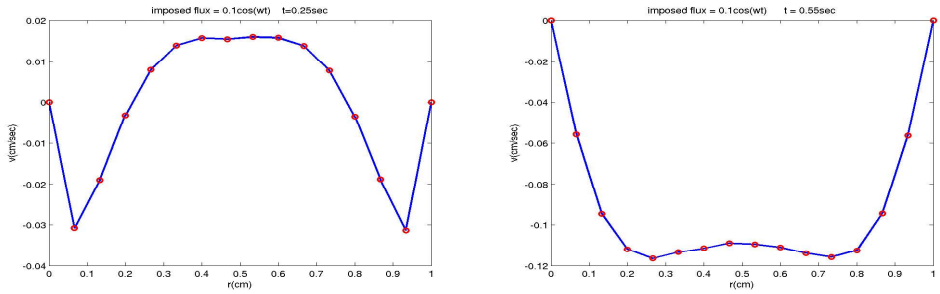

Figure 4.7: Axial velocity computed with Algorithm 11 - cosinusoidal flux imposed - toll $= 10^{-8}$ - o numerical solution, - analitical solution

4.6.2 Mean pressure problems

In the first simulation, we would like to impose a mean pressure $P = 1\, g/s^2 cm$ at the outlet of a trapezoidal domain T (see Figure 4.8). We indicate with $\boldsymbol{a}$ the axial direction. In this case it is given by $y = 0.5$ (see Figure 4.8). Using Algorithm 12, an undesiderable radial velocity, a dirty axial velocity at the outlet and a dirty pressure on the corner of the outlet occur (see Figure 4.9, left, and Figures 4.10). To avoid these effects, we solve Problem 26 minimizing functional (4.17), with the same iterative scheme. Figure 4.9, right, and Figures 4.11 show that this strategy is able to reduce these effects of several order of magnitude.

The same effects occur using the "complete" treatment of the viscous term. In particular, we would like to impose the mean pressure $P = 1\, g/s^2 cm$ in the domain R (see Figure 4.12). Both minimizing functional (4.19) (refer to Problem 28, to Figure 4.13, left, and to Figures 4.14) and minimizing functional (4.17) (see Figure 4.13, right and Figure 4.15), the boundary effects reduce significantly. Finally, we used the "complete" treatment of the viscous term in the trapezoidal domain T. In this case we expect that the boundary effects due to the formulation and to the geometry sum up. This is confirmed by Figures 4.16. Nevertheless,

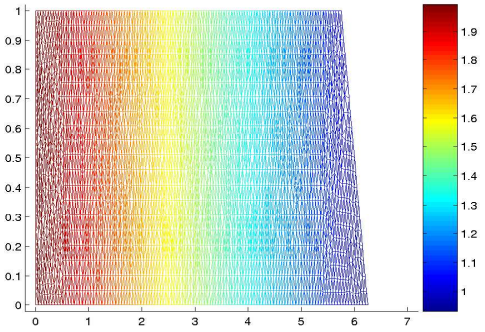

Figure 4.8: Mean pressure $P = 1\, g/s^2 cm$ prescribed at the outlet of a trapezoidal domain minimizing functional (4.15) - toll = 10^{-7}

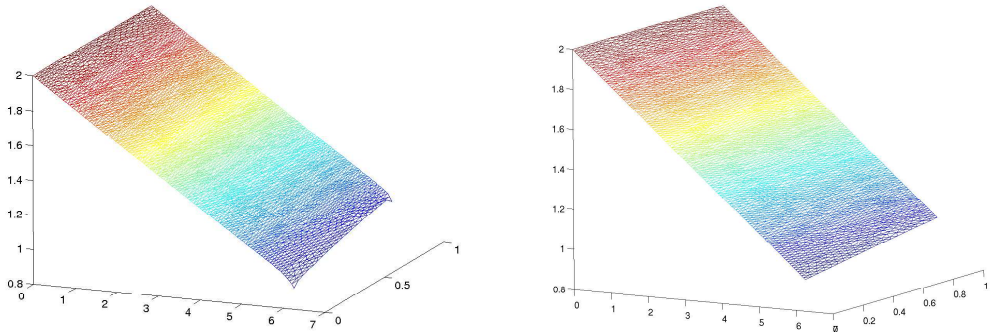

Figure 4.9: Mean pressure $P = 1\, g/s^2 cm$ prescribed at the outlet of a trapezoidal domain minimizing functional (4.15) (left) and functional (4.17) (right) - toll = 10^{-7}

minimizing functional (4.17) we reduce these effects as well (see Figures 4.17).

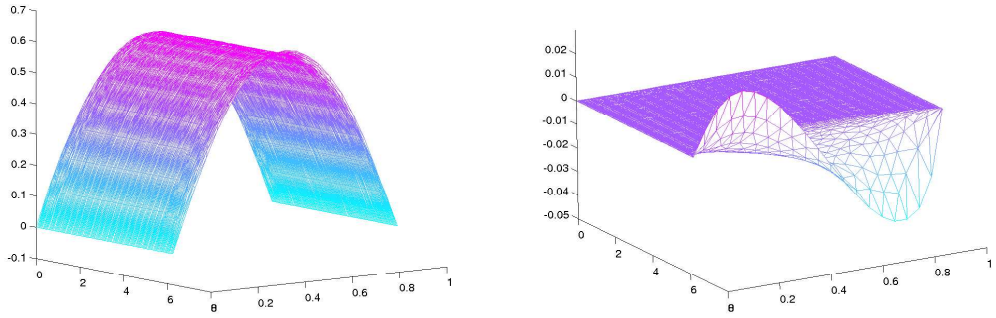

Figure 4.10: Axial (left) and tangential (right) velocity prescribing a mean pressure $P = 1\, g/s^2 cm$ at the outlet of a trapezoidal domain minimizing functional (4.15) - toll = 10^{-7}

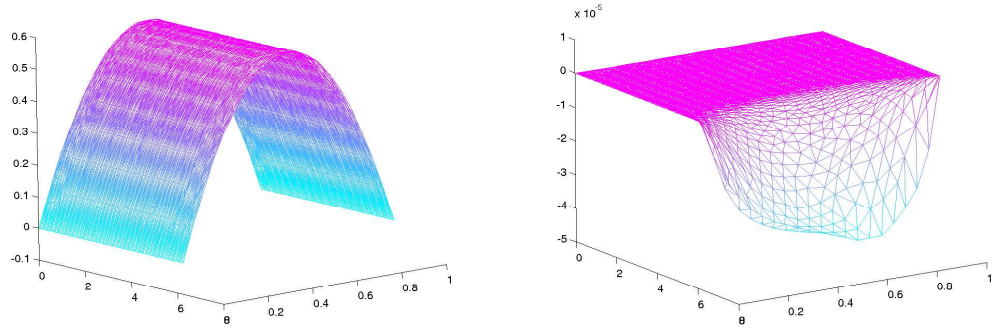

Figure 4.11: Axial (left) and tangential (right) velocity prescribing a mean pressure $P = 1\, g/s^2 cm$ at the outlet of a trapezoidal domain minimizing functional (4.17) - toll = 10^{-7}

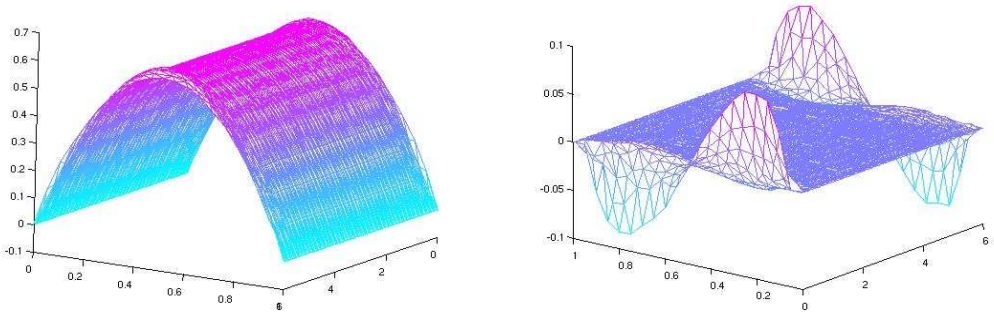

Figure 4.12: Axial (left) and tangential (right) velocity prescribing a mean pressure $P = 1\, g/s^2 cm$ at the outlet of a rectangular domain using the "complete" treatment of the viscous term and minimizing functional (4.15) - toll = 10^{-7}

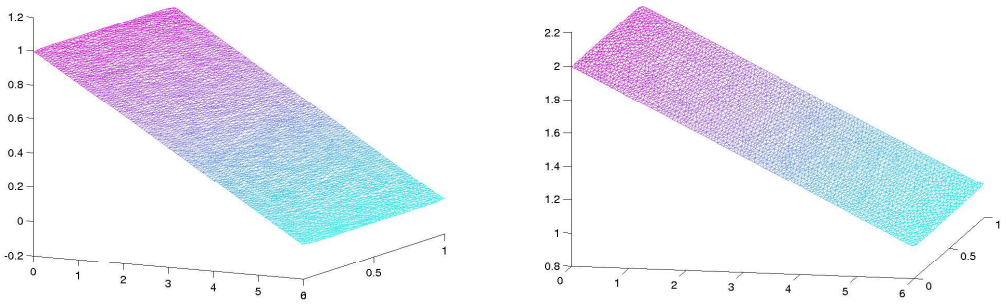

Figure 4.13: Mean pressure $P = 0\, g/s^2 cm$ prescribed at the outlet of a rectangular domain using the "complete" treatment of the viscous term, minimizing functional (4.19) (left) and functional (4.17) (right) - toll = 10^{-7}

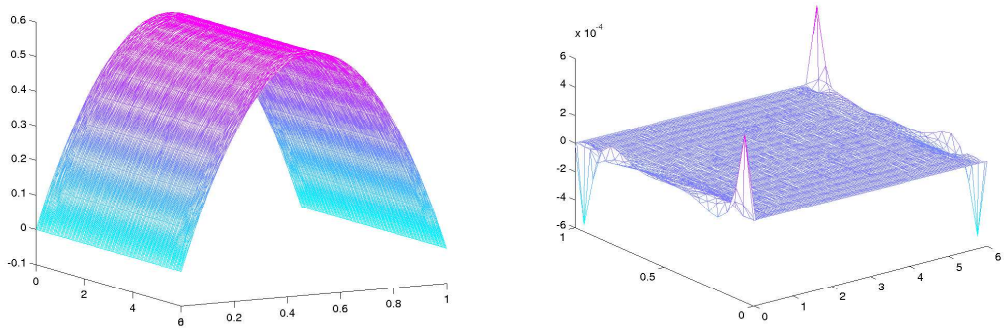

Figure 4.14: Axial (left) and tangential (right) velocity prescribing a mean pressure $P = 0\, g/s^2 cm$ at the outlet of a rectangular domain using the "complete" treatment of the viscous term and minimizing functional (4.19) - toll = 10^{-7}

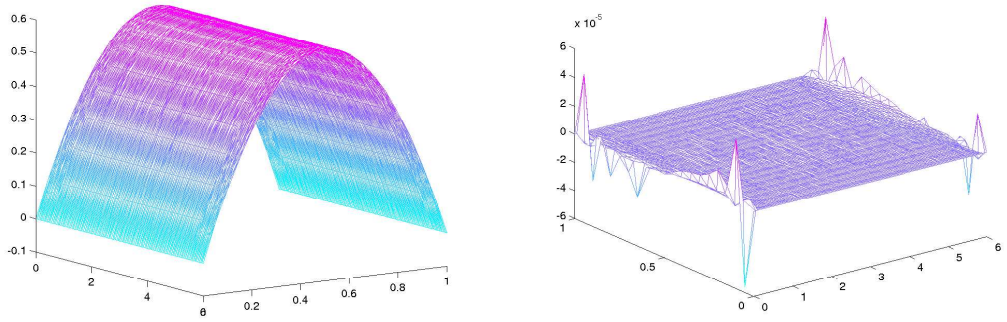

Figure 4.15: Axial (left) and tangential (right) velocity prescribing a mean pressure $P = 0\, g/s^2 cm$ at the outlet of a rectangular domain using the "complete" treatment of the viscous term and minimizing functional (4.17) - toll = 10^{-7}

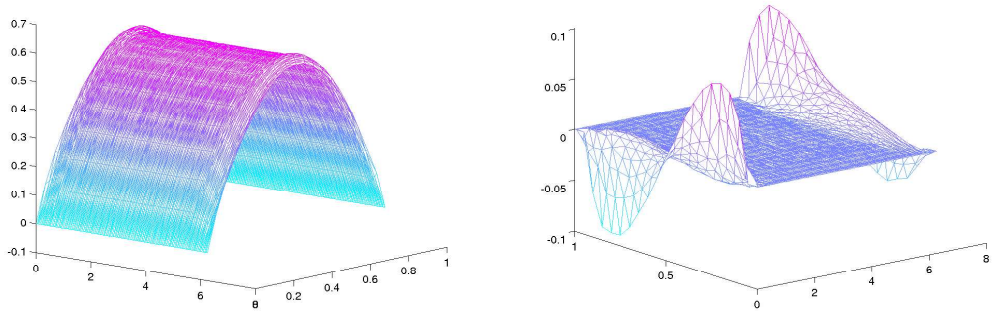

Figure 4.16: Axial (left) and tangential (right) velocity prescribing a mean pressure $P = 0\, g/s^2 cm$ at the outlet of a trapezoidal domain using the "complete" treatment of the viscous term and minimizing functional (4.15) - toll = 10^{-7}

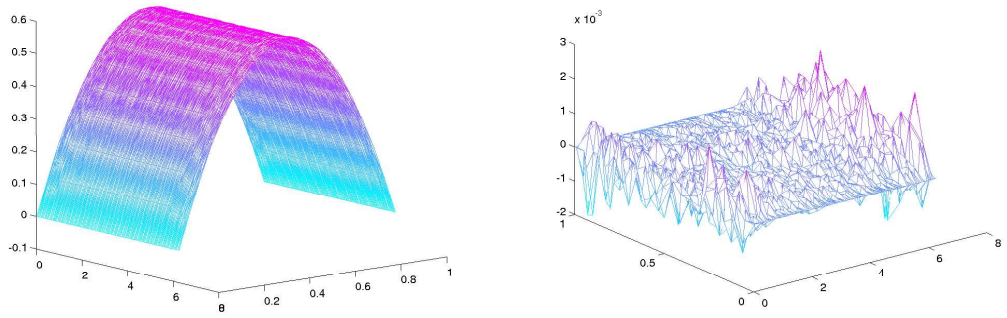

Figure 4.17: Axial (left) and tangential (right) velocity prescribing a mean pressure $P = 0\, g/s^2 cm$ at the outlet of a trapezoidal domain using the "complete" treatment of the viscous term and minimizing functional (4.17) - toll = 10^{-7}

Ringraziamenti

Ringrazio:

Il prof. A. Veneziani, con cui questo lavoro è stato interamente svolto, per l' opportunità e la fiducia datemi e per l'imponente mole di sapere scientifico trasmessami (e spero, almeno in parte, assorbita).
Alessandro V. per l'affetto fraterno dimostrato.

Il prof. L. Formaggia, con la cui collaborazione è stato svolto il lavoro presentato nel Capitolo 4, per la costante disponibilità e i numerosi consigli scientifici.
Il dott. F. Nobile, con la cui collaborazione è stato svolto il lavoro presentato nella Sezione 3.4 e le stime *a priori* nella Sezione 2.3.2, per la costante disponibilità e le numerose discussioni (lezioni) scientifiche.
L' ing. R. Ponzini e il prof. A. Redaelli del Dipartimento di Bioingegneria per avermi dato la possibilità di lavorare con loro al lavoro presentato nella Sezione 3.2.
Il prof. Quarteroni per avermi fornito l' opportunità di lavorare nel suo prestigioso gruppo scientifico.

I proff. F. Migliavacca e G. Dubini per aver fornito la geometria relativa alla connessione cavo-polmonare utilizzata nelle simulazioni presentate in Sezione 2.6.2, nonchè per la costante disponibilità.
L'ing. Luca Dedè per l'indispensabile supporto relativo al lavoro presentato nel Capitolo 4 e per la costante disponibilità.
Il dott. M. Prosi per aver fornito la geometria carotidea e i dati fisiologici utilizzati nelle simulazioni presentate in Sezione 2.6.2, nonchè per la costante disponibilità.
I proff. J. Peirò e S. Sherwin per la collaborazione durante i due mesi di lavoro presso l'Imperial College - Londra.

L' ing. Passerini, i dott.i V. Martin e L. Paglieri, G. Aloe, L. Lo Curto, il dott. P. Zunino, gli ingg. M. Perego, P. Ferrandi, L. Mirabella, A. De Vecchi, R. Balossino, T. Kendon, M. Broadhurst, P. Curci, S. Minisini, A. Moura, il prof

F. Saleri e i dott.i E. Miglio, M. Verani, S. Perotto, S. Micheletti, S. DeParis, C. Prud'homme per la costante disponibilità.

Bibliography

[1] Agoshkov V.I., Control and Inverse Problems Theory Approaches for Solving some Hydrodynamics Equations *MOX Report n. 50*

[2] Becker R, Kapp H., Rannacher R., Adaptive Finite Element Methods for Optimal Control of PDE: Basic Concept *SIAM J. Control Optim.*; **39**(1): 113-132, 2000.

[3] Begue C., Conca C., Murat F., Pironneau O., Les équations de Stokes et de Navier-Stokes avec des conditions aux limites sur la pression. In Brezis H. and Lions J. (eds) - *Nonlinear Partial Differential Equations and their applications*. College de France Seminar, Vol IX, 179-264, 1988. Pittman RNM Longman

[4] Bellhouse B.J., Bellhouse F.H., Curl C.M., McMillan T.I., Gunning A.J., Spratt E.H., McMurray S.B., Nelems J.M., *Trans. Amer. Soc. Artif. Int. Organs*; **19**, 77-79, 1973.

[5] Berggren M., Numerical solution of a flow-control problem: vorticity reduction by dinamic boundary action *SIAM J. Sci. Comput.*; **19**(3): 829-860,1998.

[6] Bloch K.J. and Maki D.G., Hyperviscosity syndrome associated with immunoglobulin abnormalities, *J. Sem. Hematol.* ; **10**: 113-126 , 1973.

[7] Brezzi F., Fortin M., *Mixed and Hybrid Finite Element Method*, Springer, 1991.

[8] Chorin A.J., Numerical solution of the Navier-Stokes equations. *Math. Comp.*; **22**, 745-762, 1968.

[9] Corno A., Prosi M., Fridez P., Zunino P., Quarteroni A., von Segesser L., The non-circular shape of FlaWatch-Pab prevents the need for pulmonary artery reconstruction after banding. Computational fluid-dynamics and clinical correlaions, *Europ. J. Cardio-thoraic Surg.*, 2005, in press.

[10] Doucette J.W., Corl P.D., Payne H.M., Flynn A.E., Goto M., Nassi M., Segal J., Validation of a Doppler guide wire for intravascular measurement of coronary artery flow velocity, *Circulation*; **85**: 1899-1911, 1992.

[11] Fernández, M., Milisic V., Quarteroni A., Analysis of a multiscale blood flow model based on the coupling of ODE's and hyperbolic PDE's, *SIAM J. on Multiscale Model. Simul.*, **4**(1): 215-236, 2005.

[12] Fernández, M., Moubachir, M., A Newton method using exact jacobians for solving fluid-structure coupling. *Computers & Structures*, **83**(2-3): 127-142, 2005.

[13] Fernández, M., Moura, A., Vergara, C., Defective boundary conditions applied to multiscale analysis of blood flow. ESAIM Proceedings, Vol. 14, CEMRACS 2005.

[14] Formaggia L., Gerbeau J.F., Nobile F., Quarteroni A., Numerical treatment of Defective Boundary Conditions for the Navier-Stokes equation, *SIAM J. Num. Anal.*; **40**(1):376-401, 2002

[15] Formaggia L., Gerbeau J.F., Nobile F., Quarteroni A., On the coupling of 3d and 1d Navier-Stokes equations for flow problems in compliant vessels. *Comp. Math. Appl. Mech. Eng.*; **191**:561–582.

[16] Formaggia L., Nobile F., Quarteroni A., Veneziani A., Multiscale modelling of the circulatory system: a preliminary analysis, *Comp. Vis. Science*, **2**:75–83, 1999.

[17] Formaggia L., Quarteroni A., Mathematical Modelling and Numerical Simulation of the Cardiovascular System, In *Modelling of Living Systems*, Handbook of Numerical Analysis, Ayache N, Ciarlet PG, Lions JL (eds), Elsevier Science, Amsterdam, 2004.

[18] Formaggia L., Quarteroni A., Veneziani A., The circulatory system:from case studies to mathematical modeling, In *Integration of Complex Systems in Biomedicine*, Formaggia L., Quarteroni A., Veneziani A. eds., Springer-Italia, Milano, 2006 (in press).

[19] Formaggia L. and Veneziani A., Reduced and multiscale models for the human cardiovascular system, *Lecture Notes, VKI Lecture Series*, 2003.

[20] Formaggia L., Veneziani A., Vergara C., new formulation of defective boundary problems in incompressible fluid dynamics. In preparation.

[21] `www.freefem.org`.

[22] Fung Y.C., *Biomechanics: Mechanical properties of living tissues*, Springer-Verlag, New York , 1993.

[23] Gauthier A., Saleri F., Veneziani A., A fast preconditioner for the incompressible Navier-Stokes equations. *Comput. and Visual. in Science*; **2-3**: 105–112.

[24] Girault V., Raviart P.A., *Finite Element Methods for Navier-Stokes Equations*, Springer-Verlag, 1986.

[25] Grandmont C., Analyse mathematique et numerique de quelques problemes d'interaction fluide structure, *Ph.D. thesis*, Paris VI, 1998.

[26] Guermond J.L. and Shen J., Velocity-correction projection methods for incompressible flows, *SIAM J. Numer. Anal.*; **41**(1): 112-134, 2003.

[27] Hale J.F., McDonald D.A., Womersley J.R., Velocity profiles of oscillating arterial flow, with some calculations of viscous drag and the Reynolds numbers, *J. Physiol.*; **128**(3): 629-40, 1955.

[28] Haywood J.G., Rannacher R., Turek S., Artificial Boundary and Flux and Pressure Conditions for the Incompressible Navier-Stokes Equations, *Int. Journ. Num. Meth. Fluids*; **22**: 325-352, 1996.

[29] He X., Ku D.N., Moore J.E. Jr, Simple calculation of the velocity profiles for pulsatile flow in a blood vessel using *Mathematica*, *Ann. Biomed. Eng.*; **21**: 45-49,1993.

[30] Hoppensteadt F., Peskin C., *Mathematics in Medicine and the Life Sciences. Text in Applied Mathematics*. Springer-Verlag, New York, 1992.

[31] Karanadiakis K.E., Israeli M., Orsag S.A., High-order splitting methods for the incompressible Navier-Stokes equation, *J. Comp. Phys.*; **97**: 414-443, 1991.

[32] Ladyzhenskaya O.A., The mathematical Theory of Viscous Incompressible Flow, *Mathematics and Apllications*, Vol. 2, 1987, Gordon and Breach Science Publisher.

[33] Laganá K., Balossino R., Migliavacca F., Pennati G., Bove E.L., de Leval M.R., Dubini G., Multiscale modeling of the cardiovascular system: application to the study of pulmonary and coronary perfusions in the univentricular circulation, *J. of Biomech.*; **38**: 1129-1141, 2005.

[34] Langtangen H. P., *Python Scripting for Computational Science*, Springer, 2004.

[35] LeVeque R., Finite Difference Methods for Differential Equations, *On line Lecture Notes*, 2005.

[36] `www.lifev.org`

[37] Lions J.L., *Optimal Control of System Governed by Partial Differential Equations*, Springer-Verlag, New York, 1971.

[38] McDonald D., *Blood flow in arteries*. Edward Arnold Ltd., London, 1990.

[39] Migliavacca F., Dubini G., Bove E.L., de Leval M.R., Computational fluid dynamics simulations in accurate realistic 3-D geometries of the total cavopulmonary anastomosis: the influence of the inferior caval anastomosis, *Journal of Biomechanical Engineering - ASME Transactions*; **125**(6): 805-813, 2003.

[40] Morris L., Delassus P., Grace P., Wallis F., Walsh M., McGloughlin T., Effects of flat, parabolic and realistic steady flow inlet profiles on idealised and realistic stent graft fits through Abdominal Aortic Aneurysms (AAA), *Med. Eng. Phys.*; **28**: 19-26, 2006.

[41] Nichols W.W., O'Rourke M.F. , *McDonald's blood flow in arteries*, (V Ed.), Hodder Arnold (Eds.), 1990.

[42] Nobile F., Numerical Approximation of Fluid-Structure Interaction Problems with Application to Haemodynamics, *Ph.D. Thesis*; EPFL, Lausanne, 2001.

[43] Nobile F., Veneziani A., Vergara C., Fluid-Structure interactions problem for incompressible fluids. In preparation.

[44] Olufsen M.S., Peskin C.S., Kim W.Y., Pedersen E.M., Nadim A., Larsen J., Numerical Simulation and Experimental Validation of Blood Flow in Arteries with Structured-Tree Outflow Conditions *Annals of Biomedical Engineering*; **28**: 1281-1299, 2000.

[45] Pennati G., Bellotti M., Ferrazzi E., Bozzo M., Pardi G., Fumero R., Blood flow through the ductus venosus in human fetus: calculation using Doppler velocimetry and computational findings, *Ultrasound in Med. and Biol.*; **24**(4): 477-487, 1998.

[46] Pennati G., Redaelli A., Bellotti M., Ferrazzi E., Computational analysis of the ductus venosus fluid-dynamics based on Doppler measurements, *Ultrasound in Med. and Biol.*; **22**(8): 1017-1029, 1996.

[47] Perktold K., Hofer M., Rappitsch G., Loew M., Kuban B.D., Friedman M.H., Validated computation of physiologic flow in a realistic coronary artery branch, *J. Biomech.*; **31** Mar(3): 217-28.1998

[48] Perktold K., Prosi M., Computational models of arterial flow and mass transport. In: Pedrizzetti, G., Perktold, K., (Eds.), *Cardiovascular Fluid Mechanics, CISM Courses and Lecture No. 446*, Springer-Verlag Wien New York, 73-136, 2003.

[49] Ponzini R., Lemma M., Morbiducci U., Antona C., Montevecchi F., Redaelli A., Doppler derived quantitative flow estimate in coronary artery bypass graft: a computational multi-scale model for the evaluation of the current theory. Submitted.

[50] Ponzini R., Vergara C., Redaelli A., Veneziani A., Reliable CFD-based estimation of flow rate in haemodynamics measures. Submitted to *Ultrasound in Med. and Biol.*.

[51] Quarteroni A., Ragni S., Veneziani A., Coupling between lumped and distributed models for blood flow problems, *Comp. Vis. Science*; **4**: 111–124, 2001.

[52] Quarteroni A., Rozza G., Optimal control and shape optimization of aorto-coronaric by-pass anastomosis, *M3AS*; **13**(12): 1801-1823, 2003.

[53] Quarteroni A., Saleri F., Veneziani A., Factorization methods for the numerical approximationof Navier-Stokes equations. *Comp. Meth. Appl. Mech. Eng.*; **1888**: 505-526, 2000.

[54] Quarteroni A., Tuveri M., Veneziani A., Computational Vascular Fluid Dynamics: Problems, Models and Methods, *Computing and Visualisation in Science*; **2**: 163-197,2000.

[55] Quarteroni A., Valli A., *Numerical Approximation of Partial Differential Equations*, Springer, 1994.

[56] Quarteroni A., Veneziani A., Analysis of a geometrical multiscale model based on the coupling of ODE's and PDE's for blood flow simulations, *SIAM Multiscale Models Simulation*; **1**(2): 173-195, 2003.

[57] Quarteroni A., Veneziani A., Zunino P., Mathematical and numerical modeling of solutes dynamics in blood flow and arterial wall, *SIAM J. Num. An.*; **39**(5): 1488-1511, 2002.

[58] Rannacher R., On Chorin's Projection Method for the Incompressible Navier-Stokes Equations, *Lecture Notes*, Springer, 1991.

[59] Redaelli A., Boschetti F., Inzoli F. The assignement of velocity profiles in finite element simulations of pulsatile flow in arteries *Comput. Biol. Med.*; **27**(3): 233-247, 1997.

[60] Robertson M. B., Khler U., Hoskins P. R., Marshall I., Flow in Elliptical Vessels Calculated for a Physiological Waveform *Journal Of Vascular research* ; **38**: 73-82, 2001.

[61] Saad Y., Iterative Methods for Sparse Linear System, PWS Publishing Company, Boston, 1996.

[62] Savader S.J., Lund G.B., Osterman F.A., Volumetric evaluation of blood flow in normal renal arteries with a Doppler flow wire: a feasibility study *Journal of Vascular and Interventional Radiology*; **8**(2): 209-214, 1997.

[63] Sheada R.E., Cobbold R.S., Johnston K.W.,Aarnink R. Three-dimensional display of calculated velocity profiles for physiological flow waveforms. *J. Vasc. Surg.*; **17**(4): 656-60, 1993.

[64] www.cfm.brown.edu/people/tcew/nektar.html

[65] Sobey I., On flow through furrowed channels. Part I. Calculated flow pattern, *J. Fluid Mech.*; **96**: 1-26, 1980.

[66] Taylor CA, Draney MT, Ku JP, Parker D, Steele BN, Wang K, Zarins CK, Predictive medicine: Computational techniques in therapeutic decision-making, *Computer Aided Surgery*; **5**(5): 231–247, 1999.

[67] Temam R., *Navier Stokes equations and nonlinear functional analysis*, SIAM, Philadelphia, 1995.

[68] Veneziani A., A Mathematical and Numerical modeling of blood flow problems, *Ph.D. thesis*, University of Milan, 1998.

[69] A. Veneziani, Block Factorized Preconditioners for High-order Accurate in Time Approximation of the Navier-Stokes Equations, *Num. Meth. PDE's*; **19**: 487-510, 2003.

[70] Veneziani A., Vergara C., Flow rate defective boundary conditions in haemodinamics simulations, *Int. Journ. Num. Meth. Fluids*; **47**, 803-816, 2005.

[71] Veneziani A., Vergara C., An approximate method for solving incompressible Navier-Stokes problem with flow rate conditions. Submitted to *Comp. Meth. Appl. Mech. Eng.*.

[72] Vergara C., Metodi Numerici per il Trattamento di Condizioni al Bordo Defettive di Portata in Simulazioni Emodinamiche, *Degree thesis*, Politecnico di Milano, 2002.

[73] Viedma A., Jimnez-Ortiz C. and Marco V., Extended Willis Circle model to explain clinical observations in periorbital arterial flow,*Journal of Biomechanics*; **30** (3): 265-272, 1997.

[74] Weiman A.E., Principles and Practice of echocardiography (second edition), Lea & Febiger, 1994.

[75] Wells R., Syndromes of hyperviscosity, *N. Engl. J. Med.*; **283**(4): 183-186, 1970.

[76] Whitaker S., *Introduction to Fluid Mechanics*, R.E. Krieger, Malabar, FL, 1984.

[77] Wolthuis R.A., Froelicher Jr V.F., Fischer J., Triebwasser J.H., The response of healthy men to treadmill exercise *Circulation*; **55**: 153-157, 1977.

[78] Womersley J.R., Oscillatory motion of a viscous liquid in a thin-walled elastic tube: I. The linear approximation for long waves, *Philosophical Magazine*; **46**: 199-221, 1955.

[79] Younis H.F., Kaazempur-Mofrad M.R., Chan R.C., Isasi A.G., Hinton D.P., Chau A.H., Kim L.A., Kamm R.D., Hemodynamics and wall mechanics in human carotid bifurcation and its consequences for atherogenesis: investigation of the inter-individual variation, *Biomech. Model Mechanobiol.*; **3**: 17-32,2004.

[80] Zunino P., Multidimensional pharmacokinetic models applied to the design of drug eluting stents, *Cardiov. Eng.*; **4**(2), 2004.

[81]